Towards rapid, high-resolution measurement of luminescence-depth profiles using 2D InfraredPhotoluminescence imaging

Elaine Louise Sellwood

Ph.D. Thesis
Technical University of Denmark
Department of Physics
December 2021

DTU

Department of Physics
Technical University of Denmark

Frederiksborgvej 399
Building 201
4000, Roskilde, Denmark
Phone +45 5017 3624
el.sellwood@gmail.com

This work is dedicated to my family and friends who have wholeheartedly supported me over the past three years, even if they have not understood a single thing that I have been doing during this time.

Preface

This dissertation fulfills part of the requirements for receiving a PhD from the department of Physics, at the Technical University of Denmark. The work presented here is part of a research project conducted between the 1st of September 2018 and the 23rd of December 2021. Research was conducted at the luminescence laboratory as part of the department of Physics located at the DTU Risø campus, Roskilde. The work was completed under the supervision of Senior scientist, Mayank Jain (main supervisor), Senior development engineer Myungho Kook (co-supervisor) and Senior researcher Kristina Thomsen (co-supervisor).

The purpose of this PhD was to further the field of rock surface dating using imaging of luminescence from feldspar. The main aims of this research were to develop and test new instrumentation for the imaging of IRSL and IRPL from large (cm-scale) feldspatic rock samples, and demonstrate the suitability of such instrumentation for various applications of rock surface dating. This thesis presents the results of the work conducted to meet these aims.

Acknowledgements

Throughout my PhD, I have met and been supported by many people, and I wish to extend the warmest gratitude to all of them. It only seems right to start by thanking Benny Guralnik, who was the person to first bring me to Risø, DTU as part of an MSc internship. The research we conducted together laid the foundations of this PhD and I thank him for all the initial support and encouragement. I next thank my supervisors Dr. Mayank Jain, Dr. Myungho Kook and Dr. Kristina Thomsen who have all played different roles in my research journey. I thank Mayank Jain for being a great source of knowledge and ideas and for motivating me to grow as a scientist. Myungho Kook has supported me and provided valuable knowledge on the technical or engineering aspects of my work. I thank Kristina Thomsen for her continuous support on a more personal level, and for understanding and supporting me when I have felt overwhelmed or lost in the never ending to-do lists of a PhD.

I wish to thank Mark Bailey, Torben Esmann Mølholt, Arne Miller, Linda Bohn and Bente Pedersen for their continuous help with the irradiation facilities at Risø. I have really appreciated your good humor and friendliness even when I was continuously turning up in your offices to get my chunks of rock or "paté" irradiated. I also thank Claus Andersen for providing information and access to irradiation facilities. I thank Lars Lindvold for being a great source of knowledge on optics. Extensive thanks to the techinal staff at Risø: Søren Vig Dalsgaard, Per Günther Sørensen, Karsten Bracht Nielsen, Finn Jørgensen who have always been happy to provide equipment and help with instrumentation. I thank the technicians Vicki Hansen and Warren Thompson for always offering help with the laboratories and for sharing their knowledge on sample processing and equipment and for always being welcoming (and happy to discuss rocks). I extend special thanks to Henrik Olesen, who I have enjoyed working closely with and who is always enthusiastic and curious and has helped me stay motivated. I thank you also for all your hard work in the lab, processing all of those rock samples. I thank Reza Sohbati, Jan-Pieter Buylaert and Eike Rades for always being willing to share their invaluable knowledge, and Kasper Grann Andersson for being a friendly face and always up for a chat. Extensive gratitude goes to Marete Holmegaard and Pia Elhauge who keep the whole department running smoothly and have always been so helpful with official matters. A thank you to Tue Strange Nygaard for always being a driving force behind the enjoyable social events, and for providing a never ending stream of entertaining memes.

A huge thank you goes to my office mates, the other PhDs and Postdoc students, and to guests who I have had the pleasure of meeting: Trine, Jakob, Magaldena, Nicola, Martin, Pavao, Amélie, Frederik and Ashkhen. I thank Antariksh the vegan, Mette and Malene for their amazing friendship. I thank also Madalina and Horia, Laure, Sahar, Nasrin, Dasha, Daria, Anna, Cobus and Estee. You have become great friends after we met here at Risø and I really treasure your friendships.

Finally, I wish to thank my partner Glenn Oxfeldt Jensen for your never ending support and patience with me. A big thank you goes to the author Annette Marie, whose books have gotten me through the past couple of years. If only I was as efficient at writing as you are. I thank the Oxfeldt family for always supporting me and understanding when I couldn't make it to family

events. I thank the Feering crew for their continuing friendship and for always welcoming me when I have come home as though I had never been away. And thank you to my Mum, Dad, sister and my Nan, who may not know what I am talking about most of the time, but who have always and will always support me. Nanny Sellwood, I know you would have been proud of me.

And thank you to anyone who I have regretfully forgotten to mention, and to anyone reading this.

All the best to all of you,

Elaine Sellwood.

Abstract

Rock surface dating (RDS) with optically stimulated luminescence (OSL) utilises the principal that upon exposure to light, the luminescence at the rocks surface will be reset. Over time, the OSL is bleached to greater depths from the surface, and from measuring the luminescence-depth profile and fitting it with age models one can determine the total exposure duration. If the exposed surface is then buried, dose will start to accumulate, and the burial age of the rock can be determined following conventional OSL methods. However, in its current form, RSD with OSL demands laborious sample collection and processing, and data sets are often of low resolution. The current age models are also limited in their representation of the true luminescence kinetics (especially of feldspar) and of the interaction of light with matter. Recently, two infrared-photoluminescence (IRPL) emissions at 880 nm and 955 nm, have been characterised in feldspar. Contrary to IRSL, these signals arise from radiative relaxation of the electrons from the excited to ground states within the principal trap, with thousands of photons able to be generated per second, and high stability due to more distal location with respect to recombination centres. These characteristics make it suitable for luminescence imaging purposes. Imaging of luminescence would be highly beneficial for rock surface dating applications, increasing the data resolution and speeding up sample preparation and measurement times.

The main purpose of this PhD was to improve on instrumentation for imaging of luminescence from feldspar, with a focus on the development of methods for rock surface dating. A new EMCCD-based instrument titled the Risø Luminescence Imager is described. The novelties of this instrument include its suitability for measuring both IRPL at 880 nm and 955 nm, as well as IRSL at high resolution (~170 μm). Images can be taken of large cm-scale rock samples, up to ~7 $\times$ 7 cm in size. Full IRSL decay curves can be obtained through time-lapse measurements of the IRSL.

Several applications using the Risø Luminescence Imager are presented. I demonstrate several alternative methods for normalising IRPL and IRSL luminescence-depth profiles. These include: taking the ratio between the IRPL 955/880 nm data, calculating the ΔIRPL, and normalising natural IRSL by a later part of the decay curve. These normalisation methods open up the possibility of RSD to laboratories which lack irradiation facilities. A dose recovery study is presented in chapter 4, describing measurement and analysis protocols for rock surface burial dating using imaging. Two samples with known exposure and "burial" histories were measured. The IRSL burial doses were able to be recovered from the surface ~5 mm of both rock samples, but from the IRPL data, the dose recovery was only successful for the sample with the higher "burial" dose (500 Gy). A novel application where the principles of OSL RSD are applied to three cracks of known chronological formation is presented in chapter 6. Through imaging a plane perpendicular to the crack surface, the extent of IRSL and IRPL bleaching around the crack can be assessed. Through estimating the maximum bleached regions for the three cracks, a relative chronology of crack formation was established, consistent with field observations.

Until now, age models for determining the exposure durations have not been applied to IRPL data sets. Chapter 5 presents a novel in-depth study of the development of IRSL and IRPL luminescence-depth profiles as a function of time and specific wavelength, and explores the

suitability of first-order and general-order age models for representing the data. The IRPL-depth profiles progress deeper from the surface with increasing exposure time, along with a decrease in attenuation coefficient due to the preferential attenuation of higher-energy wavelengths. It was established that IRPL luminescence-depth profiles can be represented adequately by first order kinetics through fitting of the first order model.

The research presented in this thesis will benefit the field of rock surface dating by offering easily adaptable instrumentation for high-resolution imaging of multiple luminescence signals from feldspar. The results present measurement protocols and data analysis procedures suitable for applications of rock surface burial and exposure dating using imaging. This research also paves the road for further development of novel dating methods for cracks and cracked landscapes, as well as for developing field instrumentation which would allow *in situ* measurement of luminescence.

Dansk Resumé

Klippeoverfladedatering (RDS) med optisk stimuleret luminescens (OSL) anvender princippet om, at luminescensen ved klippernes overflade vil blive nulstillet ved eksponering for lys. Over tid bleges OSL til større dybder fra overfladen, og ved at måle luminescens-dybdeprofilen og tilpasse den med aldersmodeller kan man bestemme den samlede eksponeringsvarighed. Hvis den blottede overflade derefter begraves, vil dosis begynde at akkumulere, og klippens gravalder kan bestemmes ved at følge konventionelle OSL-metoder. Men i sin nuværende form kræver RSD med OSL besværlig prøveindsamling og -behandling, og datasæt er ofte af lav opløsning. De nuværende aldersmodeller er også begrænsede i deres repræsentation af den sande luminescenskinetik og af lysets interaktion med stof. For nylig er to infrarød-fotoluminescens (IRPL) emissioner ved 880 nm og 955 nm blevet karakteriseret i feldspat. I modsætning til IRSL opstår disse signaler fra strålingsrelaksation af elektronerne fra de exciterede til jordtilstande inden for hovedfælden, med tusindvis af fotoner, der kan genereres pr. sekund, og høj stabilitet på grund af mere distal placering i forhold til rekombinationscentre. Disse egenskaber gør den velegnet til luminescensbilleddannelsesformål. Billeddannelse af luminescens ville være yderst fordelagtig for klippeoverfladedateringsapplikationer, hvilket øger dataopløsningen og fremskynder prøveforberedelse og -målingstider.

Hovedformålet med denne Ph.D. var at forbedre instrumentering til billeddannelse af luminescens fra feldspat med fokus på udvikling af metoder til klippeoverfladedatering. Jeg beskriver nye instrument designs til billeddannelse af luminescens fra klippeprøver, og demonstrationer med fokus på dateringsmuligheder for klippeoverflade. Et nyt EMCCD-baseret instrument med titlen Risø Luminescence Imager er beskrevet. Nyskabelsen ved dette instrument omfatter dets egnethed til at måle både IRPL ved 880 nm og 955 nm samt IRSL ved høj opløsning (~170 ţm). Der kan tages billeder af stenprøver i stor cm-skala, op til ~7 x 7 cm i størrelse. Fuld IRSL henfaldskurver kan opnås gennem time-lapse målinger af IRSL.

Flere anvendelsesmuligheder for brug af Risø Luminescence Imager, præsenteres. I kapitel 3 præsenteres et studie, hvor IRSL og IRPL fra naturligt blegede bjergarter blev afbilledet, og hvorfra luminescens-dybdeprofiler blev rekonstrueret. Det blev fastslået, at ved at tage forholdet mellem IRPL 955/880 nm-dataene, beregne IRPL samt normalisere naturlig IRSL ved en senere del af henfaldskurven, kan luminescens-dybdeprofiler rekonstrueres uden behov for en strålingsdosis til regenerering til normalisering, hvilket åbner op for muligheden for datering af klippeoverflader ved hjælp af billeddannelse hos laboratorier, hvor bestrålingsfaciliteter ikke er tilgængelige. En demonstration af en gængs SAR-sekvens ved hjælp af billeddannelse til at

genskabe kendte overfladedoser fra stenprøver findes i kapitel 4 i en demonstration af billeddannelsesprotokol, der er egnet til datering af begravelseshistorik af klippeoverflader. To prøver med kendt blegning og "begravelseshistorier" blev målt. IRSL begravelses-doserne var i stand til at blive genskabt fra overfladen ~5 mm af begge stenprøver, men ud fra IRPL-dataene lykkedes dosisgengivelsen kun for prøven med den højere "begravelsesdosis" (500 Gy).

En ny anvendelse, hvor principperne for OSL RSD anvendes på tre sprækker med kendt kronologisk dannelse, er præsenteret i kapitel 6. Gennem billeddannelse af et plan vinkelret på sprækkeoverfladen kan omfanget af blegning af IRSL og IRPL omkring sprækken vurderes. Ved at estimere de maksimale blegede områder for de tre sprækker, blev der etableret en relativ kronologi af sprækkedannelse, i overensstemmelse med feltobservationer. Kapitel 5 præsenterer en ny dybdegående undersøgelse af udviklingen af IRSL og IRPL luminescens-dybde profiler som en funktion af tid og specifik bølgelængde, og udforsker egnetheden af første-ordens og generel-ordens aldersmodeller til at repræsentere dataene. Luminescens-dybdeprofilerne udvikler sig dybere fra overfladen med stigende eksponeringstid sammen med et fald i dæmpningskoefficienten på grund af den foretrukne dæmpning af højere energibølgelængder. Det blev fastslået, at IRPL luminescens-dybde profiler kan repræsenteres tilstrækkeligt af første ordens kinetik gennem tilpasning af første ordens model.

Forskningen præsenteret i denne afhandling vil gavne området for overfladisk rockdating ved at tilbyde let tilpasningsdygtig instrumenter til billeder med høj opløselighed af adskillelige luminescenssignaler fra feldspat. Resultaterne præsenterer måleprotokoller og dataanalyseprocedurer, som er egnet til anvendelser af klippeoverfladebegravelse og eksponeringsdatering ved hjælp af billeddannelse. Denne forskning baner ligeledes vejen for yderligere udvikling af nye dateringsmetoder for revner og opsprækkede landskaber, samt for udvikling af feltinstrumenter, som vil tillade in situ måling af luminescens.

Contents

Abbrevaiations

2D	Two Dimensional
3D	Three Dimensional
Ca	Calcium
CB	Conduction Band
CCD	Charge Coupled Device
D_R	Dose Rate ($Gyka^{-1}$)
EMCCD	Electron Multiplying Charge Coupled Device
Fe	Iron
FOM	First Order Model
GOM	General Order Model
HR	High-Resolution
IR	Infrared
IRPL	Infrared Photo-Luminescence
$IRSL_t$	Infrared Stimulated Luminescence, at temperature t
K	Potassium
Ln	Natural Luminescence
Lx	Regenerated Luminescence
MAAD	Multiple Aliquot Additive Dose
Na	Sodium
NIR	Near-Infrared
OSL	Optically stimulated luminescence
PH	Pre-heat
$pIRIR_t$	Post Infrared Infrared Stimulated Luminescence at temperature t
RSBD	Rock Surface Burial Dating
RSD	Rock Surface Dating
RSED	Rock Surface Exposure Dating
RT	Room Temperature
SAR	Single Aliquot Regenerative
SD50%	50% of Saturation Depth
SAAD	Single Aliquot Addative Dose
TL	Thermo-Luminescence
Tx	Test dose
UV	Ultra-Violet
VB	Valance Band
μ-XRF	Micro X-Ray Flourescence

Table 1: List of abbreviations

CHAPTER 1

Introduction

1.1 Motivation and purpose

From crustal uplift, erosion and weathering to the transportation and deposition of natural material, there are a multitude of processes continuously shaping the Earths' surface. It has been well established that these processes are tightly coupled with climate systems on both a local and global scale, and with the current discussions over climate changes and the human impact on our environment, it is ever more crucial to obtain a full understanding of how our natural environment has developed. One such angle of investigation follows the determination of the rates of change of these Earth-surface processes. How much soil erosion occurs when land use changes? How fast is a mountain eroding? How far is sediment transported along catchment areas? Such questions are being asked by scientists around the world and several methods involving the measurement of luminescence have been established which are helping us to answer these questions.

Luminescence dating techniques offer a means to determine the ages of geological or archaeological events over the Late Quaternary Period (Lian et al., 2006). The techniques utilise quartz and feldspar minerals which are ubiquitous in the Earths crust. Upon deposition and burial, these minerals absorb ionising radiation from the natural surrounding environment, which accumulates as a function of time. Part of the absorbed energy is stored in the form of a trapped charge population and can be released by exposure to heat or light (e.g. daylight). Under laboratory conditions, measurement of this trapped charge population can be conducted by stimulating the chosen minerals with either heat (thermoluminescence; TL; Daniels et al., 1953) or light at specific wavelengths (optically stimulated luminescence; OSL; Huntley et al., 1985), and measuring the luminescence emission. This signal can be translated into an age, informing us as to how long a sample has been accumulating charge for, and thus how long the deposit has been emplaced (i.e., buried). Over the past few decades there has been a continuing stream of methodological and technical advancements for obtaining accurate and reliable luminescence chronologies. Such advancements include definition of new measurement protocols to isolate stable OSL or TL signals (e.g. Wintle, 1977; Duller, 1991; Wallinga et al., 2002; Buylaert et al., 2009; Thomsen et al., 2011; Kars et al., 2012; Duller et al., 2020b), extending the datable range of deposits (e.g. Li et al., 2013; Wallinga et al., 2015; Bailiff et al., 2021), and developments of instrumentation to maximise measurement efficiency and allow measurement of different materials (Stanley, 1983; Bøtter-Jensen et al., 2010; Kook et al., 2011; Chauhan et al., 2014; Mundupuzhakal et al., 2014; Thomsen et al., 2015; Kook et al., 2018).

One of the more recent developments in OSL dating has been towards dating the exposure or burial durations of rock surfaces. When a previously buried rock is first exposed to sunlight, the luminescence at its surface is quickly zeroed, while the traps located further into the rock are unaffected due to the rapid attenuation of light in rocks (Habermann et al., 2000; Vafiadou et al., 2007; Ou et al., 2018). With increasing exposure times, these traps further from the surface will also be emptied. By measuring the luminescence signal as a function of depth into the rock (i.e., the luminescence-depth profile), and fitting the profile with models, one can establish how

long a rock has been exposed to sunlight (Theocaris et al., 1997; Polikreti et al., 2002; Polikreti et al., 2003; Sohbati et al., 2011; Chapot et al., 2012; Sohbati et al., 2012c). Should this now bleached surface be buried again, charge will begin to accumulate and a burial duration of the rock surface can be established through OSL measurement (Vafiadou et al., 2007; Chapot et al., 2012; Sohbati et al., 2015; Gliganic et al., 2021). However, further applications of OSL rock surface dating are hindered by a lack of a fundamental understanding of how light interacts with heterogeneous materials. There is also a need to improve the current age models which describe the bleaching of luminescence with depth. Currently, the models make several assumptions of how light is transmitted through rocks and of the kinetics of the luminescence processes. The models are becoming increasingly recognised to be insufficient to represent nature (Sohbati et al., 2012a; Freiesleben et al., 2015).

A second recent development in luminescence dating has been the identification of two IR-stimulated photoluminescence (IRPL) emissions from feldspar (Prasad et al., 2017; Jain et al., 2020; Kumar et al., 2020a). Conventional luminescence measurements from feldspar utilise an infrared ($\sim$ 860 nm, Hütt et al., 1988) stimulated emission detected in the blue region (Hütt et al., 1988; Hutt, 1989), which is known to have problems with stability (i.e. the trapped charge population can exit the trap and recombine without optical or thermal stimulation; Wintle, 1977; Spooner, 1994; Thomsen et al., 2008) and can experience sensitivity changes during measurement sequences in response to bleaching or heating (e.g. Li et al., 2013; Colarossi et al., 2018). The two recently characterised infrared-photoluminescence emissions with peaks at 880 nm and 955 nm, result from intra-trap radiative relaxation of charge from the excited to ground state, instead of from recombination with hole centres, as is the case with IRSL. Upon stimulation, thousands of photons can be produced from the same trap, instead of single photons representing a recombination event. IRPL is highly stable and can be measured multiple times, or for extended measurement duration without significantly releasing the trapped charge, making its use highly enticing for dating applications where feldspar is the mineral in focus. So far, only a handful of publications have used these signals for dating applications (e.g. Duller et al., 2020a; Kumar et al., 2021b). Thus there are still significant questions concerning the bleachability of IRPL, the sensitivity to radiation doses and the suitability of these signals for burial age determination or rock surface dating.

The research objectives for this PhD were defined following the need for improved methodology for OSL dating of rock surfaces (through all stages from sampling to profile modelling), and for exploring the applicability of IRPL to dating applications. The work presented here directly followed from the publication by Sellwood et al. (2019), who recognised and demonstrated the potential of spatially resolving IRPL from heterogeneous rock samples for RSD. Through developing a prototype EMCCD-based imaging system, they imaged the natural IRPL luminescence-depth profiles for rock surface exposure dating. The steady-state nature of IRPL allowed for integration limits to be defined as to maximise the signal-to-noise ratio, and the resulting images were high-resolution allowing mineral boundaries and structures to be easily identified. This initial study highlighted the suitability of IRPL for spatially resolved measurement, and was a clear demonstration of how applications of RSD could be improved as imaging of large rock slabs avoided the laborious sample preparation stages, and greatly increased the data resolution.

The purpose of my PhD was to develop and test a robust 2D imaging system for IRPL and IRSL measurement from large rock samples, with a focus on rock surface dating techniques. The project had a significant focus on investigating the behaviour of IRSL and IRPL in exposed and buried rock surfaces and establishing the suitability of IRSL and IRPL imaging for such dating applications. The implications of my research expand from instrumental development to understanding of the optical responses of IRSL and IRPL in rocks. I hope my scientific findings

and novel instrumentation for spatially resolving IRSL and IRPL will open the door for many researchers interested in rock surface dating using feldspar.

1.2 Luminescence Mechanisms

Luminescence dating is dependent on the trapping and long-term (on geological timescales) storage of charge which accumulates as a function of time and the surrounding dose rate from surrounding radioactive elements. When minerals such as quartz or feldspar are exposed to ionising radiation in the form of alpha, beta and gamma particles, energy is absorbed and the crystalline lattice becomes ionized. This leads to the formation of charge carriers (free electrons and holes) which can subsequently be trapped at distinct sites within the crystal lattice as metastable states (Aitken, 1985) (see Figure 1.1a). These trapping sites occur at specific energy levels below the conduction band, within the band gap, and can be at locations in a material where defects or compositional impurities occur (Poolton et al., 2003; Malins et al., 2004).

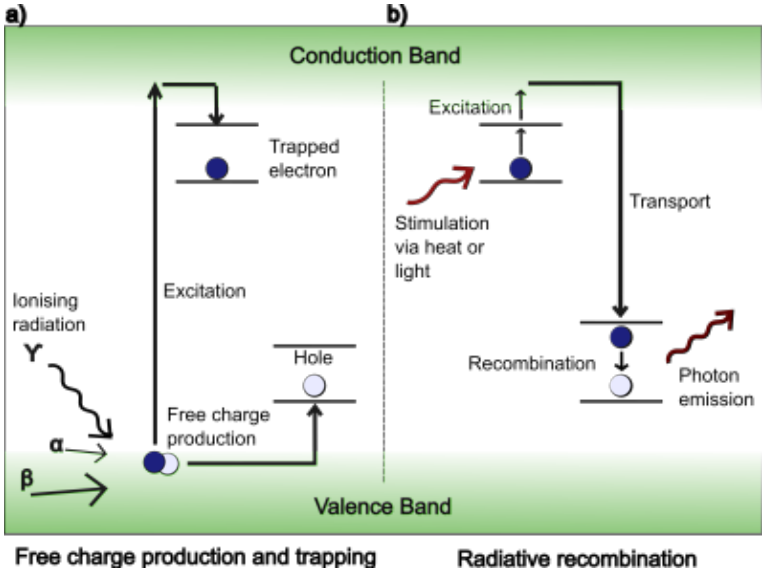

Figure 1.1: a) Basic schematic of trapped charge mechanisms, and b) radiative recombination upon stimulation with heat or light.

The energy level at which the trapping sites occur is a characteristic of the trap (the trap depth) and is representative of the energy required to release the trapped charge (Randall et al., 1945; Hütt et al., 1988; Aitken, 1998; Preusser et al., 2008; Kars et al., 2013). Upon re-excitation with a suitable stimulation energy, charge is moved to the excited state or straight to the conduction band, exiting the trap, and recombining with a recombination centre (hole; Figure 1.1b). Here, luminescence refers to the radiative recombination wherein a photon is produced as a result of this recombination. The number of emitted photons is considered proportional to the number of recombining charge pairs, which in turn represents the absorbed dose in the material under certain boundary conditions (Huntley et al., 1985).

1.2.1 OSL Dating

Methods of luminescence dating bvegan with using thermal stimulation (thermoluminescence; TL) for releasing trapped charge (Daniels et al., 1953; Aitken, 1985). However, more often than not, the zeroing of latent luminescence in nature (resetting) is reliant upon the optical

bleaching via sunlight exposure. This led to a significant residual often being encountered in TL signals (Wintle et al., 1980; Liritzis et al., 1999), preventing accurate determination of the original absorbed dose. This pushed the dating method towards using optical stimulation for measurement of charge populations (Huntley et al., 1985), as the resetting of these signals is easier. Through stimulation with isolated wavebands of light, different trap populations can be probed, and detection of the resulting OSL is done through specific detection windows through defined filter set-ups. To translate the measured luminescence emission into a burial age, two main pieces of information need to be acquired: 1) the palaeodose (i.e. the dose absorbed during burial) and, 2) the dose rate from the contributing ionising radiation. Once the palaeodose (Gy) has been established, it can be divided by the measured dose rate to determine the burial time (Eq.1.1):

$$Age\ (\mathrm{a}) = \frac{Palaeodose\ (\mathrm{Gy})}{Dose\ rate\ (\mathrm{Gy\ a^{-1}})} \tag{1.1}$$

There are multiple measurement protocols by which the absorbed dose can be estimated (e.g., additive dose determination, multi-aliquot and single-aliquot regenerative dose determination) (Duller, 1991; Murray et al., 1998; Murray et al., 2003; Duller et al., 2020b). In general, the number of photons released during charge recombination are counted following stimulation. This is calibrated against luminescence from known laboratory given doses to establish the natural equivalent dose (D_e, Gy), representative of the natural palaeodose. The dose rate (Gy a^{-1}) is calculated as the total contribution from alpha, beta, and gamma irradiation from radioactive elements such as ^{238}U, ^{232}Th, ^{40}K, ^{226}Ra from the natural surrounding environment, cosmic rays, and internal radioactive elements within the sample itself. The bulk concentrations of the radioactive elements are often determined using high-resolution gamma spectrometry, and through using conversion factors (Guérin et al., 2011) transformed into infinite-matrix dose rates. The time elapsed since a sample was buried and shielded from light or heat can be determined according to Eq.1.1.

1.2.2 Luminescence Mechanisms in Feldspar

The term feldspar refers to a group of tectosilicates, which are one of the most abundant rock-forming mineral groups found in the Earths crust. The feldspar series follows the general structure of MT_4O_8 (T = tetrahedral sites, M = cation sites) (Deer, 2001). Compositionally, the series follows a continuous solid-solution between three end members: orthoclase ($KAlSi_3O_8$) - albite ($NaAlSi_3O_8$) - anorthite ($CaAl_2Si_2O_8$); compositions are classified into either plagioclase (Ca - Na) or alkali feldspar (K - Na). The feldspar lattice hosts multiple defects via elemental substitutions; Fe^{3+} is known to substitute at Al^{3+} sites (T1 sites) in alkali feldspars, and Mn2+ substitutes for K, Na or Ca (M sites, especially in plagioclase) (Krbetschek et al., 1997). Whilst the band gap in feldspar has been established to be ~7.7-7.8 eV (Malins et al., 2004), the presence of such aforementioned defects define different traps and recombination centres within feldspar. The presence of randomly distributed defects and such impurities also leads to the formation of band-tail states just below the conduction band (see Figure 1.2a) (Poolton et al., 2002). These states are of localised energy levels, and are known to actively participate in the transition of excited electrons to and just below the conduction band (Jain et al., 2011).

The main dosimetric trap used for OSL dating with feldspar was first characterised by Hütt et al. (1988), who identified an IR-stimulated luminescence emission (IRSL) detected within the violet region (~405 nm; see Figure 1.3). Whilst there is still some ambiguity over the defect

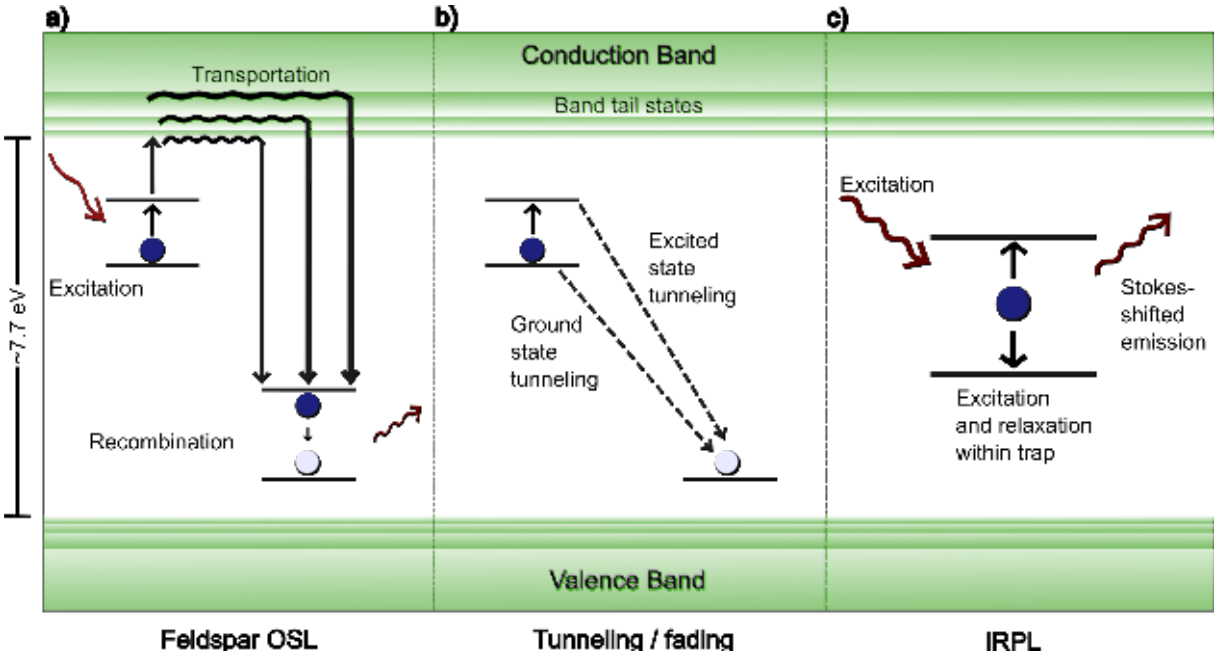

Figure 1.2: a) Schematic of OSL mechanisms in feldspar, including transition of electrons via the band-tail states, stimulation and the production of anti-Stokes emissions. b) Schematic of ground and excited state tunnelling. c) Schematic of electron behaviour in the generation of the Stokes-shifted IRPL from the principal trap. Diagrams have been adapted from Jain et al. (2011)

which is responsible for this trapping site, multiple studies have tried to identify the trap depth (e.g. Huntley et al., 1985; Hütt et al., 1988; Poolton et al., 2002). It is generally considered that the IRSL emission results from a combination of several excited states, with trap depths between 1.9 eV and 2.5 eV (Hütt et al., 1988; Bøtter-Jensen et al., 1994; Jain et al., 2011). Following excitation of charge from the principal trap via NIR - IR wavelengths, electrons undergo detrapping and can traverse the band-tail states, or dropping into a recombination centre (Figure 1.2a) (Poolton et al., 2002; Jain et al., 2011).

One phenomenon observed from the principal trap is the athermal loss of charge over time. This anomalous fading (Wintle, 1977; Spooner, 1994; Huntley et al., 2001) of the trap population results in an underestimate of the true trap population, which in turn results in age underestimates. The relation between proximal trapping sites and holes can result in the direct transition of the electron (from either the ground or excited state; Wintle, 1977; Poolton et al., 2009) to the hole site via quantum mechanical tunnelling - without passing through the conduction band (see Figure 1.2b) (Jain et al., 2011). This can be non-radiative and can occur without extra energy input into the system (Krbetschek et al., 1997). This phenomenon occurs often in feldspar of plagioclase composition and less so within the alkali feldspar making these favourable for dating applications. When using feldspar for dating applications, a correction for any potential fading is applied to the age. This correction can be obtained by either making a measurement of the fading rate (g-value %; Auclair et al., 2003) determined by irradiating feldspar samples in the laboratory and incrementally measuring the remaining luminescence after different times, or from taking the ratio between the laboratory and natural saturation levels in the sample (Rades et al., 2018).

1.2.3 Infrared-Photoluminescence

With the problems surrounding IRSL stability as mentioned above, it is highly desirable to identify luminescence emissions from feldspar which do not display such undesirable characteristics. Through stimulation of the principal trap with IR wavelengths, it is possible to isolate a Stokes-shifted emission (of longer wavelength than the stimulation) still within the IR range. Contrary to OSL, this emission is not dependent on radiative recombination of free charge, but on the oscillating transition of charge from excited to ground state within the principal trap. Excitation with IR and NIR wavelengths can lead to the electron transitioning to the excited state of the trap. As the electron drops back to the ground state, a photon is produced; such an emission is termed infrared-photoluminescence (IRPL) (Figure 1.2c). Compared to IRSL, IRPL measurements boast several advantages: 1) non-destructive measurements allowing multiple and extended read-out times, 2) distal location to recombination sites means IRPL is considered to have a stable steady state component (i.e. non-fading; Jain et al., 2020), and 3) electron oscillation within the trap produces thousands of photons per second, offering unprecedented measurement sensitivity (Jain et al., 2020). These advantages are enticing for luminescence dating applications, as a correction for fading would not need to be applied to the burial age. The high sensitivity is especially promising for luminescence imaging purposes, where the luminescence could be mapped at the micron-scale.

Prasad et al. (2017) extensively characterised a Stokes-shifted emission peak from the principal trap at 955 nm (~1.30 eV; $IRPL_{955}$) following excitation with an 885 nm (1.40 eV) laser (see Figure 1.3). Following this work, Kumar et al. (2018) identified two separate IRPL peaks, with a second centred around 880 nm (1.41 eV; $IRPL_{880}$). Full analysis of the excitation spectra of IRPL provides information of the excited-to-ground state transitions within the trap itself. The two IRPL centres respond similarly to dose, but differ in thermal stability, and have different bleachabilities. The $IRPL_{955}$ centre is found to be at more proximal distances to recombination centres than the $IRPL_{880}$ centre, thus presenting greater bleachability upon exposure to light, and is affected to a greater extent by IRSL measurement where up to 50% of the trapped charge population can be lost, compared to the $IRPL_{880}$ centre (Jain et al., 2020). Such considerations are crucial for applications involving determination of burial doses where it is paramount that the luminescence is completely reset prior to burial.

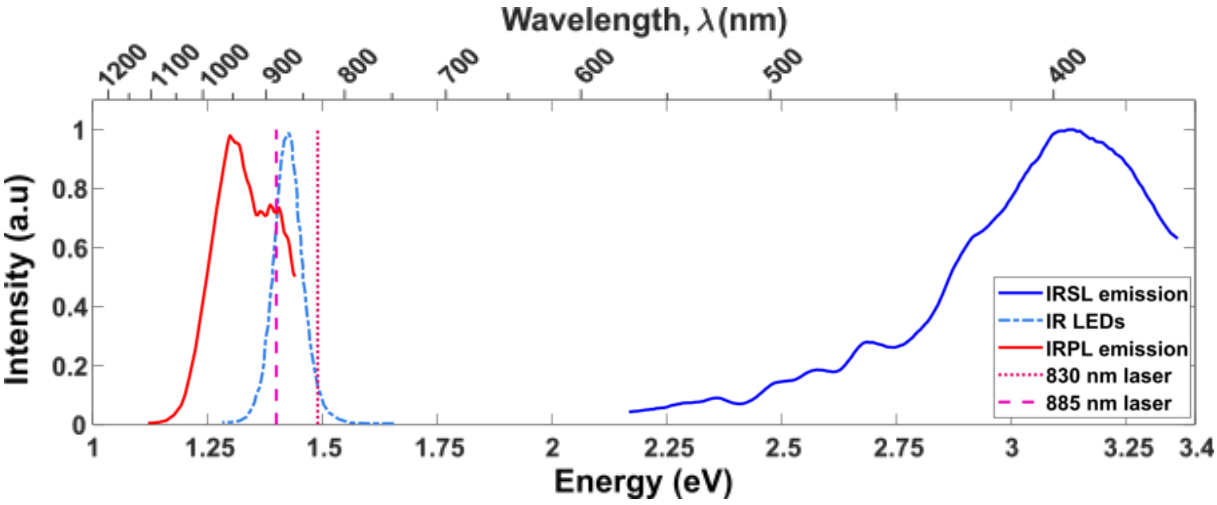

Figure 1.3: IRSL and IRPL stimulation and emission spectra. The 885 nm and 830 nm lasers are used for stimulating the IRPL, and were used by Prasad et al. (2017) and Sellwood et al. (2019), respectively. The IR LEDs are used for IRSL. Data was taken from Sellwood et al. (2019)

1.3 Rock Surface Dating

The dating of rock surfaces is based on the same principals of charge trapping and detrapping as a result of ionising radiation and optical stimulation by sunlight, respectively. The first applications of rock surface dating (RSD) using luminescence used TL measured from archaeological artefacts made of calcitic rock. These had been exposed to sunlight for durations long enough to bleach the luminescence both at and below the rock surfaces (Liritzis et al., 1997; Theocaris et al., 1997). The TL was plotted with increasing depths from the surface of the rock, resulting in a sigmoidal-shaped profile representing increasing luminescence with depth. From this a mathematical model was established to characterise the optical interactions of sunlight with the trapped charge, and determine the exposure duration of the archaeological artefacts in question (Polikreti et al., 2002). Since then, several developments have been made both with the measurement methodology and with the model. Measurements have moved over to using OSL (again, to avoid the unbleachable component found in TL), and measurements are made on either grains abraided from a rocks' surface (e.g. Liritzis et al., 1997; Theocaris et al., 1997; Morgenstein et al., 2003), or from small rock slices which can be placed directly onto the OSL reader (e.g. Vafiadou et al., 2007; Freiesleben et al., 2015; Luo et al., 2018; Meyer et al., 2018). The age model has been expanded upon, and today accounts for the total photon flux and the ionisation cross section of the trap under investigation (Sohbati et al., 2011; Sohbati et al., 2012c) and follows the general form (Eq.1.2):

$$L(x) = e^{-\overline{\sigma\varphi_0}te^{-\mu x}} \tag{1.2}$$

Where $L(x)$ describes the luminescence at depth $x(mm)$, $t(s)$ is the exposure duration of the rock surface. The parameter $\sigma\varphi_0$ (s^{-1}) is the net detrapping rate on the exposed surface as defined by a combination of the photon flux (φ, cm^2/s), and the photoionisation cross-section σ (cm^2). The parameter μ (m^{-1}) is the light attenuation coefficient of the rock, assumed to be constant for all wavelengths. This model describes the progression of sigmoidal-shaped luminescence-depth profiles which progress with depth from the rock surface as a function of time (Figure 1.4a).

Unlike with sediments, such luminescence-depth profiles record the exposure history of the rock, which is valuable information when attempting burial dating of the rock surface. Upon burial of a previously exposed rock surface, charge begins to accumulate again, which with regards to the shape of a luminescence-depth profile, leads to elevated OSL values in the previously bleached region of the rock (Figure 1.4b). Parametrisation of the net detrapping rate and light attenuation via fitting of the resulting profile (Sohbati et al., 2012a; Sohbati et al., 2012c) enables modelling of the initial bleaching extent from exposure; it can then be established as to whether the sample was sufficiently bleached prior to burial, and thus whether the final burial ages are reliable.

Freiesleben et al. (2015) have progressed the modelling of luminescence-depth profiles even further, through establishing multiple models which describe the development of luminescence-depth profiles which record multiple exposure-burial cycles (Figure 1.4c). So far, applications of such RSD models have provided exposure or burial chronologies for multiple archaeological sites (e.g. Sohbati et al., 2015; Gliganic et al., 2018; Liritzis et al., 2019; Gliganic et al., 2021). Applications in geological settings have dated a variety of cobble-rich deposits (e.g. moraine, river bed and deposits) or to determine rates of coastal evolution and sea level changes (e.g. Simms et al., 2011; Jenkins et al., 2018; Rades et al., 2018; Souza et al., 2019; Souza et al., 2021).

Research has also stemmed into using similar measurements and adapted models to establish erosion rates of hard rock surfaces (e.g. Brown et al., 2019; Lehmann et al., 2019; Smedley et al., 2021).

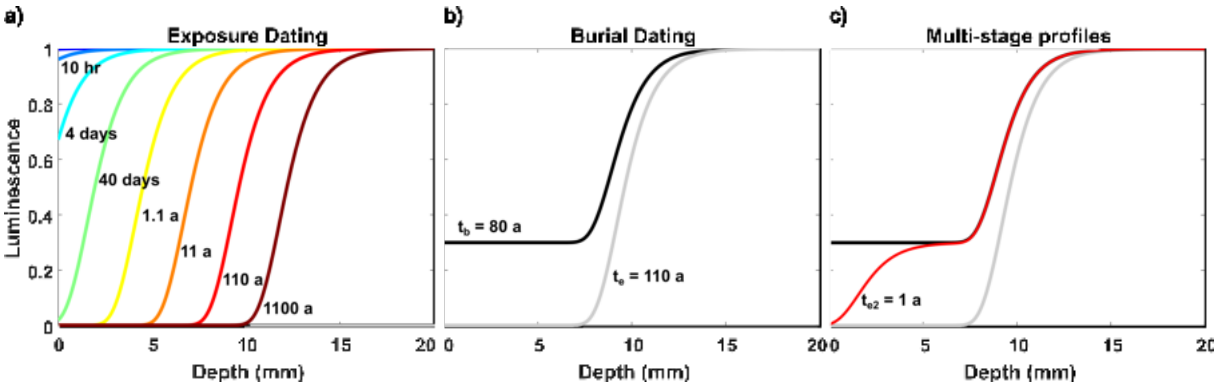

Figure 1.4: a) The progressive bleaching of luminescence-depth profiles with increasing exposure times, as described by Eq.1.2. b) Modelled burial profile (black line) with the initial exposure profile estimated from the fitted burial profile parameters. c) Multi-stage profile development. The red profile shows a history of two exposures and one burial period. The profiles in b) and c) follow the equations developed in Freiesleben et al. (2015)

1.4 Luminescence Imaging

With the ever increasing list of potential luminescence dating applications, there is a correlating demand for appropriate instrumentation, high-resolution data, as well as for stream-lined sample collection, measurements and data analysis. Imaging of luminescence has been considered a method by which these demands could be met. If one could image OSL, the spatial information of the samples could be retained. This would also allow measurements on mineral fractions which are not able to be separated from the host material (e.g. archaeological samples which cannot be destroyed, grains in hard cement or meteorites with fused crusts) (Chauhan et al., 2014). Significant time spent on sample preparation stages, where laborious stages of mineral grain separation or coring and slicing could be skipped altogether, as measurements could be made on large sections of a sample. Arguably, one of the most enticing aspects of OSL imaging is the possibility of developing a field instrument. With *in situ* imaging of OSL, one could determine whether the desired emissions or (for example) a luminescence-depth profile for RSD can be quickly measured from a sample. Such sample screening in the field would vastly increase the overall efficiency of sample collection, and potentially allow relative dating to be conducted in the field.

Until recently, the popularity of imaging of luminescence has been restricted by the state of technology. The main challenges revolved around the detection and quantification of low-light levels and maximising the signal to noise ratio of detectors (Hooper et al., 1994). Initial attempts focused on methods involving measurements of OSL with a laser and photomultiplier tube (PMT), imaging small sections of a sample at a time (Duller et al., 1999; Bailiff et al., 2003), and then with imaging photon detectors (IPDs) which could image OSL from a whole sample at once (Smith et al., 1991; McFee, 1998). However, it was not until the development of charge-coupled devices (CCDs) through the 1960s, 70s and 80s that the field of TL and OSL imaging really progressed (Rieser et al., 1994; Duller et al., 1997; Baril, 2004; Olko et al., 2008). The solid-state detectors in CCDs are capable of detecting low-light levels and provide a means of photon counting over wider dynamic ranges than conventional photomultiplier tubes (PMTs). Later developments in CCDs were aimed at further reducing the detection limits and expanding

the dynamic range and quantum efficiency of the cameras. With the application of an electron-multiplying (EM) gain on the photoelectrons before they reach the CCD detector, it is possible to detect light levels down to individual photons, and reduce the necessary integration times (Pool et al., 2005; Clark-Balzan et al., 2012). Quantum efficiency of these EMCCDs is also high so that detection of photons with energies spanning from deep UV to NIR is possible.

The high-resolution data obtainable through imaging also boasts benefits for applications of rock surface dating, where the whole luminescence-depth profile can be rapidly reconstructed without loss of material usually experienced with conventional measurements (Sellwood et al., 2019; Sellwood et al., 2022). With high-resolution data, it is easier to observe the full bleaching and burial cycles which a rock surface has experienced (the true shape of a profile can be lost when only a few data points can be obtained), and fitting of age models can therefore be more robust. The obvious benefits and the current state of appropriate technology have been points which have driven the research in this thesis.

1.5 Aims and objectives

With increasing interest in rock surface dating using OSL, it is necessary to develop new measurement methods which can be reliably used in the vast variety of desired applications. Currently, there are several limitations which are preventing the progression of OSL RSD, including: 1) the lengthy sampling and preparation requirements for conventional RSD, only to achieve low-resolution data, 2) concern over the appropriateness of the current RSD models for representing the kinetic processes of feldspar, and 3) problems with using IRSL from feldspar, including fading and low sensitivity. The work presented here builds upon a previous publication by Sellwood et al. (2019) which presents a novel demonstration of imaging IRPL from a naturally exposed rock slab. The data they acquired was of high-resolution, and the reconstructed luminescence-depth profiles were suitable for rock surface dating. However, that study was only scratching the surface of the potential of both IRPL and the instrumentation for imaging of near-infrared luminescence. The purpose of this PhD is thus to further the field of OSL and IRPL rock surface dating using imaging, in an attempt to overcome the aforementioned limitations. To achieve this, the following objectives were defined:

1. Create a conceptual design, develop and test a high-resolution IRPL imaging system for rock surface dating. The final outcome will be a description and presentation of new instrumentation for spatially resolved imaging of IRSL and IRPL at both 880 nm and 955 nm.

2. Demonstration of the instrument for rapid, *in situ* assessment of luminescence-depth profiles. As previously stated, it is of high interest to improve on the efficiency of sample collection, preparation and measurement times, and the new instrumentation will improve on all three aspects. I demonstrate how large samples can be measured quickly, after simply cutting a sample perpendicular to the rock surface of interest (i.e. the exposed or buried surface), and the whole luminescence-depth profile can be imaged at once.

3. Application of different luminescence models on IRPL and IRSL-depth profiles, and an understanding of the geochemical and compositional constraints on IRPL signal in feldspar. The current age models used in OSL rock surface dating were built upon the assumption that the luminescence follows first order kinetics. However, this is known not to be the case for IRSL from feldspar. Therefore, it is necessary to investigate the suitability of different age models for representing IRSL and IRPL, through the fitting of such models to natural and laboratory bleached rocks.

4. IRPL rock surface dating applications. Attempts at both rock surface exposure and burial dating using IRPL and IRSL imaging will be made, along with investigation into appropriate measurement and data analysis protocols.

The findings of this research will have significant implications on how rock surface dating using feldspar is conducted in the future. The new instrumentation will present novel opportunities for obtaining high-resolution data, and also holds significant promise to the future development of field instrumentation. The results presented here will help to improve our understanding of the responses of IRSL and IRPL in rocks upon exposure to different wavelengths of light and demonstrate how both rock surface exposure and burial dating is achievable via imaging.

1.6 Thesis outline

This thesis contains seven chapters. A brief description of each chapter is provided below:

Chapter 1: Introduction
Chapter one hosts an introduction, with general background information on luminescence, feldspar, rock surface dating and OSL imaging.

Chapter 2: A 2D imaging system for mapping luminescence-depth profiles for rock surface dating
Presented here is a detailed description of the instrumentation developed and tested in this research project. The specifications of the instrument are described, along with demonstrations of system stability and IRSL and IRPL measurement reproducibility. The chapter concludes with examples of applications for which the instrument can be used. This chapter is presented as an article, which was recently accepted for publication in the journal Radiation Measurements. An appendix to this chapter (not included in the accepted publication) presents a short study into the attenuation of light through rocks and the effective stimulation and measurement depth NIR wavelengths through slices of K-feldspar and granite.

Chapter 3: Rapid *in situ* assessment of luminescence-bleaching depths for deriving burial and exposure chronologies of rock surfaces
In this chapter I demonstrates how luminescence-depth profiles can be reconstructed from rapid and high-resolution imaging of IRSL and IRPL from naturally exposed rocks. This article explores different methods for normalising the natural IRSL or IRPL, other than using a regeneration dose. The work presented in this chapter was accepted for publication in the journal Quaternary Geochronology in August 2021.

Chapter 4: Investigations on dose recovery in rocks using spatially-resolved IRPL and IRSL
Chapter four hosts a study into using imaging of IRSL and IRPL for recovering known doses from rocks, in a controlled experiment representative of rock surface burial dating. In this chapter I measure IRPL and IRSL from two rock samples with known exposure histories and surface "burial" doses, which, through following a SAR-style measurement protocol, are recovered. I was able to reconstruct 2D dose distributions for the samples. This data was presented at the LED2021 conference and the article was submitted to the journal Radiation Measurements for publication as conference proceedings.

Chapter 5: Investigating the development of IRPL-depth profiles in rocks
Chapter five presents data from controlled bleaching experiments where IRPL and IRSL luminescence-depth profiles have been reconstructed from images. Granitic rock samples were bleached with either monochromatic light, broad-wavelength halogen lamps or natural daylight, for progressively longer exposure times. The IRPL and IRSL-depth profiles were reconstructed and fitted with two models, representing either first order or general order kinetics. This chapter presents a novel data set, displaying the development of IRPL-depth profiles with increasing exposure time, and provides a discussion on the appropriateness of the current age models for representing IRPL.

Chapter 6: An application of luminescence to study crack formation in naturally exposed rocks
This chapter presents a novel application where the principles of rock surface dating are applied

in an attempt to create a relative chronology of crack formation. IRSL and IRPL was imaged from surfaces perpendicular to crack planes from three cracks in a granitic boulder. This allowed us to view the extent of bleaching both down the cracks and into the crack planes. Through qualitative assessment of the relative bleaching extents around the three cracks enabled a crack-formation chronology to be established, which was consistent with field observations.

Chapter 7: Summary and conclusions
The final chapter hosts a general summary and conclusions of the work in the thesis, with regards to the initial research aims and objectives. Future outlook of the research is also included.

CHAPTER 2

A 2D imaging system for mapping luminescence-depth profiles for rock surface dating

Sellwood, E.L.[a], Kook, M.[a], Jain, M[a].
[a] Department of Physics, Technical University of Denmark, Risø Campus, 4000, Denmark

Presented in this chapter is the EMCCD-based instrumentation, named the Risø Luminescence Imager, suitable for imaging of IRPL and IRSL from large (cm-scale) rock samples. This article presents a detailed description of all components and their configuration for imaging of rock samples. This manuscript was accepted for publication and first version of this article is available at: `https://doi.org/10.1016/j.radmeas.2021.106697`. An appendix is also provided at the end of this chapter, where an investigation into the effective stimulation and emission depth of NIR wavelengths in rocks and feldspar minerals was conducted. This appendix was not included in the publication.

Abstract

Spatially resolved optically stimulated luminescence (OSL) offers a means for rapid assessment of dose distributions in retrospective dosimetry and geochronology. Until recently, OSL imaging systems have largely been restricted to measurements of millimetre scale samples; this approach is not well suited for applications where the physical process of interest operates on centimetre scale (e.g., depth dependent trap eviction in exposed rocks, sediment mixing in soils, attenuation of gamma radiation, etc.). Here we describe and demonstrate the Risø Luminescence Imager - an electron multiplying charge-coupled device (EMCCD) based imaging system for measuring infrared photoluminescence (IRPL) and infrared stimulated luminescence (IRSL) from centimetre scale samples. While these signals specifically arise from feldspar, the stimulation and detection configuration may be modified to suit other target materials/dosimeters. We characterise the stability and reproducibility of the system through IRPL and IRSL measurements from a large (~4 × 5 cm) heterogeneous rock sample, and a slice of K-feldspar mineral. Finally, we present examples of suitable applications, including the reconstruction of luminescence-depth profiles from IRPL and IRSL images, and reconstruction of IRSL decay curves. Measurement of luminescence-depth profiles with high resolution using the Risø Luminescence Imager is expected to improve our understanding of the trap emptying mechanisms (kinetics) in rocks. This system also opens new avenues for the development of field imaging instrumentation and provides opportunity to study feldspar luminescence in relation to its geochemistry.

Key words

Spatially-resolved luminescence; Electron-multiplying charge coupled device; Infrared-photoluminescence; infrared-stimulated luminescence; Risø Luminescence Imager.

2.1 Introduction

Optically stimulated luminescence (OSL) is an important tool for dosimetry and for constructing detailed chronologies over the Quaternary period. The majority of OSL dating methods are based on the separation of quartz and feldspar signals; this separation is not always feasible, especially when the target is hard rock material. However, over the last decade OSL dating has rapidly advanced to include rocks, where one is often dealing with composite samples (polymineral grains or whole rock slices). The OSL rock surface dating (RSD) method is of particular interest because of its unique ability to measure exposure ages or burial ages based on well bleached samples (e.g. Liritzis, 1994; Liritzis et al., 1999; Habermann et al., 2000; Polikreti et al., 2002). It allows estimation of the time scales of natural processes such as hard-rock transport, erosion rates, and catastrophic events (e.g. large floods or rock falls, etc., Vafiadou et al., 2007; Luo et al., 2018; Sohbati et al., 2018; Souza et al., 2019). Rock surface dating with OSL has generally focused on measurements from whole rock slices or grains abraded from different depths (e.g. Liritzis et al., 1997; Theocaris et al., 1997; Morgenstein et al., 2003; Chapot et al., 2012; Sohbati et al., 2012a; Liritzis et al., 2019). Both of these methods are cumbersome, involving coring and subsequent slicing or abrasion of the core. Additionally, there is unwanted loss of material during slicing. Recently, it has been shown that direct imaging of luminescence-depth profiles, instead of profile reconstruction through combining data from measurement of individual slices, can circumvent this cumbersome sample preparation process. In this imaging method, it is only required to cut a large rock slice perpendicular to the surface of interest (exposed or buried surface). Spatially-resolved luminescence measurement of this surface then reveals the entire luminescence-depth profile after appropriate normalisation; this method significantly reduces the measurement time as well as increases the precision and accuracy of the RSD method (Sellwood et al., 2019). Furthermore, in contrast to measurement of bulk luminescence through a photomultiplier tube, luminescence imaging helps to differentiate between the signals from different mineral phases. However, in order to use such an imaging method based on large cm-scale samples, it is imperative that we have instrumentation that has sufficient sensitivity, precision and reproducibility for reliable reconstruction of dose or luminescence-depth profiles. This study presents the Risø Luminescence Imager to address this need.

Previous studies on luminescence imaging have been based on imaging photon detectors (IPDs; Smith et al., 1991; McFee, 1998), colour films pressed directly onto samples to capture phosphorescence (Hashimoto et al., 1995; Hashimoto et al., 2003), or scanning systems where a laser beam is scanned across a sample and the emission is detected by a standard photomultiplier tube (PMT) to construct a 2D map of OSL intensity (Bailiff et al., 2003). The development of charge-coupled devices (CCDs) has allowed TL and OSL detection with a high quantum efficiency over a wide dynamic range of wavelengths. This has enabled investigations of OSL and TL from a range of sample sizes, from multiple-grain aliquots (Duller et al., 1997; Greilich et al., 2002; Baril, 2004; Olko et al., 2008) or ~1 cm slices of rocks (Hashimoto et al., 1995; Hashimoto et al., 2003). Applications using CCDs however are limited by the OSL intensities of the samples and relatively slow measurement speeds of the CCD devices (i.e., inadequate for capturing OSL decay curves, or limiting use to very bright samples). Some of these limitations have been overcome by the development of an electron-multiplying (EM) step by which photoelectrons are

first amplified by an EM-gain factor before it is readout in the CCD. An electron-multiplying CCD (EMCCD) can increase the signal-to-noise ratio and is able to provide single photon counting in extremely low light levels, whilst providing rapid frame transfer and relatively fast measurement times.

Previously, Sellwood et al. (2019) demonstrated the suitability of using an EMCCD camera for imaging a novel emission from feldspar: Infrared-photoluminescence (IRPL; Prasad et al., 2017). Contrary to OSL or IRSL which is emitted as a result of electron-hole recombination, IRPL is a steady-state emission arising from excitation - radiative relaxation within the principal trap in feldspar (Prasad et al., 2017; Kumar et al., 2018). Thus, unlike OSL, IRPL measurement selectively probes only the trap population and offers a great increase in sensitivity (beneficial for imaging) because of its steady state nature (Prasad et al., 2017; Kumar et al., 2018; Kumar et al., 2020b). Sellwood et al. (2019) detected the IRPL emission at 955 nm ($IRPL_{955}$) from a large granite slab with the purpose of reconstructing luminescence-depth profiles suitable for rock surface exposure dating. Since then a second IRPL emission at 880 nm ($IRPL_{880}$) has been identified (Kumar et al., 2018). Kumar et al. (2020a) also measured three well-defined excitation peaks for the $IRPL_{955}$ emission at 1.45 eV (885 nm), 2.05 eV (604 nm) and 3.35 eV (370 nm), and two excitation peaks for $IRPL_{880}$ at 2.15 eV (576 nm) and 3.55 eV (350 nm); the near-infrared (NIR) peak for the $IRPL_{880}$ was not fully resolved. From an instrumental viewpoint, this makes IRPL even more appealing as there is flexibility to design the instrument with excitation sources in either the NIR or the visible region.

We present here a description and demonstration of the Risø Luminescence Imager. This EMCCD-based system is suited for imaging of both IRPL at 955 nm and 880 nm, as well as IRSL at room temperature. We discuss the reliability and reproducibility of the measurements and demonstrate the stability of the system. We conclude with a few examples of data obtainable with the instrument. We expect the Risø Luminescence Imager to give a significant impetus to the field of rock surface dating. Additionally this system can also be adapted for rapid measurement of large sample areas in environmental or industrial dosimetry.

2.2 Instrument design

The Risø Luminescence Imager is a system based on an EMCCD camera with interchangeable filters and five external light sources, linked to the control system. A schematic of the instrument is shown in Figure 2.1a. It comprises of two basic units: 1) the detector and optics and 2) light sources for illumination. The target measurements with the current configuration are IRSL and IRPL. The system is built on a 60 × 60 cm Nexus optical breadboard, encased in blackout construction hardboards (TB4 hardboard, Thorlabs) further covered in light-absorbing blackout paper to reduce IR reflectance (adhesive flock paper, Edmund Optics). A fan is installed on the side to help cool the system. Samples are placed on an adjustable 7.6 × 10.1 cm lab jack stage (L200 lab jack, Thorlabs) directly below the camera, with a vertical translation range of 26.5 mm (maximum height of top surface is 47.8 mm) enabling manual focus on the measurement surface. Samples can be up to ~8 × 8 cm in size. Access to the sample stage and all components is facilitated by a large vertically sliding door panel on the front. No heating facility was installed in the system to do *in situ* preheat or annealing. The instrument is suitable for a wide range of sample sizes and thickness and therefore it was considered that using an external oven was more practical and efficient for achieving a uniform heating of the sample.

2.2.1 Detector and optics

Images are captured using an Evolve 512 electron-multiplying charge coupled device (EM-CCD, Photometrics). The camera is internally cooled to -80°C to minimise dark counts, and hosts a chip size of 512 × 512 pixels at 16 μm^2. The EMCCD camera is ideal for our purposes as it is capable of detecting single photons over a band width of 300-1100 nm, with a quantum efficiency of ~45% at 880 nm ($IRPL_{880}$), ~30% at 955 nm ($IRPL_{955}$), and up to ~60% for 400 nm (IRSL). With the option of time-lapse imaging up to 33 frames per second without a mechanical shutter, the camera can rapidly and continuously collect data. This makes it suitable for applications where the IRSL decay curve should be measured. The electron multiplication minimises readout noise to <1 electron, allowing extremely low-light imaging.

The optics consists of a 23 mm focal length C-mount lens (Xenoplan 1.4/23-0902 from Jos. Schneider Optische Werke GmbH), with F# 1.4 and an angular field of view of ~20°. The lens allows transmission between 400-1000 nm, without the need for re-focussing when switching between desired detection windows. A filter mount with sliding modular inserts houses the 25 mm diameter filter sets attached to the lens: a) an 880 ± 10 nm band-pass (BP) and 2 × 850 nm long-pass (LP) filters (TECHSPEC) with optical density = 4 for $IRPL_{880}$ measurement, b) a 950 ± 50 nm BP and 2 × 925 nm LP filters (TECHSPEC) for $IRPL_{955}$, and c) a blue filter combination, consisting of a Schott BG-3 UV band-pass filter and a Schott BG-39 for IRSL measurements (see Figure 2.1b).

2.2.2 Light sources

Based on the work by Kumar et al. (2020a) who identified three main peaks in the IRPL excitation spectra, we installed three different light sources for IRPL stimulation with wavelengths at 532 nm, 830 nm, and 885 nm (Figure 2.1b). The 532 nm source is a 10 mW solid-state laser diode (Laser Component, FLEXPOINT). A 20°C circle top-hat Engineered Diffuser ^{TM} is placed in front of the 532 nm laser to homogenise the beam, resulting in a power density of ~0.051 mW/cm^2 at the sample stage. A circle pattern Engineered diffuser^{TM} is placed in front of the 830 nm laser (Power Technology Incorporated) reshaping the beam to a round uniform power distribution of ~0.8 mW/cm^2 at the sample stage. The 885 nm light source is a 500 mW diode laser (Changchun New Industries Optoelectronics Tech co. Ltd.) with central wavelength of 885 nm coupled to an optical fibre. A circular Engineered Diffuser TM is placed at the end of the fibre to homogenise the beam, providing ~2.2 mW/cm^2 at the stage centre. Such low power for excitation is adequate for measuring the IRPL signal because of its high sensitivity (Kook et al., 2018). Furthermore, desirable counting statistics are achievable from adjusting measurement times depending on sample intensity. The three IRPL stimulation light sources were each mounted on articulate post heads, ~20 cm above the sample stage, each at ~60°from the horizontal. This configuration optimised the intensity distribution for the desired illumination area.

The IRSL is measured via twenty 850 nm light-emitting diodes (LEDs) mounted on a 30 cm diameter aluminium ring. The LEDs are angled at 40°, ~17 cm above the base of the set-up, resulting in a maximum stimulation power density of ~60 mW/cm^2. For optical imaging of samples, a 1020 nm LED is installed on another articulate post head. A conventional DC power supply (RS-Pro RPE-3323) provides constant current (~0.6 A) to the IR LEDs. The power supply is synchronised to the camera and computer via a USB-6341 control box (National Instruments). A computer program was built allowing light source and measurement durations

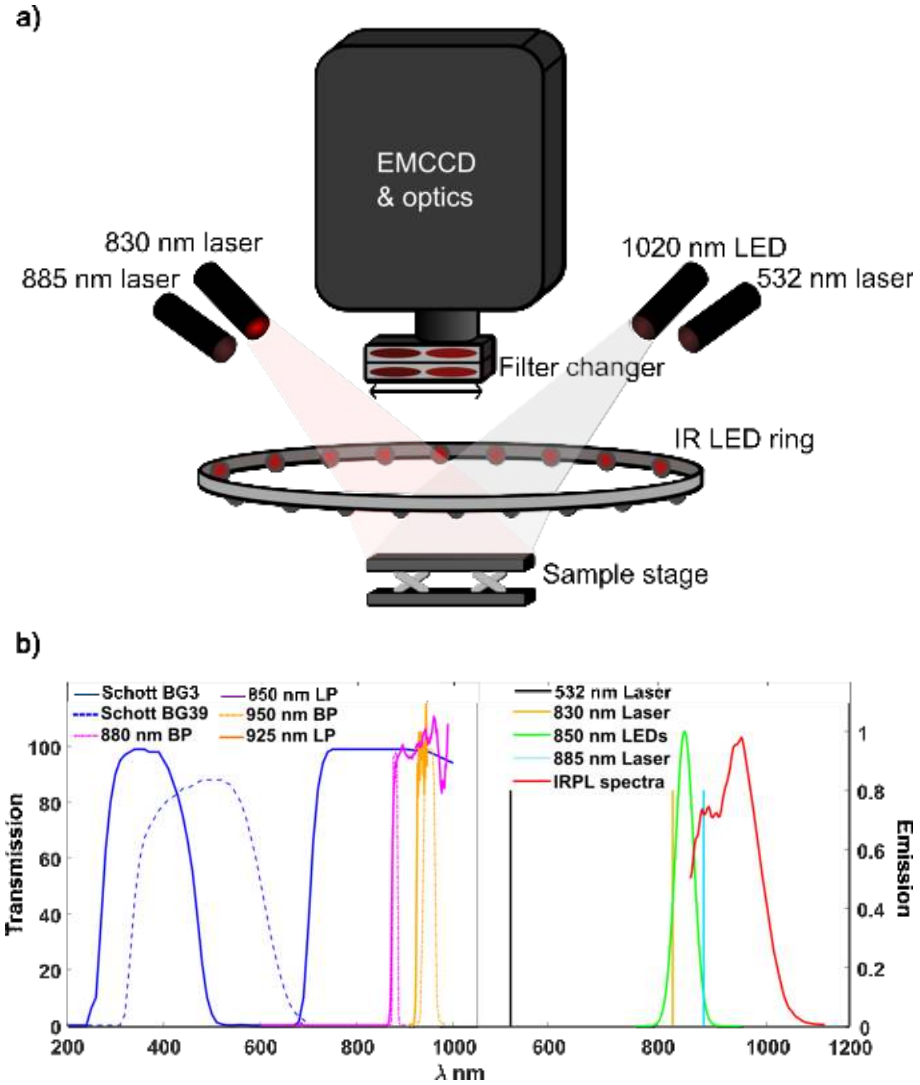

Figure 2.1: a) Schematic of the Risø Luminescence Imager. b) Transmission spectra of filters (left axes) and measured luminescence emissions and light sources (right axes)

to be set. Images are acquired using OCULAR software where the external trigger settings are selected to allow synchronisation of the camera and light sources via the control box.

2.3 Data acquisition and image processing

Described below are the basic steps for measuring IRPL and IRSL from a rock sample. Samples are first placed on the adjustable lab jack and illuminated with the 1020 nm LED illumination to visually check the samples position. For reproducible positioning the sample can be glued to a plate (coated with anti-reflective black paint), which in turn can be directly screwed onto the lab jack. Alternatively, a series of pegs or an L-shaped plate can be mounted on the lab jack, acting as guides for the sample position during a series of sequential measurements. After positioning, manual focusing of the camera is done by adjusting the sample stage height. Images with the 1020 nm LED are always taken prior to luminescence imaging, in case the sample had been displaced for external irradiation, bleaching, etc. between measurements; these optical images can be used for registration purposes during image analysis. Once the sample is in the desired position and in focus, we measure IRPL or IRSL. For IRPL we are able to utilise the

non-destructive nature of IRPL at these very low stimulation powers and determine appropriate exposure times by following a trial-and-error approach. The optimal measurement frame duration can be identified so as to capture enough signal and to not saturate the EMCCD. However, for IRSL measurement we measure a test sample before hand to estimate an appropriate frame duration. Previous investigations of imaging IRSL have shown that for most heterogeneous rock samples with K-rich feldspar, a 5-10 s exposure per frame is suitable for capturing sufficient IRSL in a single frame, whereas exposures down to 1 s per frame are enough for very pure K-feldspar mineral samples. For particularly low light levels (when 10 s integration is inadequate for capturing sufficient IRSL) EM-gain can be applied. An entire sequence of images can be automatically captured to cover the whole IRSL decay down to a background level through setting the exposure time and number of desired frames. Data is captured as 16-bit grayscale images enabling a wide dynamic detection range for varying luminescence intensities. Analysis can be conducted in any image or matrix processing software. Figure 2.2 shows a flow chart for standard analysis of IRPL and IRSL images.

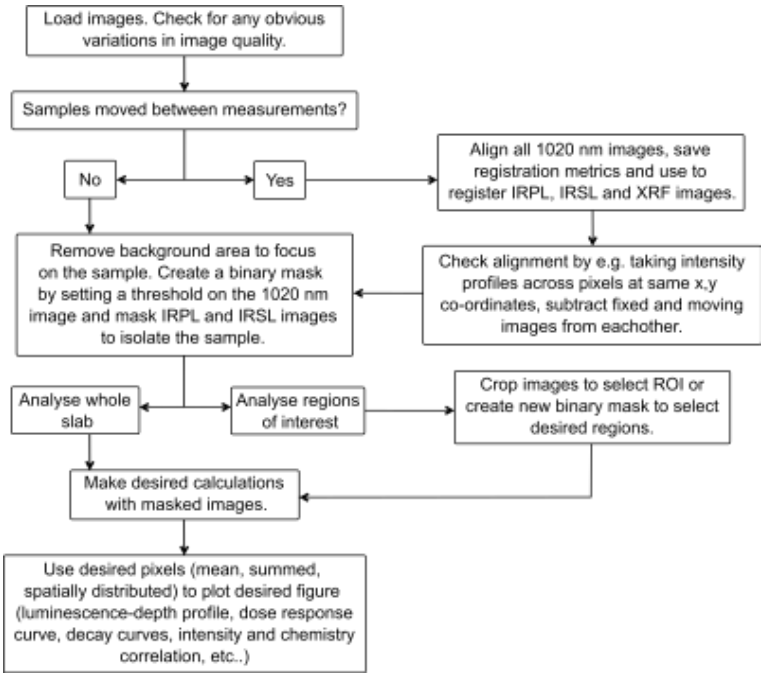

Figure 2.2: Flow chart of standard analysis for IRPL and IRSL data images.

2.4 System performance

We describe below the performance of the Risø Luminescence Imager with regards to IRPL and IRSL measurement reproducibility and stimulation light stability.

2.4.1 Detector and optics

Minimising breakthrough to the EMCCD from the excitation sources is a priority, especially due to the relative proximity in wavelengths between the excitation and desired detection windows (see Figure 2.1b).With each filter set-up and light source combination (without EM gain), the number of detected photoelectrons does not reach above 50 photo-electron counts/pixel over 1 s integration when no sample is placed in the instrument. We concluded that our selected filter combinations are adequate for minimising breakthrough from the selected light sources.

As a background check to give an indicator of effects of reflection from typical sample surfaces in the system, a 1 cm diameter slice of bleached quartz arenite was imaged with 1 s integration using each filter combination (IRPL and IRSL) and each excitation source. The quartz slice was considered a representation of a non IRPL/IRSL emitting mineral surface of similar texture and surface roughness as feldspar. When using the IRPL filter combinations and either the 532 nm, 830 nm or 885 nm laser, the contribution from reflection from the rock slices does not exceed ~150 photo-electron counts/pixel, which is insignificant in comparison to a typical IRPL measurement (counts in the order of 10^3). Similarly, when testing reflectance from the slice with the 850 nm LEDs stimulation and BG3 and BG-39 filter combination, there was negligible (<30 counts/pixel) influence of reflectance from the rock slice.

The maximum resolution of the images is limited by the lowest allowed position of the camera relative to the sample stage. The lowest vertical position of the camera is constrained by the presence of the 850 nm LED ring to be >17.5 cm above the instrument base; below this distance the camera would come into the path of the stimulation light. The resolution of the EMCCD images was estimated with the camera at this lowest position and the sample stage at maximum height (+ 47.8 mm from the base), using a negative USAF 1951 target (from Edmund Optics). Focus of the camera onto the sample stage at this position was possible down to 2.83 line pairs per mm; this suggests that detail down to 170 μm (1 line) is observable in images, enabling imaging of fine rock textures and mineral inclusions that may be emitting IRPL. Of course, if IRSL is not going to be measured, the LED ring can be removed and the system readjusted to bring the sample into even closer proximity with the camera.

2.4.2 Light sources

The homogeneity of the IRPL excitation and IRSL stimulation sources was investigated by imaging the light intensity distributions on white paper. The left column in Figure 2.3 (panels a, c, e and g) presents the images of the white paper illuminated by each light source, with colour bars representing pixel intensity. Mean intensity profiles were then taken vertically and horizontally across the centre of each image (right column in Figure 2.3), and the intensities were normalised to maximum intensity.

The images of white paper illuminated with the 532 nm (Figure 2.3a) and 830 nm (Figure 2.3c) light sources show speckles contributing to fluctuations in the intensity profiles in Figures 2.3b and d. Across the 7.3 × 7.3 cm field of view (FOV), the mean intensity of the 532 nm laser decreases by up to ~65% (Figure 2.3b). The centre ~30 mm of the FOV shows only a ~5% change in intensity in both the horizontal and vertical axes. In Figure 2.3d the 830 nm intensity profiles show a similar intensity distribution as seen in Figure 2.3b, with ~60% decrease in intensity from the centre to edge of the field of view. Again, the light distribution in the centre ~30 mm is relatively homogeneous, only varying in intensity by ~5%. The results from illuminating with the 850 nm LED ring are shown in Figures 2.3e and f. The intensity profiles show a more rounded intensity distribution at the centre of the FOV, with up to ~70% decrease in intensity from the centre to the edge of the FOV. The results from illumination with the 885 nm laser are shown in Figures 2.3g and h. The intensity of this laser shows a clear peak in the centre of the FOV, and up to ~70% decrease in power from the centre to the edge. Arguably for all stimulation sources, placing the sample in the centre of the sample stage will minimise effects of power distribution heterogeneity. If the position of the sample in each subsequent image (e.g. after a removing the sample to give a regeneration dose) is reproduced adequately (see section 2.3), these images will still be comparable and any heterogeneity in power distribution is accounted for during a normalisation stage (e.g. L_n/L_x). If it is crucial that the sample receives

a uniform illumination, (e.g. the luminescence will not be normalised), we suggest limiting the sample size to fit within the ~3 × 3 cm region in the centre of the sample stage.

The stability of each light source was assessed by measuring light intensity as a function of time directly through using either a photodiode (Ophir Starlight power meter) placed in the centre of the sample stage (for the 830 nm laser and 850 nm LEDs), or through imaging time-series of the illumination area on a white paper using EMCCD (for the 532 nm laser and 885 nm laser). In the latter case, the mean value of a central region of each frame was used for constructing the series.

Figure 2.4a shows the results from the 532 nm laser of taking mean intensity values from each 10 ms frame for a 60 s period (data is normalised to the maximum intensity). The laser shows a steady output with an overall <1% decrease over the 60 s on-time. The 830 nm laser (Figure 2.4b) shows a 3% decrease in intensity over 60 seconds. The results for the 885 nm laser (Figure 2.4c) using mean values from images show there is a lag of ~5 seconds between laser on-time and the laser reaching a steady intensity. This lag likely results from the transistors thermal effect in the on/off switching circuit. As IRPL is steady-state, showing negligible loss with stimulation, it is possible to turn the 885 nm light source on and wait until the laser reaches maximum intensity before imaging the sample. The results from the 850 nm LEDs are seen in Figure 2.4d. Again we see a lag of <1 s in intensity from the on-time until the power reaches its maximum. Subsequently, there is undetectable change in power over the remaining 60 s period. As IRSL measurements are usually integrated over longer measurement periods (5-10 s), any effects from this short lag from on-time until maximum power are considered negligible.

2.4.3 Measurement reproducibility

We demonstrate here the reproducibility of the Risø Luminescence Imager for measuring IRPL and IRSL, as well as the stability of IRPL measured at room temperature. Using a ~4 × 5 cm heterogeneous slab of granite, duplicate $IRPL_{880}$ measurements were made, stimulated with the 830 nm laser. The slab was mounted on a metal plate coated in non-reflective matte black paint, and had received a 5 kGy regeneration dose to saturate the traps. Three IRPL measurement sequences were followed:

1. **Sample in, camera on:** the sample was positioned in the Risø Luminescence Imager and left untouched whilst twenty sequential measurements of $IRPL_{880}$ with 3 s exposures were made. Whilst nothing in the system was changed, there was approximately a 10 seconds gap between each measurement, to ensure the system had completely returned to a similar background level.

2. **Sample in, camera on-off:** the sample was left undisturbed on the sample stage and the whole imaging system was turned off for at least half an hour to equilibrate with room temperature. It was then turned on again and left for 10-12 minutes to reach the set -80°C system temperature. This entire operation required about ~45 minutes to make one measurement; these were collected over a period of one working day.

3. **Sample in-out, camera on:** the same slab was removed from the system and placed back on the sample stage between each measurement to check the effect of sample movement on the measurement reproducibility; there was approximately 20 s gap between each measurement during which the sample was removed and replaced before the next measurement. The camera was kept on during the entire set of measurements.

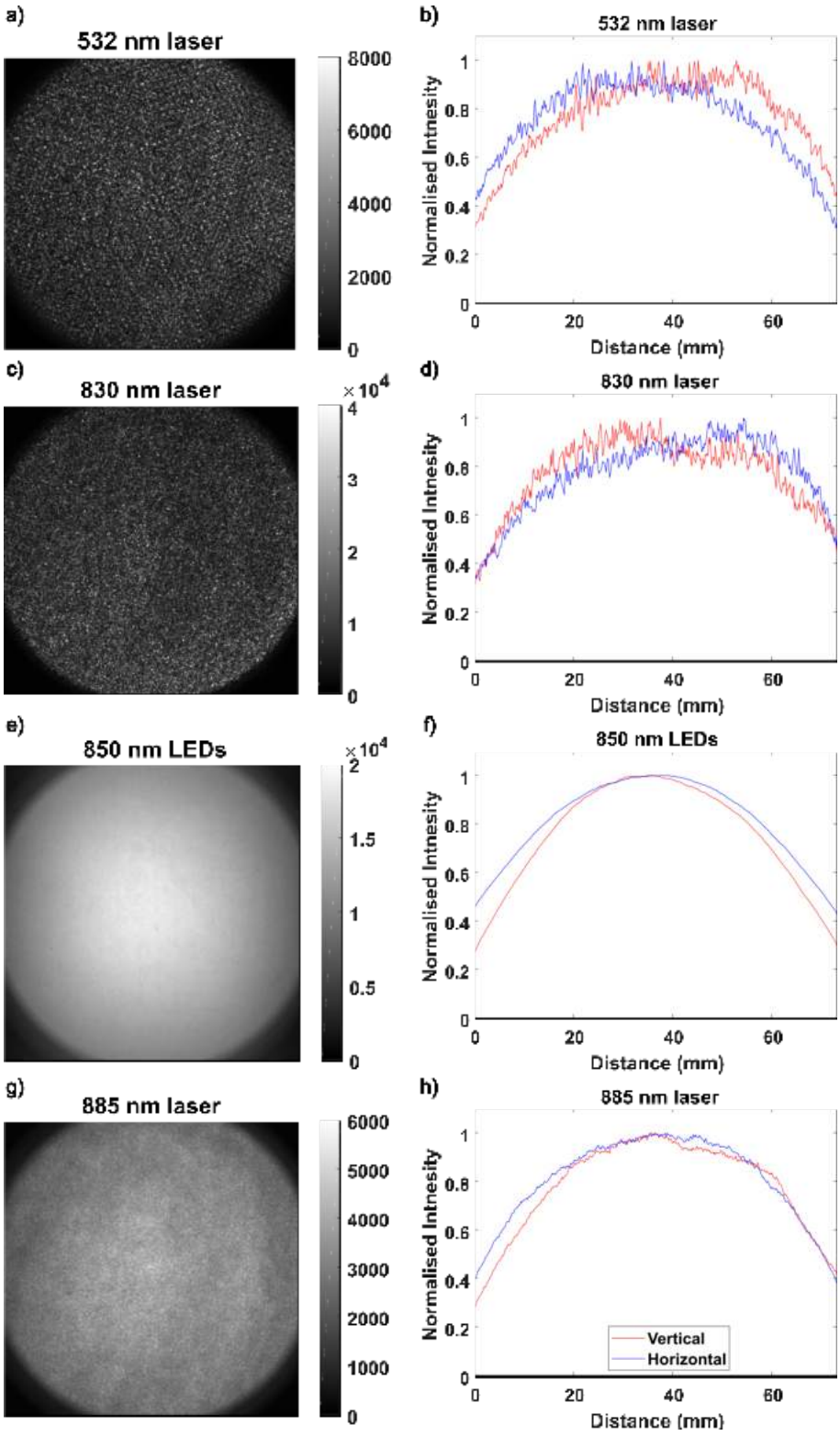

Figure 2.3: a) Image of white paper, illuminated by the 532 nm laser. b) Mean intensity profiles across the vertical and horizontal axes of a), normalised to maximum values. c) and d) White paper image and intensity profiles when illuminating with the 830 nm laser, respectively. e) White paper illuminated with the 850 nm LEDs, and f) vertical and horizontal profiles taken across e). g) White paper illuminated with the 885 nm laser, and h) shows the mean intensity profiles taken across g). The colour bars next to each image represent pixel intensity

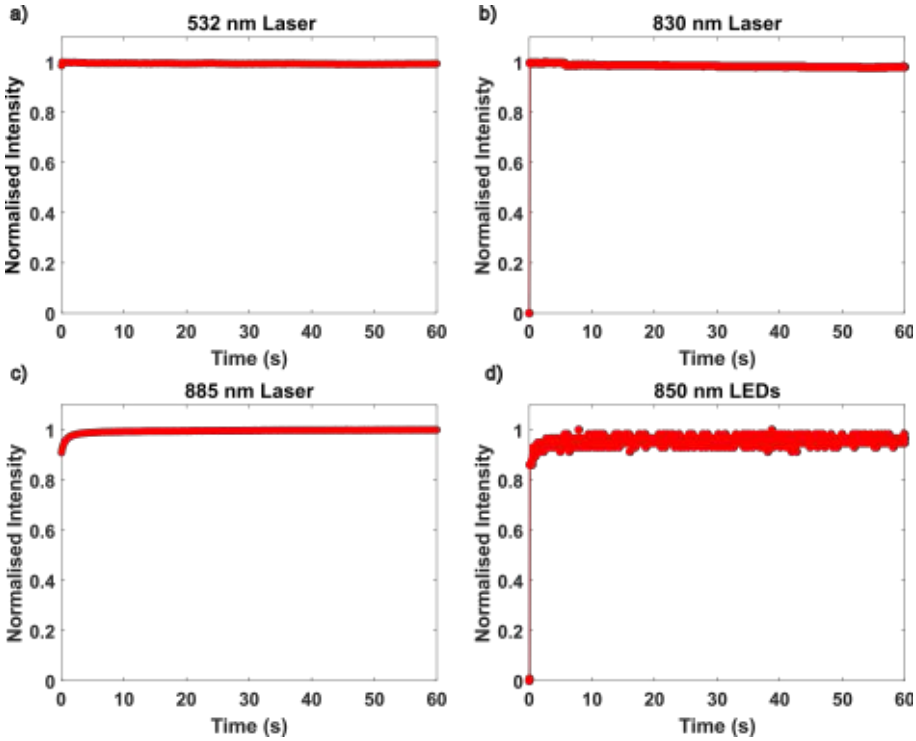

Figure 2.4: Stimulation source stability over time for a) the 532 nm laser, b) 830 nm laser, c) 885 nm laser and d) the 850 nm LEDs

A mask was created from one of the images, where the brightest 50% of pixels were selected. This mask was applied to all other images in the data sets, and the averages of these pixels (normalised to the first measurement point) were plotted against the time elapsed (seconds) since the first measurement in the sequence (Figure 2.5a). There is good consistency between all three data sets. The data from measurement sequences 1) (red circles) and 3) (blue squares) show a decreasing trend in average intensity with each measurement. This observation is not attributed to IRPL fading; the data for sequence 1) was acquired before that in sequence 3), but from the raw data (see supplementary information) there is no continuing decrease in IRPL intensity in the data images from sequence 1) to 3). Instead, this negative trend is likely due to slight temperature variation of the EMCCD chip. We argue that this is also the source of the scatter seen in the data from sequence 2), where the measurements were conducted over a longer experiment duration (a whole day) and there were likely slight temperature fluctuations in the room and instrument. Such thermal effects can be avoided by having a tighter temperature regulation in the measurement room, and monitoring the internal temperatures of the instrument and components.

For testing the reproducibility of IRSL measurement, a single 1 cm diameter slice of pure K-feldspar was preferred over a large rock slice for practical reasons. Unlike IRPL, IRSL is a destructive measurement; hence reproducibility measurements necessitate repeated cycles of irradiation and bleaching which can be more easily achieved in a Risø TL-OSL reader with a cm-sized sample. For each IRSL measurement, the slice was thoroughly bleached with IR LED stimulation at 350°C for 200 seconds in a Risø TL/OSL reader, then given a beta dose of 150 Gy before a preheat at 260°C for 60 s. IRSL was then measured in the Risø Luminescence Imager with a 3 s exposure per frame, over 60 frames, totalling a 180 s measurement. After masking the images, to remove the background area around the rock slice, all remaining pixel values were summed and plotted as a function of measurement time to build the decay curves. The three curves are presented in Figure 2.5b. Whilst the shapes of each of the IRSL decay curves are similar, showing the same decay rate of IRSL with each measurement, the initial intensity of

the third IRSL curve (blue stars in Figure 2.5b) is nearly 10% smaller than that of the first two measurements. While unconfirmed, this intensity change is considered to be due to changing sensitivity in the slice during the emptying process, and not due to the measurement system, since neither the LED power (see Figure 2.4) nor the EM-CCD sensitivity showed such a drift during their separate assessments.

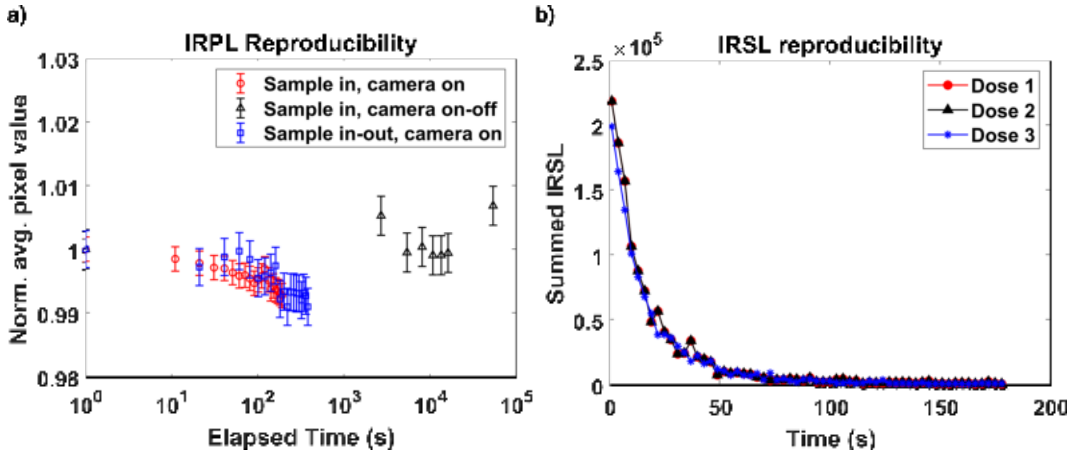

Figure 2.5: a) Reproducibility of measuring IRPL, following three sequences: 1)Sample left in and camera left on, 2) sample left in and system is turned on and off between measurements, and 3)sample is removed and replaced between each measurement. Note the x-axis is logarithmic to show the relative time scales over which the measurements were made. b) IRSL decay curves from a slice of pure K-feldspar

2.5 Demonstration and examples of applications using the Risø Luminescence Imager

Presented in the section below are a few examples of datasets that can be obtained with the described Risø Luminescence Imager. The data are discussed alongside examples of applications where spatially resolving IRPL and/or IRSL is beneficial.

In most luminescence dating applications (including rock surface dating), the natural signals are normalised by a test dose to account for variations in mineral sensitivities and spatial distributions of luminescence intensity. We present in Figure 2.6, examples of images of natural and regenerated IRPL 880 nm and 955 nm and IRSL from a second naturally exposed slab of heterogeneous granite, suitable for a rock surface exposure dating application. Here, only the 830 nm laser was used for IRPL excitation, with frames captured over 3 s exposures. The images were masked to remove the area outside of the sample area, and are presented in false colour with pixel intensities represented in the colour bars. Figures 2.6a and b show the very similar natural (L_n) IRPL 880 and 955 nm, respectively, from the granite slab. Figure 2.6c presents the natural IRSL which was imaged over 18 frames with 10 s exposures (only the first frame is shown here). The intensity of the IRSL data presented here is several orders of magnitude larger than that from the first IRSL image (from the same rock type) by Sellwood et al. (2019) (available in the respective supplementary information), with clear IRSL-emitting minerals distinguishable from non-luminescing areas. The IRPL and IRSL images in Figures 2.6 a, b and c clearly show a region at the surface which is void of luminescence resulting from the natural sunlight exposure. IRSL shows significantly deeper bleaching depth than IRPL because of its relatively greater bleachability. After the slab received a 5 kGy regeneration dose (L_x), we can see the locations of all possible $IRPL_{880}$ and $IRPL_{955}$ (Figures 2.6d and e respectively) and IRSL-emitting (Figure 2.6f) minerals which were previously bleached. This second set of images

can be used for normalising the natural IRPL and IRSL, and the resulting ratio maps indicate more clearly where the transition zone from bleached to saturated IRPL (Figures 2.6 g and h) and IRSL (Figure 2.6i) lies.

Figure 2.6j presents the luminescence-depth profiles from taking mean pixel values and standard error from each pixel column (i.e. with increasing depth from the surface) across the natural $IRPL_{880}$ (black points), $IRPL_{955}$ (red points) and IRSL (blue points, right axis) images. We see a clear influence of mineral heterogeneity on the shapes of the luminescence-depth profiles. These fluctuations are smoothened out when reconstructing the profile from the L_n/L_x ratio images (Figure 2.6k). The larger background in the IRPL profiles compared to IRSL is due to a larger un-bleachable residual, and can be reduced by bleaching the sample under a solar simulator, imaging IRPL again, and subtracting these bleached images as background. Figure 2.6l presents a natural IRSL decay curve from the imaged granite slab. The brightest 50% of pixels were selected from the first frame, and used to create a mask that was applied to all subsequent frames. The pixels per frame were summed and plotted over measurement time. The decay rate of the IRSL is significantly slower than what is usually observed from a conventional OSL reader, due to the significantly lower optical power of the 850 nm LEDs compared to conventional reader (~300 mW/cm^2). As we have access to the spatial information of the rock sample, it is possible to select different regions of interest from the rock sample, and investigate (for example) IRSL depletion of natural or regenerated signals and variation in IRSL decay rates across different feldspar compositions. To demonstrate the suitability of each excitation light source for measuring IRPL, we imaged $IRPL_{955}$ from another naturally exposed slab of heterogeneous granite. We focus here on the $IRPL_{955}$ as the 885 nm light is unsuitable for measuring $IRPL_{880}$. Figure 2.7a presents $IRPL_{955}$ luminescence images from the granite, excited with either the 532 nm (left), 830 nm (middle), or 885 nm (right) light source. All images were captured with a 3 s exposure. The images were processed in the same manner as the data in Figure 2.6. While each light source excites IRPL in the same regions in the slab, the variations in $IRPL_{955}$ intensity seen between these images is a product of the different excitation powers and wavelengths of the respective light sources (strongest power for the 885 nm laser). The three resulting profiles for each light source (Figure 2.7b) show very similar shapes; there is a clear bleached region near the surface of the slab followed by increasing intensity to reach saturation at ~10 mm below the surface. We clearly see the effects of high breakthrough of the 885 nm light source to the camera (red stars, left axis in Figure 2.7b) resulting in the large off-set in the surface region of the slab due to the close proximity between the excitation and detection wavelengths (see Figure 2.1b). Note that the significantly lower $IRPL_{955}$ intensity from the 532 nm excitation is represented on the right axis of Figure 2.7b, and is a result of the much lower excitation optical power than the NIR lasers, as well as the lower excitation efficiency at this wavelength (Kumar et al., 2020a). Our experiments with IRPL measurement using the 532 nm laser also showed that up to 4% of the IRPL (880 nm or 955 nm) can be bleached over 100 s of stimulation time. This bleaching is deemed insignificant when the majority of IRPL measurements are made over short (seconds) durations (e.g. Kook et al., 2018; Duller et al., 2020b; Kumar et al., 2021b; Sellwood et al., 2022). Our data suggests that excitation with each of these light source is clearly suitable for measuring $IRPL_{955}$. Considering selecting the ideal excitation wavelength for both IRPL 880 nm and 955 nm, we argue for the preference of the 830 nm laser source. This excitation energy was demonstrated by Kumar et al. (2020a) to have a higher excitation efficiency for both IRPL peaks, than within the green region, and we are able to avoid breakthrough to the detector with our selected filter combinations. However, all the excitation sources discussed here are suitable for spatially resolving IRPL from rock and sediment samples.

Whilst we only demonstrate measuring luminescence-depth profiles suitable for rock surface exposure dating, it is possible to apply similar measurement protocols to obtain equivalent dose information for dating burial events from rocks. For example, imaging will allow one to quickly

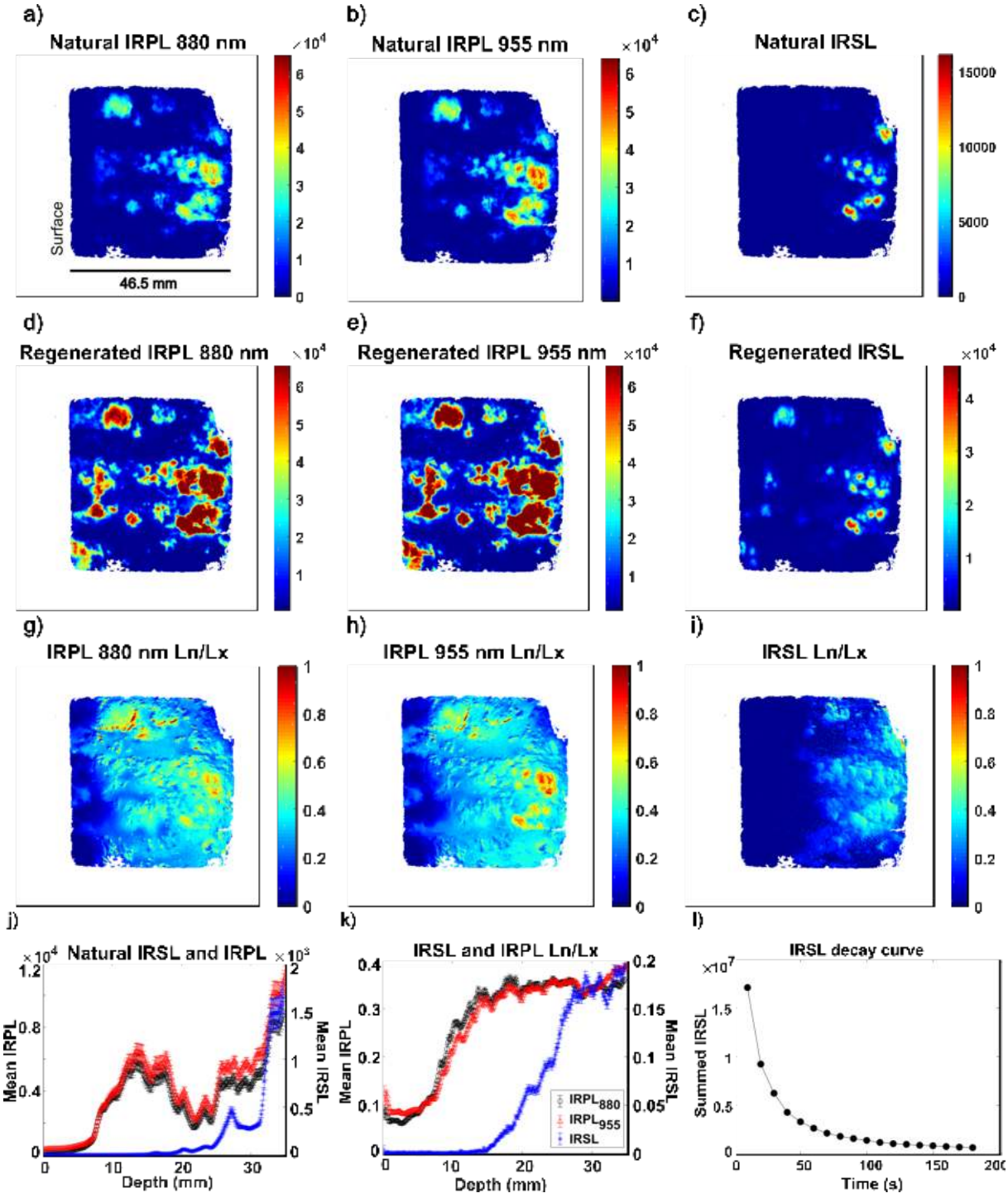

Figure 2.6: Natural $IRPL_{880}$ (a), $IRPL_{955}$ (b) and IRSL (c) images, with colour bars representing intensity. The rocks natural surface is labelled in panel a), on the left-hand side of the images. Regenerated $IRPL_{880}$ (d), $IRPL_{955}$ (e) and IRSL(f). A 5 kGy regeneration dose was given. Figures g, h and I show the L_n/L_x ratio for $IRPL_{880}$, $IRPL_{955}$ and IRSL respectively. J) Natural IRPL and IRSL luminescence-depth profiles. K) L_n/L_x IRPL and IRSL luminescence-depth profiles. l) IRSL decay curve constructed from summing the same pixels from each frame of the time lapse measurement

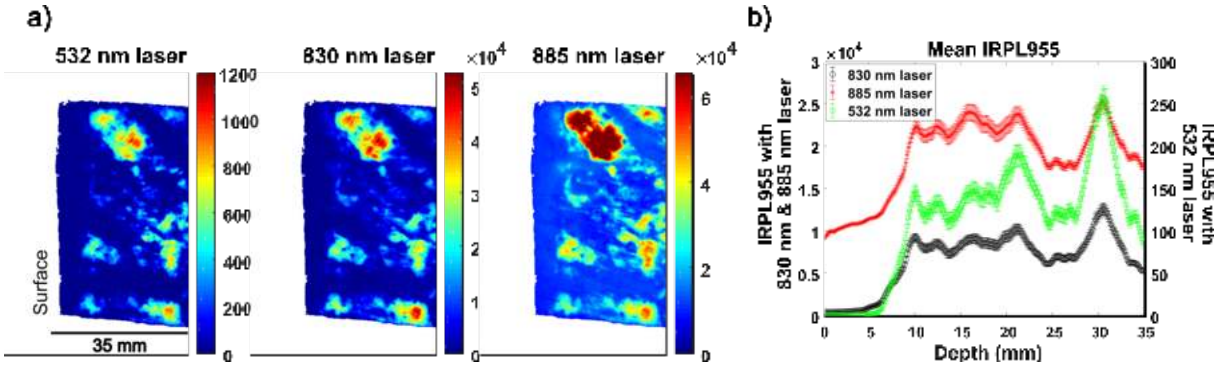

Figure 2.7: a) Images of $IRPL_{955}$ excited with either the 532 nm (left), 830 nm (middle) or 885 nm laser (right), from a naturally exposed slab of granite. The natural surface is located on the left side of the images. b) Mean $IRPL_{955}$ luminescence-depth profiles taken across each image in a. Note, the 830 nm and 885 nm data corresponds to the left axis, and the 532 nm data to the right axis

view whether the sample has been adequately bleached prior to its burial. Through modifications of standard measurement protocols which are usually conducted on an OSL reader (e.g. a regenerative dose sequence where the whole rock slab is irradiated with different regeneration doses, and preheated in an oven before measurement), dose response curves for select surface regions of the sample will be able to be reconstructed and equivalent doses will be able to be estimated from these regions.

Imaging of regenerated IRPL and IRSL can also be used to investigate luminescence characteristics of individual minerals and their sub-regions from whole rock samples. This information can be directly correlated to spatial information on geochemistry. Figure 2.8 shows the 1020 nm image of the granite slab (Figure 2.8a) used to align the regenerated $IRPL_{880}$ image (Figure 2.8b) with a potassium content map (Figure 2.8c) from micro X-ray fluorescence measurement (measured using μ-XRF; M4 Tornado); this allows a direct cross-correlation of IRPL emitting minerals and geochemistry. It is also possible to identify different mineral fractions from the μ-XRF measurement, which can be used to create a mask which is applied to the IRPL and IRSL images. These specific mineral regions can then be assessed for sensitivity to (e.g.) excitation wavelengths, bleaching rates, intensity and sensitivity to dose, depending on the desired information and available data set (e.g. natural or regenerated IRPL or IRSL).

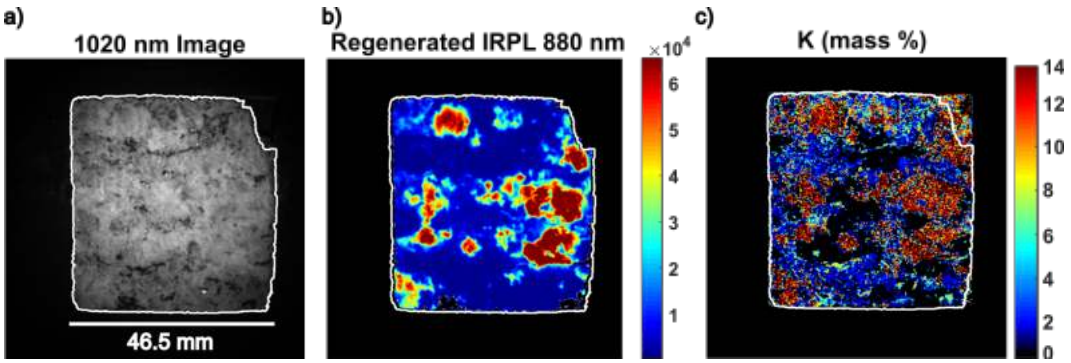

Figure 2.8: a) Image of the granitic rock sample using the 1020 nm LED. b) $IRPL_{880}$ after rock has received 5 kGy regeneration dose. c) Map of K mass % from $\mu - XRF$

2.6 Conclusions

Here, we have described the EMCCD-based Risø Luminescence Imager for measurements at ambient temperature of IRPL (both 880 nm and 955 nm emissions) and IRSL from geological or archaeological samples of up to ~8 × 8 cm size. Rapid readout speeds, a large dynamic range, good quantum efficiency in the IR range, combined with high sensitivity makes it possible to achieve high resolution luminescence images from large (cm scale) sample sizes. The 830 nm LED ring makes it possible to measure IRSL with a higher signal-to-noise ratio compared to the previous studies. We demonstrate that $IRPL_{955}$ can be measured with three (830 nm, 885 nm and 532 nm) and $IRPL_{880}$ with two different excitation wavelengths (at 830 nm and 532 nm). The filter selections for transmitting each desired emission ensure negligible breakthrough to the detector. The light sources allow relatively uniform stimulation within the centre 3 × 3 cm centre region, but adequate stimulation over a ~8 × 8 cm region. We show the suitability of the Risø Luminescence Imager for rapid sample measurement for (e.g.) exposure or burial profiles for rock surface dating and IRSL decay curves. In addition to dating and dosimetry, this system offers a means for investigating local mineral sensitivities to stimulation wavelength, dose and bleaching responses and the possibility to correlate these observations with geochemistry to provide further insight into the behaviours of IRPL and IRSL down to micro-scales. Equally, the Risø Luminescence Imager may be adapted to other applications in environmental or industrial dosimetry where a rapid measurement of cm-scale samples is important. We believe that this instrument will pave the way for the design of a field instrument for *in situ* measurement of luminescence-depth profiles for both burial and exposure dating.

Acknowledgements

We wish to thank the valuable contributions from Henrik Olesen and Søren Vig Dalsgaard who helped with the design and building of the instrument. We also extend gratitude to our colleagues Arne Miller, Mark Bailey and Torben Esmann Mølholt at the High Dose Reference Laboratory at Risø for providing access to the irradiation facilities. We thank Benny Guralnik for providing the rock samples.

2.7 Supplementary information

S1: Raw data from IRPL reproducibility measurements

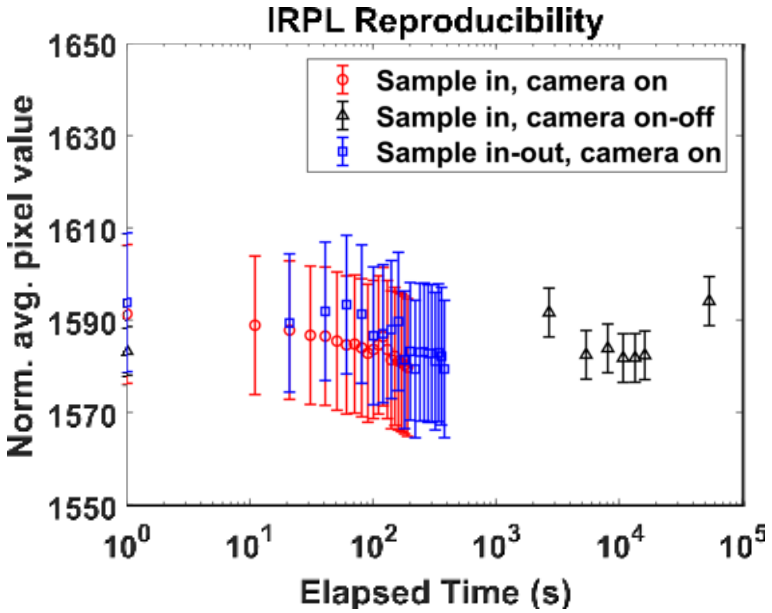

Figure 2.9: Raw data points from the three IRPL reproducibility tests as discussed in section 2.4.3, and shown in Figure 2.5

2.8 Appendix: Effective depth of IR stimulation and detection

There are several optical properties of materials which will determine the interaction of light and material including the refractive index, transmissivity, reflectivity and absorptivity. With regards to using OSL for applications in dosimetry, it is paramount to have an understanding of how multi-bandwidth or monochromatic light interacts with the chosen dosimeter. Understanding which wavelengths experience significant attenuation through media or which wavelengths are most efficient at exciting trapped charge will help us to better constrain how sediments are effectively zeroed and how luminescence-depth profiles progress from a rocks surface with time. It will also inform us of the effective 3D volume of sample which is actively contributing during the measurement of luminescence. This latter question arose during the development of the Risø Luminescence Imager, where sample sizes can be a range of thickness's and surpass the conventional volume of 10 $\times$ 1 mm of rock slices, which are measured on a reader (where the whole volume of rock slice is assumed to contribute to the OSL readout). We observed from multiple samples, low light levels from regions which did not completely correspond to surface feldspar - indicating that there were luminescing minerals located just below the surface which were contributing to the total measurement photon count. If we actually want to fully understand how dose is distributed through our samples and trust our equivalent dose estimates, we need to estimate the total 3D volume of the sample being stimulated and measured.

What this appendix aims to address is the effective stimulation and measurement depth of IR wavelengths in natural rock samples and feldspar. To do this we have defined two aims: 1) determine the penetration depth of IR wavelengths (the effective stimulation depth), and 2) determine from which depth IRPL is being measured from (i.e. the effective volume). To investigate these aspects, we have devised three small experiments:

1. **Determine light attenuation coefficients and transmittance**.
   Attenuation coefficients for wavelengths between 300-900 nm through both pure K-feldspar mineral and heterogeneous rock sample (granite) are measured. This will demonstrate how different wavelengths are actually attenuated or transmitted through the materials favoured for IRSL and IRPL.

2. **Determine the effective stimulation depth of near-infrared wavelengths.**
   This is investigated by calculating the change in IRPL intensity (ΔIRPL) from rock samples of different thicknesses due to measurement of IRSL on the opposing side of the rock. This experiment will give an indication of the attenuation of IR stimulation light with depth.

3. **Estimate effective stimulation and measurement depth.**
   This involves: a) calculating the effective sample thickness using an adapted version of the Lambert-Beer law for light attenuation, and b) measuring the total IRPL from increasingly thicker stacks of pure K-feldspar. The total measured IRPL should increase with increasing feldspar thickness until the maximum effective depth is reached.

These experiments and their results are described below, following a brief introduction of how light interacts with media.

2.8.1 Basic principles of light interaction through media

The relationship between the properties of a material with the attenuation of light along the optical path length is described by the Lambert-Beer law. The transmittance (T) of light through a media can be described as (Eq.2.1):

$$T = \frac{I}{I_0} = e^{-\mu x} \tag{2.1}$$

Where I and I_0 define the transmitted and incident intensity respectively, and the relationship defined by the exponential attenuation of light which is defined by the linear attenuation coefficient (μ; mm^{-1}) over path length (x; mm). Reduction of the transmitted light can result from both scatter and absorbance (A) of the light. Values of A can be calculated according to Eq. 2.2:

$$A = \varepsilon \ell C = log_{10}\frac{I_0}{I} = log_{10}\frac{1}{T} \tag{2.2}$$

The value of A is directly proportional to the path length ℓ (mm), concentration of attenuating species, c and the proportionality constant ε describing absorptivity of the material. From this relationship, a value of A of 0 defines complete transmittance. The light intensity as a function of depth can be described through Eq.2.3:

$$I(x) = I_0 e^{-\mu x} \tag{2.3}$$

For a sample of given thickness (t, mm), the attenuation coefficient μ (mm^{-1}) can be defined as:

$$\mu = \frac{1}{t} L_{\mathrm{n}} \frac{I_0}{I} \tag{2.4}$$

Absorbance can be measured using simple instrumentation such as a photospectrometer. If information on scatter and reflectance is also needed, these values can be obtained by measuring in an integrated sphere. From such absorbance measurements, the attenuation coefficient can be calculated by dividing the absorbance by the sample thickness.

2.8.2 Light attenuation and transmittance

The absorbance of wavelengths from 300 - 900 nm through slices of pure K-feldspar and granitic rocks are measured here, and translated to values of μ. From the absorbance, estimates of the transmittance of specific wavelengths specific to IRPL measurement are also derived.

2.8.2.1 Materials and methods

Two sample materials were investigated here: a pure K-feldspar mineral sample and a pale white granite. The granite sample is a medium-grained pale rock which has been used for several other studies in this thesis (see chapters 3-5). A 1.43 mm thick slice of the feldspar was cut using a 0.3 mm diamond wire saw, and a 1.03 mm thick slice of granite was also cut. Using a Shimadzu UV-2700 spectrophotometer, the absorbance of each slice was measured for wavelengths between 300-900 nm. Values of μ (mm^{-1}) were then calculated by dividing the absorbance by slice thickness (Eq.2.4), and plotted over wavelength. Transmittance values were calculated for specific wavelengths of interest regarding IRPL bleaching or stimulation: 405 nm, 532, 830, 850, 880 and 885 nm.

2.8.2.2 Light attenuation and transmittance results

The attenuation coefficients calculated from the absorbance measurements are presented in Figure 2.10a. The data points around 300 and 900 nm are slightly noisy, due to combined effects of changes in detection efficiency at these wavelengths, and a need for re-calibration of the equipment (which could not be performed at this point). Regardless, both the feldspar (pink triangles) and granite data (grey circles) show a decrease in μ with increasing wavelength, with smaller attenuation coefficients through the feldspar for all wavelengths. Figure 2.10b shows the transmittance (T, %) of specific wavelengths relevant to IRPL bleaching and stimulation. Observed is the expected increase in T(%) with increasing wavelength. Through the 1.03 mm granite slice, ~3% of near-infrared (NIR) wavelengths are transmitted. This increases to ~5% through the more homogeneous 1.43 mm thick feldspar slice.

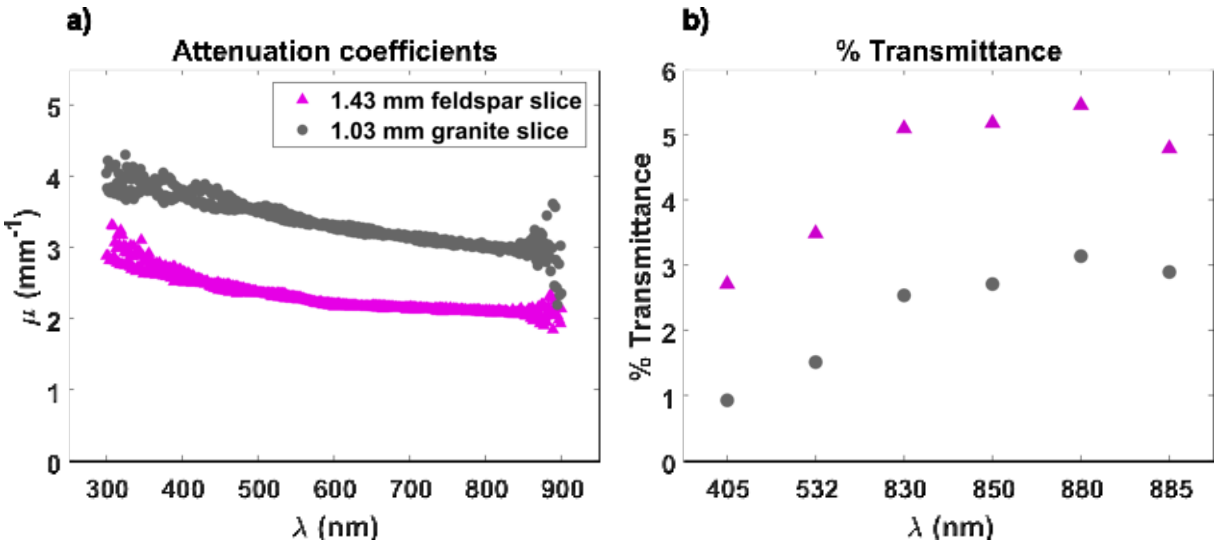

Figure 2.10: a) Attenuation coefficients calculated from absorbance measurements for a slice of pure K-feldspar (pink triangles) and a slice of granite (grey circles). b) Percentage transmittance through the feldspar and granite slices for specific wavelengths relevant for measuring IRPL.

2.8.3 Effective stimulation depth: ΔIRPL as function of slice thickness

Presented in this section is an investigation into the effective stimulation depth of 850 nm wavelengths through granitic rock. This is assessed by observing the effects of IRSL measurement on one side of a rock slice, on the IRPL on the opposing side of the slice, following the knowledge that the IRPL trap population can be depleted by IRSL measurement (see Jain et al., 2020). The IRPL is measured from one side of a rock slice, followed by IRPL, IRSL and a second IRPL measurement on the opposite side of the slice, before remeasuring the IRPL on the first side. The change in IRPL from before and after IRSL measurement (ΔIRPL) is calculated for both sides of the slice according to Eq.2.5:

$$\Delta IRPL = \frac{IRPL_i - IRPL_a}{IRPL_i} \times 100 \tag{2.5}$$

where $IRPL_i$ is the initial IRPL measurement, and $IRPL_a$ is the second measurement of IRPL after IRSL measurement. It is expected that with increasing sample thickness, the 850 nm wavelength is attenuated more, and thus the total flux reaching the opposite side of the slice will decrease with increasing slice thickness. As ΔIRPL should be proportional to the flux of the IR photons bleaching the traps, one can use ΔIRPL as a surrogate for the effective stimulation power on the opposite side of the slice.

2.8.3.1 Materials and methods

Multiple slices of the heterogeneous granite were cut at different thicknesses, ranging between 1.11 mm and 2.06 mm. The IRPL was imaged using the Risø Luminescence Imager from side 1 of each slice, before the slices were flipped over and IRPL, IRSL and IRPL again was measured from the side 2. The slices were then flipped back to side 1 and the IRPL measured again. The IRPL was integrated over 3 seconds for each slice, and the IRSL was measured over 20 frames, each integrated over 10 seconds. This measurement duration was long enough to reduce the IRSL to background levels. To calculate the ΔIRPL from side 1, the images from before and after the IRSL measurement were registered onto one another allowing pixel-wise calculation, and regions (~2 × 2 cm) from the centre of each slice were defined. The summed IRPL values from these regions from each image pair was taken and used to determine the ΔIRPL values (Eq.2.5). For side 2 (where the IRSL was measured from), the images did not require registration onto one another. The same size region of interest as for side 1 was used, and the summed pixel values of these regions was used to calculate ΔIRPL for side 2. The percentage difference between the ΔIRPL from side 1 to side 2 was calculated, and plotted as a function of slice thickness, and fitted with an exponential model (representing the expected decrease in stimulation power following the Lambert-Beer law). With these values, we were able to estimate the decrease in effective stimulation power of the 850 nm stimulation LEDs.

2.8.3.2 Effective stimulation depth - ΔIRPL Results

Presented in Figure 2.11a are the individual ΔIRPL values from side 1 (solid data points) and side 2 (hollow data points) from all measured slices. The ΔIRPL values from side 2 (where the IRSL was measured) are all fairly similar between all measured slices, with and average and

standard deviation of 5.4 ± 0.6% for the $\Delta IRPL_{880}$, and 15 ± 1.4% for the 955 mn data. The ΔIRPL data from side 1 show decreasing values of ΔIRPL with increasing slice thickness.

Shown in Figure 2.11b are the ΔIRPL values from side 1 divided by those calculated from side 2 (where IRSL was measured). The data are plotted as a function of slice thickness, where 0 mm depth represents the top surface of side 2. The data are fitted with single exponential models (equations shown on figure), which provide an estimate of how ΔIRPL on side 1 (and thus the effective stimulation power) decreases with increasing slice thickness. The $IRPL_{880}$ and $IRPL_{955}$ data both present a negative correlation between the difference in ΔIRPL calculated for side 1 and side 2, with increasing slice thickness. For a slice 1.1 mm thick, the $\Delta IRPL_{955}$ calculated from side 1 is 75% of the ΔIRPL calculated from side 2. For the slice with a thickness of 2.06 mm, the $\Delta IRPL_{955}$ from side 1 is ~34% of that calculated from side 2. Thus, even at 2 mm thickness, the IRSL is still being stimulated from side 1 during measurement on side 2. According to the exponential fit through the data, the stimulation power will be reduced to somewhere between 23 and 38% of the starting power after transmitting through 2.1 mm. This is a significantly higher transmittance than what was estimated in experiment 1. It was surprising to see differences between the $IRPL_{955}$ and $IRPL_{880}$ and that fitting the data gives slightly different attenuation coefficients between the different two signals, but this is likely due to the scatter in the data (greater for the $\Delta IRPL_{880}$), which limits the reliability of the model fitting.

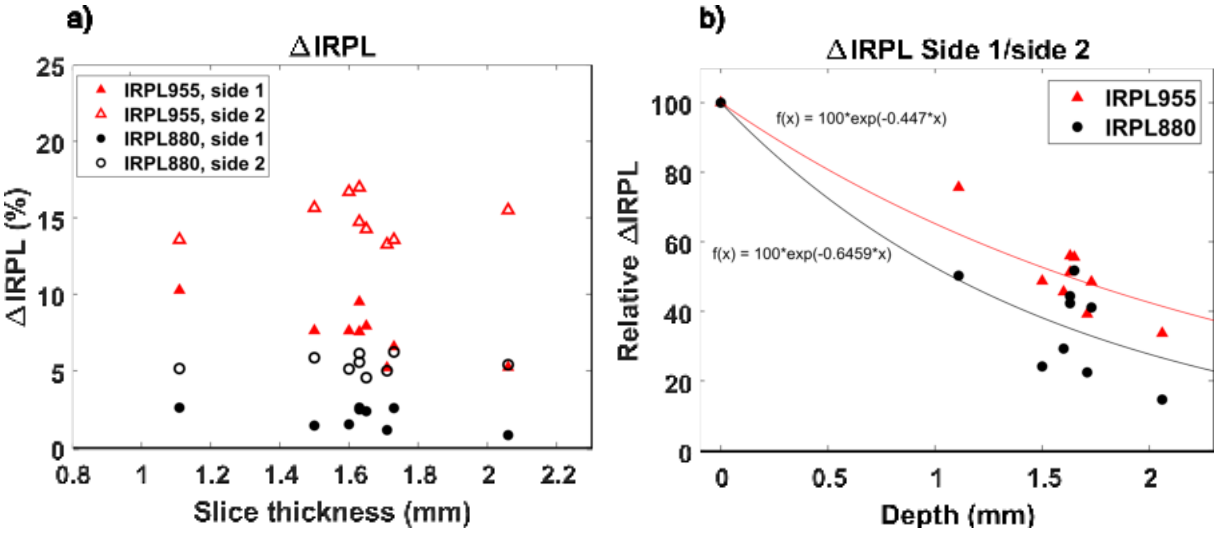

Figure 2.11: a) Individual ΔIRPL values (%) from side 1 (solid data points) and side 2 (where IRSL was measured; hollow data points) over slice thickness. b) Relative ΔIRPL from dividing ΔIRPL from side 1 by that from side 2 (where IRSL was measured). A single exponential model is fitted to each data set. The depth on the x-axis represents the relative vertical position of side 1, where depth 0 mm is the top surface of side 2 during IRSL measurement.

2.8.4 a) Effective thickness estimation

Following the results above addressing the effective stimulation depth, it is of interest to obtain an estimate of the effective thickness of a slice where the attenuation of both the stimulation and emission is accounted for. Following the Lambert-Beer law, it is possible to obtain such an estimate according to Eq.2.6 (see Nyemann et al., 2020):

$$t_{eff}(mm) \approx \int_0^t (T \cdot 10^{-0.434 \cdot \mu \cdot t})^2 \cdot dt \tag{2.6}$$

where t_{eff} (mm) is the effective thickness of a slice of thickness t (mm). T is the transmittance (%) at a given wavelength and μ is calculated according to Eq.2.4. We consider the t_{eff} (mm) for wavelengths at 830, 850 and 880 nm through the 1.03 mm thick slice of granite and the 1.43 mm thick slice of feldspar. As this equation accounts for attenuation of both the stimulation and emission wavelengths, the wavelengths should be similar. Therefore an average of these three t_{eff} estimates was calculated as representative of an $IRPL_{880}$ measurement. For the granite slice, the average estimates of t_{eff} was 0.14 ± 0.01 mm, and 0.29 ± 0.05 mm for the feldspar slice. These estimated t_{eff} are significantly smaller than what was experimentally shown in experiment 2 (section 2.8.3), where the effective depth of the stimulation alone was greater than 2 mm. If we instead use the estimate of μ obtained from the fitting of the $\Delta IRPL_{955}$ data (less scatter in the data, thus the fit is considered slightly more reliable than that for the 880 nm data) shown in Figure 2.11b, for a granite slice 1.03 mm thick an estimate of 0.51 mm is obtained. This is larger than that calculated from the transmittance data, but as the fit of the $IRPL_{955}$ data is not considered particularly robust (few data points with scatter) it is unclear as to whether this estimate is reliable.

2.8.5 b) Effective stimulation and measurement depth: IRPL intensity with increasing sample thickness

As a final investigation into the effective stimulation and emission measurement depth, we conduct an experiment by which increasingly larger vertical stacks of pure K-feldspar are stimulated by the 830 nm laser and the IRPL is measured. We expect that the total IRPL measured from increasingly larger volumes of the feldspar to increase until a thickness beyond which the total IRPL does not change, as the maximum effective stimulation and measurement depth is reached.

2.8.5.1 Materials and methods

Slices of the same pure K-feldspar sample as used in experiment 1 were used here. Small feldspar slices (~1.5 × 2 cm in size) were cut at different thicknesses ranging from 1.40 mm to 2.04 mm (see Table 2.1). The samples had been exposed to natural light, yet still produced significant IRPL, and therefore no dose was given to the slices. First, IRPL measurements of the individual slices were made using the Risø Luminescence Imager, integrating the IRPL over 1 second.

Keeping slice 1 (thinnest slice) as the top slice, slices 2 to 6 were then individually placed beneath slice 1, and the IRPL imaged. Thus, with the known intensity of slice 1, it was possible to determine how much IRPL from the bottom slice (slices 2 - 6) was adding to the total intensity of the stack measurement. Three duplicate measurements were made of both the individual slices and the stacks to check the reproducibility of the measurements.

Slice	1	2	3	4	5	6
Thickness (mm)	1.40	1.43	1.46	1.57	1.71	2.04

Table 2.1: Slice numbers and thicknesses of the feldspar slices used in section 2.8.5.

For each of the images, a 5 × 5 mm region of interest was defined within the feldspar slices and the average of these pixel values was taken. The mean and standard deviation of the three duplicate measurements made per individual slice or per stack were then calculated. The ratio between the IRPL of slice 1 and the IRPL from each stack (slice 1 + slice x) was calculated. Any influence of the change in vertical height on the IRPL intensity was also checked. For this, the IRPL was measured from slice 1. Then, individually the remaining slices were placed on the sample stage, but covered in light-tight tape to avoid any IRPL contribution. Slice 1 was then placed back on top and the IRPL intensity measured again. The ratio of the IRPL from the initial position to the second stacked position was then calculated.

2.8.5.2 Effective stimulation and measurement depth results

Figure 2.12a presents the mean IRPL intensities of the individual slices as a function of their individual slice thickness. Each data point is the average and standard deviation of the triplicate measurements. The individual intensities are variable, with slice 3 having the highest IRPL intensity. Figure 2.12b presents the mean IRPL intensities from the stacked feldspar slices (slice 1 + slice x), plotted over the total thickness of the respective stack (note the y-axis is the same as for panel a). There is a clear increase in total IRPL intensity for both IRPL signals, already indicating that the IRPL is being stimulated and measured from depths >1.4 mm. The insert presents the results of the test where any influence on the changing position of slice 1 was measured. All ratio values are within 3% of unity, which is within the reproducibility uncertainty limits, and thus no significant influence on relative slice height on the IRPL intensity is inferred. Panel c) presents the results of calculating the IRPL from slice 1 over the IRPL from each slice stack. We observe a positive correlation between the IRPL ratio and total stack thickness. For a stack of 3.44 mm total thickness (slice 1 + slice 6), there is a ~33% increase in $IRPL_{955}$ and a ~30% increase in $IRPL_{880}$ from the individual intensity of slice 1. This again confirms that the effective stimulation and measurement depth is greater than 1.4 mm (thickness of slice 1), and and lies somewhere between 1.4 and 3.44 mm (as we are not measuring 100% of the IRPL from slice 6 beneath slice 1).

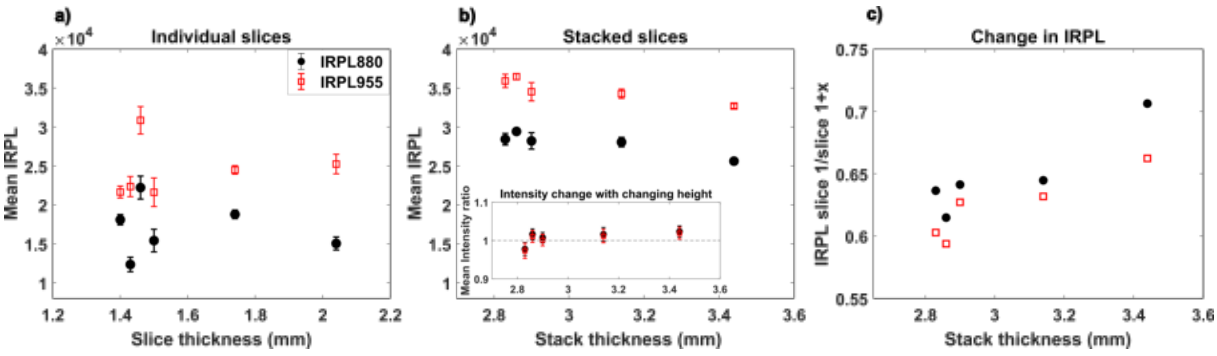

Figure 2.12: a) $IRPL_{880}$ (black circles) and $IRPL_{955}$ (red squares) mean intensities of the individual feldspar slices, plotted over their respective slice thicknesses. b) IRPL intensities measured from the slice stacks (slice 1 + slice x, where x = slices 2-6). The insert shows the results of the test for checking for any influence on the relative height of slice 1 on the measured intensity, with the dashed line representing unity. The data in panel b) and the insert are plotted over the total stack thickness. c) Plot of IRPL intensity from slice 1 divided by the intensity of slice 1 + slice x, plotted over the total stack thickness.

2.8.6 Discussion and conclusions

An attempt at estimating the effective stimulation depth and measurement depth of different wavelengths through samples of pure K-feldspar and granite was made, with a focus on NIR wavelengths relevant to IRPL. From measuring the absorbance and estimating values of μ (mm^{-1}) over wavelengths from 300-900 nm, we observe the expected decrease in attenuation coefficient with increasing wavelength. The transmittance (T %) calculated for the NIR wavelengths suggests that only 3% of light will be transmitted through a 1.03 mm heterogeneous slice of granite. However, as effects of scattering and reflectance were not accounted for during the absorbance measurements, it is uncertain as to how reliable these estimates of transmission are. It is expected that scattering of certain minerals (i.e. with relatively greater refractive indices) and at mineral boundaries will be significant in the granite, and should be accounted for if trustworthy estimates of μ and T are to be obtained.

As an experimental investigation into the effective stimulation depth of NIR wavelengths through granitic samples, calculating the ΔIRPL from two opposing sides of granite slices of increasing thicknesses indicates that the effective stimulation power is reduced to ~30% of the power at the slice surface, after transmitting through a 2.1 mm slice. This is much greater than the estimated transmittance in section 2.8.2 from the μ calculation. This power is however still enough to reduce the IRPL by ~18% and 30% for the $IRPL_{880}$ and $IRPL_{955}$ respectively. However, there is scatter in the ΔIRPL data sets (especially in the $IRPL_{880}$ data in Figure 2.11b) and the fit through this data is not well constrained. It is also currently unclear as to why we see a difference between the $\Delta IRPL_{880}$ and the $\Delta IRPL_{955}$ data. From the raw data points shown in Figure 2.11a, we see that the actual decrease in $IRPL_{880}$ on side 1 is very small (~2%), which is likely the cause of the scatter and poorer estimation of flux. The $IRPL_{955}$ data is considered more reliable. In the future, a higher resolution data set with a large range of slice thicknesses would be beneficial to obtain to fully and reliably quantify the effective stimulation depth. There is a large discrepancy between the calculated (t_{eff}, see Eq.2.6) and experimental (feldspar stacking exercise) estimates of the effective stimulation and measurement depths of NIR wavelengths through feldspar slices. The experimental data indicates that we are actually stimulating and measuring IRPL from depths greater than the 1.4 mm slice (slice 1, placed on top of the stack), which is already an order of magnitude greater than the t_{eff} (mm) estimate.

In conclusion, we demonstrate that NIR wavelengths have a lower attenuation through both homogeneous and heterogeneous materials, compared to shorter wavelengths. From attempting to estimate the effective stimulation depth, we experimentally show that the stimulation depth of 850 nm light extends at least to 2.1 mm. We also experimentally demonstrate that the effective depth of stimulation and measurement for NIR wavelengths is also greater than 1.4 mm. If we accept the values from the experimental data and consider the average slice thicknesses of the samples measured in chapters 3 and 5 to be 1.3-2 mm, we can assume that the IRPL is being stimulated through the whole slab volume. These estimates of the effective depth are greater than those calculated using an equation adapted from the Lambert-Beer law describing the transmittance of stimulation of emitted light integrated over a sample of known thickness. It is suggested that to obtain more reliable estimates of both the effective stimulation depths of NIR wavelengths and the effective thickness of stimulation and measurement, effects of scatter and reflectance from the surface and within the samples under investigation should be accounted for when measuring transmittance. Future work should also use samples of thicknesses covering a larger range than those presented here, and that materials of different compositions are also investigated.

CHAPTER 3

Rapid *in situ* assessment of luminescence bleaching depths in rocks for deriving burial and exposure chronologies of rock surfaces

Sellwood, E.L.[a], Kook, M.[a], Jain, M[a].
[a] Department of Physics, Technical University of Denmark, Risø Campus, 4000, Denmark

Presented here is an investigation in to reconstructing luminescence-depth profiles from spatially resolved measurements of IRSL and IRPL, without using a test dose for normalisation. The publication presented in this chapter was accepted in the journal Quaternary Geochronology in August 2021, and is available at: https://doi.org/10.1016/j.quageo.2021.101227.

Abstract

Recent developments in luminescence dating offer new ways to date exposure and burial durations of rocks. The new rock surface dating methods ideally require high-resolution data, faster sample preparation and measurement times, and field screening methods to select samples with appropriate luminescence characteristics and bleaching histories. Presented here is a demonstration of an EMCCD (electron multiplying charge coupled device) based system capable of imaging high-resolution infrared stimulated luminescence (IRSL) and infrared photoluminescence (IRPL) from rock samples. The IRPL can be detected at both 880 nm and 955 nm. Using this instrument, the entire luminescence-depth profile can be reconstructed by imaging a single surface cut perpendicular to the exposed rock face. We demonstrate the possibility of reconstructing luminescence-depth profiles suitable for rock surface dating from large (cm-scale) rock samples, without using a regeneration dose for normalisation of the natural luminescence signals. Based on the different bleaching characteristics of the IRSL and IRPL emissions at 880 nm and 955 nm, we show that it is possible to gain reliable estimates of bleaching depths from measurement of as few as two images of the IRPL signal (one for each emission), or from measurement of the IRSL decay curve. We thus by-pass laborious sample preparations and the need for a gamma source to estimate the bleaching depth, thereby extending the 2D luminescence-depth profile imaging technique to other laboratories that lack access to ionising radiation facilities. This study also makes a significant progression towards development of a field instrument for in situ relative exposure dating, and sample screening for rock surface burial dating.

Key words

Rock surface dating; Infrared-photoluminescence; Luminescence bleaching profiles; Spatially resolved.

3.1 Introduction

Building chronologies of past geological and archaeological events often requires a range of methods applicable to different types of deposits and materials over different age ranges. One such newly developed method is optically stimulated luminescence (OSL) dating of exposed or buried rock surfaces. This method is based on the progressive re-setting of luminescence with depth into the rock as a function of time. The OSL intensity with depth into the rock is described by a double exponential function (Laskaris et al., 2011; Sohbati et al., 2012c; Freiesleben et al., 2015; Galli et al., 2017; Meyer et al., 2018; Ou et al., 2018), where the depth of the inflection point of the profile depends on the exposure time, daylight flux and the opacity and internal dose rate of the rock (Freiesleben et al., 2015; Ou et al., 2018). The resulting luminescence-depth profile can be exploited for estimating exposure durations or erosion rates on timescales of up to 10^5 years (Sohbati et al., 2012c; Lehmann et al., 2018; Sohbati et al., 2018; Guralnik et al., 2019). This method of Rock Surface Exposure Dating (RSED) relies on finding a suitable calibration sample with known exposure time. If an exposed rock surface or artefact is subsequently buried by a geological or archaeological event, its surface or near surface region where luminescence was zeroed prior to burial begins to accumulate dose, and can then be dated through conventional OSL means (equivalent dose determination from surface slices); this method is called Rock Surface Burial Dating (RSBD). Unlike in sand-silt grains, the luminescence-depth profile can inform us as to whether the sample was sufficiently bleached prior to burial or not; this can be achieved by analysing the profile by curve fitting or visual examination (Sohbati et al., 2012c; Freiesleben et al., 2015; Rades et al., 2018; Liu et al., 2019). Thus, we can establish whether the derived luminescence age from the slices at a particular depth indeed dates the burial event.

Rock surface dating (RSD) with OSL is gradually bridging a gap in dating applications where conventional methods may not be applicable. Recent applications demonstrate the suitability of OSL RSD for dating glacial moraines (e.g. Jenkins et al., 2018; Rades et al., 2018), marine and fluvial deposits (Narama et al., 2007; Lüthgens et al., 2017; Souza et al., 2019; Brill et al., 2020), rock-falls and mass-movements (Chapot et al., 2012; Sohbati et al., 2012b; Brill et al., 2020; Tsakalos et al., 2020), archaeological artefacts (Liritzis, 1994; Liritzis et al., 1999; Rhodes et al., 2006; Liritzis et al., 2010; Gliganic et al., 2018; Khasawneh et al., 2019; Liritzis et al., 2019; Ageby et al., 2020) and rock art (Chapot et al., 2012). However, whilst several exciting applications are emerging in literature, OSL RSD measurement techniques are cumbersome and time consuming. In particular, RSBD requires a significant number of suitable specimens that were sufficiently bleached prior to burial; however the bleaching status of the sample can only be determined from laboratory investigations after an expensive sampling campaign. It has been the experience of our lab that the proportion of bleached rock samples from high-energy environments (such as flood deposits) can be as low as 10%. The sample preparation stages for OSL RSD often involve abrading grains from the surface, or coring, slicing and sometimes chemical treatment to select mineral fractions before measurement, all of which are very time consuming and introduce uncertainties in depth measurement. Profiles are generally also only constructed from ~10 - 20 slices, which for exposure dating can restrict the reliability of model fitting and subsequently age determination as the model parameters are poorly constrained. It is therefore highly desirable to have a rapid and accurate high-resolution measurement of OSL

intensity with depth into rocks, both in the field to guide sample collection, and in the lab to decrease sample processing times and obtain a more robust dataset.

Spatially resolved OSL and TL measurements can potentially solve these problems, but until recently measurements have largely been restricted to small rock slices ~1 cm in diameter due to size constraints of the TL/OSL readers (e.g. Hashimoto et al., 2003; Clark-Balzan et al., 2012; Duller et al., 2015; Kook et al., 2015; Duller et al., 2020b).The recent discovery of infrared-photoluminescence (IRPL) from feldspar (Prasad et al., 2017) has piqued further interest in spatially resolving luminescence, as IRPL shows very high sensitivity (Kook et al., 2018; Kumar et al., 2018) and allows the same area to be measured multiple times without a significant depletion in signal intensity (steady state emission). These characteristics together allow IRPL to be suitable for high-resolution imaging where minerals can be clearly identified to be easily obtained. Recently, Sellwood et al. (2019) demonstrated that IRPL based imaging can directly capture high-resolution (~140 μm) luminescence-depth profiles from large (~4 $\times$ 5 cm) rock slabs, circumventing the need for conventional coring and slicing. Requiring only to cut a slab of rock perpendicular to the exposed surface, they imaged the IRPL emission at 955 nm from feldspar (Prasad et al., 2017) from a granitic rock. The measured IRPL depth profile was directly comparable to that constructed using post-IR IRSL at 225°C ($pIRIR_{225}$) from conventional rock slices measured on the Risø TL/OSL reader. However, like for any luminescence signal, it is necessary to normalise the natural IRPL signal by that obtained using a regeneration dose; this is because the absolute light emission from the sample varies spatially depending on feldspar sensitivity as well as the emitting volume under each pixel (a function of the 3D distribution of each mineral). Thus, although IRPL imaging is a powerful method allowing rapid measurements of high-resolution luminescence-depth profiles, it requires facilities for irradiation of large centimetre-scale samples. Unfortunately, such facilities are not easily accessible for most luminescence laboratories and certainly not available during field sampling to enable screening of bleached samples. This need for normalisation with irradiation doses is therefore a significant limitation on the usability of imaging of luminescence for rock surface dating, and poses significant hindrance in the routine application of the technique, both for the field and laboratory applications.

We present here a thorough investigation into different normalisation methods that do not require a regeneration dose for constructing spatially resolved luminescence-depth profiles. We believe such a methodological development will open the door for many OSL labs to using spatially resolved luminescence for rock surface dating applications, and also avoid potential problems associated with sensitivity changes induced from regeneration doses (Li et al., 2013). In order to achieve this goal, we have further developed our instrumentation reported in Sellwood et al. (2019) to improve the precision of IRSL signal (greater stimulation power) and extended the IRPL detection to image the newly characterised 880 nm emission (Kumar et al., 2018; Kumar et al., 2020a), alongside the original 955 nm window. We demonstrate that it is possible to assess IRSL and IRPL bleaching depths in rocks using as little as two images (both IRPL emissions), or from the IRSL decay curve alone, obtaining comparable information to profiles normalised with a regeneration dose.

3.2 Methods and instrumentation

Three granitic samples were measured in this study. A pale crystalline granite (G02) with <2 mm diameter K-rich feldspar crystals was selected. The sample had been thermally annealed at 700°C and irradiated with a 7 kGy saturation dose before being bleached outside for 566 days. A core was drilled perpendicular to the exposed surface using a 40 mm diameter diamond drill

bit, and a 36 × 20.7 × 1.3 mm section was cut from this using a 0.3 mm diamond wire precision saw. The second sample is a coarse crystalline (~1 cm crystals) heterogeneous granite (GOT12) from Switzerland. The sample was taken from glacially polished bedrock and has a known exposure of ~11 ka (Hippe et al., 2014). A cubic block of the sample was cut perpendicular to the exposed surface to produce a 50 × 47 × 10 mm slab for imaging. Third, a pink fine crystalline low-metamorphosed granitic-gneiss cobble (GL2) was collected from the front of a glacier in southwest Greenland. The sample is assumed to have been recently deposited by the glacier, but an actual exposure duration has not been established. This sample was also cored and sliced into a 19 × 41 × 1.5 mm section. Photographs of the three samples are available in the supplementary information.

Images were captured using an Evolve electron multiplying charge-coupled device (EMCCD) camera internally cooled to ~80°C, with a 512 × 512 pixel chip size. IRPL was stimulated with an 830 nm laser with a power distribution of 0.8 mW/cm^2 over a 7 cm diameter area. The IRSL was stimulated at room temperature (~22°C), via twenty 850 nm LEDs mounted on a 30 cm diameter ring with a 60 mW/cm2 power distribution at the sample stage. Three filter combinations were mounted for measuring the different emissions. The $IRPL_{880}$ was transmitted through an 880 nm band-pass filter (BP) and 2 × 850 nm long-pass (LP) filters, the 955 nm peak through a 950 nm BP and 2 × 925 nm filters, and the IRSL was detected through a BG-3 and BG-39 combination. A 1020 nm LED was also mounted for visual imaging the samples. Samples were placed on a vertically adjustable lab jack, enabling manual focusing of the camera on the sample.

Step	**Result**
1. $IRPL_{880}$	$IRPL_{880}$ L_n, L_x
2. $IRPL_{955}$	$IRPL_{955}$ L_n, L_x
3. IRSL	IRSL L_n, L_x
4. $IRPL_{880}$	$IRPL_{880}$ after IRSL
5. $IRPL_{955}$	$IRPL_{955}$ after IRSL
6. Bleaching in solar simulator	Background
7. Gamma dose	

Table 3.1: Measurement sequence for IRPL and IRSL. Step 7 was used to reconstruct regeneration-dose normalised profiles to act as a reference to profiles constructed with the new normalisations methods discussed in this article. After step 7, steps 1-5 were repeated.

The exposure times for the IRPL images were set according to the intensities of the samples to prevent saturation in the EMCCD camera. The IRSL was measured with a 10 s exposure for either 12 frames (GOT12) or 18 frames (G02 and GL2), which was sufficient for capturing the full IRSL decay curve until background levels. After measuring the natural IRPL and IRSL, then IRPL again, the slab was bleached in the solar simulator for 6 days and then given cumulative gamma doses from a Cobalt-60 gamma cell facility (High dose rate reference laboratory, DTU), totalling a final test dose of 5 kGy. Here, we do not subtract a residual or background from our data. There is negligible background noise from the instrumentation and we observed that there was minimal influence of any residual signal on the shape of the luminescence-depth profiles. Therefore, we disregarded such a background subtraction to make the data acquisition and analysis as simple and fast as possible. The full measurement sequence for all samples is outlined in Table 3.1.

For profile reconstruction, analysis was performed in MATLAB, using the image processing toolbox (Mathworks, 2017, script and data set available in the supplementary information). The data used for profile construction were: a) the $IRPL_{955}/IRPL_{880}$ ratio, b) ΔIRPL, as per Jain

et al. (2020) (see Eq.3.1; $IRPL_i$ is the initial IRPL measurement, and $pIR_{RT}IRPL$ is the IRPL after IRSL at room temperature (RT)), and c) the ratio between the first and a later frame (F1/Fx) of the IRSL decay curve.

$$\Delta IRPL = \frac{IRPL_i - pIR_{RT}IRPL}{IRPL_i} \tag{3.1}$$

For method c, an appropriate frame for normalisation was chosen arbitrarily through visually assessing the clarity of the profile structure (clear transition zone from bleached to saturated IRSL). IRSL decay curves were constructed by summing the IRSL from each frame and plotting over cumulative stimulation time. Regeneration-dose normalised profiles were made after the samples received the final gamma dose. Luminescence-depth profiles were constructed by taking the mean and standard error of each column across the images. The bleaching depth was defined as the depth at which luminescence intensity is 50% of the saturation level (or saturation half-depth; SD50%; Sohbati et al., 2012a). These depths were estimated by assessing the mean intensity from the saturated part of the luminescence profile, determining the value at half this intensity and taking the corresponding depth.

3.3 Luminescence-depth profiles in rocks: theoretical considerations

In order to fully understand the normalisation methods discussed in this article, an understanding of the relationships between the two IRPL emissions and IRSL, and their respective bleaching behaviours is needed. Infrared stimulated luminescence (IRSL) from feldspar arises from electron detrapping from the principal trap followed by transportation through the conduction band tail states to recombination centres (holes; Poolton et al., 2002). In contrast to IRSL, Infrared photoluminescence (IRPL) is a stokes-shifted emission, arising from radiative excited to ground state transition in the principal trap following near-Infrared (NIR) excitation (i.e. no detrapping or recombination with holes; Prasad et al., 2017). IRPL examines the two distinct principal trap populations at 880 nm (1.41 eV; $IRPL_{880}$) or 955 nm (1.30 eV; $IRPL_{955}$) (Kumar et al., 2018). Where IRSL measurement empties part of the trap population and informs us of the proximal hole populations, IRPL results in a steady state emission with little to no alteration in trap population from measurement (Jain et al., 2020). Thus, measurement of both IRSL and IRPL enables investigation of the proximal electron-hole populations as well as the total electron trap populations, respectively (Jain et al., 2020).

3.3.1 Correlation between $IRPL_{880}$ and $IRPL_{955}$

Jain et al. (2020) and Kumar et al. (2020a) have extensively characterised IRPL at both 880 nm and 955 nm, concluding that the emissions arise from the same defect but from different sites (hereafter referred to as the 880 nm and 955 nm trapping centres). They demonstrated that both emissions have the same electron-capture cross-sections, but the two IRPL signals bleach at different rates to different residual intensities; the higher residual for the $IRPL_{880}$ compared to $IRPL_{955}$ (Kumar et al., 2020a). Furthermore, the two IRPL centres have different interaction cross-sections for a given wavelength (Kumar et al., 2020a) indicating that they will bleach at different rates when exposed to the same daylight spectrum. Differences in bleaching may result due to factors such as different mineralogy, crystallinity, defect density, opacity, etc..

Considering this, if the two IRPL trapping centres are homogeneously distributed across the sample (on the spatial scale of a pixel when considering spatially resolved measurements), it raises the possibility to self-normalise the IRPL signal (e.g. 955/880 nm) to account for the variations in sensitivity between the two emissions. Taking the IRPL ratio from an exposed rock would therefore yield a luminescence-depth profile which is dependent on the different bleaching rates of the two IRPL centres, and daylight fluence.

With this idea we examined the correlation between the two IRPL signals from the three granitic rock samples used in this study, after receiving a 5 kGy test dose. Figure 3.1 presents the pixel-wise correlations between the $IRPL_{880}$ and $IRPL_{955}$ from each sample. The two emissions are clearly correlated, with correlation coefficients of 0.99, 0.99, and 0.98 for G02, GOT12 and GL2 respectively. These trends indicate that the ratio between the populations of the two centres (880 nm and 955 nm) must be constant on a pixel scale, irrespective of which feldspar grain is measured in the slice. Given that the two IRPL signals occur in the same proportion in a given slice, a profile based on the ratio of the two IRPL signals is expected to account for the spatial variations in absolute sensitivity. If the two IRPL signals had the same bleachability, such a ratio profile would be flat. Instead if they have different bleachabilities as expected from previous work (Kumar et al., 2020a; Kumar et al., 2021b), then we expect that taking the ratio between the two emissions will result in a profile with a structure that yields information on the bleaching depth.

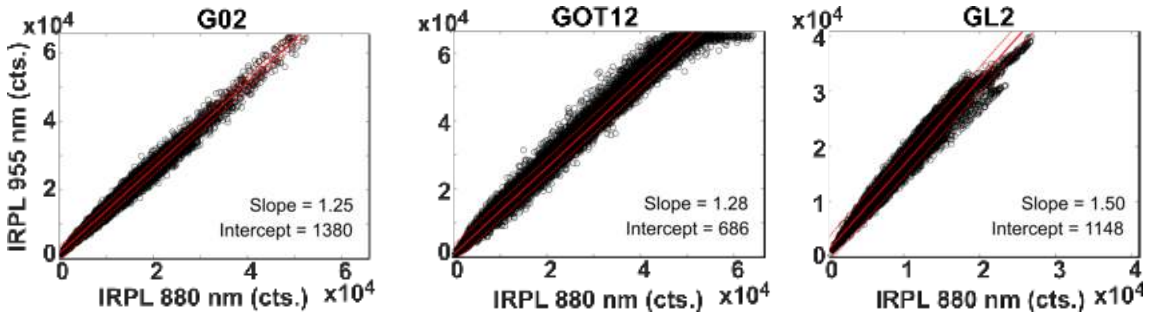

Figure 3.1: Pixel-wise correlation between the $IRPL_{955}$ and $IRPL_{880}$ images for the three granitic samples imaged in this study, after receiving a 5 kGy gamma dose. The red line shows a linear regression fit, with 95% confidence bands shown by the dashed lines.

Interestingly in Figure 3.1, there exists a small intercept on the $IRPL_{955}$ axis for all three samples when a free linear regression is performed on the data. Note that the intercept cannot be due to either the stimulation source breakthrough in the detection window, or the unbleachable residual $IRPL_{955}$ signal; this is because the background measured after bleaching the samples in a solar simulator has been subtracted from these data. While we do not know the origin of the intercept, it is small and has an insignificant effect on the ratio of the two signals.

3.3.2 Effect of $\sigma\varphi_0$ and μ on the IRPL ratio profiles

Here we investigate based on simulations, what shape such a profile based on the ratio of the two IRPL signals can take, and how useful can such a ratio profile be in informing us on the bleaching depth. We consider the first order function used for RSD modelling (Eq.3.2):

$$L(x) = e^{-\overline{\sigma\varphi_0}te^{-\mu x}} \tag{3.2}$$

Here, L is the luminescence at depth x (mm), t (s) is the exposure duration, $\sigma\varphi_0$ (s^{-1}) is the net detrapping rate on the exposed surface and μ (mm^{-1}) is the light attenuation coefficient of the rock (Sohbati et al., 2011).

This bleaching profile has a sigmoidal shape with luminescence rising gradually from zero at the surface to a saturation value at depths with negligible bleaching. We modelled multiple IRPL profiles (Figure 3.2) to simulate the effects of different effective wavelength attenuations (μ, mm^{-1}) and the different photoionization cross-sections (σ) and resulting detrapping rates through the combined parameter $\sigma\varphi_0$ (s^{-1} as a function of the same exposure time, t) of the two IRPL centres.

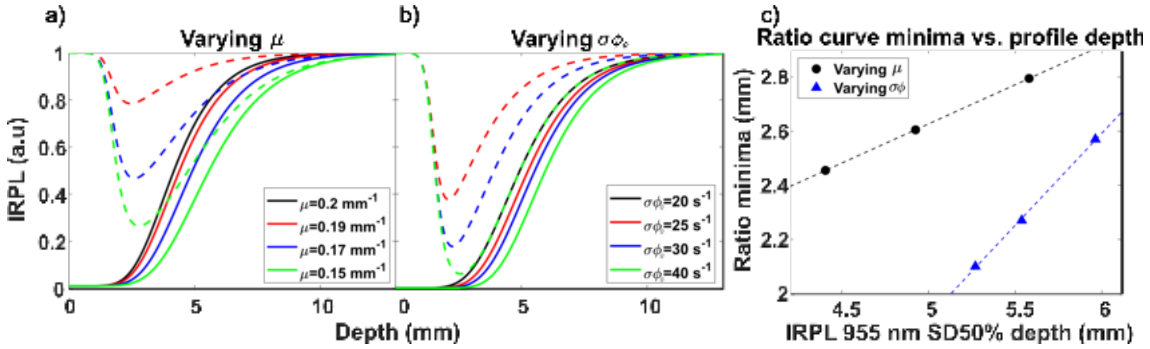

Figure 3.2: Simulated profiles (solid lines) and resulting ratio profiles (dashed lines) after varying either μ (a), or σ, as the combined parameter of $\sigma\varphi_0$ (b). c) Relation between the depth of the ratio curve minima and the SD50% depth of the $IRPL_{955}$ profiles. A linear regression was plotted through each data set.

We considered the benefit of addressing these model parameters separately to try to simplify our understanding of how the two IRPL centres behave upon exposure to light. The $IRPL_{955}$ curves (solid red, green and blue curves) result from decreasing μ (Figure 3.2a) or increasing $\sigma\varphi_0$ (Figure 3.2b) with respect to a reference $IRPL_{880}$ profile (black curve), as we would expect from a natural exposure. We can see that the relatively smaller attenuation coefficients in the $IRPL_{955}$ profiles lead to more gentle slopes in the transitions zones of the profiles (between the bleached and saturated regions), and an apparent deepening in the SD50% depths of the profiles. Variation in the photoionization cross-section between $IRPL_{880}$ and $IRPL_{955}$ leads to profiles which diverge in SD50% depth, but not in slope or shape of the profile (Figure 3.2b). Taking the IRPL 955/880 nm ratio results in a valley shaped profile (dashed lines) with increasing width and depth of the valley as the μ is decreased or $\sigma\varphi_0$ is increased relative to the $IRPL_{880}$ reference curve. The depth of the ratio curve minima of these modelled profiles depends on the separation in depth between the two IRPL profiles used for calculating the ratio. The value of the ratio curve at the surface reaches unity as the $IRPL_{880}$ and $IRPL_{955}$ profiles reach a constant residual value (assumed background in the model) in the simulated data. However, in experimental data this residual level may be different for $IRPL_{880}$ and $IRPL_{955}$ due to different sensitivities and bleaching rates of the two signals (Kumar et al., 2020a), thus leading to a surface ratio deviating from unity. Furthermore, in case there is a burial component in the profile we still expect a valley structure resulting from the bleached components of the luminescence-depth profiles; however the burial doses will determine the ratio at the surface (greater than unity) as well as the relative minima position of the ratio curve. The simulation results are summarised in Figure 3.2c, where we observe a positive relation between the depth from the rock surface of the ratio curve minima (dashed lines in Figures 3.2a and b), and the SD50% depth of the $IRPL_{955}$ profiles.

The results of these simulations suggest that we can utilise the slight differences in IRPL bleachability and that plotting the IRPL 955/880 nm ratio curve can be used to detect whether a sample has been sufficiently bleached in nature or not, while accounting for the spatial variations

in IRPL sensitivity. It is also apparent that the width and depth of the ratio curve can inform us of the extent to which IRPL at 880 nm and 955 nm differ in their bleachability across individual samples.

3.3.3 Correlation between the first and later frames of the IRSL decay curve

In general the IRPL signals are much more difficult to bleach compared to the IRSL signal; Sellwood et al. (2019) estimated that the bleachability of the $IRPL_{955}$ signal was similar to that of the $pIRIR_{225}$ signal. Given that there will always be some samples where IRSL has been sufficiently bleached but the IRPL has not, it is therefore desirable to also have a rapid method for assessing the degree to which the IRSL signal has bleached. Sellwood et al. (2019) were unsuccessful in producing clear IRSL images, largely because of the low stimulation light flux in that study. We have remedied this issue, increasing the stimulation light power enough that IRSL imaging of large rocks slices is now also viable. The obvious question then is how to normalise the natural IRSL measurement without using a test dose. As IRSL has a relatively rapid decay during measurement, whole IRSL decay curves are usually captured from rock samples allowing us to view and compare relative decay rates and sensitivity of IRSL from different regions of interest in the rock. We considered the benefit of dividing the natural IRSL (first frame from the start of the decay curve; F1) by a later frame from the measurement (later part of the decay curve; Fx) representing the harder-to-bleach portion of the trap population.

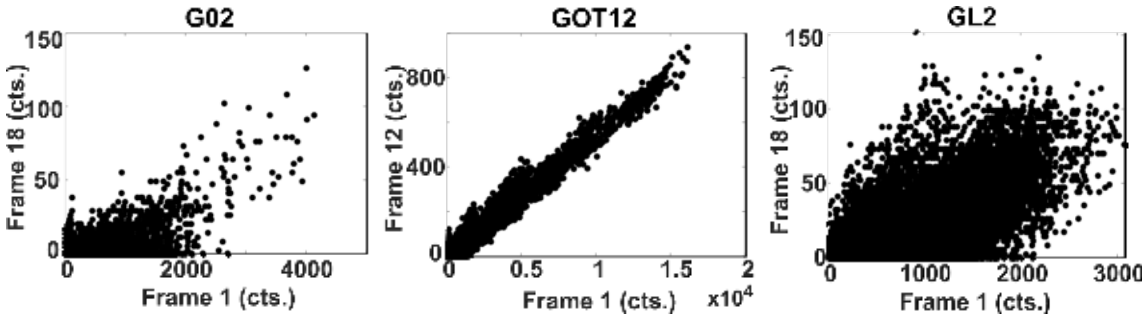

Figure 3.3: Pixel-wise correlations of IRSL intensity between the first frame and the last frame from the IRSL decay curves for each sample.

Figure 3.3 shows the pixel-wise correlations between the first frames of the IRSL decay curves (after 5 kGy) and the final frames for each sample. The scatter, especially for G02 and GL2, is a result of the varying decay rates and sensitivities of the IRSL on a pixel-by-pixel (or sub-crystal) scale. GOT12 has the brightest IRSL, with a much clearer distinction between the IRSL-emitting minerals and non-luminescing regions, leading to a tighter correlation. The differences in IRSL intensities between the three samples is likely a product of slightly different mineralogy, but further investigation into specific geochemistry has not been conducted here. Regardless, it is the general positive correlative relationship which we see between the IRSL from the first and final frames which supports our hypothesis for F1/Fx as a normalisation method. Through normalisation with a later frame from the IRSL decay curve, a luminescence-depth profile can be established where pixel-wise (crystal) variation in IRSL intensity and sensitives are accounted for via decay instead of sensitivity to regeneration dose. As the decay of IRSL is relatively rapid, it is possible to use any frame from the decay curve for normalisation.

3.3.4 ΔIRPL as a surrogate for IRSL

As a final normalisation method, we consider the much higher measurement sensitivity of IRPL compared to IRSL, and the fact that IRSL comes from a subpopulation of traps giving rise to IRPL (Jain et al., 2020). Jain et al. (2020) have demonstrated that the proportion of trapped electrons, which participate in IRSL, can be approximated by the difference between the IRPL from before and after IRSL measurement (ΔIRPL; Eq.3.1). They also found that $IRPL_{955}$ centres are more easily bleachable and have a relatively larger contribution to IRSL compared to the $IRPL_{880}$ centres, likely due to $IRPL_{955}$ sites being located at more proximal distance to recombination sites (Jain et al., 2020). For $IRPL_{955}$, there can be up to 50% of the trapped charge participating where as for $IRPL_{880}$, only 20-30% participates in IRSL (Jain et al., 2020). Through measuring both IRSL and IRPL, we are able to investigate whether ΔIRPL may be used as a surrogate for IRSL. Figure 3.4 presents the correlations between IRSL and the change in $IRPL_{955}$ due to IRSL measurement ($\Delta IRPL_{955}$), after the rock slice had received a 5 kGy regeneration dose to saturate the traps. We see here that, whilst there is a large scatter indicating the IRPL loss due to IRSL measurement varies grain-to-grain (and pixel-to-pixel) for the three samples, there is positive correlation between the two data sets. With regards to a bleached rock, the ΔIRPL profile will show minimal change in IRPL where the IRSL is zeroed, with increasing ΔIRPL with depth from the surface. The ΔIRPL measurement is thus considered an appropriate surrogate for IRSL, and could be used for establishing a proxy IRSL-depth. This possibility is especially significant when it is difficult to collect IRSL data (i.e. where instrumentation may not be sensitive enough for IRSL detection, e.g. in portable instruments). In this article we investigate the potential of using ΔIRPL for reconstructing luminescence-depth profiles, and discuss the results with respect to IRSL profiles.

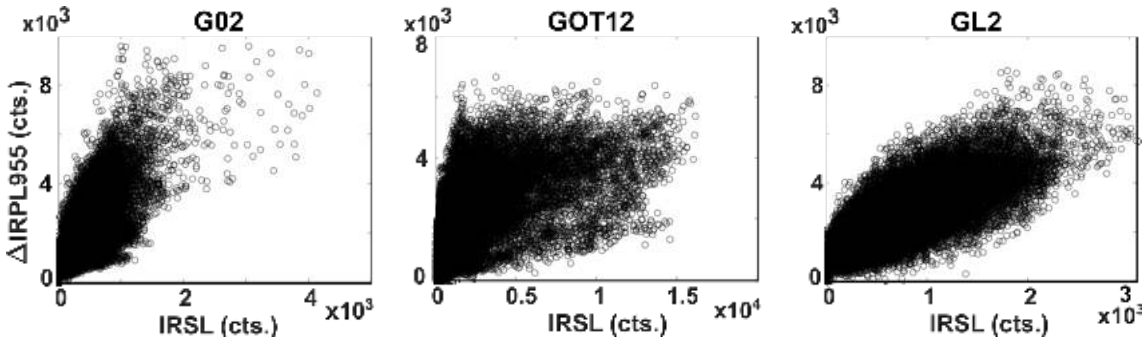

Figure 3.4: Pixel-wise correlation between $\Delta IRPL_{955}$ and IRSL for G02 (left), GOT12 (middle) and GL2 (right).

3.4 Results

In the following sections we present and discuss the results of imaging the natural and regenerated IRPL and IRSL in detail. The luminescence images and luminescence-depth profiles are grouped by sample for easier comparisons between their respective profiles from the various normalisation methods. Figures 3.5 to 3.7 present the data from G02, GOT 12 and GL2 respectively. In each figure, the natural IRPL and IRSL data (both images and profiles) are presented in panels a and b, respectively. Panels c and d present the images and profiles after normalisation with the regeneration dose for IRPL and IRSL, respectfully. Panels e show the ΔIRPL profiles and ratio maps, and panels f show the results of normalised IRSL using the first and later frames (F1/Fx) from the natural decay curve. The results of taking the 955/880 nm ratio are presented in Figure 3.8. All raw IRPL images and ratio maps are presented in false

colour, with legend bars representing the signal intensity or ratio values.

3.4.1 Natural IRPL and IRSL images and profiles

In order to fully assess the necessity of a normalisation step for reconstructing luminescence-depth profiles, it is important to view the natural (L_n) data without any normalisation method.

3.4.1.1 IRPL

The natural $IRPL_{880}$ and $IRPL_{955}$ data are shown in panels a, for G02 (Figure 3.5), GOT12 (Figure 3.6) and GL2 (Figure 3.7). From first observations, it is clear that all three samples have been exposed to sunlight for durations long enough to deplete both $IRPL_{880}$ and $IRPL_{955}$ within the first few mm of the surface in each slab (dark blue regions on the left side of the inset images). However, the translation of these images into luminescencedepth profiles shows large fluctuations due to spatial variation in the sensitivity, necessitating an appropriate normalisation method to account for these variations. There is significant ambiguity in SD50% estimation for all the natural profiles, and therefore estimated SD50% values are not given. The natural IRPL profiles from G02 (Figure 3.5a) show that IRPL has been reduced to residual levels below a depth of ~2 mm. Beyond this the intensity increases until the profile starts to fluctuate. This fluctuation is related to the 2D spatial variations in IRPL sensitivity or possible variations in the emitting volume due to changes in mineral thickness below the surface with respect to the mean attenuation depth of near-IR light (3D sensitivity). The natural IRPL profiles for GOT12 (Figure 3.6a) show similar behaviour, with a clear bleached region at the surface, followed by a peak and a further irregular increase to the saturation region. The irregular peaks in the saturation region of the profile (>10 mm from the surface) correspond to the positions of the IRPL-emitting minerals. A decrease in IRPL intensity is seen between 20 and 25 mm depth, where IRPL sensitive minerals are lacking in abundance (see inset IRPL images). In comparison, GL2 (Figure 3.7a) appears to have a much shorter exposure duration compared to GL2 and GOT12, reflected as a small surface region void of luminescence in the raw images. The luminescence intensity as a function of depth follows the almost foliated texture in the rock visible in the raw images, and is clearly the factor preventing SD50% depth estimation. It is also worth noting the differences in intensity between the $IRPL_{880}$ and $IRPL_{955}$, seen in all three samples. Whilst the fluctuations in the $IRPL_{880}$ profile mimic those in the $IRPL_{955}$ profile, we see that the $IRPL_{955}$ emission has a slightly greater intensity across the whole profile, with a slightly larger residual at the surface and a greater divergence in intensity within the saturated region. This is likely due to the larger detection window in the filter set-up for $IRPL_{955}$ detection (bandwidth of 950 ± 50 nm).

3.4.1.2 IRSL

The natural IRSL image for G02 (Figure 3.5b insert) highlights the preferential difference in bleaching between the IRSL and IRPL, with a remarkably deeper bleaching depth compared to that of the IRPL. The individual IRSL-emitting minerals are relatively harder to distinguish in the IRSL image. This is due to the IRSL intensity being over an order of magnitude smaller than IRPL preventing clear observation of mineral boundaries but demonstrating the superiority of the latter emission for imaging. The second insert in Figure 3.5b presents the IRSL decay curve, constructed from summing all pixels in each frame of the IRSL measurement. At the end of the measurement, the IRSL reaches a residual level.

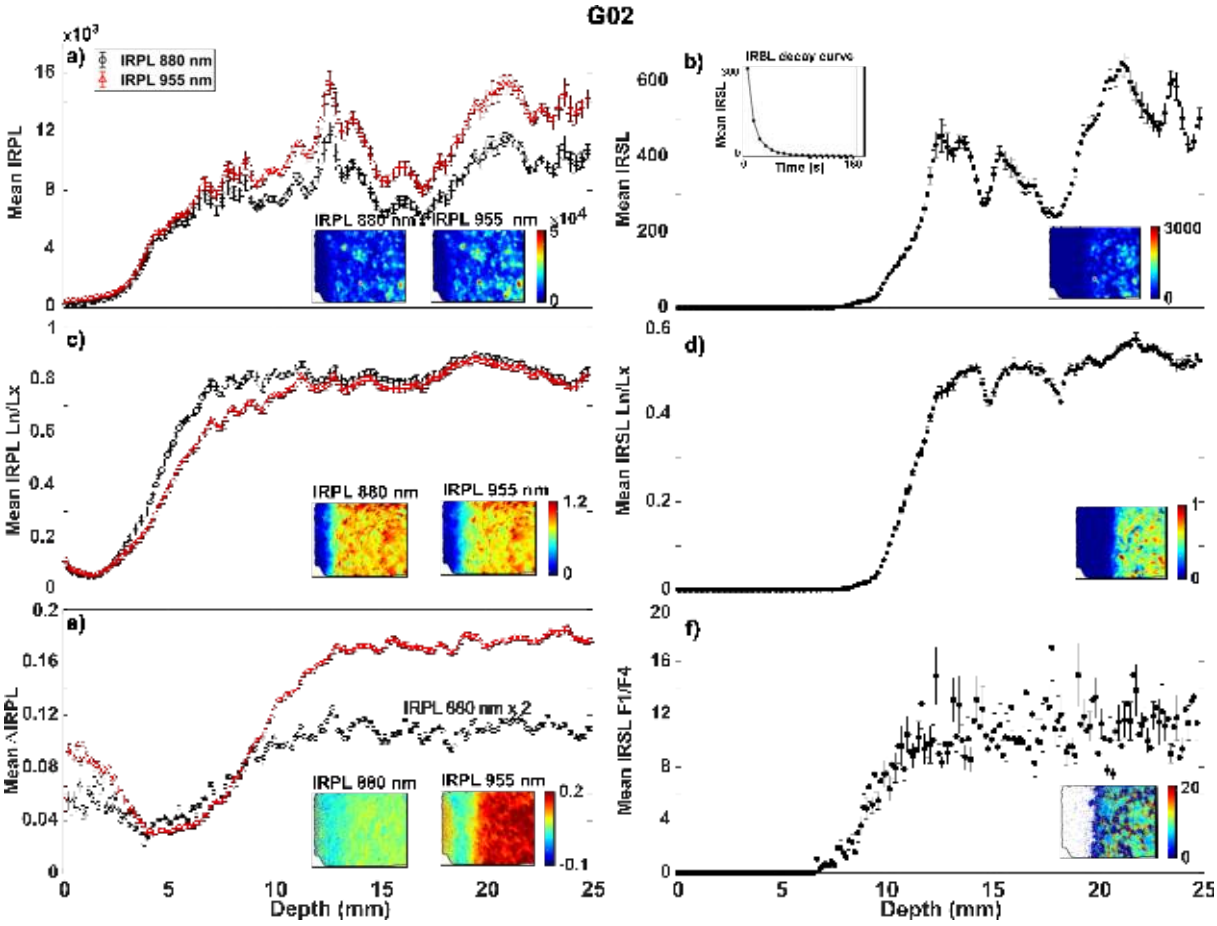

Figure 3.5: IRPL (left panels)and IRSL (right panels) images and profiles from G02. a) Natural IRPL profiles with insert false-colour IRPL images with colour bars representing intensity. b) Natural IRSL profile, with inset intensity map and decay curve. c) IRPL profiles after normalisation with the regeneration dose (L_n/L_x), with ratio maps. d) IRSL profile after normalisation with a regeneration dose. e) $\Delta IRPL$ profiles. Note that the $\Delta IRPL_{880}$ data has been scaled by a factor of two for easier comparison. f) IRSL profile from normalising first frame in IRSL decay curve by frame 4 (F1/F4).

The natural G02 IRSL-depth profile (Figure 3.5b) shows how the IRSL has been zeroed from the surface down to ~7 mm in depth, where intensity starts to increase up to saturation. Contrary to the IRPL profiles (Figure 3.5a) there is no residual IRSL seen at the surface of the rock (zero depth) confirming the higher bleachability of the IRSL. The natural IRSL image from GOT12 in Figure 3.6b shows how the IRSL has been bleached over almost half of the depth of the slab. As outlined in the discussions of the GL2 natural IRPL profiles above, the 2D and 3D spatial variations in IRSL-emitting minerals are limiting the estimation of SD50% depth, with very few luminescing minerals visible. In contrast to the uncertainty in bleaching depth in the IRPL profile from GL2, the IRSL image and profile (Figure 3.7b) show a very clear ~4 mm bleached region from the surface of the slab. However, the variation in IRSL intensity within the profile still hinders a clear transition zone being distinguished between the bleached and saturated regions.

3.4.2 Regeneration dose normalised (L_n/L_x) IRPL and IRSL depth profiles

The natural IRPL and IRSL images were normalised by measuring the IRPL and IRSL after a 5 kGy regeneration dose, and the resulting profiles and ratio maps serve as a benchmark for the proceeding normalisation methods discussed in this article.

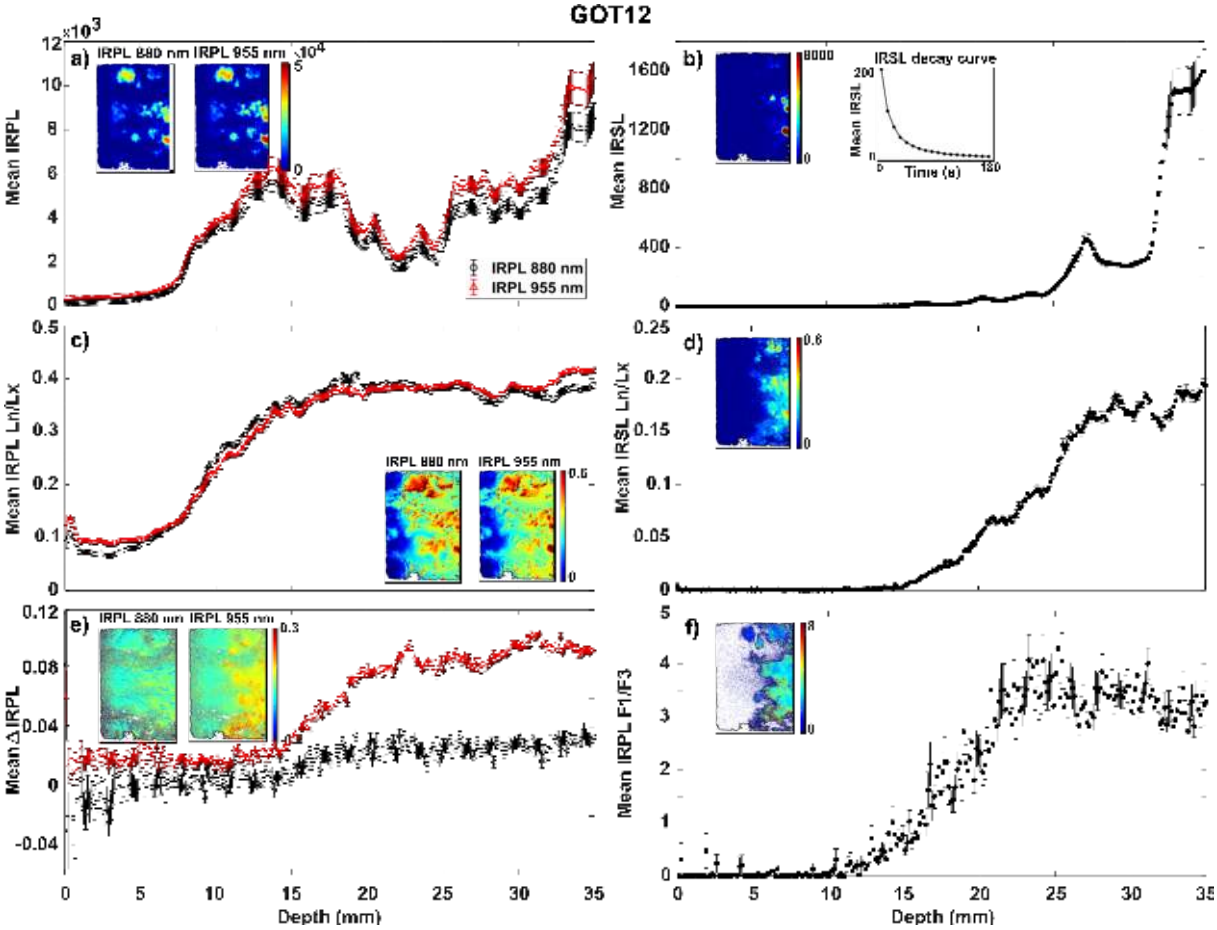

Figure 3.6: IRPL and IRSL Results from GOT12. a) Natural IRPL profiles with insert false-colour IRPL images. b) Natural IRSL profile with inset intensity map and decay curve. c) Regeneration-dose normalised IRPL profiles. d) Regeneration-dose normalised IRSL profile. e) ΔIRPL profiles. No re-scaling of the $IRPL_{880}$ data was necessary with this data set. f) IRSL profile from normalising first frame in IRSL decay curve by frame 3 (F1/F3).

3.4.2.1 IRPL

Figure 3.5c shows the IRPL L_n/L_x profiles for G02 with inset ratio maps. Normalisation has resulted in profiles that now show the familiar smooth sigmoidal form expected in luminescence-depth profiles. What is instantly apparent is the divergence in slope of the transition zones (region between bleached and saturated part of the profile) between the two IRPL profiles. The $IRPL_{955}$ L_n/L_x profile has a shallower slope within the transition zone, and an SD50% of 5 mm (Table 3.2), relative to the $IRPL_{880}$ profile that has a steeper slope, and a shallower depth of 4.5 mm. This divergence in slope likely reflects an apparent difference in μ between the two IRPL profiles (relatively larger μ for $IRPL_{880}$, than $IRPL_{955}$). This observation is consistent with

our conjecture in section 3.3 regarding the different effective bleaching wavelengths for the two IRPL signals based on their excitation spectra (Kumar et al., 2020a). The two GOT12 IRPL L_n/L_x profiles show very similar slopes in the transition zones and the $IRPL_{880}$ and $IRPL_{955}$ have very similar SD50% depths at 8.2 mm and 8.9 mm respectively, with a difference in L_n/L_x seen within a few mm at the surface.

Figure 3.6c presents the L_n/L_x profiles and inset ratio maps for GL2 where it is now clear to which depth the IRPL has been bleached. Similar to what is seen in the L_n/L_x profiles from G02 (Figure 3.5c), there is a difference in the slope of the transition zones between the two IRPL profiles, with the $IRPL_{955}$ profile showing a slightly deeper bleaching depth (2.5 mm) compared to the $IRPL_{880}$ profile (SD50% at 2.2 mm). Interestingly, all L_n/L_x profiles show a slight rise in the surface 12 mm of the profiles; this effect is especially prominent in samples G02 and GOT12. It is apparent from looking at the L_x images that these surface regions experience a decrease in surface dose sensitivity. This observation will be addressed further in the discussion section. It is also observed that the L_n/L_x ratio within the saturated region of the profile does not reach unity (~0.8 for G02 and GL2; ~0.4 for GOT12). From previous experiments, this is due to unstable or shallow charge not being removed after receiving a regenerative dose (Kumar et al., 2021b). Introducing a pre-heat stage in the measurement sequence will remove such charge and push the ratio towards unity, although the shape of the profile should remain the same.

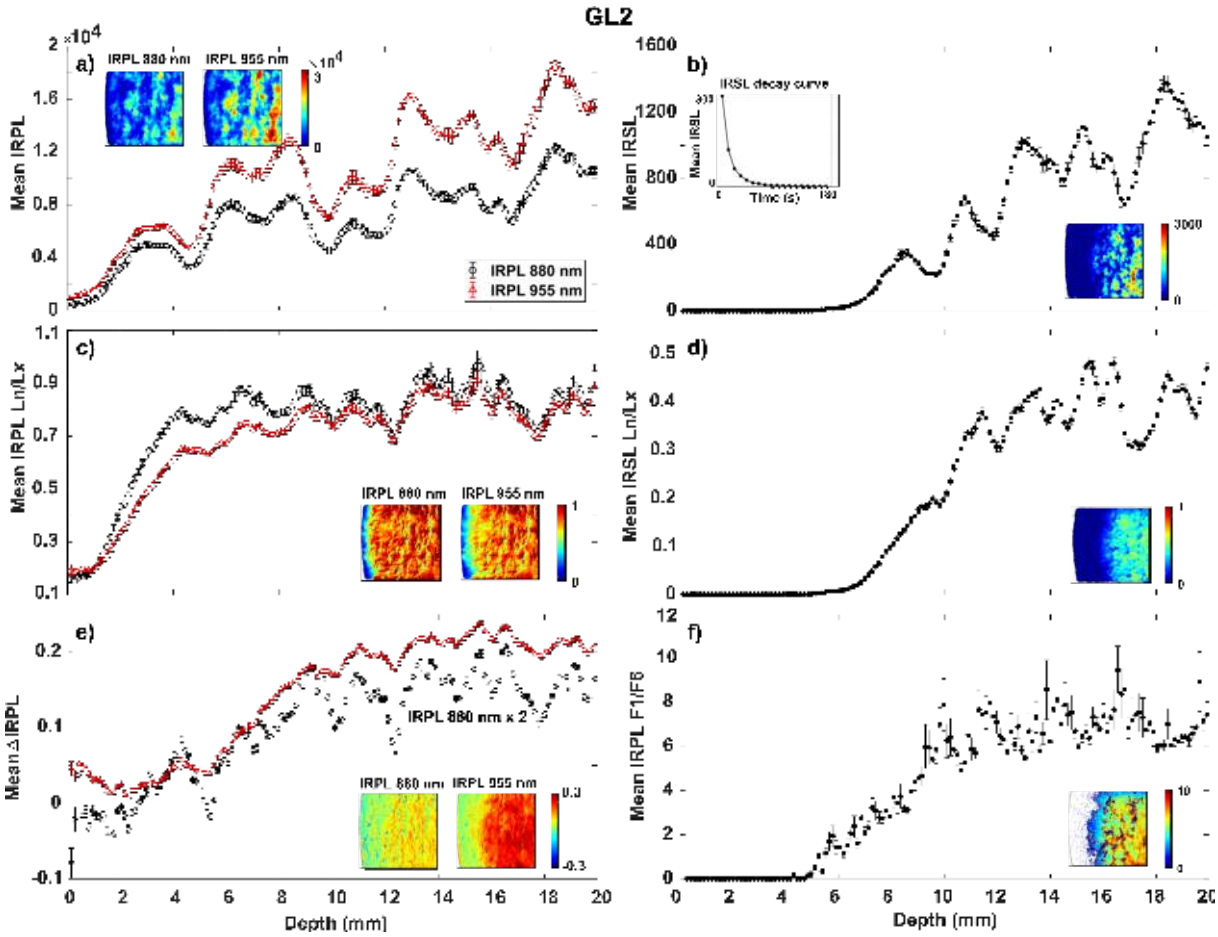

Figure 3.7: GL2 profiles and inset false-colour maps. a) Natural IRPL profiles with insert false-colour IRPL images. b) Natural IRSL profile, with inset intensity map and decay curve. c) IRPL L_n/L_x profiles and ratio maps. d) IRSL L_n/L_x profile and map. e) ΔIRPL profiles. Note that the data from $IRPL_{880}$ has been scaled by a factor of two for easier comparison between the two emissions. f) IRSL profile from normalising first frame in the IRSL decay curve by frame 6.

3.4.2.2 IRSL

The IRSL data for G02 (Figure 3.5d) presents similar information to that seen in the natural data (Figure 3.5b), with negligible surface values. The transition zone and saturated region of the profile is smoother, and we estimate an SD50% depth of 11.1 mm (Table 3.2). Normalisation of the natural GOT12 IRSL with a regeneration dose has now produced a sigmoidal profile with a shallow slope in the transition zone up to an identifiable saturation zone (Figure 3.6d). This normalisation has made identification of the bleaching depth significantly easier and is estimated at 23.1 mm. The result of normalising the natural IRSL from GL2 (Figure 3.7d) with a regeneration dose is also highly beneficial, as we can now see that the SD50% depth actually lies at ~9.6 mm information not obtainable from the L_n data alone.

	IRPL SD50% (mm)						Minima position (mm)	IRSL SD50% (mm)		
	$IRPL_{880}$	$IRPL_{955}$	L_n/L_x880	L_n/L_x955	$\Delta IRPL_{880}$	$\Delta IRPL_{955}$	955/880 nm	IRSL	IRSL L_n/L_x	IRSL F1/Fx
G02	-	-	4.5	5.0	7	8.7	4.4	-	11.1	9.6
GOT12	-	-	8.2	8.9	-	16	9.4	-	23.1	16.6
GL2	-	-	2.2	2.5	6.5	7	3.1	-	9.6	8.1

Table 3.2: Estimates of the SD50% depths for IRPL and IRSL profiles, as well as the depth corresponding to the position (depth) of the minima of the 955/880 nm ratio profiles. Blank cells are where the SD50% depth could not be estimated. Uncertainties on the SD50% and minima depths were not included as the values are estimates. Uncertainties along the x (depth) axis are in the order of a few pixels (1 pixel = ~0.14 mm), and the uncertainty in the luminescence intensity (y axis) is relatively small, as shown by the standard errors around the data points in the profiles.

3.4.3 ΔIRPL profiles

From calculating the change in IRPL intensity from before and after IRSL measurement, we have been able to reconstruct profiles which are generally similar in shape and bleaching depth to the IRSL L_n/L_x profiles. This confirms that at least to the first order ΔIRPL measures the percentage of charge population which participates in IRSL. Interestingly, the large scatter observed in the plot of ΔIRPL vs. IRSL (Figure 3.4) is not reflected in the ΔIRPL and IRSL luminescence-depth profiles, which offer similar bleaching depth estimations with respect to each other, especially for the $\Delta IRPL_{955}$. Our data show how the magnitude of ΔIRPL varies sample to sample, but do support the findings of Jain et al. (2020), where the greatest influence of IRSL measurement is seen in the $IRPL_{955}$ emission.

Figure 3.5e shows the ΔIRPL profiles for G02, where the $\Delta IRPL_{880}$ data has been scaled by a factor of 2, to more easily compare the two IRPL data sets. The $\Delta IRPL_{955}$ profile shows a clear valley-shaped structure decreasing from the surface, and rising again up to the saturated region of the slab; this structure is less prominent in the $\Delta IRPL_{880}$ profile which is flatter near the surface. In the saturated region of the slab the $IRPL_{955}$ was depleted up to ~18% due to IRSL and only ~5% in 880 nm. The valley shape seen within the surface region in the $\Delta IRPL_{955}$ profile of sample G02 (Figure 3.5e) suggests that apparently there occurs a greater depletion of the residual signal near the surface during IRSL measurement. This could possibly be due to some charge transfer effect during exposure in nature or, this could be an artefact of change in the sensitivity of the instrument between the two IRPL measurements; this needs to be investigated in future work. Interestingly, in the transition zone of the profiles there are some pixels which showed an increase in IRPL (955 nm and 880 nm) intensity after the IRSL measurement, resulting in negative values in the ΔIRPL; the relative increase was greater for the 880 nm emission compared to the 955 emission. Ignoring this rise at the surface, the ΔIRPL profiles for G02 show SD50% depths of 7 mm ($\Delta IRPL_{880}$) and 8.7 mm ($\Delta IRPL_{955}$), which lie in-

between the SD50% depths from the natural and L_n/L_x IRPL and IRSL profiles, and is similar to the profile obtained from the IRSL F1/F4 profile (see next section). The ΔIRPL profiles for GOT12 are shown in Figure 3.6e. Here, we do not see the valley-shaped structure in the surface region of the slab. Both IRPL 955 nm and 880 nm experienced slight increase in intensity within the naturally bleached region of the slab, and only a small decrease (~8% of $IRPL_{955}$) in intensity within the saturated region of the slab as a result of IRSL measurement. The GOT12 SD50% depth cannot be estimated for the $\Delta IRPL_{880}$ as the profile is relatively flat and very noisy, but is estimated at 16 mm for $\Delta IRPL_{955}$. The data from GL2 is shown in Figure 3.7e, where the $\Delta IRPL_{880}$ data has been rescaled by a factor of two. Similar to G02 (Figure 3.5e), GL2 shows a significant difference in the response of $IRPL_{880}$ and $IRPL_{955}$ to IRSL measurement, with the $IRPL_{955}$ decreasing ~20% within the saturated region of the slab, with significantly less change in $IRPL_{880}$ intensity. Again, we see how IRPL intensity has increased in the previously bleached surface region of the slab, with a greater increase in the $IRPL_{880}$ as shown as the negative values in the inset ratio maps. The SD50% depths are estimated at 6.5 mm for $\Delta IRPL_{880}$, and 7 mm for $\Delta IRPL_{955}$. To the first order approximation there is a good agreement between the SD50% depths of the ΔIRPL (especially the $\Delta IRPL_{955}$ profile) and IRSL L_n/L_x and F1/Fx profiles (see next section and Table 3.2). The fact that they do not match completely requires further understanding of electron loss mechanisms during IR stimulation.

3.4.4 IRSL signal to background ratio (F1/Fx) profiles

Here we present the IRSL profiles after dividing the first frame (F1) measured in the IRSL time-series by a later frame (Fx), utilising the varying sensitivity of the IRSL components in our rock samples. The frames for normalisation were chosen arbitrarily, selecting the resultant profiles considered as the best representations of the normalisation method, with discernible transition zones for SD50% depth estimation.

Plotted in Figure 3.5f is the G02 ratio map and corresponding profile from dividing frame 1 by frame 4 (F1/F4). Note that within the inset ratio maps, some regions are void of pixel values and appear as white due to infinite values being produced during calculation, where there was no depletion in IRPL due to IR stimulation; such values were disregarded when plotting. The saturated region of the profile hosts significantly more scatter than seen in the IRSL L_n/L_x profile. This is due to spatial variation in the proportion of the easy and difficult-to-bleach IRSL components, dependent on the pixel-scale mineralogy and the density of the recombination centres. The G02 F1/F4 profile presents an expected sigmoidal profile clear transition zone, with an SD50% depth of 9.6 mm. For GOT12, the first frame was divided by frame 3 (F1/F3; Figure 3.6f) and has more scatter than that seen from the G02 data, indicating an apparently greater variation in IRSL decay rates and sensitivity across the sample. The GOT12 SD50% depth is shallower than that estimated from the IRSL L_n/L_x profile (Figure 3.6d), and at 16.6 mm, corresponds more closely to the $\Delta IRPL_{955}$ profile (See Table 3.2 and Figure 3.6e). The IRSL F1/F6 data from GL2 is shown in Figure 3.7f. This profile has a similar slope to the IRSL L_n/L_x profile in Figure 3.7d, but again, is slightly shallower in bleaching depth (8.1 mm), and more similarly resembles the $\Delta IRPL_{955}$ profile.

All F1/Fx profiles present shallower bleaching depths compared to those estimated from the IRSL L_n/L_x profiles. This is expected as the later parts of the IRSL decay are arguably representative of a proportion of the trap population which has lower bleachability. This is contrary to the L_n/L_x ratio which uses the first frames (most bleachable trap populations) from the L_n and L_x measurements. Therefore, as we are viewing slightly different populations of the IR trap with different bleachabilities, there is a shift in the apparent bleaching depth.

3.4.5 IRPL 955/880 nm ratio profiles

In this section, we discuss the suitability of only measuring the natural IRPL at 880 nm and 955 nm, and taking the ratio between them. As previously discussed for the IRPL L_n/L_x profiles, we are able to distinguish between the $IRPL_{880}$ and $IRPL_{955}$ profiles based on the steepness of slope of the transition zone, and the resulting SD50%, which here is considered a product of different effective μ for each IRPL emission (see section 3.3). In order to better understand our experimental results, we decided first to investigate the expected outcome of taking the IRPL 955/880 nm ratio for our data through modelling. Here, we have discounted any effects of data scatter, surface residual values or variation in σ (combined as $\sigma\varphi_0$ in the model) which may also be influencing the shape and depth of the experimental profiles (see section 3.3). First, the IRPL L_n/L_x data sets for each sample were fitted with Eq.3.2 to estimate the independent values of μ. Then, with the same arbitrary values set for $\sigma\varphi_0$, luminescence-depth profiles were modelled using these obtained μ estimates and the ratio between the profiles was taken. Figure 3.8a shows the resulting modelled IRPL profiles (solid lines) and ratio profile from dividing IRPL 955/880 nm (dashed lines). Note that through setting $\sigma\varphi_0$ the same for all modelled profiles, the apparent depths of the modelled profiles and thus the resulting ratio curve minima are not corresponding to the depths seen in the experimental data. Sample GL2 has the greatest difference in modelled μ, resulting in the deepest and narrowest valley in the ratio profile. The obtained μ parameters for the G02 IRPL profiles were 0.63 mm^{-1} for the $IRPL_{880}$ profile, and 0.42 $mm^{-1}$for $IRPL_{955}$, and the resulting modelled ratio profile is similar to that for GL2 but with a slightly wider valley. In comparison, the modelled results from GOT12 resulted in the widest valley in the ratio profile, likely due to the relatively lower μ values compared to those from G02 and GL2, and more similar values of μ between the GOT12 $IRPL_{880}$ and $IRPL_{955}$ profiles.

Our measured data is presented in Figure 3.8b, where the blue profiles are the IRPL 955/880 nm ratio curves from the measured natural IRPL images (left axis), and the faded grey profiles show the $IRPL_{880}$ L_n/L_x profiles for reference (right axis). The profile from G02 (top panel in Figure 3.8b) shows a wide valley and smooth transition to the saturation zone, and a ratio curve minima at 4.4 mm. The data from GOT12 (middle panel) presents a very wide valley with an almost flat structure; this is similar to what we observed in the modelled ratio profile in Figure 3.8a and is likely a result of similar bleaching depths and profile shapes of the $IRPL_{880}$ and $IRPL_{955}$ profiles (see Figure 3.6c). The similarity in slope and bleaching depths between the two IRPL profiles could be a result of the specific characteristics of the two IRPL signals in relation to the samples chemistry. It is feasible that in GOT12, one of the IRPL emissions is more dominant over the other, and due to the close proximity of the IRPL detection windows, it contaminates the other measurement leading to similar IRPL profiles (Kumar et al., 2018; Riedesel et al., 2020). However, further investigation into this should be done in the future. Regardless of the relatively flat valley shape in the ratio profile, rescaling of the y-axis to focus on the transition and saturated regions of the profile allowed us to establish an approximate depth of the ratio curve minima for the GOT12 profile at 9.4 mm. The ratio profile for GL2 (bottom panel) shows a clearer, narrower valley shape before increasing to a clear saturation region, with a ratio curve minima at 3.1 mm.

In all experimental IRPL ratio profiles (Figure 3.8b), the rise towards the surface is much steeper and overshoots the value of unity, contrary to the expected value as seen in the modelled profiles. In the model there were factors that were not considered and it was assumed that both 880 and 955 centres were following first order kinetics and had the same intensities at the surface. However, in actual measurements the sensitivity of 880 and 955 measurements are different; therefore the ratio at the surface deviates from unity. There is arguably good

correspondence between the depths of the ratio curve minima and the SD50% depths from the IRPL L_n/L_x profiles from either $IRPL_{880}$ or $IRPL_{955}$ (see Table 3.2). However, as shown in Figure 3.2c, although there is a correlation between the ratio curve minima depths and SD50% depths, they were not equal to each other. The difference between the modelled and experimental data is perhaps because our modelled data is, again, based on simple first order kinetics and over simplified, whereas luminescence in feldspar has been shown to follow non first-order kinetics (Jain et al., 2015).

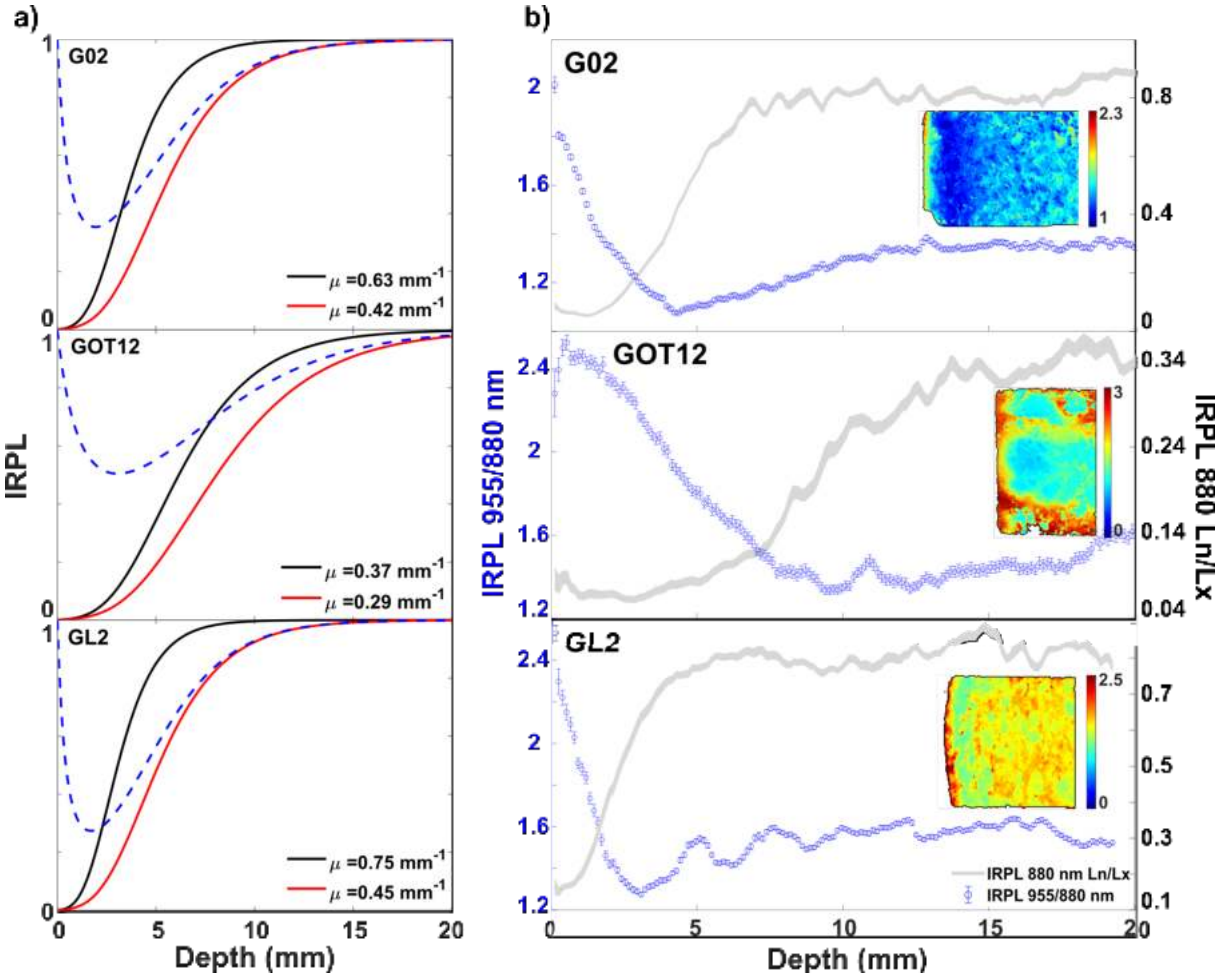

Figure 3.8: a) Modelled $IRPL_{880}$ (black) and $IRPL_{955}$ (red) profiles and resulting ratio profiles (dashed lines) after fitting L_n/L_x data with Eq.3.2, to obtain estimates of the values of μ for each sample. b) IRPL 955/880 profiles from images (blue profiles; corresponds to left axis), with $IRPL_{880}$ L_n/L_x profiles in grey for comparison (corresponds to right axis).

3.5 Discussion

Due to heterogeneity in the distribution and sensitivity of luminescence-emitting minerals, emission depth and rock texture, a normalisation step for the natural data is clearly necessary when reconstructing luminescence-depth profiles for RSD. Through spatially resolving the natural IRSL and IRPL at 880 nm and 955 nm and reconstructing luminescence-depth profiles, one is able to see the relation of the shapes of the luminescence-depth profiles to this heterogeneity (e.g. foliation in GL2 reflected in the shape of the natural luminescence-depth profile in Figure 3.7a); this information is usually lost when measuring OSL from grains or rock slices on an OSL reader. We authenticate how the different bleaching and stimulation properties of IRPL and IRSL can

be utilised, and how the natural signals alone can be used for normalising luminescence-depth profiles, in place of regeneration doses.

Estimating the bleaching depths from all the natural (L_n) profiles was difficult, with significant ambiguity in determining where the saturation depth actually begun, and in defining a representative mean saturation value as the luminescence intensities significantly fluctuated with depth. The distribution of luminescing minerals was clearly the culprit limiting the profile readability, and it is obvious that such factors will be amplified when trying to date samples with significantly shorter exposures (very small bleached region at the surface), or stronger rock textures (e.g. strong foliations). As expected and demonstrated in previous studies, the profiles obtained using the regeneration dose as normalisation (L_n/L_x) allow clear observation of the bleaching depths.

As previously mentioned in section 3.4.2, we see a slight increase in L_n/L_x ratio profile within the first 12 mm from the surface for each sample. From investigating the L_x data from each of the samples we observed a change in sensitivity at the surfaces of the rocks after the samples received regenerative doses. Figure 3.9 presents the $IRPL_{880}$ profiles (as an example) from the L_x images from G02 (a), GOT12 (b) and GL2 (c), focusing on the surface 6 mm, with the L_n profiles for reference (black data points). We see that there is an apparent decrease in IRPL intensity towards the surface, especially for G02 and GOT12, where after receiving a regenerative dose, luminescence emitting minerals are present (i.e. this intensity decrease is not a product of irregular mineral distribution; see supplementary information for L_x images of $IRPL_{880}$ and IRSL). Such an increase in L_n/L_x ratio towards the surface can also be observed in previous data reported by Sellwood et al. (2019). Whilst the reason for this is currently unknown, it is hypothesised that de-sensitisation may have arisen due to (sub)micron scale weathering not visible to the naked eye, or there may be some sensitivity change due to prolonged UV exposure within the surface region of the rock, influencing the distribution of trapping sites. However, it is currently unknown as to whether this phenomenon occurs in nature and what the implications are with regards to RSBD. If in nature, the previously exposed rock surface undergoes such sensitivity changes then dose estimates from surface slices will likely present underestimates of the real dose. These aspects require future attention.

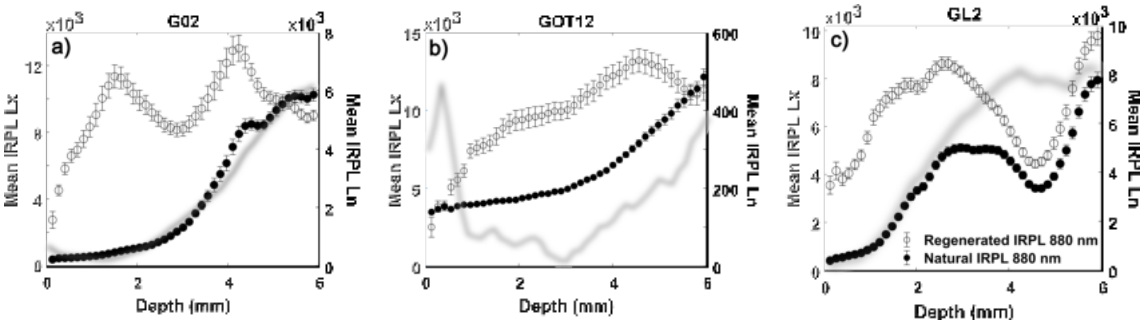

Figure 3.9: Surface 6 mm of $IRPL_{880}$ L_n (solid points, right axis) and L_x (hollow points, left axis) profiles for G02 (a), GOT12 (b) and GL2 (c). The faded grey profiles show the $IRPL_{880}$ L_n/L_x profile, in arbitrary units (without a y-axis), to indicate the effect of sensitivity change on L_n/L_x profile shape.

Our observations of IRPL and IRSL met our expectations concerning the different bleaching responses of the three measured emissions (greater bleachability of IRSL and $IRPL_{955}$ relative to $IRPL_{880}$). Following the standard double exponential function (Eq.3.2), we affirm that different bleaching depths and transition-zone slopes result predominantly from variable effective μ between the two IRPL emissions. It is again at the surface regions of the slabs where we see varying behaviour, resulting in the steep valley slope at the start of the IRPL 955/ 880 nm ratio profiles. This is a product of the different residual levels and different bleachabilities between the

two IRPL centres. But to fully understand the shapes and development of ratio profiles, further investigations in to the response of IRPL to different wavelengths and how these wavelengths penetrate through heterogeneous materials is required. Regardless of these new questions which have emerged, we were able to adequately demonstrate how using these intrinsic bleaching properties of IRPL at each trapping centre provided an adequate alternative normalisation method, with ratio curve minima providing acceptable estimates of IRPL bleaching depths and clearly show that all three samples had been exposed to sunlight. Requiring only two images, the IRPL 955/880 nm ratio can rapidly assist with sample screening both in the field and laboratory, where IRSL cannot be measured, or where one wishes to preserve IRSL for later measurement.

In this study, the ΔIRPL is significantly lower than the values reported in Jain et al. (2020) presumably because our samples have an IRSL fading component. IRSL fading has been found to be more problematic in rocks than in sediments (e.g. Vafiadou et al., 2007; Rades et al., 2018; Souza et al., 2019). The natural ΔIRPL is expected to be much smaller for a sample with high fading rate compared to a sample with lower fading rate, because in nature the fading component (i.e. $IRSL_{50}$) has already been removed to a greater extent in the former case compared to the latter. Similar to our results, Jain et al. (2020) also found a large spread in ΔIRPL from sample to sample, presumably because of the sample-to-sample variation in the density of recombination centres in feldspar. Through the ΔIRPL method we achieve profiles similar in shape and bleaching depth to the IRSL L_n/L_x or F1/Fx profiles for all three samples. It was unexpected to observe an increase in IRPL in all samples as a result from IRSL measurement, which especially influenced the transition zones in the $IRPL_{880}$. This increase is likely resulting from re-trapping of charge participating in IRSL, which then participates in IRPL and is particularly noticeable in the regions of the slab where IRPL was previously negligible. The extent to which this charge re-trapping happens holds influence over the shape of the ΔIRPL profiles is not explored here. It is apparent that we need a more thorough investigation of de/re-trapping behaviour during IR-stimulation to fully understand how it influences the ΔIRPL calculation and resulting luminescence-depth profiles. However, the ΔIRPL method underlines how it is possible to estimate the IRSL SD50% depth from the IRPL data alone; a field instrument does not need to be tuned for optimal IRSL imaging, but instead IRPL (favourably $IRPL_{955}$) can be measured before and after IRSL has been stimulated for an in situ estimate of this depth.

Where the full IRSL decay curve can be measured, we demonstrate that using a later frame from the decay curve for normalisation of the natural IRSL also results in a profile where one can clearly see the bleached region, transition zone, and the saturated region. The latter accounts for different minerals or sensitivity across the slab, but still suffers from minor fluctuations due to varying IRSL decay rates from different regions. Consideration should be taken when choosing a normalisation frame, as the shape of the profile can vary slightly, but we argue that this choice is not critical when using the method for obtaining estimates of profiles or constructing relative exposure chronologies.

Our work demonstrates that different signals and normalisation approaches may be used for reconstructing luminescence-depth profiles, depending on whether the assessment is made in the field or in the laboratory. For example, if a sample has only a short exposure to sunlight, IRSL measurement would be the most favourable signal due to its higher bleachability. This also however, means that measurements will ideally be made in the lab, as IRSL imaging requires appropriate stimulation powers and a sensitive detector (EMCCD as opposed to a conventional scientific camera inadequate for low light levels). Such a measurement could be made using a normalisation with a later frame (F1/Fx) or with a response to a regeneration dose. However, if this is not possible (or you are in the field), then the ΔIRPL measurement could be made, acting as a surrogate for the IRSL measurement. On the other hand, if the sample has received sufficient daylight exposure, taking the IRPL 955/880 nm ratio would be arguably favourable

when sampling in the field, as this does not destroy the IRSL signal. The higher sensitivity of the IRPL allows easy measurement and can be taken from small chunks of samples of interest. Samples that show a profile can then be selected, and the measurements can be repeated later in the laboratory alongside IRSL.

3.6 Conclusions

The development of the luminescence rock surface dating method has been limited by aspects such as the need for extensive sample collection and preparation stages and the requirement of access to irradiation facilities for normalisation of the natural OSL signals. We present novel methods for spatially resolving luminescence-depth profiles using IRSL and IRPL (880 nm and 955 nm) from large (cm-scale) rock samples with an EMCCD-based imaging system. We avoid time-consuming sample preparation stages by only requiring to cut samples perpendicular to the exposed surface. Spatially resolving the IRSL and IRPL provides high-resolution luminescence-depth profiles, whose structure is a function of bleaching depth as well as the spatial variation in the sensitivity and the occurrence of feldspar mineral grains. We discuss theoretically and demonstrate experimentally different normalisation methods based on the bleaching characteristics of different IR stimulated signals in feldspar. Through taking the ratio of the two IRPL emissions (IRPL 955/880 nm), we were able to estimate the bleaching depth of IRPL whilst avoiding the need for a regeneration dose altogether and only requiring two images of the natural signal. We also show that calculating the change in IRPL intensity from before and after IRSL (ΔIRPL) allows us to both view the percentage of trap charge population which participates in IRSL as well as reconstruct a ΔIRPL - depth profile that approximates the IRSL profile. The ΔIRPL method is particularly useful when IRSL cannot be measured directly (e.g. when we have unsuitable detectors or insufficient stimulation light power). Finally, we demonstrate that normalisation of the natural IRSL can be done via taking a frame from a later part of the IRSL decay curve. The normalisation methods proposed here for rapid, high-resolution IRPL and IRSL measurements avoid the need for gamma and X-ray irradiation sources for estimating the bleaching depths. These methods render the rock surface dating technique suitable for *in situ* field investigations and make high-resolution profile imaging feasible in laboratories lacking ionising radiation facilities for large samples (e.g. a gamma source). We expect that the methods proposed here will greatly assist with a) sample screening in the laboratory or in the field based on the bleaching status of a rock (e.g. for rock surface burial dating), and b) establishing relative exposure chronologies in the field.

3.7 Acknowledgements

The authors extend thanks to our colleagues at the Risø High Dose Rate Reference Laboratory: Mark Bailey, Arne Miller and Torben Esmann Mølholt for their assistance with sample irradiation, and to Henrik Olesen who played a large role in sample preparations. We also thank Benny Guralnik, Anders Anker Bjork and Kurt Kjær who were part of the initial sample collection. Finally we thank Dr. Gribenski and an anonymous reviewer for their constructive feedback on the manuscript.

3.8 Appendix A. Supplementary data

Published supplementary data to this article can be found online at:
https://doi.org/10.1016/j.quageo.2021.101227.

CHAPTER 4

Investigations on dose recovery in rocks using spatially-resolved IRPL and IRSL

Sellwood, E.L.[a], Kook, M.[a], Jain, M[a].
[a] Department of Physics, Technical University of Denmark, Risø Campus, 4000, Denmark

Contained in this chapter is a study concerning the suitability of spatially resolved IRPL and IRSL for recovering doses. This work was first presented at the 16th International Luminescence and Electron Spin Resonance Dating conference (LED2021), on the 14th September 2021. The publication has been submitted to the journal Radiation Measurements, where it is currently under review.

Abstract

Establishment of chronological frameworks is critical to understand landscape evolution. Recently, techniques for spatially resolved measurements of IRSL and Infrared-photoluminescence emissions have been developed for rock surface dating. Such spatially resolved measurements overcome the need for separating out mineral fractions, speed-up sample preparation and measurement times, and provide precise high-resolution luminescence-depth profiles. Here, we investigate the potential of spatially resolved IRPL and IRSL techniques for rock surface burial dating using two rock samples with controlled exposure and surface dose histories. We use a SAR style measurement protocol for large rock slices (cm-scale), with a test-dose normalisation step to monitor sensitivity changes, a preheat to remove unstable charges and a bleaching step to reset the IRPL signal. Through establishing the response of IRPL and IRSL to dose, we are able to construct 2D maps of equivalent doses for each sample. The results here indicate that spatially resolving IRSL and IRPL from large rock samples can be used for rock surface burial dating.

Keywords

Infrared-Photoluminescence; infrared stimulated luminescence; luminescence-depth profile; Rock surface burial dating; Equivalent dose.

4.1 Introduction

The potential of dating rock surfaces using optically stimulated luminescence (OSL) has gained ever increasing interest from geoscientists over the past few decades. Rock surface dating (RSD) with OSL is based on the daylight exposure and subsequent burial of rock surfaces (Liritzis, 1994; Liritzis et al., 1999; Sohbati et al., 2012a; Freiesleben et al., 2015). Trapped charge is optically reset at the surface of the rock, and to progressively deeper depths with increasing exposure times (Polikreti et al., 2002; Sohbati et al., 2011). The exposure duration is recorded as a bleaching front within the rock and exposure time can be determined by reconstructing the luminescence-depth profile and fitting the profile with a calibrated age model (Sohbati et al., 2012a; Freiesleben et al., 2015). Should this exposed rock then be buried, the total burial duration can be determined through conventional OSL measurements from surface slices of the buried rock (e.g. Theocaris et al., 1997; Vafiadou et al., 2007; Sohbati et al., 2015). The reliability of such dose measurements is ascertained by reconstruction of the pre-burial luminescence-depth profile through model fitting of the data (Freiesleben et al., 2015). Arguably one of the most advantageous aspects of OSL rock surface burial dating (RSBD) compared to OSL sediment dating is this easy validation of whether the rock surface was sufficiently bleached prior to burial (Khasawneh et al., 2019; Souza et al., 2021).

Applications of OSL RSD often favour the infrared-stimulated luminescence (IRSL) emission from feldspar because of its ubiquitous availability and relatively higher sensitivity compared to quartz (Simkins et al., 2016). However, the IRSL emission is known to suffer from anomalous fading (Wintle, 1977; Spooner, 1994; Huntley et al., 2001), and although various methods have been developed to overcome this (e.g. elevated temperature IRSL; Buylaert et al., 2009; Li et al., 2011; Thomsen et al., 2011), other problems arise such as thermal transfer, poor bleaching, and changing sensitivity (Duller, 1991; Liu et al., 2016; Yi et al., 2016; Colarossi et al., 2018). Since the characterisation of the infrared-photoluminescence (IRPL) emissions at 955 nm ($IRPL_{955}$) and 880 nm ($IRPL_{880}$) from feldspar (Prasad et al., 2017; Kumar et al., 2020a), there has been increasing hope in being able to overcome these problems. Contrary to IRSL, IRPL is a steady state emission reliant on the transition of electrons between the excited and ground state within the principal trap (Prasad et al., 2017; Kumar et al., 2018; Kumar et al., 2020a). IRPL is thus a non-destructive emission, where longer accumulation times can increase signal-to-noise ratios and, even at room temperature, IRPL offers high sensitivity and negligible fading (Kumar et al., 2018).

To date, only a few applications have been attempted using IRPL for sediment or rock surface dating. Sellwood et al. (2019) and Sellwood et al. (2022) recognised the suitability of using IRPL for spatially resolved measurements and demonstrated how luminescence-depth profiles can be reconstructed from naturally exposed rock slabs for rock surface exposure dating (RSED). Duller et al. (2020b) tested IRPL for determining equivalent doses (D_es) using IRPL images of single sand-sized grains. Kumar et al. (2021b) have described a suitable SAR-based protocol for determining equivalent doses without the need for a fading correction using IRPL emissions at 880 nm and 955 nm. These authors used a TL/OSL Risø reader adapted with an IRPL attachment (Kook et al., 2018). These promising results, as well as the development of appropriate measurement protocols through both imaging and reader-based measurements, have opened possibilities of using spatially resolved measurements of IRPL for rock surface burial dating (RSBD). Through imaging, the whole luminescence-depth profile can be rapidly assessed, and we can avoid the extensive sample preparation stages of coring and slicing which are required in conventional measurements. We would also be able to recreate a dose map, presenting the 2D dose distribution of the whole rock sample, and investigate IRPL characteristics (e.g. sensitivity

changes) from different locations across the sample.

Presented here is a continuation of the work by Sellwood et al. (2022) using the EMCCD-based imaging system- the Risø Luminescence Imager (Sellwood et al., 2021). We demonstrate a dose recovery protocol using IRSL and IRPL imaging which could be used for future RSBD applications. We imaged the IRPL at both 880 nm and 955 nm, and IRSL from two rock samples with controlled exposure and burial histories. A SAR method was used to measure doses and pixel-wise analysis of dose response was used to construct 2D distributions of IRPL and IRSL equivalent doses. As IRPL is a non-destructive measurement, it was possible to reconstruct 2D distributions of equivalent doses using IRPL both before and after the preheat stage. We also discuss sensitivity changes and residual IRPL levels across different regions of the rock samples, and their effect on the equivalent dose estimates. This study has implications for rapid and robust assessment of dose based on luminescence-depth profiles in rocks. This method yielding high resolution luminescence-depth profiles is especially powerful when model fitting is deemed critical to ascertain the extent of bleaching prior to burial.

4.2 Materials and methods

4.2.1 Samples

Two control samples were measured in this study: G14 and G12. These two samples were collected as 8 cm Ø × 10 cm cores from a fine crystalline granite from an unknown location in China. Prior to the experiments here, these cores were heated to 700°C for 24 hours, and were then given a saturation dose of 20 kGy using a cobolt-60 source at the Department of Health Technology at DTU, Risø campus. The edges of the cores were then wrapped in light-proof black tape, and the cores were placed on a rotating table under four halogen lamps (Osram H7 70 W bulbs; 102 mW/cm^2) for 327 days. From G14, a 2 cm diameter core was drilled perpendicular to the bleached surface. Using a 0.35 mm thick diamond wire saw, a section 18.4 × 18 × 1.4 mm is size was cut from the centre of this core (hereafter named G14E), perpendicular to the bleached surface. Section G14E was imaged to reconstruct the exposure profile. A burial dose was then administrated to the exposed surfaces of the large cores of G12 (200 Gy dose) and G14 (500 Gy) using a Cobalt-60 photon beam (1 Gy/min dose rate, DTU Health Tech department, Risø). From the irradiated cores of G12 and G14, sections for imaging were cut perpendicular to the buried surface, labelled as G12B (~22 × 43 mm) and G14B (~30 × 39 mm) respectively. Optical images of the measured samples can be found in the supplementary information.

4.2.2 Measurements

Table 4.1 outlines the measurement sequence for G12B and G14B using the Risø Luminescence Imager (Sellwood et al., 2021). For G12B, G14E and G14B, IRPL was integrated over 3 s, and the whole IRSL decay curve was captured over 20 frames, each integrated over 10 s. A preheat at 200°C for 5 minutes was given in an oven. Bleaching was achieved over 24 hours in a Hölne Solar simulator. Samples were irradiated in the Cobolt-60 gamma cells at the High dose reference laboratory facilities at Risø. Regeneration doses for G12B and G14B were 50, 250, 500, 1000 and 3000 Gy. For G14E, the first IRPL and IRSL from the exposed samples was measured. This was followed by measurement of IRPL and IRSL response to a 2 kGy saturation test dose for normalisation of the natural signals.

Step	Treatment	Result
1	Natural or Regenerated IRPL	L_n or L_x
2	Preheat (200°C, 5 minutes)	
3	Natural or Regenerated IRPL and IRSL	L_nPH or L_xPH
4	Bleach, 24 hours	
5	IRPL for background	L_nBG or L_xBG
6	T_x(100 Gy)	
7	Measure IRPL	T_x
8	Preheat (200°C, 5 minutes)	
9	IRPL and IRSL	T_xPH
10	Bleach, 24 hours	
11	IRPL for background	T_xBG
12	Regeneration dose	
13	Repeat stages 1-12	

Table 4.1: Measurement sequence for IRPL and IRSL with the EMCCD-based imaging system. Regenerative doses were: 50, 250, 500, 1000, and 3000 Gy.

4.2.3 Analysis

All analysis was conducted in MATLAB using the Image Processing toolbox (Mathworks, 2017). All images from each sample dataset were first registered onto one-another to allow pixel-wise analysis. The area outside each sample was removed from the images. The background images (data from steps 4 and 10 in Table 4.1) were subtracted from the respective L_n, L_x or $T_x$images for IRPL. For IRSL, the final frame was subtracted from the first frame, after checking that background levels had indeed been reached in the decay curves (available in the supplementary information). Luminescence-depth profiles were reconstructed by taking the mean and standard error of each column across the images, and plotted as a function of depth from the surface.

The equivalent dose calculation and analysis followed a three stage process. First, equivalent doses were calculated for each pixel of the IRPL and IRSL images measured after the preheat stage. This was achieved by interpolating the L_n/T_n of each pixel against its respective dose response curve and reconstructing the D_e map. For all data sets, a double exponential model was chosen for fitting the pixel-wise dose response curves, and pixels where the R^2 value of the fit was <0.9 were rejected. The second analytical stage followed the reasoning that it is only relevant to observe equivalent doses from pixels where IRPL or IRSL was actually detected. To achieve this, a threshold mask was applied to each D_e map to select the luminescing regions of interest. To create the masks, six 1 mm sections were defined in the full D_e maps parallel to the buried surface (facing the gamma beam), at progressively deeper depths. The pixel-wise D_e values from these sections were plotted against the corresponding pixels from the 1 kGy regeneration dose (L_x) image. We observed a very broad (sometimes bimodal) D_e distribution, with a peak present around the expected burial dose (see supplementary information). From here, an optimum threshold value was defined based on L_x intensity to filter out pixels with low intensity or no luminescence, in order to narrow down the distributions. The final D_e maps were constructed based on the selected pixels, after applying the binary masks to the IRSL D_e maps and to the IRPL D_e maps from both before and after preheat. To investigate where at the rock surfaces we could find the D_e values closest to the known doses, the mean and standard error doses were calculated from the 1 mm sections parallel to the burial surface of the final D_e maps from the previously bleached regions of the slabs. These values were plotted over depth from

the surface, with depth defined as the mid point of the 1 mm section.

4.3 Results

4.3.1 Equivalent doses

Presented below are the results for G12B and G14B. We present the L_n/T_n ratio maps and corresponding profiles for each emission, alongside the calculated D_e maps (Gy) for the IRSL and IRPL from after the preheat stage. The ratio and D_e maps are presented in false colour with colour bars representing L_n/T_n value or the D_e (Gy). The colour scaling has been adjusted to focus on the surface regions of interest. The L_n/T_n ratio maps and luminescence-depth profiles from the bleached sample (G14E) can be found in Figure 4.1. The IRSL ratio map (Figure 4.1a) presents a significant bleached region at the surface (left-hand side of the ratio map). The bleached regions in the $IRPL_{880}$ and $IRPL_{955}$ maps are smaller than IRSL; nonetheless translation of these signals into luminescence-depth profiles indicates that the 327 day exposure was sufficient to bleach the IRPL to a depth of ~2.5 mm, and the IRSL down to ~8 mm from the surface. It is within these bleached zones that investigation in the dose recovery experiments will be focused.

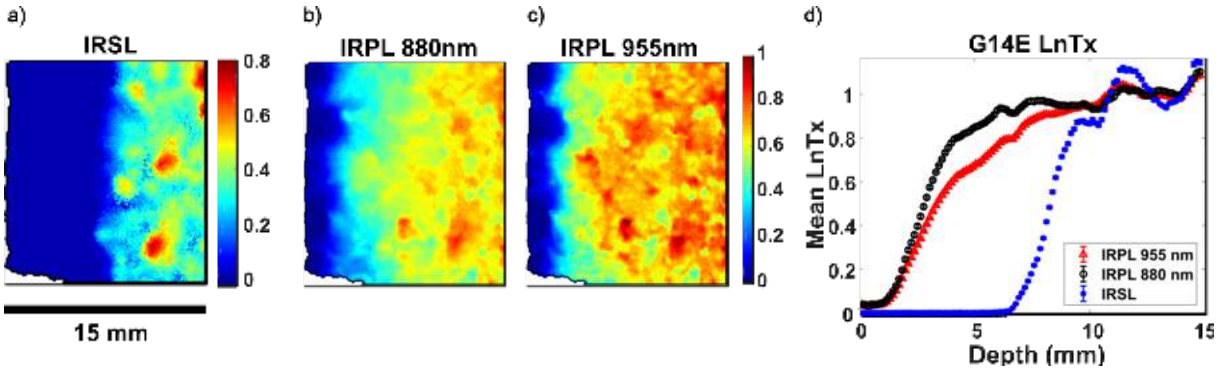

Figure 4.1: a) IRSL L_n/T_n ratio map for G14E. b) $IRPL_{880}$ L_n/T_n ratio map. c) $IRPL_{955}$ ratio map. d) Luminescence-depth profiles from the IRSL and IRPL ratio maps. The profile data here has been normalised to the saturation level

Figure 4.2 presents the data from G12B (bleached + gamma dose), where panels a, b and c display the L_n/T_n ratio maps for IRSL, $IRPL_{880}$ and $IRPL_{955}$ (after preheat) respectively. The white regions in the IRSL map indicate infinite values due to non-responsive test dose regions. In Figures 4.2a-c, it is possible to view a gradual increase in L_n/T_n from the very surface of the rock to deeper depths for each signal. The luminescence-depth profiles in Figure 4.2d show the expected sigmoidal form, with each of the profiles showing an expected raised plateau in L_n/T_n ratio values near the surface due to the burial dose (note the IRSL data corresponds to the left y-axis, and the IRPL data to the right y-axis). The IRPL profiles (black circles and red triangles) show a slight rise in ratio value at the very surface (~1 mm); this behaviour has been observed before in RSED profiles, and attributed to slight sensitivity change. On the contrary a slight decrease is observed in the same region (1-2 mm) in the IRSL L_n/T_n values.

Figure 4.2e presents the G12B IRSL D_e map (Gy). The transition in apparent burial dose is observable from the surface to deeper depths (blue to green coloured pixels). Both the $IRPL_{880}$ and $IRPL_{955}$ (after preheat) D_e maps how a very narrow band of pixels presenting doses around our dose of interest (Figures 4.2f and g). There is a more irregular distribution in apparent doses,

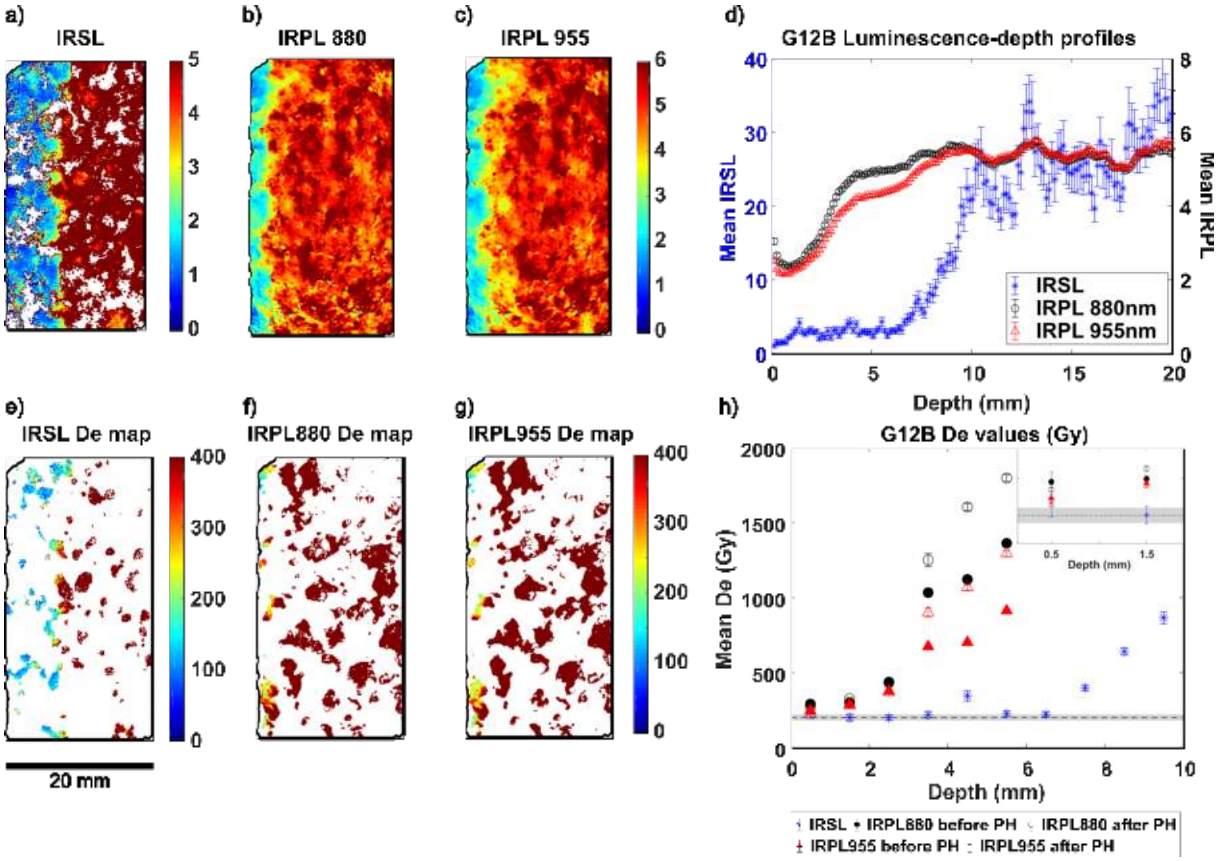

Figure 4.2: Results from G12B. a), b) and c) present the L_n/T_n ratio maps for IRSL, $IRPL_{880}$ and $IRPL_{955}$ after preheat respectively. The burial surface is on the left-hand side of each ratio map. d) Luminescence-depth profiles from the L_n/T_n ratio maps. The IRPL profiles correspond to the right axis, and the IRSL to the left. e) IRSL D_e map after masking to observe only the brightest luminescent regions. f) $IRPL_{880}$ D_e map. g) $IRPL_{955}$ D_e map. h) Average D_e values from 1 mm wide regions parallel to the burial surface from the IRSL D_e map, and the IRPL D_e maps from before and after the preheat stage. The inset window shows a zoomed view of the data points from the surface two mm. Error bars show standard error from the mean and the grey band is the expected dose-depth profile of the 200 Gy dose (± 20 Gy), based on data from Fujita et al. (2011)

with no clear progression in dose from the surface to the saturated region. The average doses from the 1 mm sections are presented in Figure 4.2h. The grey band marks the expected 200 Gy (± 10%) burial dose profile through the rock (Fujita et al., 2011). The average IRSL burial doses from 0-3.5 mm and from 5.5-7.5 mm all lie within this expected region, with an increase in dose at 4.5 mm. Beyond 7.5 mm (the bleaching depth seen in the G14E profile in Figure 4.1), the D_e values begin to increase. For $IRPL_{880}$ and $IRPL_{955}$, the surface doses from 0-3 mm from before preheat over estimate the known dose by up to 70% ($IRPL_{880}$). The recovered doses from 0-3 mm from after the preheat stage also overestimate the known dose, but are slightly lower than those from before the preheat, with the very surface $IRPL_{955}$ D_e almost falling within our expected range (see inset plot in Figure 4.2h).

The results from G14B (burial dose of 500 Gy) are found in Figure 4.3. The IRSL and IRPL L_n/T_n maps (Figures 4.3a-c) are similar to those from G12B, with the surface regions clearly distinguishable from the saturated region by the lower L_n/T_n values (blue green colour scheme). The luminescence-depth profiles (Figure 4.3d) show comparably higher surface ratio values than in G12B, with the IRPL profiles again showing an increase in sensitivity at the surface. The IRSL D_e (Gy) map (Figure 4.3e) hosts multiple regions at the burial surface with pixels representing doses ranging from ~200-600 Gy. The calculated surface doses in the $IRPL_{880}$ and $IRPL_{955}$

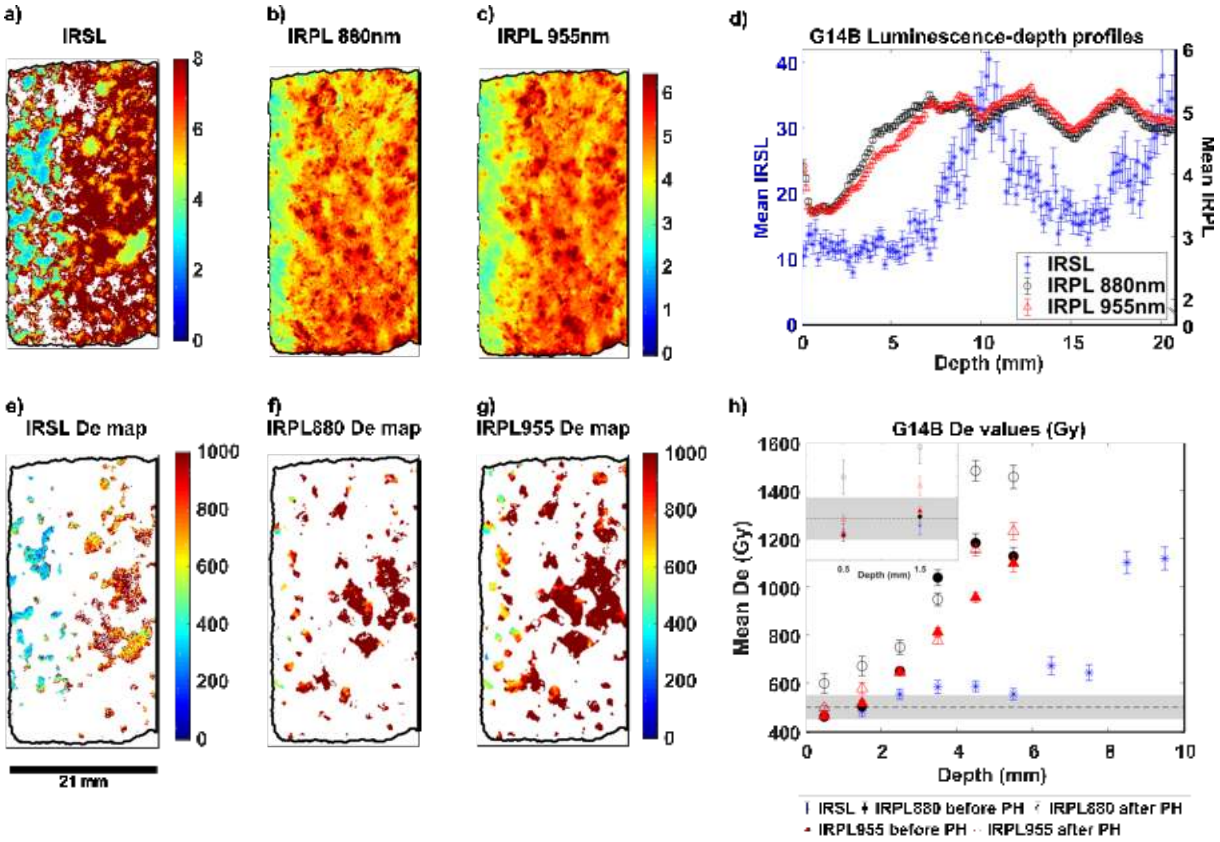

Figure 4.3: Results from G14B. a) IRSL L_n/T_n ratio map. The burial surface is on the left-hand side of the images. b) $IRPL_{880}$ L_n/T_n map. c) $IRPL_{955}$ L_n/T_n map. d) Luminescence-depth profiles from the L_n/T_n maps. e) IRSL D_e (Gy) map. f) $IRPL_{880}$ D_e map. g) $IRPL_{955}$ D_e map from before the preheat stage. h) Mean and standard error of D_es taken from 1 mm wide regions parallel to the buried surface of the rock slab. The data from the IRPL both before and after preheat is shown. The grey band represents the expected absorbed dose profile (500 ± 50 Gy). The inset window shows a zoomed view of the surface regions.

D_e maps (Figures 4.3f and g) at first glance are slightly higher than the IRSL (yellow pixels). Observing Figure 4.3h, it is only within the surface 0-3 mm that the mean IRSL D_e values fall within the expected dose range (500 Gy ± 10%; grey band on Figure 4.3h), with a slight increase in dose between 3-7 mm, before increasing towards higher doses. Across the whole rock slab, there is a significant difference between the $IRPL_{880}$ equivalent doses from before (solid circles) and after preheat (hollow circles), with an overestimate of the known dose for the data after the preheat stage. From 0-2 mm depth, the $IRPL_{880}$ from before the preheat stage, and the $IRPL_{955}$ results from both before and after preheat are within uncertainties consistent with the expected dose range.

4.3.2 Investigating IRPL sensitivity

We discuss below the suitability of our measurement protocol with regards to the test dose and IRPL bleaching. For this, we followed similar analysis as for the D_e maps discussed above. The same threshold masks as used for the D_e maps were applied to the T_x (both before and after preheat) and bleached images after the regeneration doses (step 5 in Table 4.1) for each sample. We again, defined 1 mm sections parallel to the burial surface at the slab, from 0-1 mm, 1-2 mm, 2-3 mm, 7-8 mm and 18-19 mm. We discuss the variations in IRPL or IRSL test dose responses as well as the variations in IRPL residual levels for each signal for each sample from

these regions.

4.3.3 Test dose sensitivity

Figures 4.4a-c present the G12B T_x/T_n ratio values (after preheat) at different depths across the samples from IRSL, $IRPL_{880}$ and $IRPL_{955}$, respectively. The inserts in Figures 4.4 b and c show the T_x/T_n IRPL ratios from before the preheat. The data is plotted over each regeneration cycle in the measurement protocol, with cycle 1 corresponding to measurement of the initial IRPL and IRSL after receiving the burial dose. The IRSL sensitivity at the very surface of G12B (red circles in Figure 4.4a) varies within 5% from unity for each regeneration cycle, except for cycle 5 (1 kGy regeneration dose), where the sensitivity decreases by over 25%. This decrease is consistent for data from all the depths across the slab. The G12B $IRPL_{880}$ and G12B $IRPL_{955}$ data both before and after preheat (Figure 4.4 b and c respectively), show the biggest sensitivity changes across cycles in the surface 2 mm (up to ~20%). The deeper slices show lesser variations of the order of about less than 10% across cycles; the biggest change seen at deeper depths is observed between cycle 1 and cycle 2.

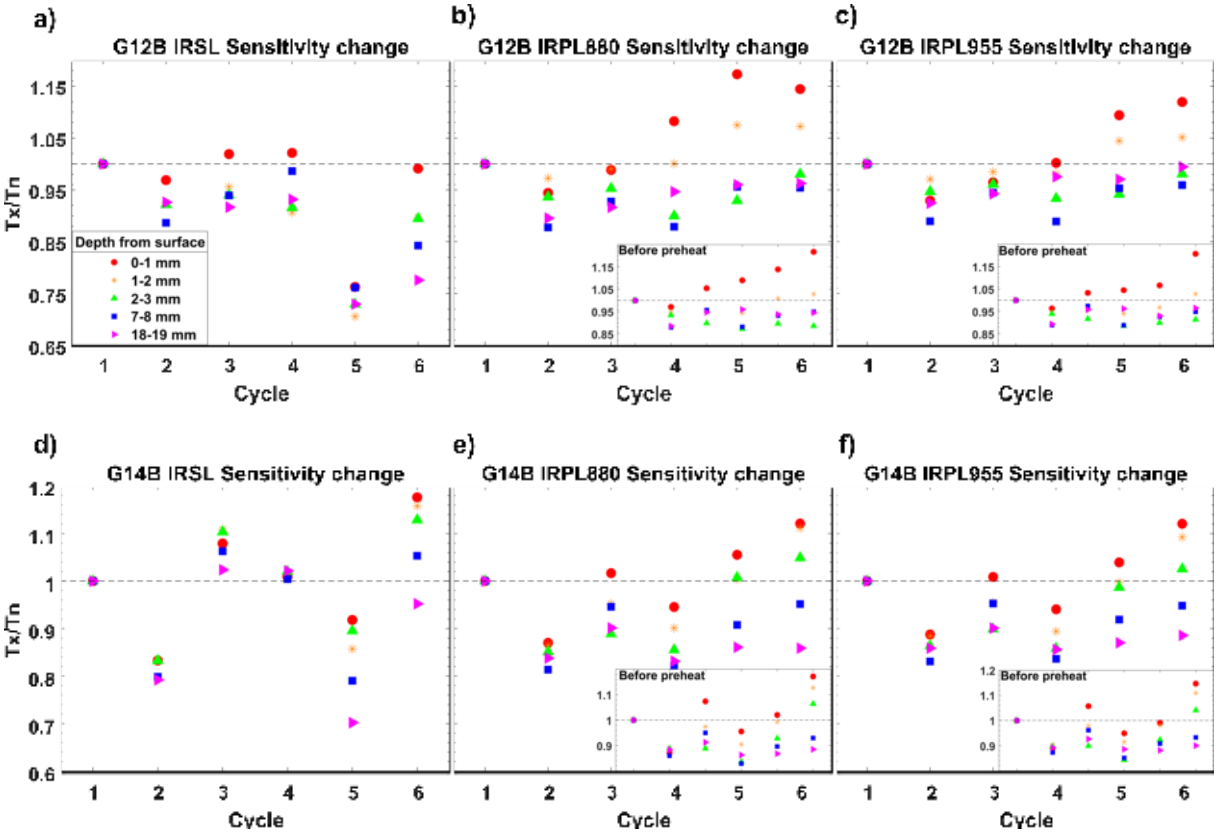

Figure 4.4: a) Sensitivity changes from G12B IRSL T_x/T_n data, from different depths across the rock slab. b)T_x/T_n ratio vales from G12B $IRPL_{880}$ after the preheat stage. The IRPL data from before the preheat is presented in the insert. c)G12B $IRPL_{955}$ T_x/T_n ratio values after the preheat, with data from before the preheat presented in the insert. d) G14B IRSL T_x/T_n data from different depths across the slab. e) G14B $IRPL_{880}$ T_x/T_n ratio values. f) G14B $IRPL_{955}$ sensitivity changes

The IRSL test dose sensitivity of G14B is irregular with no systematic changes in T_x/T_n ratio through the regeneration cycles (Figure 4.4d). The sensitivity shows significant decreases across the slabs at cycles 2 and 6, but this behaviour is not seen in the IRPL data. Similarly to G12B, the $IRPL_{880}$ sensitivity changes after preheat in Figure 4.4e indicate that the sensitivity

at the saturated region of the slabs (blue squares and pink triangles in Figure 4.4) is relatively stable with a few percent relative change after an initial decrease of ~15% from unity after cycle 2. The surface regions (red circles and orange stars) do not follow such systematic behaviour. This irregular sensitivity fluctuation at the rocks surface is also seen in the data from before the preheat stage (inset in Figure 4.4d), as well as in the $IRPL_{955}$ data (Figure 4.4f and insert). The $IRPL_{955}$ T_x/T_n ratios from the surface regions fluctuate between ± 10% from unity. The deepest regions of the slab do not show this, again presenting more stable T_x/T_n ratios (within 5% of each other) after an initial decrease at cycle 2.

4.3.4 Influence of IRPL residual on test dose

Following from the observed sensitivity changes in Figure 4.4, we address the IRPL residual levels in the L_x data for both samples, which may be influencing the test dose response. Presented in Figure 4.5a are the G12B $IRPL_{880}$ mean $T_x$values from each SAR cycle, from the 1 mm sections defined in section 4.3.2, plotted against the corresponding mean L_x residual level after the preceding regeneration dose (step 5 in Table 4.1). The data are fitted with a liner regression, and the dotted lines represent 95% prediction intervals. The 1:1 line is shown for reference. The measured $T_x$increases with increasing L_x residual (which increase as a function of increasing regeneration dose; see supplementary information), with a slope of 1.47 (± 0.38). The same trend is seen in the $IRPL_{955}$ data (Figure 4.5b) from G12B which has a greater slope, indicating a greater influence on the test dose from the non-bleached component of the $IRPL_{955}$ L_x data. This suggests that either the $T_x$dose may be building upon the remaining L_x residual level, there may be influences of thermal transfer during preheating of the test dose leading to an increase in test dose intensity. The data points in Figures 4.5 a and b fall into three groups depending on their depth from the surface. In both a and b, the IRPL $T_x$intensity and residuals for the surface of the slab (red circles) are relatively lower than at deeper regions of the slab. Slightly higher residuals and $T_x$values are seen in the 2-3 mm data (yellow stars) and the data from the saturated regions of the slab cluster together with higher residual vs. $T_x$values.

The data from G14B is shown in figures 4.5 c and d. Here, the slopes of the linear regressions are larger (and with larger uncertainties) than those for G12B, and the spread of the data is larger especially for the data from 7-8 mm depth from the slab surface (blue squares). At this depth in the slab there is an apparent high sensitivity to the test dose and a higher L_x residual value in both the $IRPL_{880}$ and $IRPL_{955}$ compared to other depths across the slab. The relatively lower L_x residual or $T_x$intensity seen in the surface region (red circles in Figure 4.5) of G12B is not observed in G14B. The residual levels and $T_x$responses at all depths from the slab are similar and all increase to similar degrees with increasing regeneration dose (apart from at 7-8 mm). The general observation from the G12B data are that the trend in the residual vs. $T_x$is similar for the surface and the deeper regions; however, the absolute response to the test dose is smaller for the surface regions compared to the deeper regions. In G14B, the residual vs. $T_x$trend, as well as the absolute $T_x$intensities, in the surface and the deeper regions are indistinguishable. The two samples (G12B and G14B) had the same test dose and the same regeneration doses so the differences observed between the two samples in Figure 4.5 could either be due to different burial doses, or simply a coincidence. This needs be confirmed in future studies.

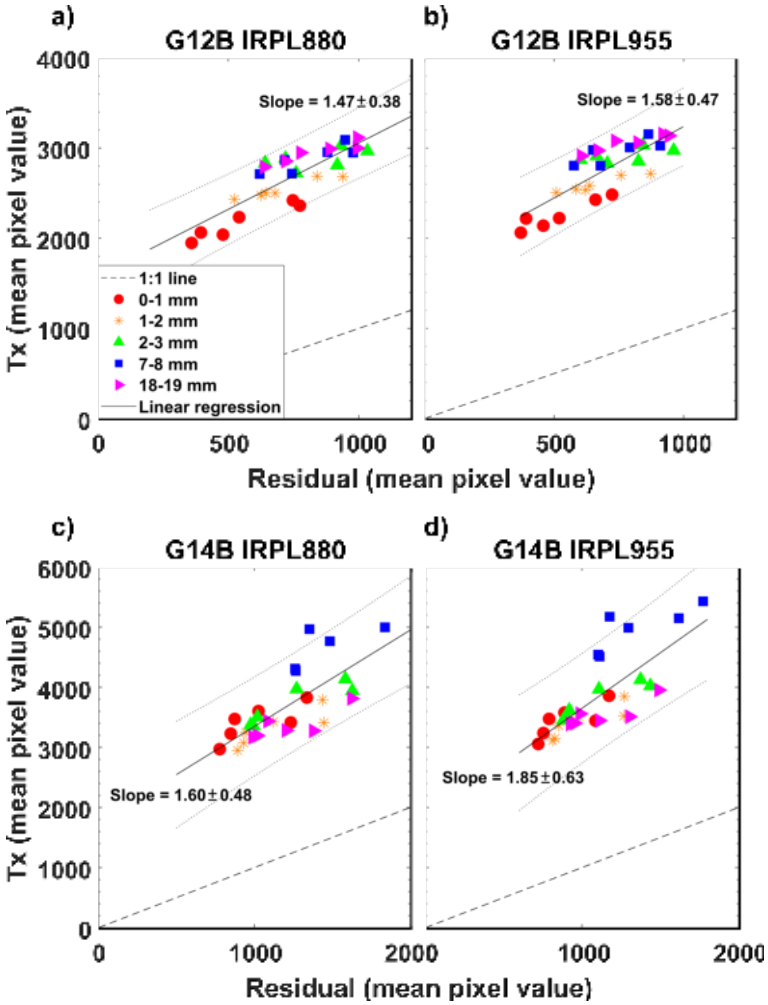

Figure 4.5: a) G12B $IRPL_{880}$ mean $T_x$values from different regions of the slab plotted against the L_x residual values after step 11 in the measurement protocol. b) G12B $IRPL_{955}$ data. c) G14B $IRPL_{880}$ correlation and d) G14B $IRPL_{955}$ correlation. The solid lines show the results of the linear regression through each data set, and dotted lines represent the 95% prediction intervals for new observations. The dashed line shows the 1:1 line for reference

4.4 Discussion

Through imaging of the initial and regenerated IRSL and IRPL from the large rock samples, we were able to clearly observe the bleaching extent of the IRPL and IRSL, and validate the presence of the simulated burial doses at the prior bleached surfaces. Pixel-wise analysis resulted in the construction of a 2D maps of equivalent doses. From these maps alone, it was possible to observe the different responses of the IRSL and IRPL to dose from different regions (e.g. Figure 4.2e-g), at a resolution which is unachievable with conventional measurements of individual rock slices.

We observe recovered IRSL equivalent doses in both G12B and G14B falling within the expected doses ranges within the surface few mm, where the IRSL was previously bleached. There is no clear trend on the effect of preheat on the ability to recover dose from the IRPL data; the before and after preheat D_e data are generally consistent with the error margin for the surface region; the only exception is the $IRPL_{880}$ after preheat data for sample G14B (Figure 4.3h), which significantly overestimates all the other signal estimates. This alone would suggest

that significant thermal transfer occurred during the preheat stage, but arguably this would have also been observed (at least to some degree) in the $IRPL_{955}$ data. It is suggested that a preheat plateau and thermal transfer tests be conducted in the future similar studies.

Investigating the sensitivity changes via test dose response from the spatially resolved data offered an indication not only as to the suitability of our measurement protocol, but also into the change in L_n/L_x ratio at the surface of luminescence-depth profiles which is observed here (Figures 4.2d and 4.3d) and in other studies (e.g. Sellwood et al., 2019; Sellwood et al., 2022). From taking the T_x/T_n ratio at different depths across the samples, it was clear that the very surface of the samples experience a significant sensitivity change in the IRPL compared to the deeper regions of the slabs which were in laboratory saturation. Both samples show an initial decrease in surface sensitivity with the first regeneration cycle before a general relative increase in sensitivity. As this behaviour is not seen at deeper depths from the surface, and considering the main difference between the surface the and deeper regions of the slab is the bleaching history, the sensitivity change arguably results from the initial bleaching of this surface (profiles shown in Figure 4.1 from G14E). There is a much larger flux and likely a greater UV component at the surface compared to the deeper regions (Ou et al., 2018). This bleaching perhaps influenced the distribution of charge in the shallow or deep traps at this location. However, it remains to be confirmed whether it is this effect of high energy wavelengths at the surface during bleaching, a change in trapping probability due to surface irradiation, or simply the individual responses of the samples which could be the source of the large sensitivity change observed at the surface. It is interesting to note that IRSL shows the opposite trend, that the sensitivity change at the surface is much smaller compared to the deeper regions. This indicates that the sensitivity change is not necessarily linked to the distribution of recombination centres at the surface, but instead with the trapping centres.

The test dose response of G14B is more variable than that seen in G12B. Previous research by Colarossi et al. (2018) and Liu et al. (2016) has demonstrated a test dose size dependency on dose recovery. They argue for the use of larger tests doses relative to the expected dose and relative to the residual dose. Here, the test dose was 50% of the burial dose for G12B, but only 20% of the burial dose for G14B. Testing the effect of test dose size is suggested for future research. There is larger scatter in the IRSL T_x/T_n compared to the IRPL (Figure 4.4). This scatter cannot be attributed to pixel misalignment as that would have also affected the IRPL data. Possible explanations could be: a) the presence of a thermal gradient in the rock sample during preheating leading to irreproducible thermal eviction of unstable charge with depth, or b) a larger change in the recombination centre population during SAR cycles (Thomsen et al., 2011; Kars et al., 2013; Li et al., 2013).

4.5 Conclusions

We apply here a SAR-style protocol for dose recovery experiments using spatially resolved IRSL and IRPL from two rock samples with known exposure and burial dose histories. We recovered IRSL doses in the prior bleached regions near the surface which were generally consistent with the given doses (200 Gy and 500 Gy). The known doses were recovered from the very surface of G14B (500 Gy) from both $IRPL_{880}$ and $IRPL_{955}$, but the recovered IRPL doses from G12B over estimated the known 200 Gy dose. Significant sensitivity changes in the IRPL signals were observed in the surface regions of the samples; the sensitivity changes were less prominent in the deeper (>2 mm) regions of the samples. This suggests that IRPL sensitivity change may be related to the initial bleaching period (resetting prior to burial) as such bleaching is most effective closest to the surface, or from changes in trapping probability due to irradiation at

the surface. The preliminary results discussed here argue that IRPL and IRSL burial doses can potentially be recovered from spatially resolved measurements. Whilst we demonstrate how 2D D_e maps can be reconstructed from spatially resolved IRSL and IRPL, we suggest that future work should focus on the understanding the effect of different preheats and test dose sizes on the regenerated IRSL and IRPL. Applications on samples with natural burial doses of different magnitudes would also be highly beneficial.

4.6 Acknowledgements

The authors wish to thank Trine Freiesleben for providing the samples used here. We are also grateful to Mark Bailey, Arne Miller and Torben Esmann Mølholt , our colleagues at the at the Risø High Dose Rate Reference Laboratory who provided access to the large irradiation facilities.

4.7 Supplementary Information

SI 1: Images of samples

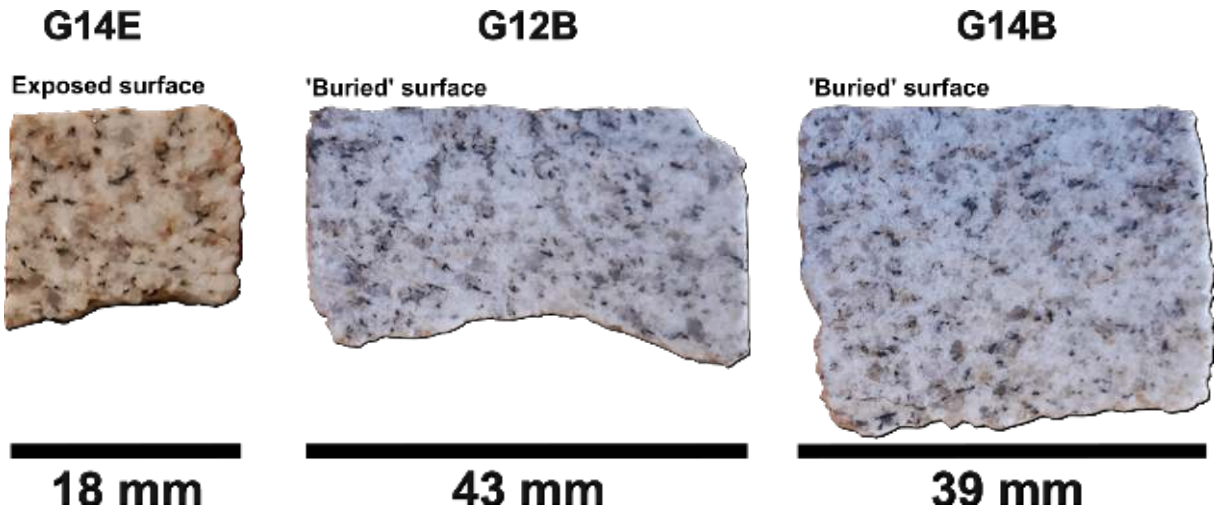

Figure 4.6: Photographs of the samples used in this study. The exposed or buried surfaces are indicated.

SI 2: IRSL Decay Curves

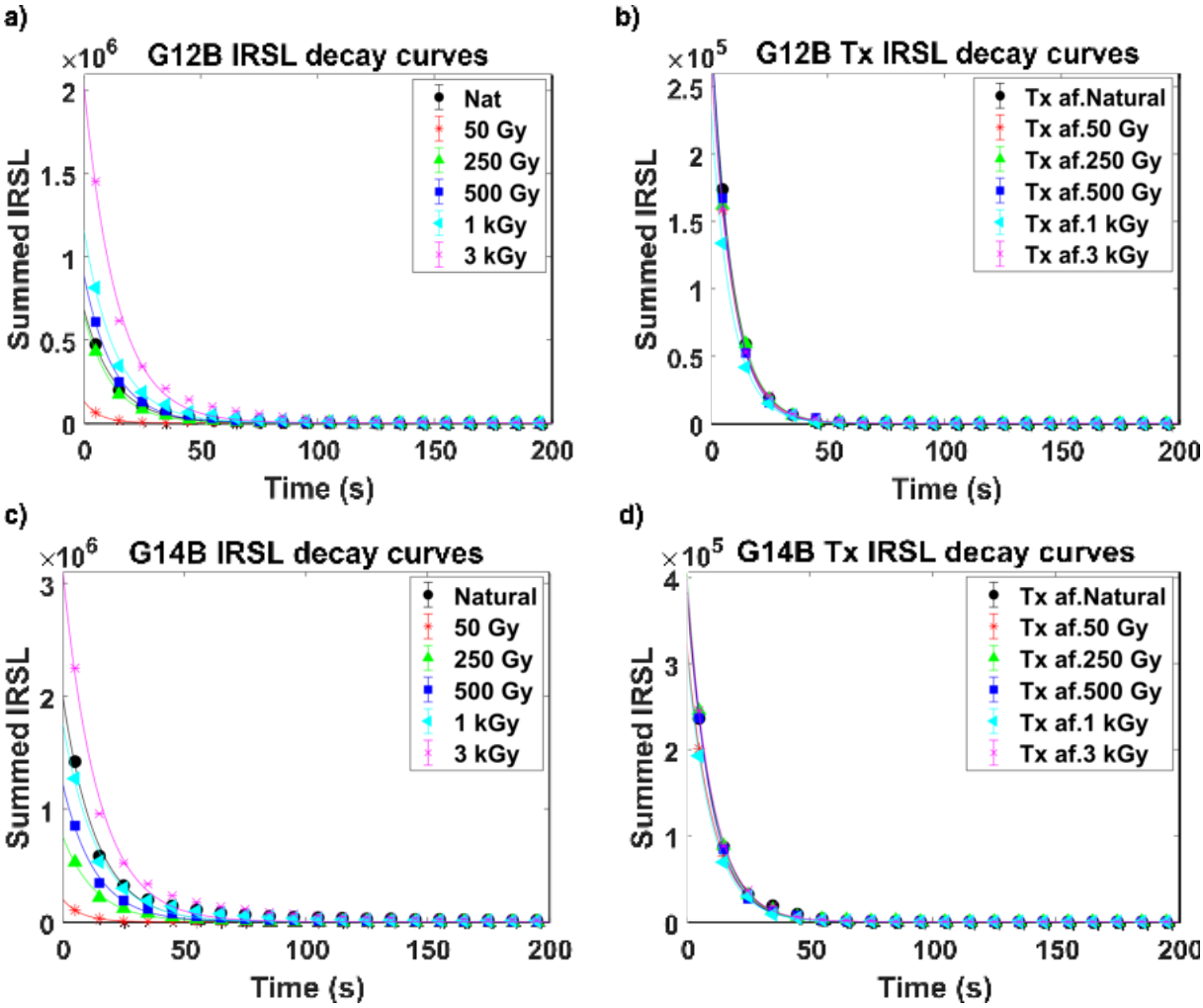

Figure 4.7: a)G12B IRSL decay curves from the natural or each regeneration dose given. b) G12B IRSL decay curves from the $T_x$doses. c) G14B IRSL decay curves from each natural or regenerative dose. d) G14B IRSL decay curves from each $T_x$dose

SI 3: Threshold values for masking of D_e maps, and 1 mm analysis sections. Sample G12B.

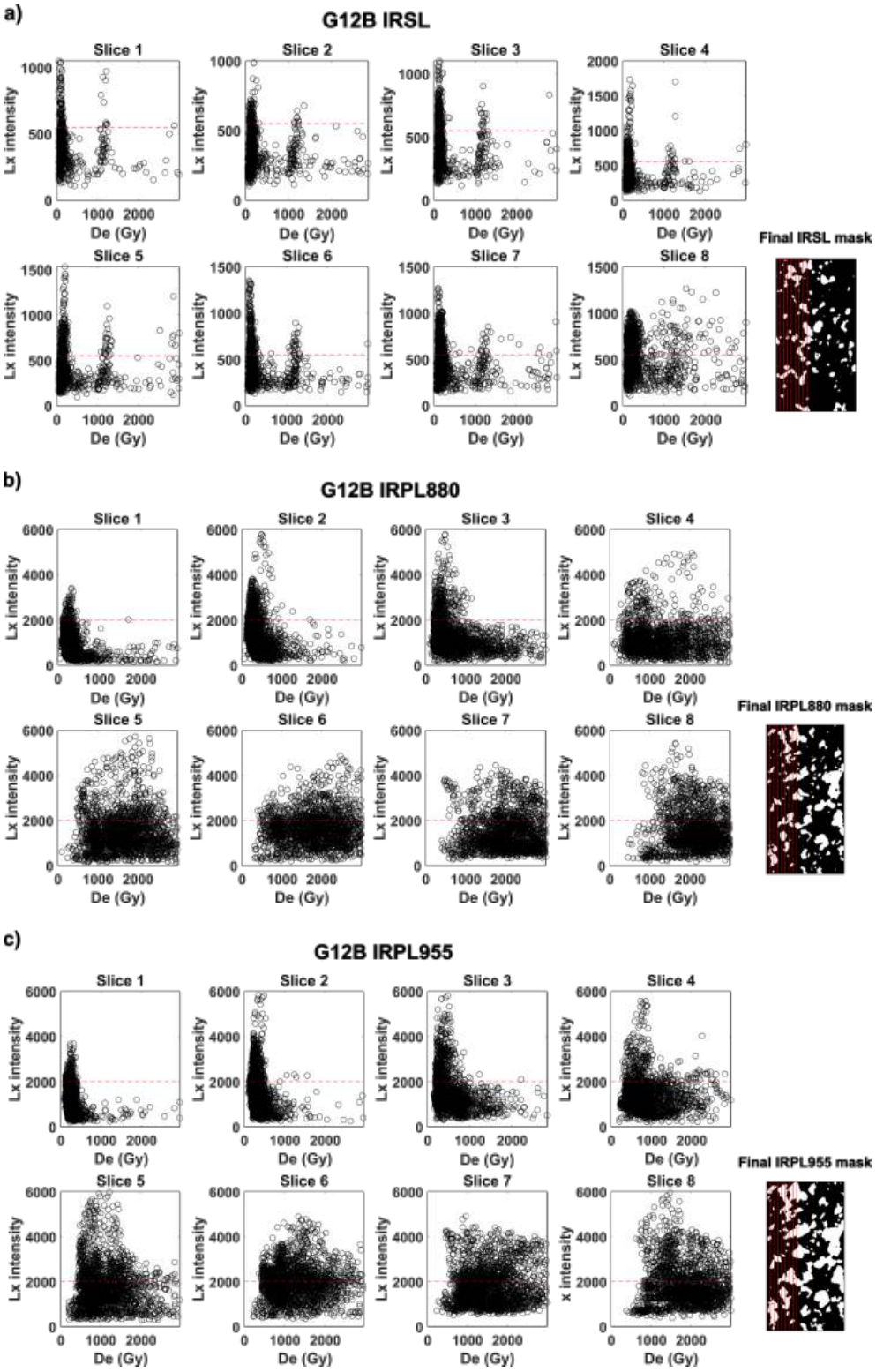

Figure 4.8: a) G12B IRSL L_x data plotted over D_e (Gy) for 1 mm sections. b) $IRPL_{880}$ plots and c) $IRPL_{955}$ plots. The red dashed line marks the threshold value used to create the binary map which was applied to the D_e maps. The final masks are shown on the right hand side, with the red boxes marking the positions of the 1 mm sections

SI 4: Threshold values for masking of D_e maps for G14B

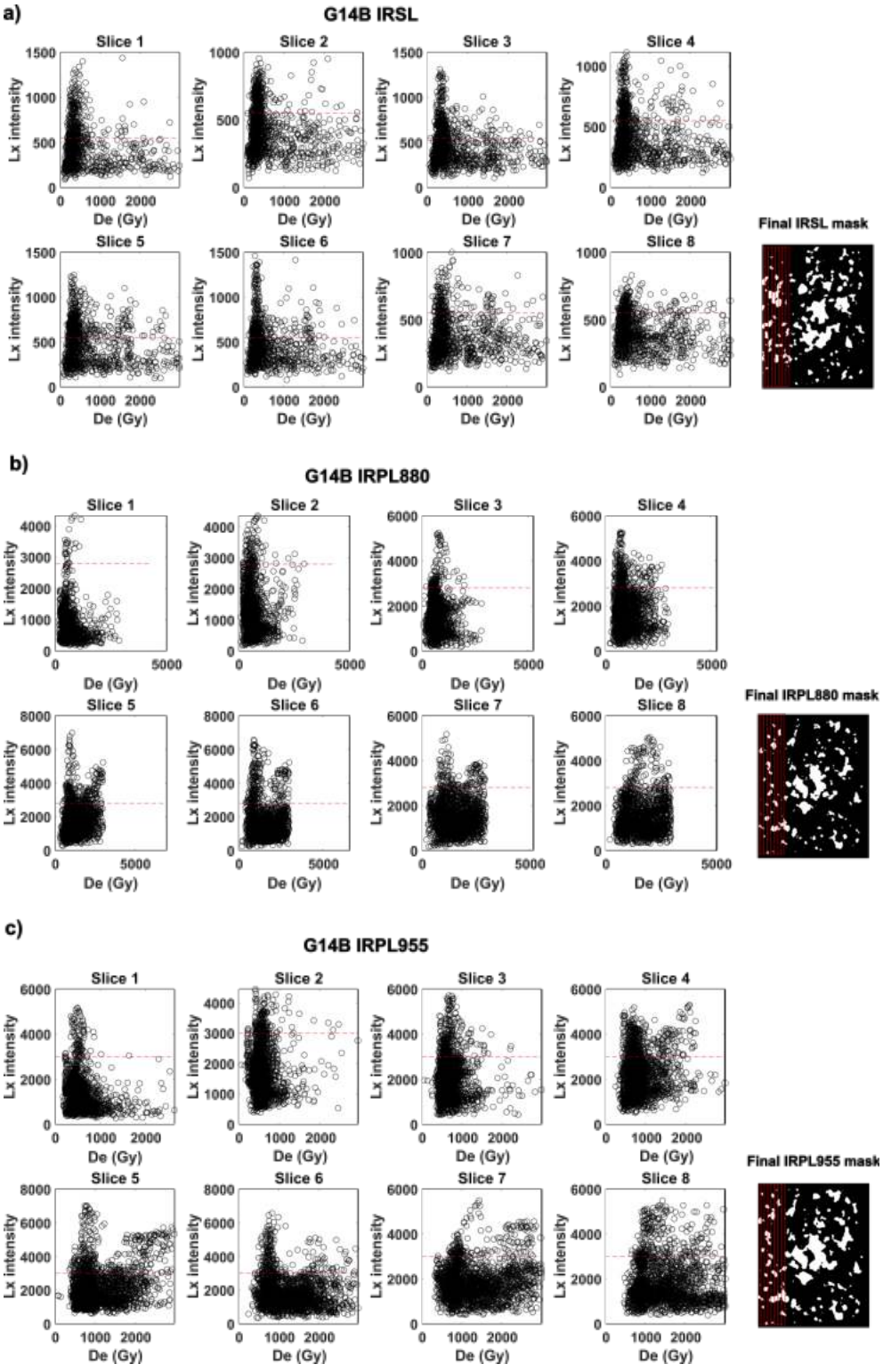

Figure 4.9: a) IRSL L_x data plotted over D_e (Gy) for 1 mm sections defined across sample G14B. b) $IRPL_{880}$ plots and c) $IRPL_{955}$ plots. The red dashed line marks the threshold value used to create the binary map which was applied to the D_e maps. The final masks are shown on the right hand side, with the red boxes marking the positions of the 1 mm sections

SI 5: IRPL L_n/T_n ratio maps and profiles from before the preheat and after IRSL measurement

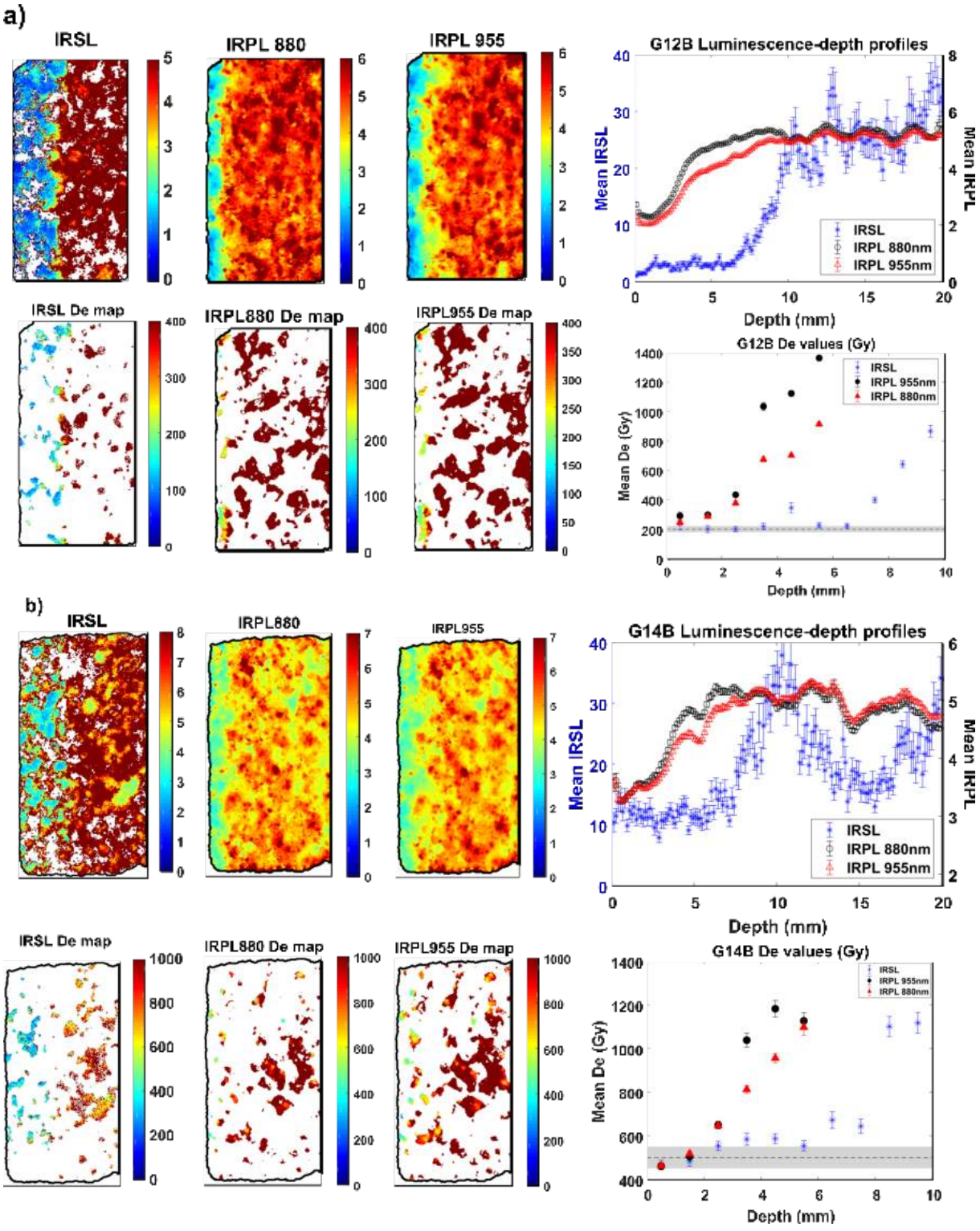

Figure 4.10: a) IRSL and IRPL ratio maps and profiles, D_e maps and recovered surface doses form G12B before the preheat stage. b) IRSL and IRPL data from before the preheat stage for G14B. The IRSL data is the same as the data in the main text

SI 6: IRPL Residual values

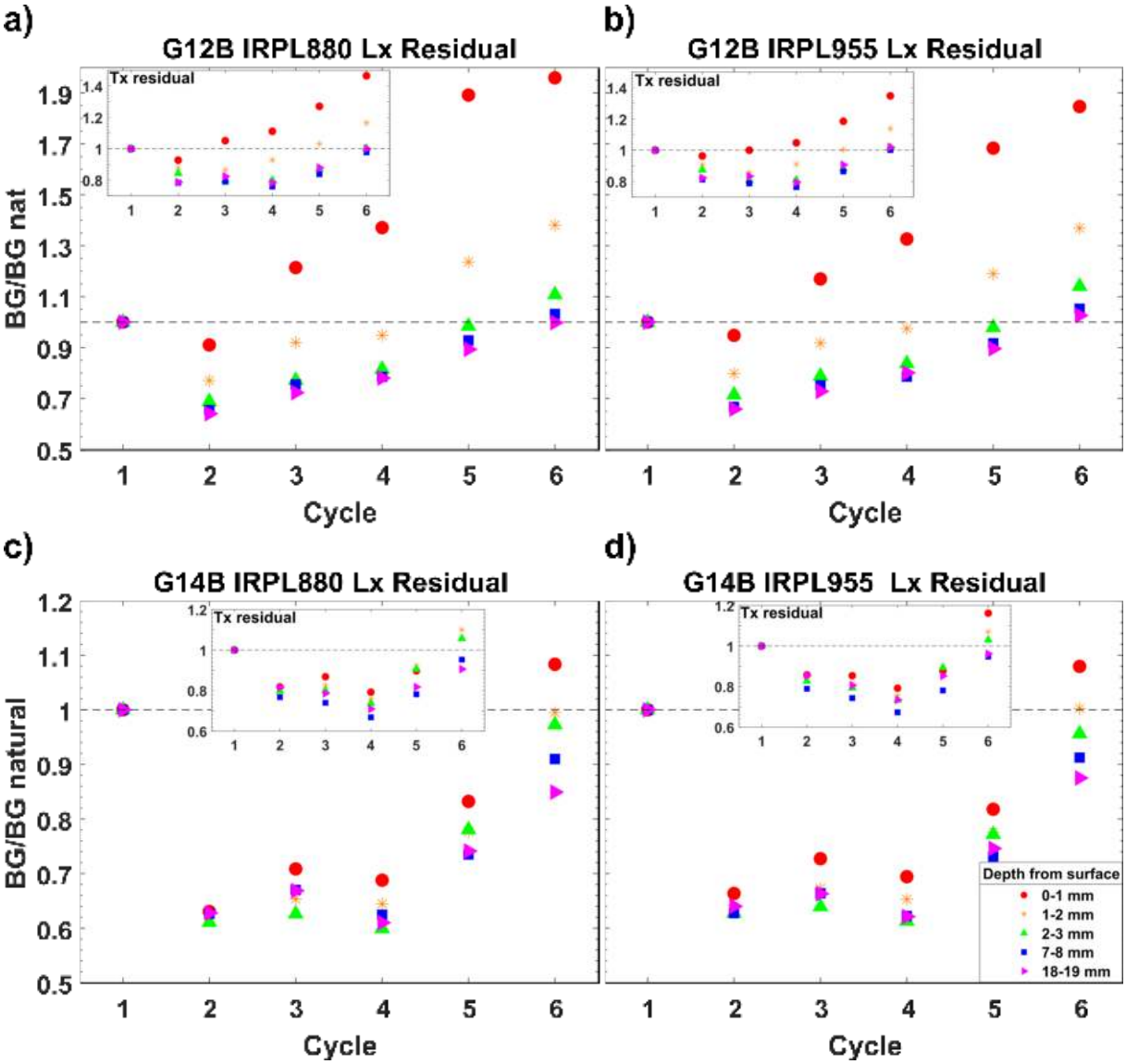

Figure 4.11: a) G12B $IRPL_{880}$ L_x residual values normalised to the natural residual level for different depths across the slab. The insert shows the residual values for the $T_x$data. b) G12B $IRPL_{955}$ L_x residual values, with $T_x$residual values inset. c) G14B $IRPL_{880}$ L_x residual levels. d) G14B $IRPL_{955}$ L_x residual values.

CHAPTER 5

Investigating the development of IRPL luminescence-depth profiles in rocks

The work presented in this chapter is part of a larger project in collaboration with Trine Freiesleben, and will eventually be compiled into a publication. The larger project centres around the development of suitable age models for rock surface dating (work conducted by Freiesleben (2021)), and the demonstration of fitting these models to data sets from controlled exposure experiments. The novelty of these experiment lies with being one of the first to thoroughly investigate the development of luminescence-depth profiles from multiple luminescence emissions (from quartz and feldspar) under tightly controlled conditions. The development of luminescence-depth profiles was observed in response to specific wavelengths, and to either broadband artificial light (halogen lamp) or daylight exposure for multiple exposure times ranging from a few hours to 2 years. The application of the models as described in Freiesleben (2021) to the data sets aims to determine which model(s) are suitable for different luminescence signals, and provide information on both the kinetics of the materials under investigation, as well as advice on modelling procedures for future applications of rock surface dating. Freiesleben (2021) applied the newly developed models to IRSL and OSL from the same samples as presented here. I entered the project with the novelty of investigating the development of IRPL luminescence depth profiles, with data acquired using the Risø Luminescence Imager. Whilst I have not participated in the development stages of the RSD age models, I apply them here to spatially resolved IRPL data. As there is increasing interest in the use of IRPL for dating applications, I hope this systematic controlled study of IRPL luminescence-depth profiles, and discussion of the fitting of age models holds high value for future researchers who wish to use IRSL or IRPL for rock surface dating applications.

Summary

Rock surface dating using optically stimulated luminescence relies on the progressive resetting of latent luminescence with depth as a function of time. In its current form, the method generally involves measuring OSL from quartz or feldspar from either abraded grains or rock slices cut perpendicular to the rock surface of interest. Luminescence intensity is plotted as a function of depth from the rock surface and the profile is fitted with models to determine the light attenuation factors and de-trapping rate. For determining an exposure age, these parameters are first established from a calibration sample with a known exposure time and then applied to luminescence depth-profiles with unknown exposure times. A recent study by Freiesleben (2021) conducted an investigation into the bleaching of $IRSL_{50}$ and pIR-IRSL signals at 225°C and 290°C in rocks as a function of time and wavelength, and fitted the luminescence-depth profiles with either a first order or general order model. We present here a second part to that study where both IRSL (at room temperature) and infrared-photoluminescence (IRPL) at 955 nm and 880 nm were spatially resolved from granite rock samples which have been bleached

under controlled conditions. Luminescence-depth profiles were reconstructed from the images, and fitted with the double-exponential model (Sohbati et al., 2011) which follows first order kinetics, as well as a general order model. The general order model accounts for higher-order kinetics, and was found by Freiesleben (2021) to better represent the IRSL data. We demonstrate the expected systematic progression of IRPL and IRSL profiles with increasing exposure time and assess the suitability of the two models for representing the measured data accurately. Our results indicate that the first order model can represent the IRPL data adequately. Our results from fitting the IRSL data do not correlate with the results from Freiesleben (2021), as estimates of kinetic order from fitting the GOM model lie close to 1.

5.1 Introduction

In the past few decades, various methods for the dating of rock surfaces have been developed. Recently the focus has turned towards optically stimulated luminescence (OSL) (Polikreti et al., 2002; Sohbati et al., 2011). In principle, OSL can be used to determine the exposure and/or the burial duration of a rock surface. Upon exposure to daylight, trapped charge is released from traps at the rock surface and bleached to increasing depths as a function of exposure time. From measuring the luminescence as a function of depth, a sigmoidal luminescence-depth profile is observed. In the case of exposure dating, the profile progresses from residual levels at the surface, followed by a transition zone up to saturated levels with increasing depth from the surface. Burial of a bleached rock surface results in the accumulation of charge. Reconstructing the full luminescence depth-profile allows one to assess the extent of bleaching prior to burial. Equivalent doses are measured from surface slices determined to have been well bleached at the time of burial (Sohbati et al., 2011; Sohbati et al., 2012c; Rades et al., 2018; Souza et al., 2019). However, obtaining accurate ages for these exposure or burial durations depends on robust fitting of suitable age models. This is limited by the low-resolution data obtained using the conventional coring and slicing sample preparation method, which can be problematic when trying to reliably fit the age models. There are also limitations of the models themselves, which make several assumptions about the kinetics (assume first order) of the mineral, and of the transmittance of multi-band light through the material.

The first mathematical description of the development of luminescence-depth profiles in rocks was by Polikreti et al. (2002), using measurements of TL from ancient marble. The model was based on quartz data, and assumes first order kinetics (i.e. simple single trap to single hole recombination, and negligible retrapping Sunta et al., 2005). The model proposed by Polikreti et al. (2002) assumes a single value represents the attenuation of all light wavelengths through a rock, and no wavelength dependence on the flux value. Sohbati et al. (2011) further developed this model for OSL RSD and used wavelength-integrated values of the incident light flux and the detrapping probability. This first order model takes the form of a nested exponential, and is given as:

$$n_1(x,t) = n_0 e^{-\overline{\sigma\varphi_0}te^{-\mu x}} \tag{5.1}$$

where n_1 describes the population of trapped charge (assumed to be proportional to the luminescence), at given depth (x, mm) and given time (t, a). n_0 is the initial trapped charge population, which is assumed to be at saturation level at the time of initial exposure. The combined parameter $\overline{\sigma\varphi_0}t$ is the effective photon flux availabe for charge detrapping, and is the product of the photon flux (φ, $cm^{-2}.a^{-1}$) and the photoionisation cross section of the trap (σ, cm^2) as well as the total exposure time (t, a). φ and σ are both assumed to be constant for

all wavelengths of the light spectra. μ (mm^{-1}) is the light attenuation coefficient, assumed to be constant for all wavelengths and the same at all depths (x, mm) in the rock. This model does not account for effects of trapping due to internal ionisation, which is usually negligible for terrestrial exposures (Sohbati et al., 2012a; Sohbati et al., 2012c). Sohbati et al. (2012a) have however, further developed the model to include this parameter for trapping, which is significant when considering OSL RSD applications in areas where the natural dose rate is high (e.g. non-terrestrial locations). Other expansions of the model have been done by Freiesleben et al. (2015) who developed the model to enable dating of multiple cycles of exposure and burial, with additional terms to account for trapping from internal and external dose rates. These basic models have also been used for estimating hard rock erosion rates (e.g. Sohbati et al., 2018; Brown et al., 2019; Lehmann et al., 2019; Smedley et al., 2021), as well as for applications in thermochronometry (e.g. Herman et al., 2010; Guralnik et al., 2015a; Guralnik et al., 2015b; King et al., 2016).

Although the current accepted model appears to be suitable for representing the response from first-order systems (e.g. quartz), there are questions surrounding the suitability of the models for representing luminescence behaviour in feldspar (Freiesleben, 2021). It is established that luminescence behaviour in feldspar does not follow first order kinetics (Bailiff et al., 1991; Thomsen et al., 2011; Jain et al., 2015). For dating applications using feldspar, infrared-stimulated luminescence (IRSL) is favoured. However, unlike in quartz the decay of the IRSL signal does not follow an exponential decay (Bailiff et al., 1991). The trapped charge population can be reduced due to a portion of the trap recombining via tunnelling (Wintle, 1977; Poolton et al., 2009; Jain et al., 2012), and retrapping instead of recombination of charge can occur following stimulation (Thomsen et al., 2008).

Recently, two stokes-shifted emissions were characterised from feldspar, originating from the principal trap in response to IR stimulation. Termed infrared-photoluminescence (IRPL), these two emission peaks have been identified at 880 nm and 955 nm (Prasad et al., 2017; Kumar et al., 2020a), and result from radiative relaxation of electrons from the excited to ground state within the trap. Thus, IRPL is not reliant upon the distribution of recombination centres, and is considered more stable than the IRSL (i.e. negligible fading) over geological time scales. Recently, Sellwood et al. (2019) and Sellwood et al. (2022) used spatially resolved measurements of IRPL to reconstruct luminescence-depth profiles from naturally exposed rock samples, and found the technique suitable for RSD applications. However, age models were not applied to these data sets. It is currently unknown as to whether the current age models (following first order kinetics) are suitable for representing the bleaching of IRPL, or whether the kinetics of IRPL follow an apparent higher order system, as is the case with IRSL. It is thus of high interest to consider appropriate age models which can be applied to IRPL data sets for rock surface dating purposes. Freiesleben (2021) found that fitting of the first order model to IRSL was not robust, and that IRSL was better represented by a general order model. This general order model (GOM) takes the form:

$$n_m(x,t) = [(r-1)\overline{\sigma\varphi_0}te^{-\mu x} + n_{m,0}^{1-r}]^{\frac{1}{1-r}} \tag{5.2}$$

Where n_m is the trap population (considered proportional to luminescence intensity), and r is the kinetic order (where $r > 1$), which reverts to the FOM when $r = 1$. This model describes how the rate of change of the trap population is proportional to the population of filled traps raised to the kinetic order, r. In both the FOM and GOM, the slope of the profile does not change with exposure time. From taking the derivative of Eq.5.1 or Eq.5.2 with respect to x, it is observed that the slope is dependent on μ (FOM) and on the the kinetic order and μ in the

case of the GOM (Freiesleben, 2021).

As demonstrated by the work presented by Freiesleben (2021), this model is able to better represent the $IRSL_{50}$ data, as any effects of tunnelling or retrapping will be accounted for by the higher order of r (values were close to 2). However, from fitting of the pIR-IRSL data measured at 225°C and 290°C, estimates of r decrease with increasing measurement temperature (with r close to 1 for the $pIRIR_{290}$ data). Regarding the application of the FOM and GOM to the data presented in this chapter, we expect to find similar results to Freiesleben (2021) when fitting the IRSL data. However, it is currently unclear as to how well IRPL data will be represented by either the first order or general order model. From previous studies into the bleachability of IRPL (e.g. Sellwood et al., 2019; Kumar et al., 2020a), the bleaching response of IRPL is considered similar to that of higher temperature pIR-IRSL signals. We then ask whether fitting the IRPL data will result in order estimates similar to those from fitting the $pIR\text{-}IRSL_{290}$ data by Freiesleben (2021) (i.e. closer to 1).

Presented here are the results of three controlled bleaching experiments in a demonstration of the progressive bleaching of both $IRPL_{880}$ and $IRPL_{955}$ as well as IRSL in granitic rock samples. We investigate the bleaching of the three signals with depth into the rocks, following: 1) bleaching by one of three monochromatic light sources (violet at 405 nm, green at 532 nm or IR at 885 nm), 2) bleaching with halogen lamps (covering the visible light spectrum) for varying durations, and 3) bleaching via daylight, also for increasingly longer exposure times. The IRPL and IRSL was imaged using the Risø Luminescence Imager (Sellwood et al., 2021, see chapter 2). The resulting luminescence-depth profiles were fitted with both the first order model and then the general order model. We discuss the suitability of each model for each data set, and assess and compare the output parameters from the models. As the data here was produced under controlled conditions (all exposure times are known), we also take this opportunity to investigate the suitability of the single-sample calibration method as first proposed by Sohbati et al. (2012c), for providing parameter estimates which can be applied to an age model fitted to unknown age profiles (in dating applications, the exposure age of this second profile is unknown). We demonstrate how the exposure time of the calibration profile influences the modelled age estimate of the unknown-age profile. The results presented here are the first to show the progressive bleaching of IRPL with depth into rocks as a function of time, as well as investigate the suitability of the current age models for dating using IRPL imaging. Our conclusions will be able to guide future rock surface dating applications by providing advice as to which age model is suitable for which data set, and important considerations over the use of calibration samples for obtaining estimates of model parameters.

5.2 Methodology

5.2.1 Samples

Each experiment used cores of the same sample material. The samples are classified as an aplite, formed from the later stages of crystallisation from a felsic melt. They contain approximately 50% feldspar and 40% quartz, with the remainder comprising of minor biotite and hornblende (see appendix for a μ-XRF map of the main feldspar constituents). The distribution of the mineral components are relatively homogeneous with a saccharoidal texture. The samples were collected from China, but the exact location is unknown. Here, we refer to the samples as granite or granitic as they host all major constituents found in regular granite. The samples were collected as 10 × 8 cm cores (see Figure 5.1). The samples were first heated to 700°C for

24 hours to anneal all OSL signals and sensitise the quartz (see Freiesleben, 2021, for further details), before receiving a saturation dose of 7 kGy at the cobolt-60 irradiation facilities at Risø. The sides of the cores were then wrapped in black light-proof plastic with rubber rings around the top to minimise light leakages on the sides of the cores.

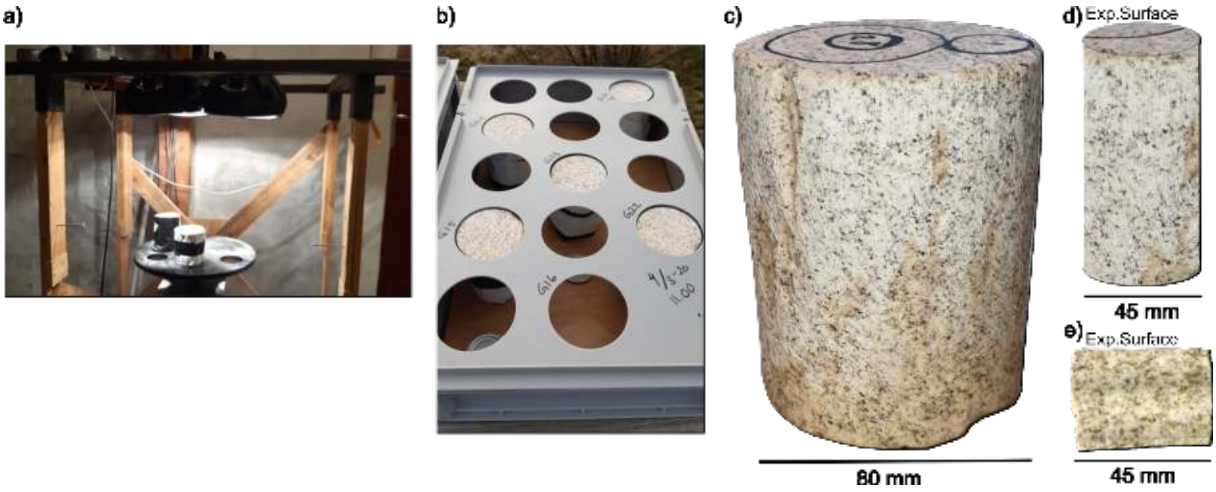

Figure 5.1: a) Photograph of the set-up used in the halogen lamp bleaching experiments. b) Sample set-up for cores bleached by daylight. c) Photograph of one of the large 10 × 8 cm cores used in the experiments here. d) Photograph of a typical 45 mm Ø core drilled from the centre of the larger core. The top of the core is the exposed surface (labelled as Exp.Surface). e) Image of a slice used for IRSL and IRPL imaging after cutting the core shown in d) with a diamond wire saw. The top of the slice is the exposed surface.

5.2.2 Bleaching experiments

Three types of bleaching experiments were conducted in this study:

1. **Bleaching with monochromatic light:**
   This experiment aimed to explore the development of luminescence-depth profiles using monochromatic light, whilst constraining the photon flux (φ). One core was bleached by a 405 nm laser (200 mW power laser). The second core was bleached by a 532 nm laser (10 mW solid-state laser diode) and the third bleached by an 885 nm, 500 mW diode laser. Exposure times were set to 4 days, 3.6 days and 0.5 days for the 405 nm, 532 nm and 885 nm lasers respectively (see Table 5.1). These exposure durations were chosen to ensure each sample received the same number of photons per unit area (φt): 1.3×10^{22} cm^{-2}. Thus, it is only the parameters μ and σ which should vary between the profiles.

2. **Bleaching under halogen lamps:**
   Six cores were wrapped in light-tight wrapping, with their top surfaces exposed and placed on a rotating platform, ~70 cm below 4 halogen lamps (see Figure 5.1a). The bulbs (H7 24 V/70 W) had a bandwidth spanning 400-1100 nm, and produced a power density of 102 mW cm^{-2} at the surface of cores. The spectrum of the lamps is given in the appendix. The cores were bleached for time periods between 1-366 days (see Table 5.1).

3. **Bleaching by natural daylight:**
   Seven of the cores were placed outside, on an elevated platform located away from objects which could cause shading and to ensure maximum exposure to natural daylight. The cores were wrapped in light-tight black plastic, with only the tops exposed (see Figure 5.1b), for the varying duration's as given in Table 5.1.

Solar radiance data was obtained from a solar spectrometer located at Risø campus by the Department of Photonics engineering (Riedel-Lyngskær et al., 2021a). Data was collected at 5 minute intervals, and covered the same time periods as the bleaching periods for the cores placed outside. This data was used to monitor seasonal variations in radiance intensity and to enable discussion of variation in bleaching depths obtained from cores bleached at different times during a year.

Specific Wavelength		Halogen lamps		Daylight		
Wavelength	t (days)	Sample ID	t (days)	Sample ID	t (days)	Period (MM,YYYY)
Violet, 405 nm	4	G20	1	G16	1	03,2020
Green, 532 nm	3.6	G35	2	G15	2	03,2020
IR, 885 nm	0.5	G11	14	G33	21	03,2020
-	-	G11B	21	G10	31	11-12,2019
-	-	G35B	118	G21	118	03-06,2020
-	-	G13	366	G02	566	04,2018 - 11,2019
-	-	-	-	G01	730	04,2018 - 04,2020

Table 5.1: Sample IDs and respective exposure durations for cores exposed to either specific wavelengths, the halogen lamps or daylight. The month and year for each of the daylight exposure periods are also stated.

5.2.3 Measurements and analysis

Once the cores had been bleached for the desired duration, smaller cores (either 2 cm or 4.5 cm in diameter, see Figure 5.1d) were drilled perpendicular to the exposed surface. Care was made to take cores from the centre of the large cores to minimise any potential influence from light leakages at the edges of the samples during bleaching. From each of the smaller cores, 1.3-1.6 mm thick flat rectangular sections were cut perpendicular to the exposed surfaces of the cores (Figure 5.1e) to produce a planar surface for imaging of the whole luminescence profile. The rest of the core was used for reader experiments conducted by Trine Freiesleben (see Freiesleben, 2021). This latter work is not discussed here.

The $IRPL_{880}$, $IRPL_{955}$, and IRSL was spatially resolved using the Risø Luminescence Imager (as described in Chapter 2) and following the measurement sequence outlined in Table 5.2. For each sample, the IRPL measurement was integrated over 1-3 s (depending on the relative intensity of the sample). IRSL was measured as a time-series, over 20 frames each with 10 s integration. This captured the whole IRSL decay curve. A 2 kGy normalisation dose was administered in the high-dose rate gamma facilities at the DTU Risø campus. Bleaching was done in a Hölne solar simulator over 24 hours.

All data processing was conducted in MATLAB, using the Image Processing toolbox (Mathworks, 2017). For each sample, all images were registered onto one another to enable pixel-wise analysis. The background images after bleaching were subtracted from the natural and regenerated IRPL images. The final frame (frame 20) from the IRSL decay curves were used as IRSL background, and subtracted from the first frames (frame 1) of the time lapse measurement. The background-subtracted L_n/L_x ratios were taken. Profiles were constructed by taking the mean and standard error of each pixel column from the surface to deeper depths across the slab images. The profile data was normalised to the saturation level.

All profiles were fitted with the FOM (Eq.5.1) and the GOM (Eq.5.2). All profiles from each respective signal data set was fitted globally. This was considered appropriate especially

for the GOM, where it was desirable to obtain a shared estimate of r, which should be the same for each profile in each respective data set. The modelled profiles were plotted with their respective 95% confidence bands. For values of thermal transfer, a value of 0 was used for the IRSL, 0.03 for the $IRPL_{955}$ and 0.05 for the $IRPL_{880}$. These values were taken from spatially-resolved measurements of a sample in saturation from before and after bleaching and preheat. Comparisons were made between profile shapes and bleaching depths (defined as the depth at which 50% of the saturation level is found; SD50% Sohbati et al., 2011) between the signals and between the respective profiles. The reduced chi-squared parameter (χ^2_ν) was used to assess the goodness of fit of the FOM and GOM to the data sets. For this, the average χ^2_ν value was calculated over all profiles in the signals' data set. The estimates of μ and $\overline{\sigma\varphi_0}t$ were compared between the different exposure experiments as a function of bleaching time or wavelength (in the case of the monochromatic bleaching).

Step	Measurement	Result
1	Optical Image	Image for registration
2	$IRPL_{880}$	L_{n880}
3	$IRPL_{955}$	L_{n955}
4	IRSL	L_n
5	$IRPL_{880}$	L_{n880} after IRSL
6	$IRPL_{955}$	L_{n955} after IRSL
7	2 kGy Regeneration dose	L_x
8	Repeat steps 1-6	
9	Bleach in sol sim	BG

Table 5.2: Measurement sequence for imaging IRPL and IRSL from all sections.

5.3 Results of bleaching experiments

The results from the three bleaching experiments are discussed separately below.

5.3.1 Monochromatic bleaching

Figure 5.2 presents the IRSL (left-hand column), $IRPL_{955}$ (middle) and $IRPL_{880}$ (right-hand column) L_n/L_x ratio maps for the three samples bleached in this experiment. The bleached surfaces are located at the left-hand side of each map, and the colour bars represent L_n/L_x pixel values. Panels a-c present the ratio maps from the samples bleached by the 405 nm laser. The IRSL (Figure 5.2a) has been completely zeroed at the surface (dark blue pixels). The bleached regions for the $IRPL_{880}$ and $IRPL_{955}$ are similar, although with slightly smaller bleaching depths than for IRSL. The ratio maps after bleaching with the 532 nm laser are shown in panels d-f. A clear bleached IRSL region is observable at the surface (Figure 5.2d), but this is not clearly observed in the $IRPL_{880}$ or $IRPL_{955}$ ratio maps. Figure 5.2g shows the extent of IRSL bleaching from exposure to the 885 nm laser. The IRSL has been bleached to deeper depths compared to the other IRSL ratio maps. A narrow region at the surface of the $IRPL_{955}$ ratio map hosts pixel values within the range of 0.2-0.7, indicating some bleaching may have occurred here. No clear bleached region is observed in the $IRPL_{880}$ L_n/L_x map (Figure 5.2i). Thus, only violet stimulation resulted in a close to complete resetting of the two IRPL signals at the surface.

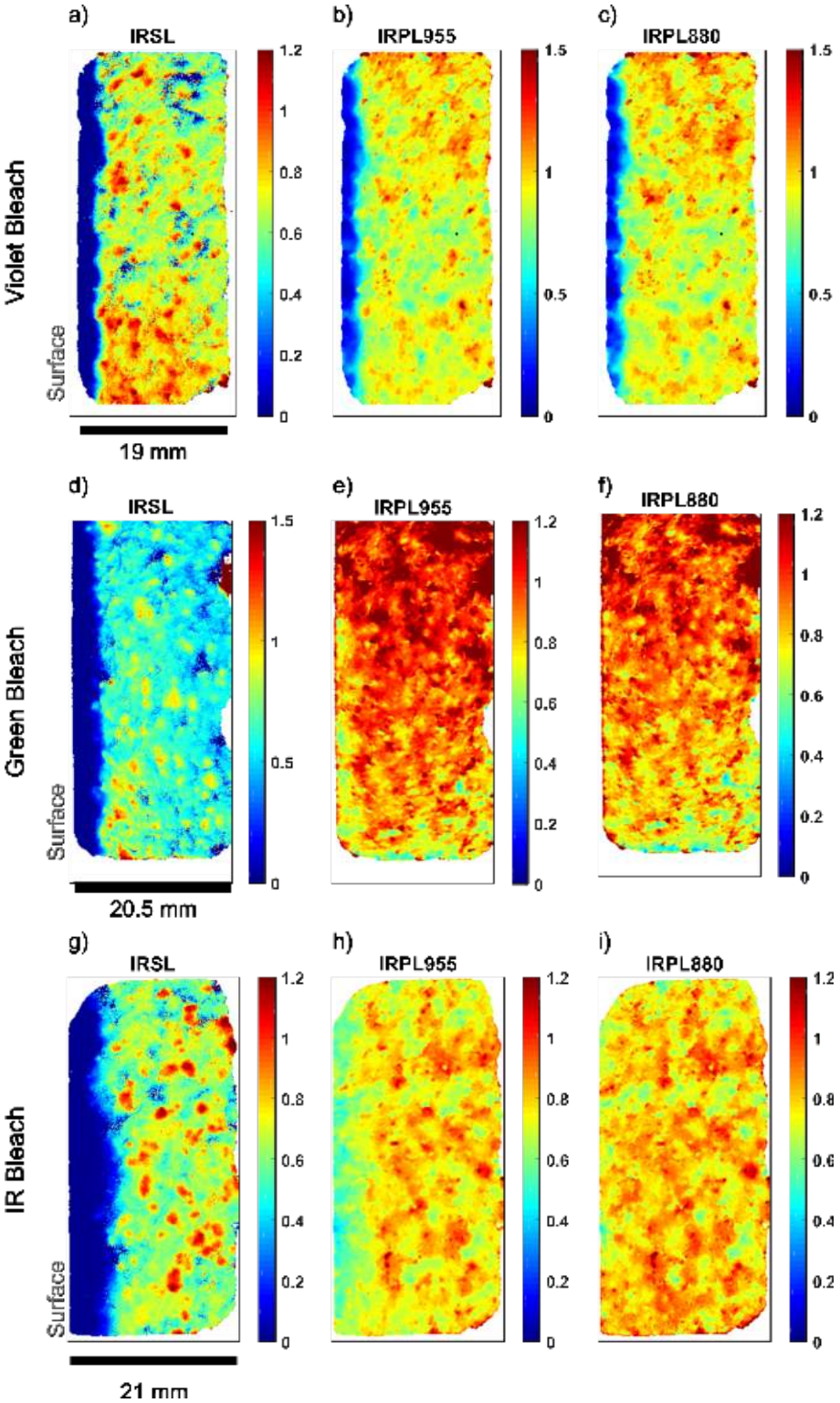

Figure 5.2: IRSL (left column), $IRPL_{955}$ (middle) and $IRPL_{880}$ (right column) L_n/L_x ratio maps after bleaching the samples with specific wavelengths. Results from bleaching with the 405 nm light for 4 days are shown in panels a-c, d-f show the 532 nm bleaching results after bleaching for 3.6 days, and panels g-i show the data from bleaching for 0.5 days with the 885 nm laser.

The luminescence-depth profiles reconstructed from these ratio maps are shown in Figure 5.3. Panels a-c show the profiles fitted with the first order model (solid lines) for the IRSL, $IRPL_{955}$ and $IRPL_{880}$ profiles, respectively. 95% confidence bands for the fitting are also shown.

The data fitted with the GOM (solid lines) are in panels d-f. The differences in bleachability between the three emissions is instantly clear, with the IRSL bleached to the deepest depths from the surface (Figure 5.3a), and the least bleaching occurring in the $IRPL_{880}$ (Figure 5.3c). The IRSL is bleached most efficiently by the 885 nm laser (red profile in panels a and d), with the least influence from the violet laser (blue profile). This is also found in the $IRSL_{50}$ data presented by Freiesleben (2021).

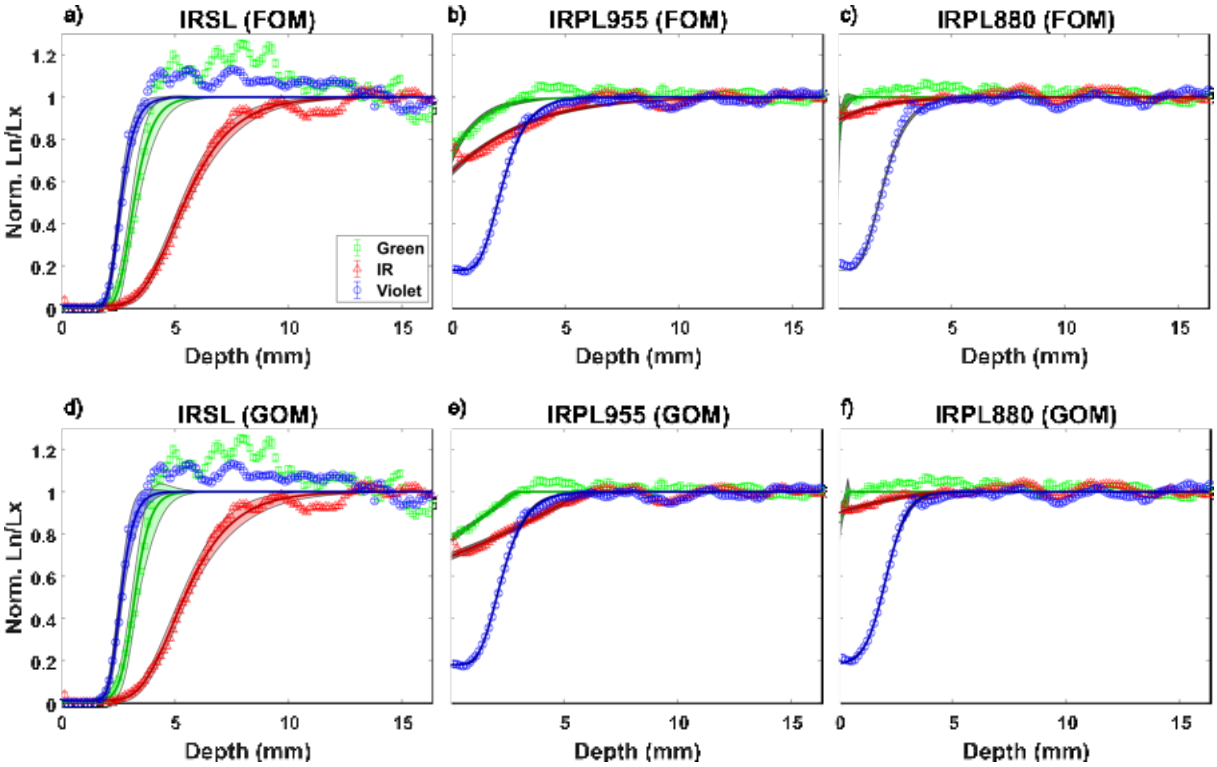

Figure 5.3: IRSL and IRPL profiles resulting from bleaching with monochromatic light (Green: 532 nm for 3.6 d; IR:885 nm for 0.5 d; Violet: 405 nm for 4 days) and fitted with either the FOM (top row) or GOM (bottom row). The profile colours serve to represent the respective bleaching wavelength. Note that the different exposure times for the different stimulation sources were chosen such that the sample surface received the same number of photons per unit area.

The opposite is seen in the IRPL data. Both the $IRPL_{955}$ (panels b and e) and $IRPL_{880}$ (panels c and f) emissions are bleached most efficiently by the violet wavelength, with least influence on the degree of bleaching from the green laser. The almost completely saturated $IRPL_{880}$ profiles following the green and IR bleaching make SD50% estimation difficult, but any values presented below are estimates from the same analysis stages used for the other data sets.

From a simple visual inspection, both the FOM and GOM seem to fit the data sets well, except for the saturated regions of the IRSL profiles. The L_n/L_x ratios of the saturated regions of the IRSL profiles are very noisy. This noise is attributed to slight variation in the L_n IRSL intensity compared to the L_x intensity, which is attributed to unstable charge not being removed from the IRSL trap following the 2 kGy test dose via a preheat stage. Any unstable charge which was acquired when the initial 7 kGy was given likely faded during the storage times of the samples. For the IRSL data, there is very little visual difference between the shapes of the FOM and GOM fits. The same can be said for the $IRPL_{880}$ data, but differences in the shapes of the fitted profiles are seen in the $IRPL_{955}$ data. Qualitatively, we observe a better fit with the FOM for the $IRPL_{955}$ profile after bleaching with the green laser.

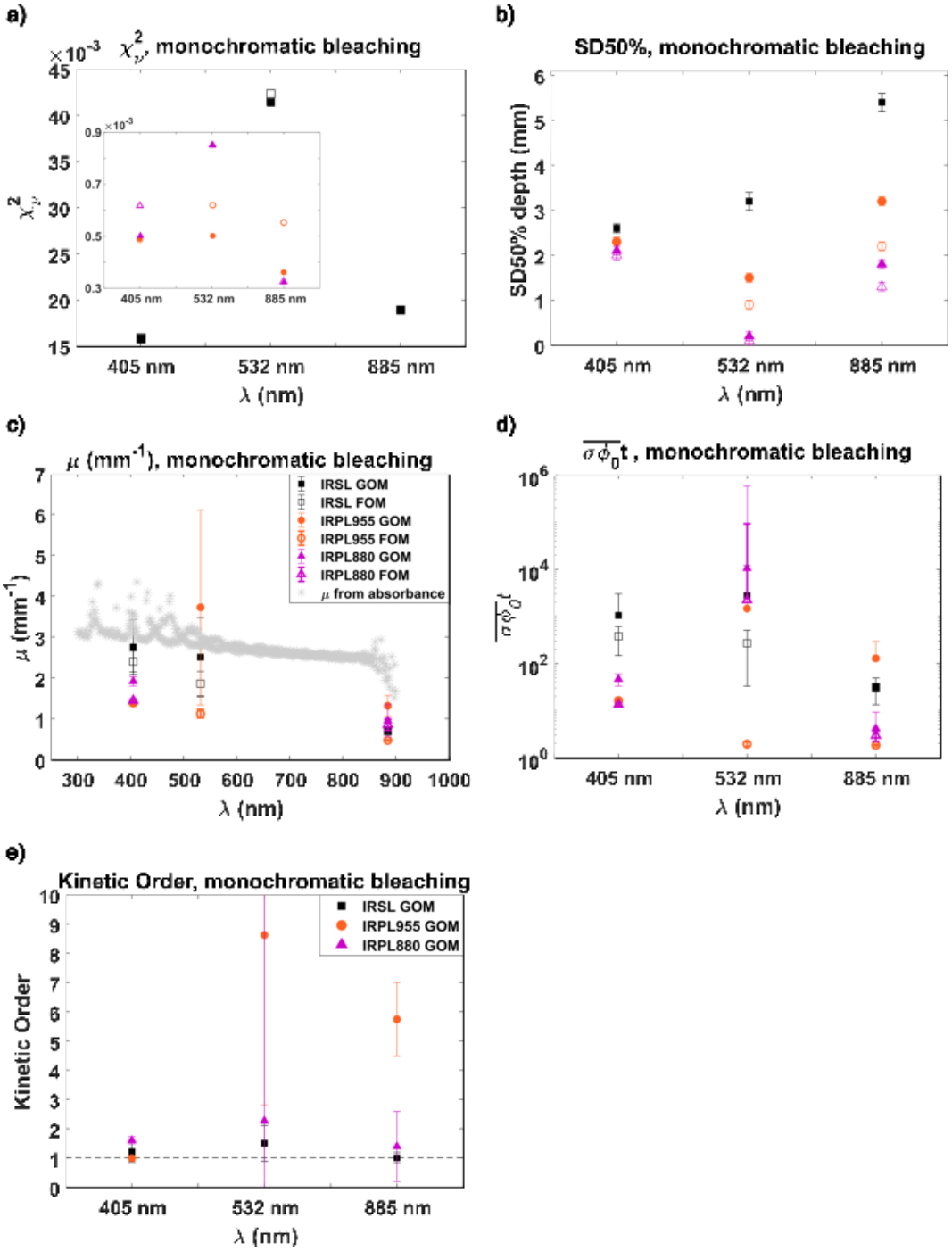

Figure 5.4: Comparison of FOM and GOM fit results from the monochromatic bleaching experiment to the data presented in Figure 5.3. Legend is given in panel c). For all plots, the open symbols represent data from the FOM, and solid points are data from the GOM. a) Reduced χ^2_ν values. b) SD50% depths from fitting of the luminescence-depth profiles. c) Values of μ (mm-1) obtained from fitting of the data with the two models, as a function of bleaching wavelength. The grey stars show the values of μ calculated from absorbance measurements conducted on a 1.43 mm thick granitic slice (same composition as the samples investigated here. See chapter 2 appendix for discussion on attenuation of light through granite). d) Modelled values of $\overline{\sigma\varphi_0}t$ from the FOM and GOM for each profile. e) The resultant kinetic order from fitting the GOM to the individual profiles.

The reduced χ^2_ν values from the profile fitting are shown in Figure 5.4a, where the insert shows the significantly smaller χ^2_ν values obtained from fitting the IRPL data. It is considered

that the larger values of χ^2_ν from fitting the IRSL data are due to the scatter seen in the saturated regions of the profiles, although there is little difference in the χ^2_ν values from the FOM or the GOM. This is also reflected in the larger confidence bands shown in Figures 5.3a and d. The IRPL data was well constrained by both the FOM (hollow points) and GOM (solid points). From closer inspection of the SD50% depths from each profile with each fit (Figure 5.3b; error bars on the data points are taken from the confidence bands around the fit), there is no difference in the resulting SD50% from the FOM and the GOM for the IRSL profiles (black squares, data points are overlapping). A slight difference in SD50% is seen for the two models for the $IRPL_{880}$ data, with bleaching depths estimates slightly lower from fitting of the FOM. The same can be said for the $IRPL_{955}$ data.

Figures 5.3c and 5.3d display the obtained model parameters from the FOM and GOM. The obtained estimates of μ (mm^{-1}) (Figure 5.3c) are variable for each emission with each bleaching wavelength. Note that the values of μ from fitting the green-bleached $IRPL_{880}$ profiles with the GOM and FOM were 32.2 and 28.5 mm^{-1} respectively, and are not shown on this plot. The estimates of μ follow the general negative trend in attenuation coefficient with increasing wavelength as seen from the values of μ calculated from the absorbance measurements (light grey stars in Figure 5.3c). However, our estimates of μ from the modelling exercise underestimate those calculated from the absorbance measurements. Generally, higher estimates of μ are obtained from the GOM, compared to the FOM.

Figure 5.3d presents the model values of $\overline{\sigma\varphi_0}t$ plotted as a function of bleaching wavelength. As is often found with this parameter (see for example Sohbati et al., 2012a; Lehmann et al., 2018; Souza et al., 2019), the estimates are highly variable, with the largest values observed from fitting the profiles bleached by the green laser. However, with the very little bleaching of the IRPL by the 532 nm laser, the reliability of this data fitting is low as also indicated by the uncertainties. The values determined for the kinetic order r using the GOM are shown in Figure 5.6e. For the IRSL, these lie close to 1. This is also the case for the $IRPL_{880}$ from the violet bleaching, but there is a large uncertainty on the estimates of r for bleaching with green or IR wavelengths. The order obtained from fitting the $IRPL_{955}$ data varies significantly, with very high estimates of the kinetic order.

Summary of results of the monochromatic bleaching experiment

Following the interpretation of the aforementioned data from the monochromatic bleaching experiment, we can summarise the main results into the following points:

1. The IRSL is more easily bleached than either of the IRPL signals. The $IRPL_{955}$ is more easily bleached relative to the $IRPL_{880}$. This is consistents with the results of Kumar et al. (2020a) and Sellwood et al. (2022).

2. The IRSL is bleached most efficiently by the IR light, followed by the green and violet light, whereas both the IRPL signals have a greater bleaching response to violet light, but very little bleaching as a result of green light stimulation. This is consistent with the IRSL results of Freiesleben (2021), as well as the results of Kumar et al. (2020a) who demonstrated how IRPL is most efficiently bleached by longer (UV) wavelengths.

3. The model estimates of μ decrease with increasing bleaching wavelength. The estimates from the IRSL data are generally higher than those for the IRPL data (either signal), with greatest absorption of the 405 nm wavelength compared to the 532 nm and 885 nm. The estimates from the FOM fitting are generally slightly lower than those from the GOM. All

model estimates (except the $IRPL_{955}$ GOM) are lower than the μ values calculated from absorbance measurements.

4. The kinetic order estimates resulting from fitting the GOM to the profiles are close to 1 for the IRSL and $IRPL_{880}$ data (from fitting the violet-bleached profile). For the $IRPL_{955}$ data the order is significantly larger that unity.

5.3.2 Bleaching with halogen lamps

Presented in this section are the results of measuring IRSL and IRPL from the samples bleached by the halogen lamps. The L_n/L_x ratio maps calculated after imaging the IRSL and IRPL are shown in Figure 5.5. These ratio images show an increasingly larger bleached region at the surfaces of the rocks (left hand side of each ratio map) as a function of exposure time for all signals. The IRSL bleaching front (dark blue pixels) progresses at a significantly higher rate than that of the either IRPL signals. Figure 5.6 presents the luminescence-depth profiles reconstructed from the ratio images presented in Figure 5.5. Whilst all data sets were fitted with the FOM, the GOM was only able to be fitted to the IRSL and $IRPL_{880}$ data. The GOM would not converge to the $IRPL_{955}$ data and so the raw profile data is presented in Figure 5.6e. When fitting the GOM to the $IRPL_{880}$ data, the model was very sensitive to the initial estimates of the model parameters. However, from the reduced χ^2_ν values (Figure 5.7a) from model fitting, there is no significant difference between the fitting of the FOM or GOM to the data sets.

As expected, the bleaching fronts of the profiles progress to deeper depths with increasing exposure times (blue to red coloured profiles) for all signals. The higher bleachability of the IRSL (Figure 5.6a) compared to either IRPL signal (Figures 5.6b and c) is easily observable, with the surface regions of the IRSL profiles showing complete zeroing of the IRSL, even after only 1 day of exposure. After 1 day exposure, the residual for the $IRPL_{955}$ is ~20%, and ~23% for the $IRPL_{880}$. Figure 5.7b summarises the increasing SD50% depths as a function of exposure time (note the log scale on the x-axis). All uncertainties of the SD50% depths (i.e. the confidence bands around the modelled profile) were between <0.6 mm. Whilst the IRSL is bleached to a further depth from the surface compared to the IRPL, the rate of bleaching of the three signals is similar. We also see how the bleaching depth for the $IRPL_{955}$ is greater than for the $IRPL_{880}$.

Qualitatively, there is a notable difference in the profile slopes between the IRSL and IRPL profiles (Figure 5.6), with an apparently greater change in μ with increasing exposure time for the $IRPL_{955}$ data compared to the IRSL. Figure 5.7b plots the values of μ obtained from fitting the FOM and GOM to each of the profiles. A slight decreasing trend in μ with increasing exposure time is observed in all data sets, following the observations of changing profile slope with exposure time in Figure 5.6. The attenuation coefficients from fitting the IRSL data were relatively larger compared to the IRPL, with mean IRSL μ values of 1.13 ± 0.13 mm^{-1} for the GOM, and 1.05 ± 0.12 mm^{-1} for the FOM. There is little difference between the μ values from the FOM (average of 0.88 ± 0.19 mm^{-1}) and GOM (average of 0.87 ± 0.19 mm^{-1}) from fitting of the $IRPL_{880}$ data, but there is a ~25% decrease in μ from the 1 day to the 366 day exposure (although this relation does not appear to be linear). The values of μ from fitting the $IRPL_{955}$ data lie in between those from the IRSL and $IRPL_{880}$, with a mean of 0.63 ± 0.10 mm^{-1} from the FOM.

Figure 5.7c presents the estimated $\overline{\sigma\varphi_0}t$ values from each profile for each measured signal. The IRPL results are shown in the insert. The IRSL parameter estimates are orders of magnitudes larger than those from the IRPL. The $\overline{\sigma\varphi}_0 t$ estimates increase with increasing exposure time for all signals, and show increasingly larger uncertainties. The uncertainties of the esti-

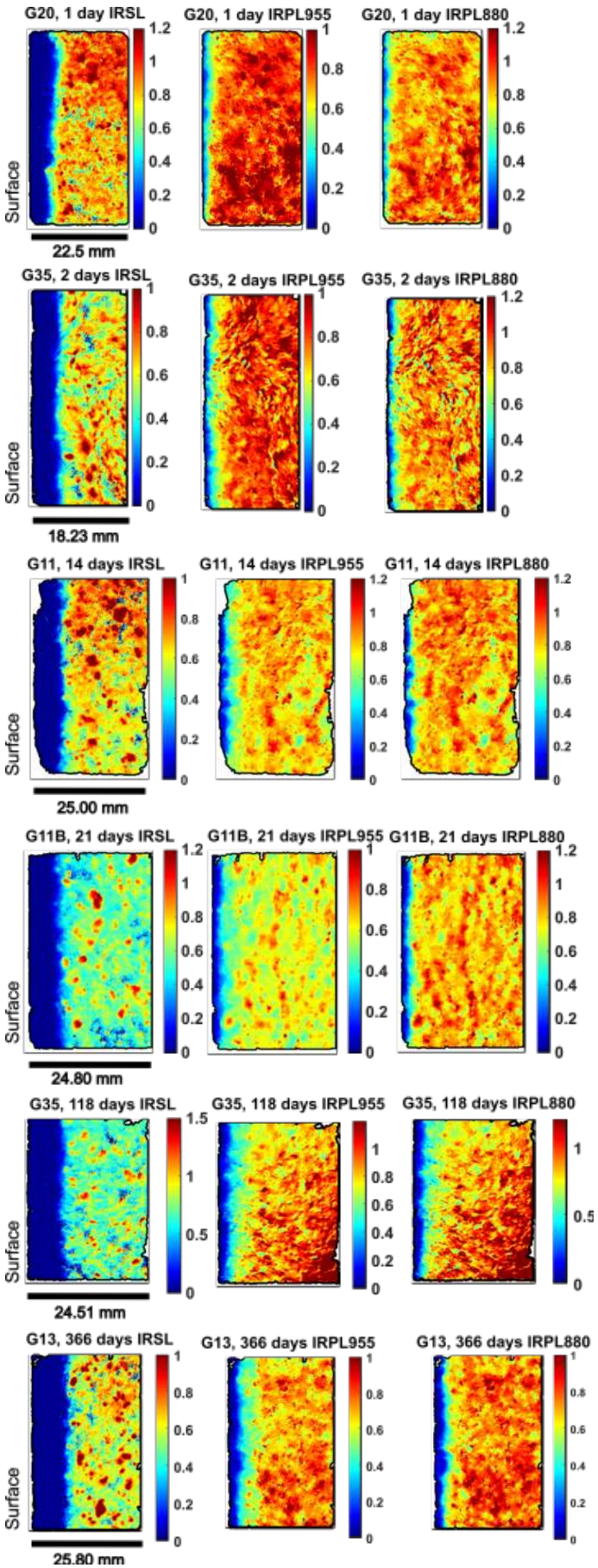

Figure 5.5: IRSL (left column), $IRPL_{955}$ (middle) and $IRPL_{880}$ (right column) L_n/L_x ratio maps for all samples used for the halogen lamp bleaching experiments. Each row holds the data for a single sample. A scale bar for each sample slice is provided beneath the IRSL ratio maps. Note, the images have not been scaled relative to each other

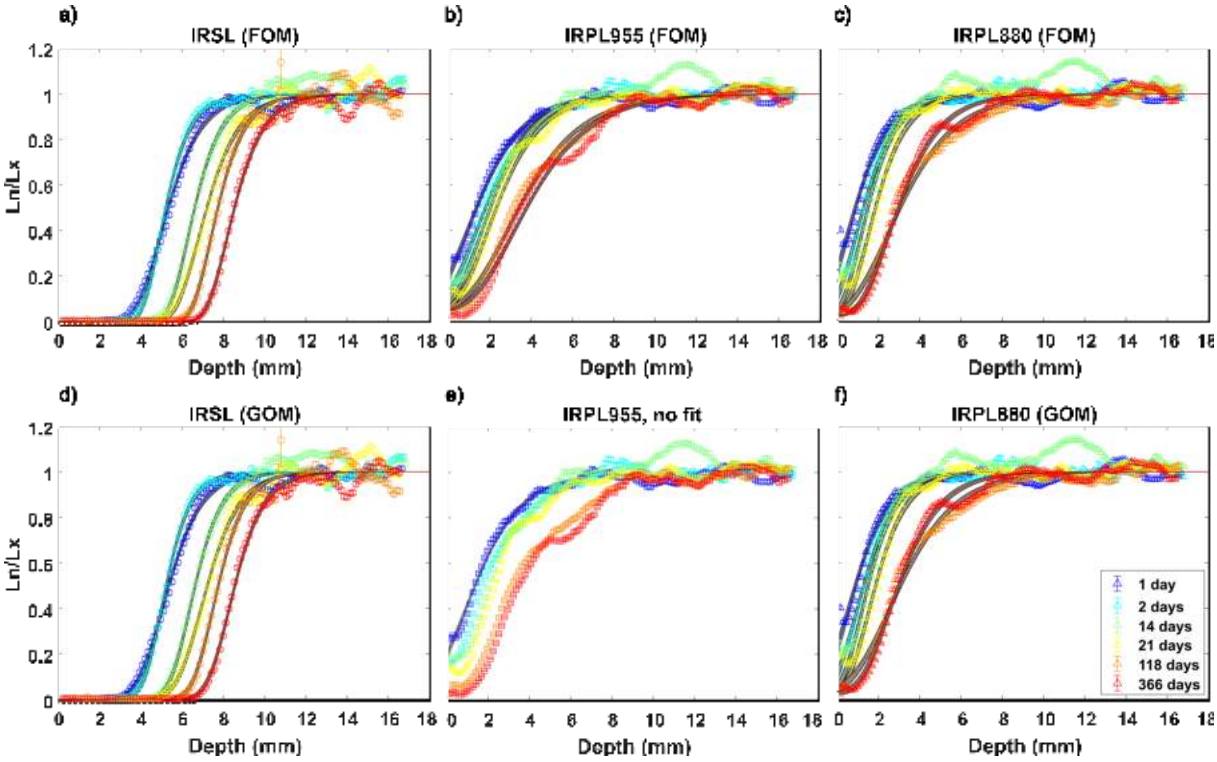

Figure 5.6: IRSL and IRPL profiles (normalised to saturation) reconstructed from the ratio maps in Figure 5.6, after bleaching using the halogen lamps. a) IRSL profiles fitted with the FOM. b) $IRPL_{955}$ profiles fitted with the FOM. c) $IRPL_{880}$ profiles fitted with the FOM. Panels d and f show the IRSL and $IRPL_{880}$ profiles fitted with the GOM, respectively. Note that it was not possible to fit the $IRPL_{955}$ profiles using GOM, and thus the data in panel e is the raw profile data.

mates from the IRSL data are larger than for the IRPL, likely due to the higher level of scatter in the saturated regions of the profiles. The kinetic orders from fitting the GOM to the IRSL and $IRPL_{880}$ data were 1.19 ± 0.06 and 1.06 ± 0.08, respectively. This is similar to the results obtained from fitting the IRSL and IRPL data in section 5.3.1.

Summary of results of the halogen lamp bleaching experiment

The results of the halogen lamp bleaching experiment can be summarised as follows:

1. The IRSL and IRPL bleaching fronts progress further from the rock surface with increasing exposure time. The IRSL is bleached to deeper depths than the $IRPL_{955}$, which is bleached to deeper depths than the $IRPL_{880}$.

2. A 1 day exposure is sufficient to completely zero IRSL from the first ~3 mm of the surface. For the IRPL data, the residual is close to ~20% of the saturated level.

3. The GOM could not be fitted to the $IRPL_{955}$ data. This, coupled with the observation that the estimates of r from fitting GOM to the $IRPL_{880}$ data in this section, and from fitting both IRPL data sets in section 5.3.1 are all close to 1, suggests that first order kinetic model (i.e. Eq.5.1) may be adequate for representing the bleaching of IRPL.

4. A decreasing trend in μ estimates with increasing exposure time is observed in all data sets.

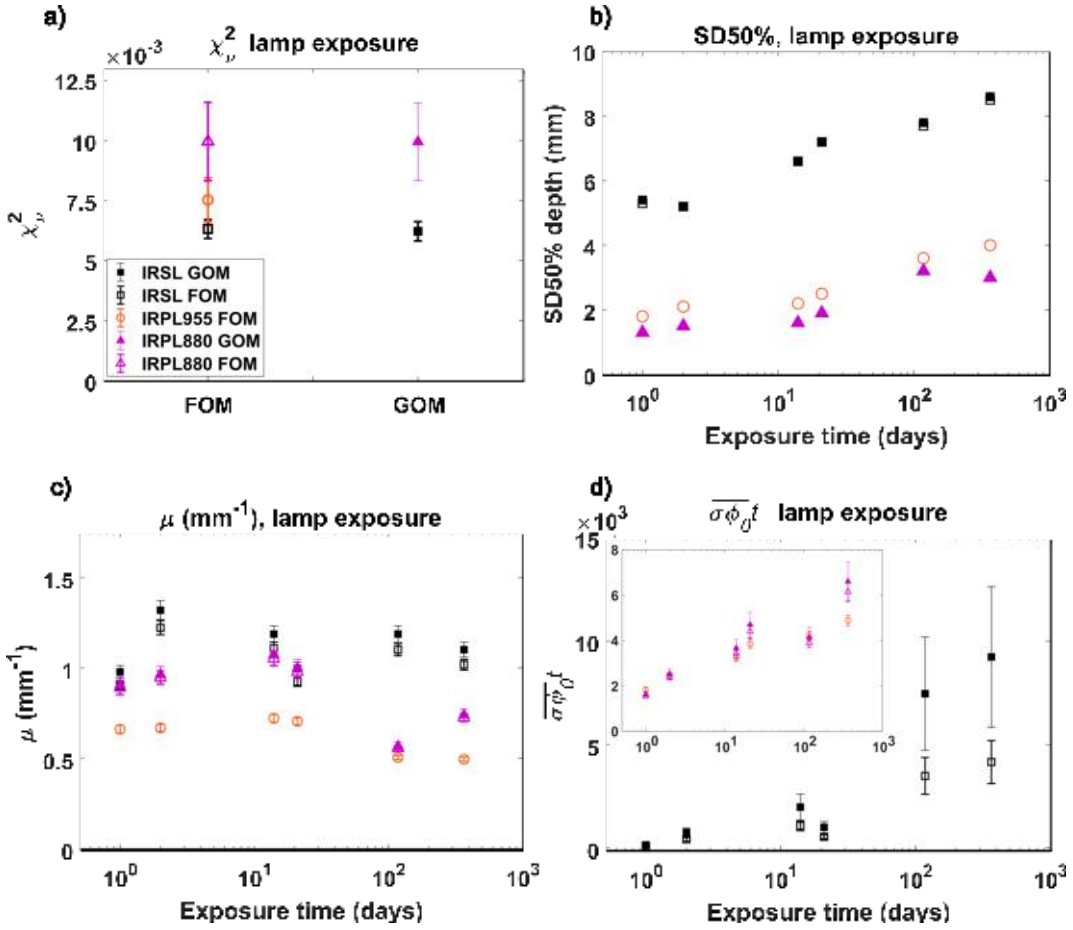

Figure 5.7: Summary of the FOM and GOM fit results from the halogen lamp bleaching experiments from the data presented in Figure 5.6. Legend is given in a). For all plots, the open symbols represent data from the FOM, and solid points are data from the GOM. a) Reduced χ^2_ν values from model fitting. b) SD50% values from the IRSL (black squares), $IRPL_{955}$ (orange circles) and $IRPL_{880}$ (pink triangles) plotted against exposure time (log scale). c) Values of μ (mm^{-1}) obtained from fitting the luminescence-depth profiles. d) values of $\overline{\sigma\varphi_0}t$ obtained from model fitting for the IRSL, with the IRPL results shown in the insert.

5. Estimates of $\overline{\sigma\varphi_0}t$ are highly variable between the IRPL and IRSL data sets, but all estimates show an increase with increasing exposure time.

5.3.3 Natural daylight bleaching

Presented in this section are the results from the natural daylight exposures. Figure 5.8 presents all the L_n/L_x ratio maps for the measured samples. The left-hand column shows the IRSL data, with the $IRPL_{955}$ data in the middle, and the $IRPL_{880}$ in the right-hand column. The data from all three signals show an increasingly larger bleached region at the surface with increasing exposure time (from top to bottom of the figure. Note that the depth scale is not the same for all samples.). The shapes of the bleaching fronts, however, are not completely regular, with local fluctuations in bleaching depth (light blue - green coloured pixels). This is attributed to the presence of non-luminescing minerals, locally restricting the bleaching extent. Again, the differences in bleachability between the three emissions are clear, with the slowest progression of the bleaching front with time seen in the $IRPL_{880}$ data, and the fastest seen in the IRSL data. The luminescence-depth profiles taken from these ratio maps are presented in Figure 5.9.

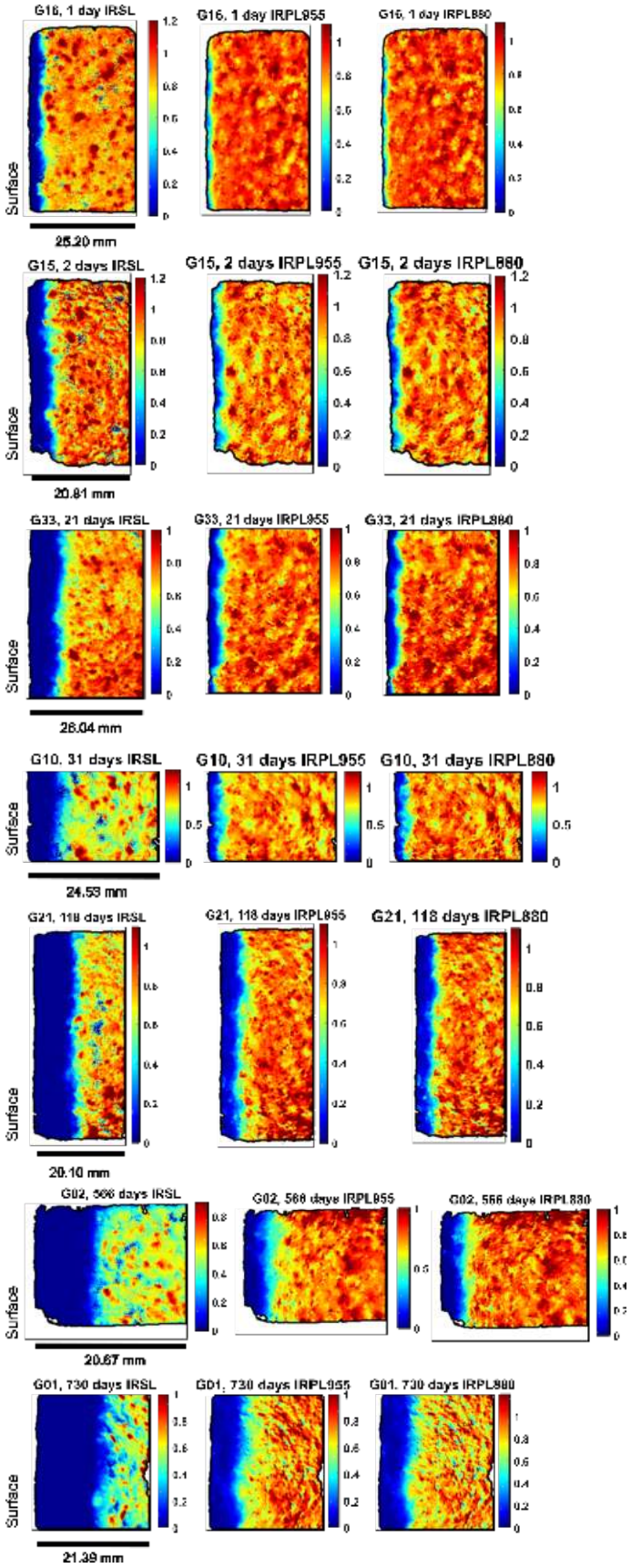

Figure 5.8: L_n/L_x ratio maps from imaging of the samples which were bleached outside by natural daylight. The left-hand column shows the IRSL data, the middle column shows the $IRPL_{955}$, and the $IRPL_{880}$ is on the right-hand side. Each row presents the IRSL and IRPL data for a single sample with increasing exposure time from top to bottom in the figure.

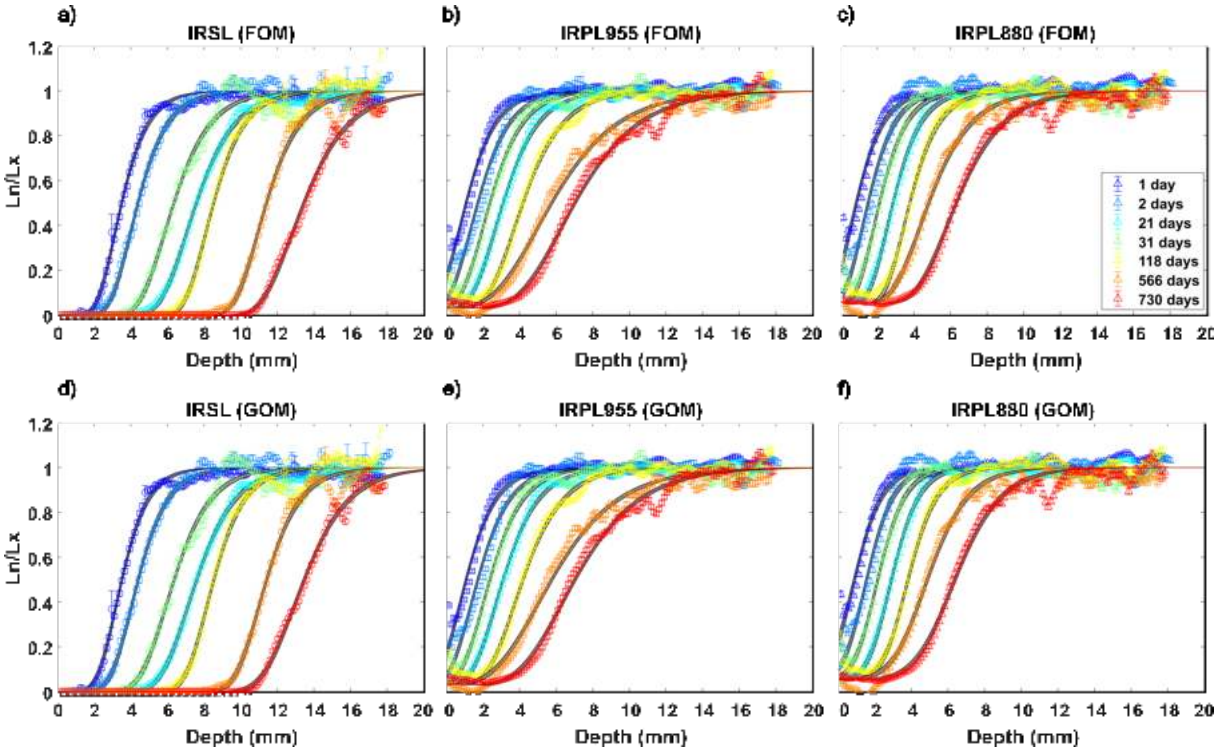

Figure 5.9: IRSL and IRPL profiles after bleaching by natural daylight, fitted with either the FOM (top row) or GOM (bottom row).

The first column shows the IRSL profiles fitted with the FOM and GOM, respectively (i.e. Figure 5.9a and Figure 5.9d). Again, a 1 day exposure was sufficient to completely zero the IRSL up to ~2 mm from the surface (dark blue profile). The IRPL profiles in Figures 5.9b (955 nm), and 5.9c (880 nm) show how a single day exposure is sufficient to reduce the IRPL at the very surface to about 26% of the saturation level. However, this residual is in fact still observed in the profiles for the 730 day long exposures (red profiles), although it is reduced down to ~7%. Contrary to the halogen lamp bleaching data, both the FOM and GOM was able to be fitted to all data sets here. Qualitatively, the FOM and GOM both fit the data well. The χ^2_ν values shown in Figure 5.10a indicate that both models perform similarly when representing the real data, with the largest standard deviations in χ^2_ν values from fitting the IRSL data. This is again likely due to larger scatter in the saturated regions of the profile influencing the fitting. The average values for the kinetic order obtained from the GOM fittings are 1.10 ± 0.06, 1.01 ± 0.05, and 1.42 ± 0.08 for IRSL, $IRPL_{955}$ and $IRPL_{880}$, respectively. Thus, the order determined for IRSL and $IRPL_{955}$ is consistent with unity (within 2 standard deviations). However, the results from Freiesleben (2021) found r estimates closer to 2 from fitting the GOM to the IRSL data, which is in contrast to the results presented in this study, which suggest that the FOM is suitable for both the IRSL and IRPL data sets.

Figure 5.10b plots the SD50% depths from all profiles resulting from the natural bleaching. All uncertainties of the SD50% depths (from the confidence intervals of the fits) were between <0.5 mm. Again, the bleaching fronts of the three signals progress to deeper depths with time, at similar rates (i.e. the slopes of the profiles for the different signals are similar to each other for similar exposure times). One important thing to notice is that the 21 day exposure appears to result in a larger SD50% than the 31 day exposure (see also the green and turquoise profiles in Figure 5.9). However, this apparent inversion is caused by the exposures taking place at different times of the year (see Table 5.1). The 21 day exposure (G33) was made during July (with e.g. IRSL SD50% of 7.6 mm) whereas the 31 day exposure (G10) was made in November

(IRSL SD50% of 6.4 mm). The solar radiance data obtained from the solar spectrometer showed that the sample exposed for 31 days in November did in fact receive fewer photons than the sample exposed for 21 days in July (see Freiesleben, 2021, and the appendix to this chapter which presents the total photon flux per wavelength for the various exposure durations). All profiles in Figure 5.9 show a progressive decrease in profile slope with increasing exposure time. Qualitatively, this seems most prominent in the $IRPL_{955}$ data. The estimates of μ are plotted in Figure 5.10c as a function of exposure time (note the log scale). The change in slope of the IRSL profiles with increasing exposure time is less pronounced than that seen in the $IRPL_{955}$ data (orange circles in Figure 5.10c). Estimates of μ for the $IRPL_{955}$ decrease by ~60% from the 1 day exposure profile to the 730 day exposure profile. For the IRSL data, the estimates of μ decrease by up ~42% from the 1 day to 730 day exposures. The change in μ estimate is similar in the progressively deeper $IRPL_{880}$ profiles (pink triangles) to the $IRPL_{955}$, where we also observe slightly lower μ estimates from the FOM compared to the GOM. Note the relatively larger estimate of μ for the 31 day exposure compared to that from the 21 day exposure in all signals. This is again a result of the seasonal differences in solar irradiance which the samples received.

Plotted in Figure 5.10d are the estimated values of $\overline{\sigma\varphi_0}t$. Similar as to what was observed in the halogen lamp bleaching data, the magnitude of this parameter generally increases with increasing exposure time, for all signals. Again, the estimates from fitting the IRSL data (from either the FOM or GOM) are an order of magnitude larger than those from fitting the IRPL data. Comparing the $\overline{\sigma\varphi_0}t$ estimates from fitting the IRPL data, the $IRPL_{880}$ estimates (pink triangles in inset figure) are almost four times that of the $IRPL_{955}$ when the longest exposure profiles are fitted. Considering the 21 and 31 day exposures again, there is a slight decrease in the estimated $\overline{\sigma\varphi_0}t$ values from the 21 to 31 day profiles, contradicting the overall positive trend between $\overline{\sigma\varphi_0}t$ estimate and exposure time.

Summary of results from the daylight exposure experiment

The results from reconstructing luminescence-depth profiles from daylight bleached rock samples and fitting with both the FOM and GOM can be summarised into the following points:

1. Again, the depths of the IRSL bleaching fronts progresses further than the IRPL, for the same bleaching duration. The $IRPL_{880}$ has the slowest bleaching rate.

2. We see a clear influence of seasonal solar irradiance on the development of the IRSL and IRPL luminescence-depth profiles, with the 21 day exposure in July bleaching the luminescence to greater depths from the surface than the 31 day exposure conducted in November. Effects of this different photon flux is also reflected in the estimated values of μ and $\overline{\sigma\varphi_0}t$.

3. Estimates of μ and $\overline{\sigma\varphi_0}t$ are generally lower from fitting the FOM, compared to the GOM, even though both models present a similar goodness of fit.

4. The estimates of the kinetic orders from fitting the GOM to the IRSL and IRPL data sets are all very close to 1 (within 2 standard deviations), with the largest estimate for the $IRPL_{880}$ data.

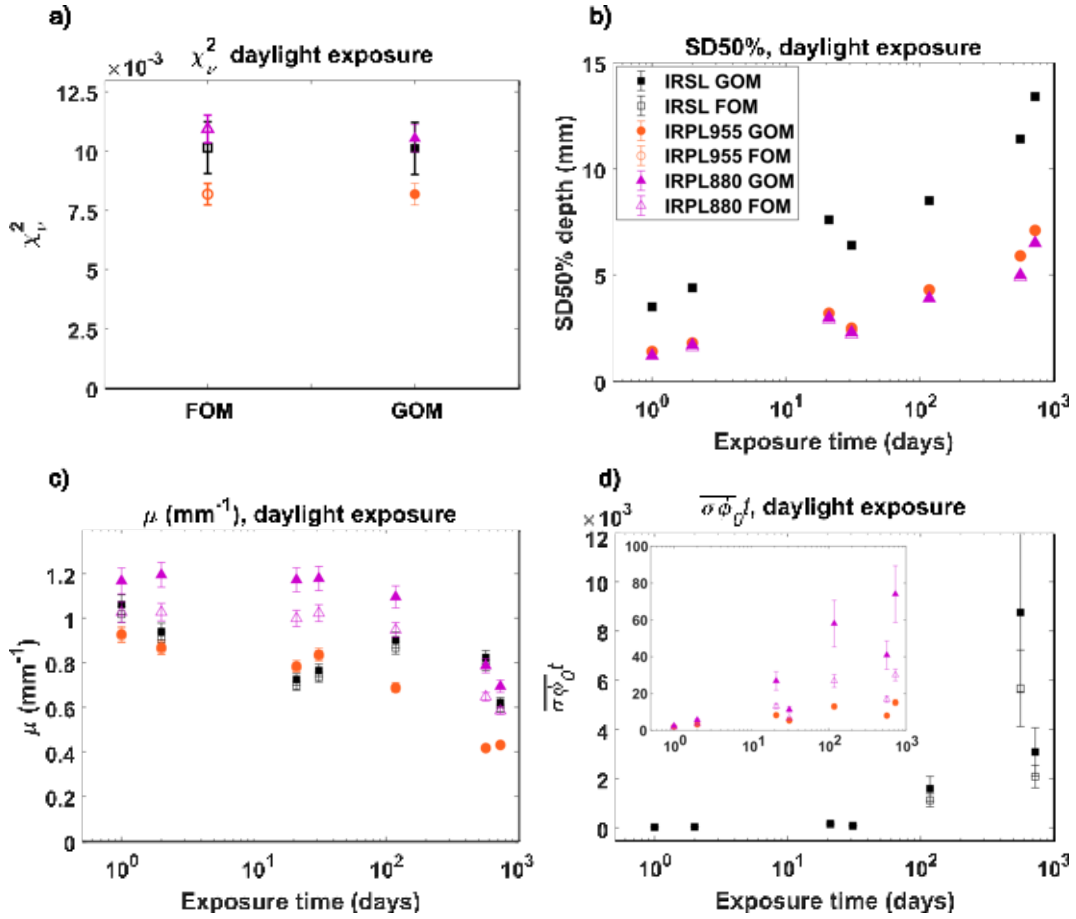

Figure 5.10: a) Reduced χ^2_ν values from fitting the age models to the profiles resulting from natural daylight bleaching. b) SD50% estimates from the profiles as a function of time. c) Estimates of μ (mm^{-1}) from fitting the FOM and GOM. d) Estimates of $\overline{\sigma\varphi_0}t$ from fitting the FOM and GOM.

5.3.4 Using 'known-age' calibration samples for determining the exposure age of 'unknown-age' samples

Following fitting of the data, an investigation into using the single-sample calibration method for obtaining rock surface exposure ages was conducted. The single-sample calibration method was demonstrated by Sohbati et al. (2012c). In this approach, the luminescence-depth profile with a known exposure is reconstructed from a rock of similar lithology to the rock with unknwon exposure age. The resulting luminescence-depth profile is fitted using an age model to obtain estimates of μ and $\sigma\varphi$. The determined values of these parameters are then used in the age model applied to the profile of unknown age. This section investigates whether the relative age of the calibration profiles compared to the unknown age profile has an effect on the final modelled age. This analysis involved using the obtained values of μ and $\sigma\varphi$ from each profile, and using these as calibration parameters to fit the remaining profiles in that respective data set. The resulting ages ($t_{apparent}$) from these newly fitted profiles can then be compared with their known ages (t_{known}). If there is no dependency on the exposure time of the calibration profile used for providing μ and $\sigma\varphi$ estimates (i.e. the model fits are robust and represent the luminescence behaviour), the slope of the correlation between the two will be 0 (see Freiesleben, 2021, for further details).

Figure 5.11 presents the results of using the μ and $\sigma\varphi$ values from each profile to fit and model

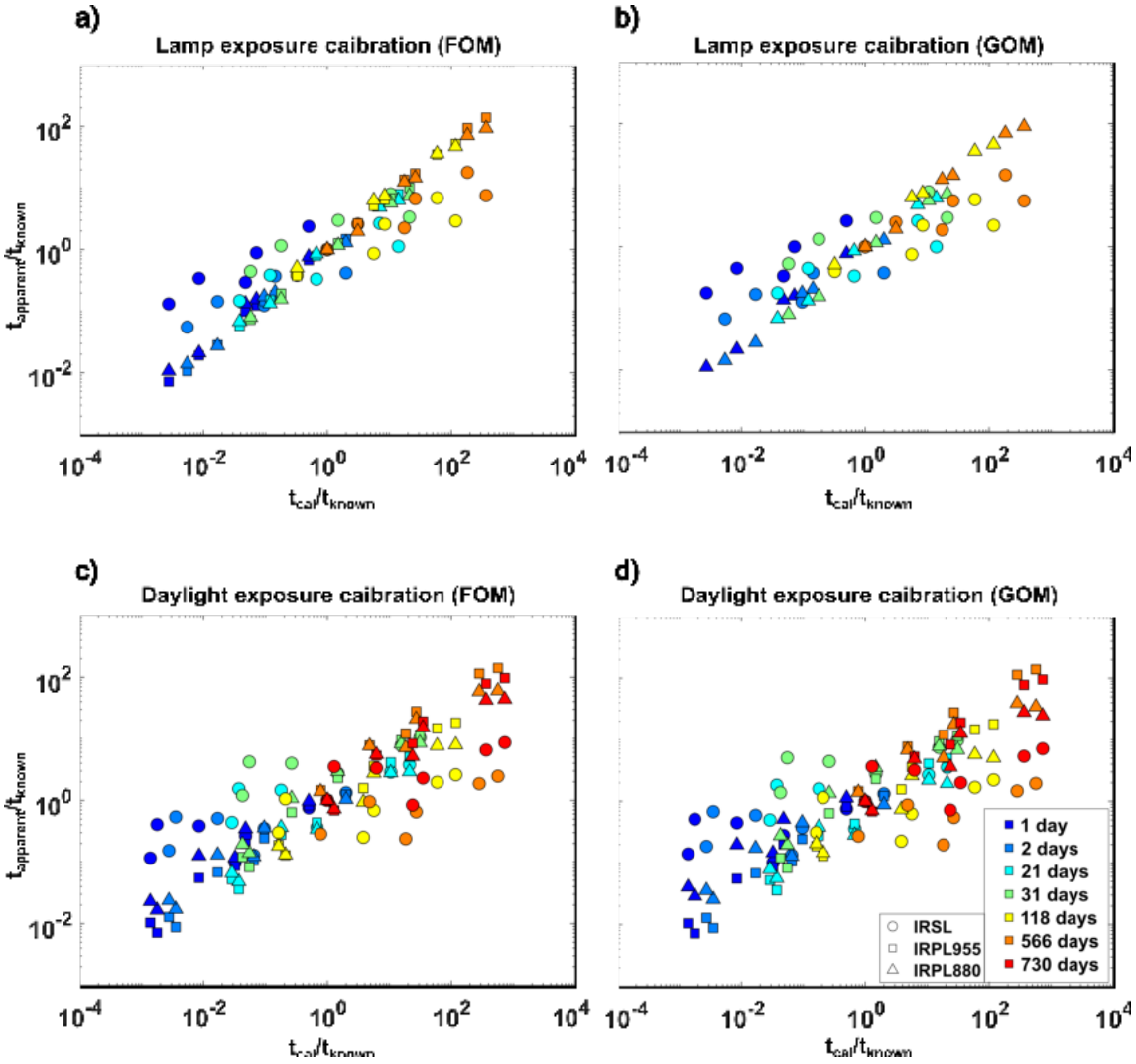

Figure 5.11: Correlation of apparent exposure time ($t_{apparent}$) divided by known exposure time (t_{known}) as a function of the ratio of the calibration exposure time (t_{cal}) and the known exposure time (t_{known}). Circles represent the IRSL data, squares represent the $IRPL_{955}$ data and triangles show the $IRPL_{880}$ data. The colour scheme follows that used for the luminescence-depth profiles, with colour progressing from dark blue to red with increasing exposure duration. a) Results for the halogen lamp bleaching experiment when fitting with the FOM. b) For the halogen lamp bleaching experiment fitted with the GOM. c) Results from the natural bleaching data fitted with the FOM. d) For the natural bleaching data fitted with the GOM.

the exposure ages of the other luminescence-depth profiles in the respective data set. The data is plotted according to ($t_{apparent}/t_{known}$) vs. (t_{cal}/t_{known}), where t_{cal} is the exposure duration of the profile being used for model calibration. What is clear in all four plots is that there is a strong dependency between the exposure age of the calibration sample, and the resulting age of the 'unknown-age' profile. The data in Figures 5.11a and b show the calibration results from using the the halogen lamp bleaching experiments fitted with the FOM and GOM respectively. The data shows very similar positive trends in both the IRSL (circles) and both IRPL data sets (suqares and triangles for 955 nm and 880 nm data, respectively). The IRSL data is more dispersed in both panels a and b. Estimating the slope of the IRSL data sets provides slopes of 0.41 for the FOM fitted data (Figure 5.11a), and 0.41 for the GOM fitted data (Figure 5.11b). Slopes of all the IRPL data points are larger, and were estimated at 0.82 and 0.79 for the FOM and GOM fitted data, respectively. Thus, the resulting unknown profile age is more sensitive to the initial calibration age when fitting the IRPL data compared to the IRSL data. The data from the daylight bleaching experiment are shown in panels c and d. Similar results are seen

here as for the halogen lamp data, with a greater dispersion in the IRSL data. Estimated slopes for the IRSL data are 0.35 and 0.33 for the FOM and GOM fitted data respectively, and 0.71 and 0.64 for the FOM and GOM fitted IRPL data, respectively.

All data sets in Figure 5.11 indicate that using estimates of μ and $\sigma\varphi$ from fitting a calibration profile which has an exposure age significantly younger than that of the unknown-age profile will result in an underestimation of the actual exposure age of the rock surface. For example, if the calibration sample is ~10% of the 'unknown-age' then the estimated age will be only ~5-10% of the 'true' exposure age (t_{known}). The same problem occurs with using parameter estimates from a calibration profile with a significantly longer exposure duration than that of the profile which you are trying to date. In fact, only if the exposure duration of the calibration sample is very similar to the exposure duration of the the 'unknown-age' sample will an accurate estimate of the exposure age be obtained. A similar conclusion was also reached by Freiesleben (2021), which is not a very encouraging observation for the application of these models to accurately date the exposure duration of a rocks surface exposure.

5.4 Discussion

The data presented in this chapter is a novel demonstration of a controlled experiment by which the progressive bleaching of IRSL and IRPL is observed as a function of bleaching wavelength and time. The expected progression of the SD50% depth is observed with increasing exposure time, with the greatest bleaching efficiency seen in the IRSL data, followed by the $IRPL_{955}$, and finally the $IRPL_{880}$ (lowest bleachability). The progressive bleaching is clearly observed in both the L_n/L_x ratio maps from imaging with the Risø Luminescence Imager, and the derived luminescence-depth profiles.

From bleaching the granitic samples with monochromatic wavelengths, all wavelengths are effective at bleaching the IRSL, with IR being the most efficient. If we consider previously published values of the photoionisation cross-section σ for IRSL from loose grains of feldspar (Spooner, 1994), we would expect that violet wavelengths would be most effective at bleaching the IRSL. However, for consolidated rocks, we also need to consider the light attenuation of various wavelengths. As shown in Figure 5.3c shorter wavelengths are attenuated more rapidly than longer wavelengths, i.e. the value of μ is ~50% larger for violet than for IR. The σ at green wavelengths is lowest relative to those from the IR or violet (Spooner, 1994), yet the profile after green bleaching is deeper than the violet, likely from a lower attenuation of the green wavelengths through the rock.

Interestingly, the response of the IRPL is the opposite, with the highest-energy wavelength (violet, 405 nm) bleaching the IRPL signals the most efficiently. This result follows the work by Kumar et al. (2020a), who also demonstrate the differences in bleachability between the $IRPL_{955}$ and the $IRPL_{880}$ (slowest bleaching) in response to different wavelengths (UV was the most efficeint at bleaching IRPL) and is similar to the observation made by Freiesleben (2021) for higher temperature (290°C) pIRIR signals. The decrease in apparent μ estimates with increasing wavelength from fitting the FOM and GOM to both the IRSL and IRPL data sets are as expected, following the knowledge that higher-energy wavelengths are attenuated more rapidly than lower-energy wavelengths (Ou et al., 2018). The deviation of the μ values estimated from modelling from those obtained from absorbance measurements (grey stars in Figure 5.4c) could be due to 1) poor model constraints (especially when fitting the IRPL profiles from the green and violet bleaching), and/or 2) a need to account for scatter and reflectance when measuring absorbance (e.g. Freiesleben, 2021, and see chapter 2 appendix).

Considering the fact that the φt parameter was the same for all samples in the monochromatic-bleaching experiment, it is surprising that there is such variation in the model estimates of $\overline{\sigma\varphi_0}t$. However, observing such high variability in the estimates of this parameter has also been reported elsewhere (e.g. Sohbati et al., 2011; Sohbati et al., 2012b; Gliganic et al., 2018; Lehmann et al., 2018; Sohbati et al., 2018). The larger uncertainties on the $\overline{\sigma\varphi_0}t$ estimates of the IRSL data seen in all experiments is likely due to the higher scatter in the data points in the saturated regions oft the profiles.

The results of the halogen-lamp and daylight bleaching experiments demonstrate clearly the response of IRSL and IRPL to multi-band wavelengths with increasing exposure time. From both data sets, and with all three signals measured, we observe a change in profile slope with exposure time. This is a function of decreasing μ with increasing exposure time, as a result of the preferential attenuation of shorter wavelengths with depth into the rock. The significant difference in the magnitude of the $\overline{\sigma\varphi_0}t$ estimates between the IRSL and IRPL data for a single exposure time (e.g. all data from the 1 day daylight exposure) likely represents the individual values of σ for the IRSL and IRPL trapping centres, considering that the photon flux is the same per individual sample of specific exposure time. It would be beneficial for future work to calculate the individual values of σ from the model estimates. As we have access to the solar irradiance data covering the same time periods as the exposures of our daylight-experiment samples it would be possible to calculate the total flux received by each sample, and to be able to compare this to values of σ for the principal trap in feldspar. However, currently this data is only available for quartz or $IRSL_{50}$ (see Spooner, 1994).

From fitting the GOM to the IRSL and IRPL data sets, it was highly surprising that the estimates of the kinetic order were all close to 1; discounting fitting the GOM to the $IRPL_{955}$ data after bleaching with the green and IR lasers (see Figure 5.4e) which resulted in high order estimates, presumably from poor parameterisation. These estimates were especially surprising for the IRSL data, as Freiesleben (2021) for the same samples determined a kinetic order close to 2 when fitting with the GOM. The differences between these estimated model parameters presented here and those in (Freiesleben, 2021) are difficult to explain. It could be considered that the fitting of the models performs differently on the higher resolution data presented here, but that should not influence the output of the kinetic order estimate, which results from the fundamental luminescence behaviour. However, for the IRPL data, with the estimates of kinetic order close to 1, and the fact that the $IRPL_{955}$ data from the halogen lamp experiment could not be fitted, it is difficult to argue for the application of the GOM to IRPL data. We can also consider that IRPL is more similar to the higher temperature pIRIR signals and in Freiesleben (2021) the order estimates from fitting the pIR-$IRSL_{290}$ data with the GOM were also close to 1. We can conclude from the results presented in this study that the first order model is adequate for representing the bleaching of IRPL in rocks.

The differences in the SD50% depths from the 21 day and 31 day natural exposures indicates how seasonal effects of total solar irradiance significantly influence the bleaching of the IRSL and IRPL. This observation poses as a warning to applications where a controlled calibration sample is being used to provide model estimates for a sample of unknown exposure age. If the calibration duration is short (e.g. only over a season), the total photon flux will have a stronger influence on the relative position of the profile and thus on the model parameter estimates. A demonstration of using the estimated model parameters from the 21 and 31 day exposures for modelling luminescence-depth profiles of different times is provided in the appendix. The results from the calibration exercise in section 5.3.4 highlight the importance of finding an appropriate calibration sample, ideally with an exposure time similar to that of the unknown profile, although, we are aware that the requirement of finding a calibration sample with a known exposure similar to the unknown sample is somewhat paradoxical and is a limiting factor on the

applications which can be conducted.

5.5 Conclusions and future outlook

Presented here is a novel investigation of the development of luminescence-depth profiles in granitic rocks in response to either monochromatic light, multi-band halogen lamps or natural daylight. Using the Risø Luminescence Imager, spatially resolved measurements of IRSL and IRPL were made to view the extent of surface bleaching in response to different light exposures, and from which, luminescence-depth profiles were reconstructed. From bleaching the granitic rocks with monochromatic light (IR, violet or green), we demonstrate how the higher absorption of shorter (violet) wavelengths leads to a shallower luminescence-depth profile, compared to that produced via IR bleaching, for the IRSL. The opposite is seen for the IRPL. Bleaching with halogen lamps or by natural daylight progressively pushes the bleaching front further from the surface, as a function of increasing exposure time (fastest bleaching for the IRSL, followed by the $IRPL_{955}$, and finally the $IRPL_{880}$). From fitting the luminescence-depth profiles with the general order model, it was found that the estimates for kinetic order for the IRPL data sets were close to 1, suggesting that the IRPL data can be adequately represented by the first order model. Contrary to the results found in Freiesleben (2021), fitting of the GOM to the IRSL data presented here resulted in estimates of the kinetic order also being close to 1. This is surprising as it is known that feldspar IRSL follows higher order kinetics. It is currently not known as to why there is a difference in the fitting of the data. Also briefly discussed here is the suitability of the single-sample calibration method, by which a profile of known exposure age is fitted, and the model parameters used to fit the profile of an unknown exposure. It is shown how the relative exposure age of your known profile to the unknown profile influences the final age estimate of the profile you are trying to date. Whilst the results presented here indicate that IRPL luminescence-depth profiles can be appropriately represented by first order kinetics, further investigation into understanding feldspar kinetics in general is suggested, especially if we wish to continue improving the reliability of age models for rock surface dating using luminescence from feldspar.

5.6 Acknowledgements

I wish to thank Søren Vig Dalsgaard for helping Trine and I with the set-up of the bleaching experiments, and Henrik Olesen for his invaluable help with sample preparation. I thank Torben Esmann Mølhol, Mark Bailey and Arne Miller for providing access to the radiation facilities at Risø.

5.7 Appendix

5.7.1 A1. μ-XRF map of samples

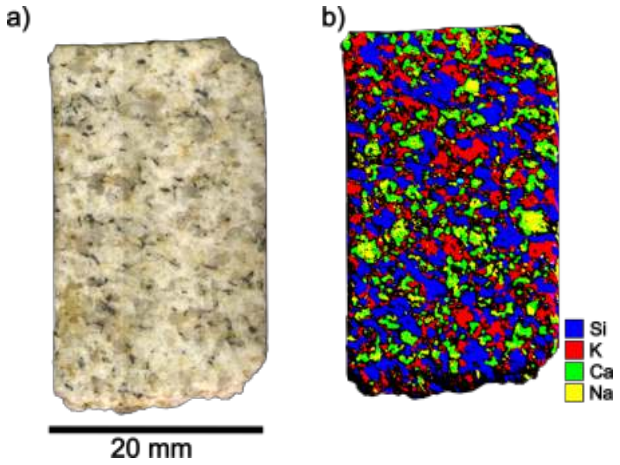

Figure 5.12: a) Image of a granitic slice and, b) the corresponding μ-XRF map showing the main feldspar constituents, K, Na, Ca and Si. This figure was edited from that shown in Freiesleben (2021).

5.7.2 A2. Halogen lamp spectrum

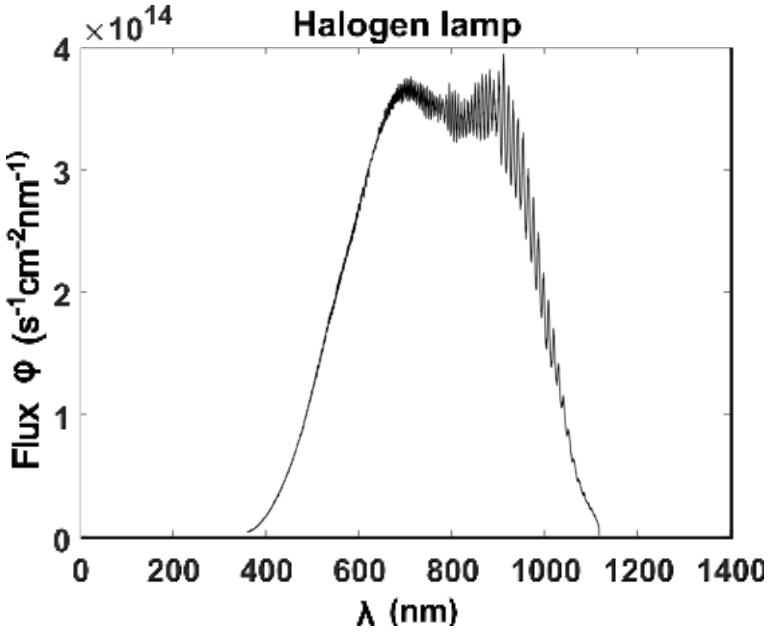

Figure 5.13: Spectrum of the halogen lamps used for the controlled bleaching experiment. The spectrum was measured using an Ocean Optics QE6500 CCD calibrated spectrometer.

5.7.3 A3. A note on the 21 and 31 day daylight exposure data

Presented in the appendix is a small investigation in to the 21 day and 31 day natural exposure data. The bleaching depths of the two profiles are a clear results of the seasonal differences of solar irradiance between winter and summer. Spectral data from a spectrometer placed at the Risø campus DTU was collected (Riedel-Lyngskær et al., 2021b), covering the exposure periods for these two samples, at 5 minute resolution. The total photon flux ($s^{-1}m^{-2}nm^{-1}$) was calculated over these two separate periods, and the results are shown in Figure 5.14. There is a huge difference in photon flux received in July (red line) compared to November (black line). This serves to explain why the bleaching front of the 21 day exposure lies at a deeper depth than the 31 day exposure, and can explain why a slight decrease in the estimate of $\overline{\sigma\varphi_0}t$ is seen from the 21 day to the 31 day exposure.

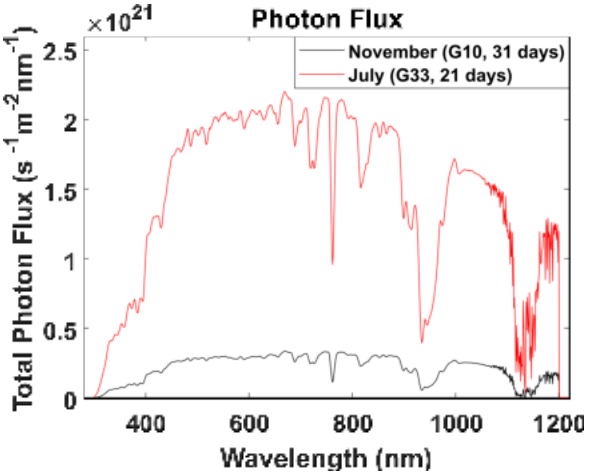

Figure 5.14: Total photon flux over the 21 day exposure of G33 and 31 day exposure of G10.

Considering the short exposure duration's of these two profiles, one may be tempted to bleach a sample as a calibration profile for a known time period in a controlled environment. However, as mentioned above, the seasonal disparity of solar irradiance would likely pose as a problem when trying to obtain reliable model estimates. From taking the estimates of μ and $\sigma\varphi$ from the 21 and 31 day profiles, fitted with the FOM, profiles with exposure ages of 1 day, 118 and 730 days were modelled. Figure 5.15a shows the resulting profiles, where the solid lines represent the profiles from using the parameters from the 21 day exposure, and the dashed lines are from using the model estimates from the 31 day exposure. There is a clear discrepancy between the profiles, with using the parameters from the 31 day exposure resulting in shallower bleaching depths of the profiles.

Figures 5.15b and c plot the SD50% depths from the modelled profiles in panel a, against the SD50% depths from the naturally bleached profiles of the same exposure time for the IRSL and IRPL respectively. The SD50% depths centre around the 1:1 line. When using the model estimates from the 21 day exposure, it is slightly more probably that the profiles' SD50% will be slightly deeper than that when using the 31 day profile parameters. As a concluding note, it is suggested that a controlled calibration profile be produced after a whole year of bleaching, to represent an average of the yearly solar irradiance.

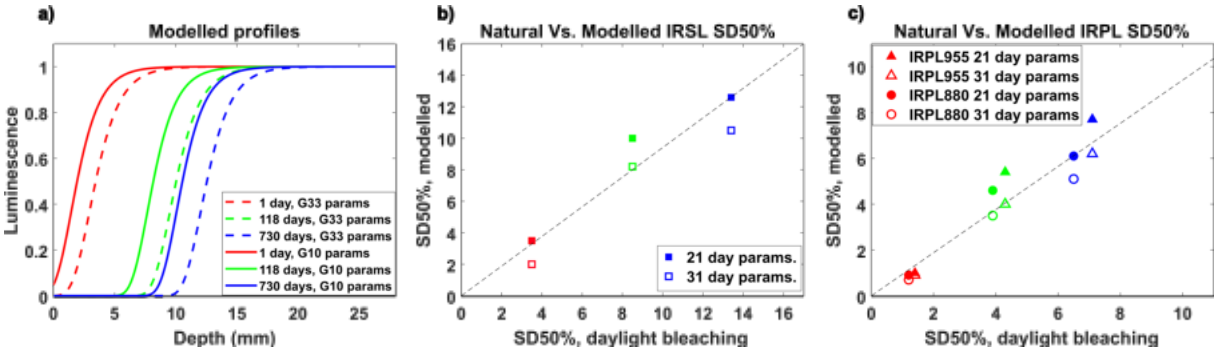

Figure 5.15: a) Modelled luminescence-depth profiles for 1 day (red), 118 days (green) or 730 days (blue) when using the model estimates from fitting the 21 day (solid lines) or the 31 day (dashed lines) exposure profiles. b) Correlation between the IRSL SD50% depths from the daylight exposure profiles and the SD50% depths from the modelled profiles of the saame exposure times, as presented in panel a. c) Correlation between the IRPL SD50% depths from the daylight exposure profiles and the SD50% depths from the modelled profiles.

CHAPTER 6

An application of luminescence to study crack formation in naturally exposed rocks

Sellwood, E.L.[a], Andricevis, P.[a], Olesen, H.[a], Eppes, M.C.[b], Kook, M.[a], Jain, M[a].
[a] Department of Physics, Technical University of Denmark, Risø Campus, 4000, Denmark.
[b] Department of Geography and Earth Sciences, University of North Carolina at Charlotte, 9201 University City Blvd. Charlotte, NC 28223

Presented in this chapter is a novel application of rock surface dating using IRSL and IRPL imaging for establishing a temporal chronology of the formation of cracks in a glacially deposited boulder. The 2D data from the images can be interpreted to establish the relative bleaching extents around the cracks, from which a relative chronology of crack formation can be inferred. This preliminary study introduces the idea of applying established rock surface dating methods to luminescence data from cracks and sets the ground work for future studies where absolute ages of the cracks may be determined. The work presented here is currently in preparation for submission to a journal, either Geology or Geophysical research Letters.

Abstract

Cracks play an important role in the processes of weathering and erosion, yet their origin and forcing factors remain unresolved, largely because of our inability to constrain the exact timings of crack formation. At best we can date the host stratigraphic layer and thereby obtain an upper age on crack formation. However, this method is only applicable to restricted sites and is beset with poor temporal resolution. Recent developments in optically stimulated luminescence (OSL) dating have made it possible to estimate exposure or burial ages of rock surfaces. Here we extend the principle of OSL rock surface exposure dating to investigate its potential of constraining the timing of crack formation in rocks. Using novel spatially resolved luminescence measurements, we imaged infrared-photoluminescence (IRPL) and infrared-stimulated luminescence (IRSL) from three cracks in a glacially deposited boulder from the Sierra Nevada. The extent of optical bleaching transverse to the crack surface is a function of the width and the azimuthal orientation of the crack, as well as the age of the crack. We assess the extent of luminescence bleaching away from the crack based on high resolution IRPL and IRSL images, and based on this information construct a relative chronology of crack formation consistent with the field observation. While establishing a potential tool for relative dating of cracks, this study paves way for future method development for absolute dating of crack formation. Furthermore, this technique potentially offers a way to assess how light propagates through rocks and cracks.

Key words

Cracking; Mechanical weathering; Rock damage; Infrared Photoluminescence; Infrared stimulated luminescence; Spatially resolved.

6.1 Introduction

There are many geomorphological features indicative of past temperatures and precipitation fluctuations. One set of such geomorphological features, which has been observed throughout multiple landscapes, are cracks and fractures in bedrock and coarse sediments. These cracks often have a preferred orientation or occur in particular patterns (McFadden et al., 2005; Chan et al., 2008; Moores et al., 2008; Eppes et al., 2010; Eppes et al., 2015; Gallach et al., 2021), and the processes behind their formation is a point of continuing investigation. The debate has generally centred around thermal stresses as well as hydrological weathering (i.e. the dominant climate) as being the predominant driver of their formation (Simmons et al., 1978; McFadden et al., 2005; Moores et al., 2008; Eppes et al., 2020).

With this connection between fractured landscapes and climatic states, it is desirable to find methods for dating the formation of these features. If we can date such landscape formations or collections of similarly-orientated rocks, we can try to link these ages to other palaeo-climatic and geomorphological markers, increasing the resolution of the geological record for that region. Within the field of geosciences optically stimulated luminescence has been a tool of interest for dating and understanding the evolution of different landscapes, but recent advances in OSL rock surface dating (RSD) methods have made it possible to unravel the evolution of hard-rock landscapes or deposits (e.g. Rades et al., 2018; Sohbati et al., 2018; Brown et al., 2019; Lehmann et al., 2019; Brill et al., 2020; Smedley et al., 2021).

Typically, OSL is used for determining the time elapsed since sediment was last exposed to light. Over the past decade there have been significant methodological developments to underpin the systematics of daylight induced bleaching of OSL on the scale of tens of millimetres below a rock surface (e.g. Sohbati et al., 2011; Meyer et al., 2018; Ou et al., 2018) and in quantifying the OSL bleaching front in terms of a surface exposure age (e.g. Chapot et al., 2012; Sohbati et al., 2012a; Sohbati et al., 2012c; Gliganic et al., 2018; Lehmann et al., 2018; Brill et al., 2021) or an erosion rate (Herman et al., 2010; Sohbati et al., 2018; Brown et al., 2019; Lehmann et al., 2019). Upon exposure of a rocks surface the latent luminescence will be bleached. With continued exposure to sunlight, extension of this bleached region pushes deeper into the rock as a function of time. From measurement of the luminescence at increasing depths from the rocks surface, a luminescence-depth profile can be constructed and the exposure duration can be determined through the fitting of age models with parameterisation via measurement of a calibration sample (Sohbati et al., 2011; Sohbati et al., 2012a; Freiesleben et al., 2015).

This study is based on the premise that daylight infiltrates along the crack plane, as soon as the crack is created; this in turn leads to progressive emptying of luminescence traps both along the crack face and into the crack surface. Thus, just as in surface exposure dating, the bleaching front can be used as an estimator of how long the exposure was, and thus provide a formation age of the crack. However, unlike exposure dating, the actual daylight flux is expected to be dependent on the width of the crack. Furthermore, orientation of the crack relative to solar insolation can be an important factor depending on the relative fluxes of direct vs. diffused/scattered daylight inside a crack; these factors are currently unexplored. Luminescence

investigations of cracks can potentially provide several important pieces of information:

Luminescence investigation of cracks can potentially provide several important pieces of information:

1. Absolute crack ages, if suitable calibration for the age model is available,
2. Relative dating of cracks in single stratigraphic unit or across different units in the same area, and linking these ages to crack parameters (width, orientation and dip) or other geomorphic variables,
3. Assessing the speed or episodicity of crack propagation and the resulting bleaching of luminescence with increasing crack size.

Acknowledging this potential, we present here a proof of concept study that demonstrates the use of luminescence as a chronometer of crack formation. Such an application has become possible only recently because of the discovery of novel high sensitivity luminescence signals such as IRPL (Prasad et al., 2017; Kumar et al., 2020a), and the complimentary development of high-resolution imaging of large sample areas (Sellwood et al., 2019).

6.2 Materials and methods

6.2.1 Sampling site

Our sample was collected from a boulder bar of a Tioga outwash terrace in the vicinity of Lundy Canyon along the eastern flank of the Sierra Nevada Mountains in California, USA (38.03166, -119.17085). Extensive published mapping and chronological studies of glacial deposits in the Sierra Nevada Mountains attributes them to the Tioga Glacial period, during global marine isotope stage 2 (MIS2; ~28-14.5 ka; Rood et al., 2011). The terrace from which our sample was collected has been dated to 17.7 ± 1.0 ka using cosmogenic ^{10}Be on several meter-scale boulders (Rood et al., 2011). At the location of the sample collection, multiple studies of cracks in boulders ranging from 15-50 cm in diameter show a N-S and E-W bimodal distribution in crack orientation (e.g. McFadden et al., 2005; Eppes et al., 2010; Rood et al., 2011; Eppes et al., 2015; Aldred et al., 2016). This pattern has been observed globally and is linked to thermal stresses originating from solar insolation.

6.2.2 Sample selection and preparation

We chose a single boulder with three generation of cracks so as to be able to verify of our hypothesis regarding the relative dating of crack surfaces using luminescence. A single granitic boulder was selected from the top of the outwash terrace in the same vicinity of the transect measurements of prior work (Berberich, 2020). The boulder was characterized by two cracks (roughly N-S and E-W oriented) already through-going, splitting it naturally in three pieces (Figure 6.1a). Other, incipient cracks were evident on the boulder as well. The southern half of the boulder was collected for a separate study not discussed here, and the northern half (~30 × 13 × 27 cm in size) of the sample was collected at night, wrapped in black light-tight bags.

In the sampled rock, Crack A (top red semicircle in Figure 6.1a) is believed to be the oldest crack, initially splitting the whole boulder in half. The crack runs with a strike of 287°and a dip of 45°down to the north, and was measured to be on average 4-5 mm wide. Crack B was a bit narrower, at ~3 mm in width with a strike of 190°and a dip of 87°down to the west. Crack C was on the other hand a closed hairline fracture, that is interpreted to be less mature than the fully opened Crack B. Upon handling in the lab, Crack C was found to run through the entire thickness of the eastern piece. Field measurements of the precise orientation of this incipient crack were not made, but from our laboratory preparations and field images, we determined that the plane of crack C was striking roughly south and dipping at ~45°towards west. Given that we observed no continuance of Crack B or C into the southern half of the boulder, it is reasonable to interpret these cracks as post-dating Crack A.

For each crack, the IRSL and IRPL was imaged on a plane perpendicular to the crack, also capturing the bleaching extent corresponding to the top (exposed) surface; estimation of bleaching depth downwards from the top surface as well as across the crack surface was then possible. For luminescence measurements, cores were drilled across each of the three cracks (red circles in Figure 6.1a), using a 45 mm diameter diamond drill bit. Crack A was drilled down to a depth of ~83 mm from the exposed top surface, in two separate vertical sequential cores (Figure 6.2a; 0-42 mm depth, and ~43-83 mm depth from the natural rock surface). Using a water-cooled 0.3 mm diamond wire saw, sections were cut perpendicular to the crack surface for imaging (dashed blue lines in Figure 6.1a represent the surfaces which were cut and measured). The two vertical sections were imaged separately. Previous studies have established that thermal heating of the sample during cutting stages does not adversely affect the luminescence signal. For extracting a core across crack B, the two large halves of the rock were bound together with tie-wraps and the drill was positioned over the crack (red circle in Figure 6.1a). Two cores were sequentially drilled to reach a depth of ~85 mm from the surface (cores from 0-46.4 mm and 47 -88 mm). The cores were both cut in half, perpendicular to the crack (dashed blue lines in circle B) so that the full bleaching profile adjacent to the crack could be imaged (see Figure 6.2e). Preliminary measurements were made of the first half of the core, and this data can be found in the appendix, along with preliminary measurements from slices of crack A and C. A core was drilled and extracted across crack C, down to a depth of ~46 mm. Sections ~26 × 46mm in size were cut from one half of the core, perpendicular to the crack (Figure 6.2i).

6.2.3 Measurements and analysis

Recently, Sellwood et al. (2021) developed instrumentation for spatially resolving infrared-stimulated luminescence (IRSL) and two emission peaks of infrared-photoluminescence (IRPL) at 880 nm and 955 nm (Prasad et al., 2017; Kumar et al., 2020a) from exposed rock surfaces. They demonstrate the suitability of such measurements for high-resolution rock surface exposure dating of cobbles and bedrock, where assessment of the whole spatial distribution of luminescence can be conducted. In this study, we explore the utility of combining this instrumentation with the developing tools of OSL rock surface dating (RSD) to determine the relative ages of different cracks in naturally exposed rocks.

Using the EMCCD-based system described in Sellwood et al. (2021), the natural (L_n) and laboratory regenerated (L_x) IRPL at 880 nm and 955 nm, and IRSL at room temperature was measured on the rock cuts described above. The exposure time for IRPL measurement was set at 10 s for all samples, and whole IRSL decay curves were captured over 20 frames, with each frame integrated over 10 s. For regenerated signals, a 2 kGy saturation dose was administrated in a cobalt-60 gamma facility at the Risø High Dose Reference Laboratory; this was used to

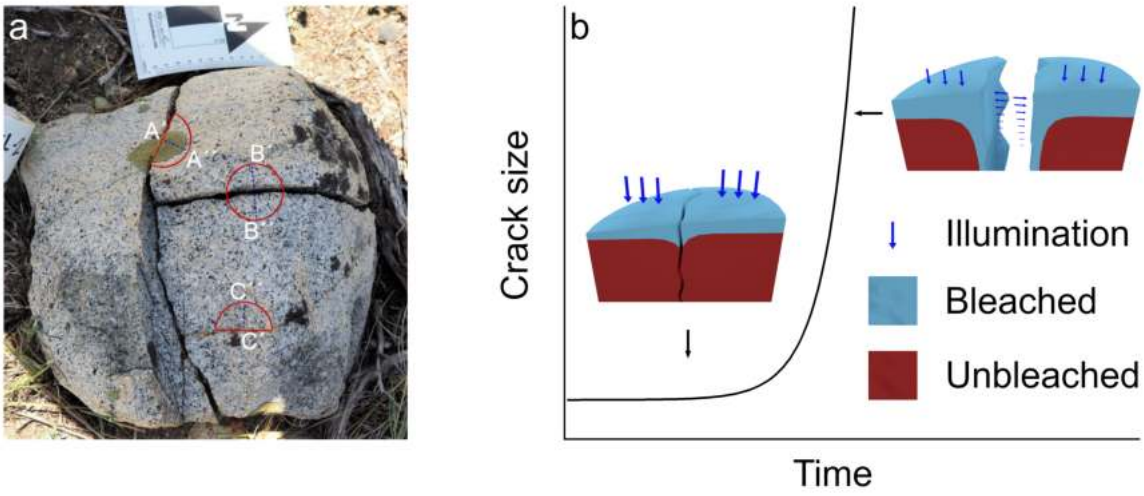

Figure 6.1: a) Image of the boulder sampled in this study. The red circles indicate where cores were drilled over the cracks. The blue dashed lines indicate the planes along which slices were cut and from where the IRSL and IRPL was imaged. b) Conceptual diagram of the speed of crack formation over time (black line). The bleaching of luminescence at the rock surface, and along and into the crack plane is shown in respect to the relative crack formation. Blue regions indicate where luminescence would be bleached, and the arrows indicate the light insolence on and through the rock.

normalise for any spatial variations in the sensitivity of natural IRPL and IRSL signals. Analyses were conducted using the Imaging processing toolbox in MATLAB (Mathworks, 2017). The L_x images were registered onto the L_n images to allow pixel-wise analysis. The images were cropped and masked to remove pixels from the sample stage area, outside of the respective rock faces, and the L_n/L_x ratio was calculated.

In conventional rock surface dating methods, the luminescence intensity is plotted as a function of depth into the rock. The depth to which the luminescence is zeroed can be used as a parameter for comparing the relative bleaching durations of multiple samples. Here, we have significantly more luminescence information in the 2D spatial domain; reducing these data to 1D luminescence-depth profiles inevitably results in loss of such information. Therefore, we tried several image analysis stages in order to trace the transition boundary between the bleached (no luminescence) and non-bleached regions observable in the IRSL and IRPL images. First, the non-luminescing regions in the slabs were also removed. For this analysis, the distribution of L_x pixel intensities were plotted in a histogram for each sample. A threshold was defined to separate the low-intensity pixels from the pixels representing bright luminescence. This threshold was used to create binary masks with the L_x images which were then applied to their corresponding L_n/L_x ratio maps. For cores A and B where two cores were drilled sequentially, down vertically from the surface, the data images are stitched along the conjoining edges.

Secondly, these luminescing regions in the binary map were expanded via several stages of image processing (morphological erosion and dilation) until the areas corresponding to the luminescing regions connected together. The final binary map consisted of two regions, representing either the part of the slab where IRSL or IRPL was detectable above the threshold, or where no luminescence was detected. Finally, the pixel co-ordinates representative of the boundary between the luminescing and non-luminescing regions were selected and plotted for each crack for each signal (x-axis representing the horizontal distance from the crack, and y-axis representing the depth from the boulders surface). The stages of this morphological analysis can be found in the appendix. From these boundary profiles we were able to better compare the extent of bleaching adjacent to the crack and at the natural rock surface at each crack location. Thus, the

bleaching fronts around the cracks and from surface bleaching can be estimated and compared between all cracks.

We expect the same bleaching depths from the top since each crack shares the same top surface. However we expect different bleaching extents across the cracks because of their different widths and exposure ages. The conceptual diagram in Figure 6.1b visualises how the development of cracks has been seen to follow a gradual formation of microcracks, before reaching a critical point beyond which the length and width suddenly increases (black line in Figure 6.1b) (Kumar et al., 2021a). The luminescence at the rocks surface will be bleached to deeper depths from the exposed surface, and with progressing crack development (i.e. from crack A to crack C), increasing bleaching will occur along and into the crack plane (blue regions in cores in Figure 6.1b).

6.3 Results

Figure 6.2 presents optical images of the measured samples as well as the IRSL, $IRPL_{880}$ and $IRPL_{955}$ L_n/L_x ratio maps from cracks A, B and C. Data are presented in false colour with colour bars representing L_n/L_x pixel ratio value ranging from unbleached (red/yellow pixels) to fully bleached/non-luminescing (blue). The white regions in the ratio maps represent the non-luminescing regions. The traced bleaching boundaries are shown as red lines on the IRSL ratio maps, and black lines on the IRPL ratio maps. Where the boundary could not be traced (i.e. where non-luminescing regions were found), the bleaching boundary was estimated and is represented by a dashed line. The IRSL, $IRPL_{880}$ and $IRPL_{955}$ bleaching boundary profiles are presented in Figure 6.3 for easier comparison.

Figure 6.2a shows the image of the rock sample for crack A. The solid curve represents the opposite wall of the crack and the striped fill represents the rock on the other side of the crack. The irregular face of the crack (side A) informs us that minimal weathering has occurred along this crack plane. This is a crucial observation if we are to trust that the observed bleaching extent around the crack represents the full bleaching duration since crack formation. The IRSL L_n/L_x ratio map is shown in Figure 6.2b, with the bleaching boundary highlighted by the red line. The natural IRSL was only detected from a few regions, and the intensity of the IRSL after the normalisation dose was 10 times that of the natural. Therefore, there are many pixels with L_n/L_x values at or close to 0. We assume this intensity difference is due to fading of the IRSL, but this has not been investigated further here. As expected, the regions towards the top surface and around the cracks show no detectable IRSL because of signal zeroing due to daylight exposure. With increasing depth down the crack face, the bleached region becomes narrower. We do not see the full downward extent of IRSL bleaching along crack A, as the bleached region extends further beyond our measured sample depth. The $IRPL_{880}$ L_n/L_x ratio map is shown in Figure 6.2c. with the traced boundary indicated by the black line. Compared to the IRSL, the $IRPL_{880}$ has been bleached to less extent both down from the rocks surface and inward from the vertical face of the crack. The bleached region inward from crack A extends down only to a depth of ~72 mm from the rocks surface. The $IRPL_{955}$ data in Figure 6.2d shows how the $IRPL_{955}$ has been bleached to a greater extent than the $IRPL_{880}$, both downward from the surface (to ~9.9 mm) and inward from the crack face, extending down to a depth of ~81 mm from the surface. The bleaching fronts are consistent with previous studies which show that IRSL bleaches faster than $IRPL_{955}$ which in turn bleaches faster then $IRPL_{880}$ (Kumar et al., 2020a; Sellwood et al., 2022).

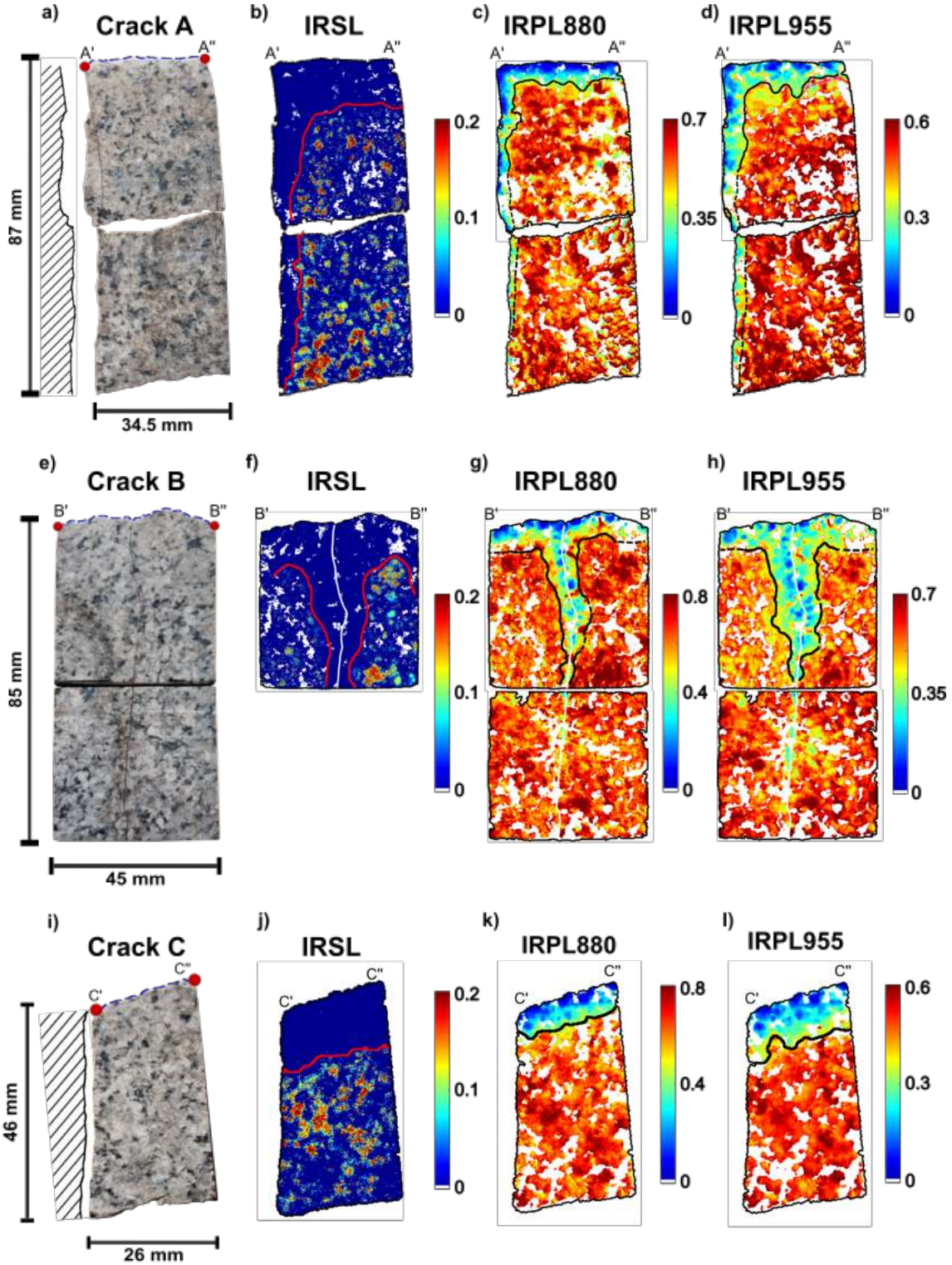

Figure 6.2: a) Image of the rock samples from crack A. The striped section to the left indicates the relative position of the opposite side of the crack which was not investigated here. b) IRSL L_n/L_x ratio map from crack A. The red lines on the IRSL images, and the black lines on the IRPL images indicate the estimated boundaries between the bleached and non-bleached regions. The lines are dashed when the bleaching boundary was uncertain, e.g. due to lack of luminescent minerals in that area. Colour bars represent L_n/L_x value. c) $IRPL_{880}$ ratio map and d) $IRPL_{955}$ ratio map for crack A. e) Image of rock sample from crack B. Panels f-h show the L_n/L_x ratio maps for IRSL, $IRPL_{880}$ and $IRPL_{955}$ respectively. The white line down the middle of each image traces the crack. i) Image of crack C sample. The relative position of the opposite side of the crack is shown as the striped section on the left. j) IRSL from crack C. k) and l) show the $IRPL_{880}$ and $IRPL_{955}$ L_n/L_x ratio maps for crack C

The image of the sample cut from crack B is shown in Figure 6.2e. Whilst in the field, there was an offset between the western and eastern sections of the boulder, we were able to directly refit the luminescence images from two pieces together, indicating that there has been negligible erosion or alteration to the crack surface since the pieces cracked. In Figure 6.2f, the IRSL has been completely bleached at the top surface and parallel to the crack (white line on Figure 6.2f). We note that almost no natural IRSL was detected from the bottom core from crack B and thus we have omitted the data from this figure. Following the fact that we do see IRSL emitted in the top core, it is logical to assume we would detect similar IRSL from at least the top portions of the bottom core; this lack of IRSL suggests that the bottom core from crack B had accidentally been exposed to light prior to measurement. Whilst this is problematic for IRSL, IRPL has a much lower bleachability than IRSL (Kumar et al., 2020a) and a short light exposure would not be overly influential to the IRPL. This relatively lower bleachability can be seen in the $IRPL_{880}$ and $IRPL_{955}$ L_n/L_x ratio maps in Figures 6.2 g and h. From these maps, clear v-shaped beaching region along the crack is observed, extending from the rock surface to depths of ~37 mm and ~48 mm for $IRPL_{880}$ and $IRPL_{955}$ respectively. Some bleaching is seen in the bottom halves of the samples, but these areas are hard to confidently define. Figure 6.2i presents the image of the crack C section. The IRSL ratio map (Figure 6.2j) shows similar bleaching has occurred at the natural up-facing rock surface as with cracks A and B, but we do not see any bleached region extending from the vertical crack face (side C). Considering the $IRPL_{880}$ (Figure 6.2k) and $IRPL_{955}$ (Figure 6.2l) ratio maps, there is also no observable bleaching extending from the crack face.

6.3.1 Comparison of bleaching fronts across the three cracks

Figure 6.3 presents the plotted traced IRSL and IRPL bleaching boundaries from each crack. Note that the x-axis spans from −20 mm to +20 mm, with 0 mm representing the position of the vertical crack surfaces for all samples (marked by the dashed line). The following inferences can be made:

- For a given signal, the extent of bleaching from the top is similar for each section. This observation serves to confirm the reliability of determining the position of luminescence bleaching fronts since the top surface of the rock should experience the same daylight flux at all positions. This also informs us that no part of the boulders surface has been locally eroded.
- The bleaching front from the top as well as the bleaching along and perpendicular into the crack varies between the three measured signals. The bleaching extent is greatest for IRSL, intermediate for $IRPL_{955}$ and less for $IRPL_{880}$. This is consistent with our understanding of the relative bleaching of these signals and again serves to qualitatively benchmark the reliability of our bleaching front estimates.
- Along the crack surfaces, we observe that IRSL bleaching is both the deepest and the widest along crack A, intermediate for crack B, while there is no perceptible bleaching along crack C. The bleaching perpendicular to the crack is similar for the $IRPL_{880}$ and $IRPL_{955}$ signals for cracks A and B. However, crack A shows that IRPL has been bleached to a greater depth along the crack plane.
- The bleaching extent along the western side of the crack B (side B in Figures 6.1a and 6.2e) is larger than that on the eastern side. The two pieces across crack B were slightly displaced. It is therefore possible that one face received more direct light flux then the other because of geometrical effects; this should be explored further in future work.

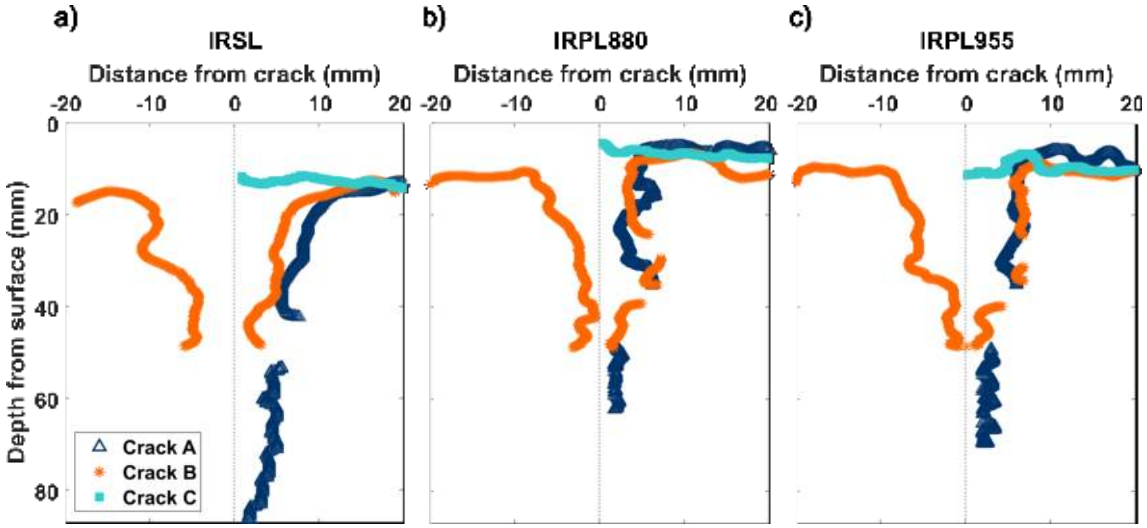

Figure 6.3: a) IRSL bleaching boundary profiles from the three cracks. The x-axis at 0 mm represents the position of each of the crack surfaces, to show the full extent of bleaching around both sides of crack B (orange stars). The top surface of the boulder is at 0 mm depth from the surface (y-axis). b) $IRPL_{880}$ traced bleached boundaries, and c) $IRPL_{955}$ bleached boundaries from the three rocks.

Although, in the absence of a calibration method, these profiles are only qualitative estimates of the bleaching extent in response to different exposure durations, they still offer a means for testing the reliability of the proposed method, as we known the relative ages of cracks A and B based on field observations. If we consider our hypothesis that the luminescence both down and away from the crack plane will be bleached to greater extents with increasing time, we can argue that the greater IRSL bleaching around crack A, and the deeper IRPL bleaching depths along crack A compared to crack B is a result of a longer exposure period. Thus crack A must have formed at an earlier date than crack B. However, with this assumption we are discounting any effects of the crack geometry (i.e. width and orientation), which are different between cracks A and B. The apparent lack of bleaching along crack C may be due to its relatively younger formation age or due to the crack size being too small for bleaching to occur down its face.

6.4 Discussion

We demonstrate here that principle of luminescence exposure dating can be applied to study to chronologies of crack formation. Through using IRSL and IRPL imaging one can make a rapid assessment of 2D bleaching around a crack (about 5 min per measurement). It is considered that with suitable calibration , these bleaching depths could potentially be converted into a crack exposure age. Whilst the method of analysis here (tracing the boundary between bleached and non-bleached regions) offers a means by which the bleaching extents can be visually compared, it lacks a robust quantitative assessment of the total light flux received by each crack plane. Quantifying this parameter will allow an estimation of the total exposure time (i.e. time since crack formation). The relative positions of the cracks on the boulder and their orientation undoubtedly play a large role in determining the total insolation received and water retention in the crack (Hall et al., 2008; Moores et al., 2008), and thus the rate or timing of crack formation and the subsequent luminescence bleaching. At first consideration, one could argue that the greater bleaching extent seen around crack A could simply be resulting from the slightly larger crack width (~1-2 mm wider than crack B). However, if we consider the dip and the strike of crack A (287°, 45°to the north) it is possible that the total direct received irradiance in this crack differs from that in crack B. At this orientation, crack A may have experienced shadowing of

the crack plane during times of high solar inclinations. This may not have been as significant in crack B which had a much steeper dipping crack plane and likely received more of the southern-orientated sun throughout the whole year. If this is the case, then the slightly smaller bleaching region in crack B is indeed a result of the relatively younger age of the crack compared to crack A.

As a (very) rough estimate of the differences in total irradiance which the cracks at their different orientations may have received, we used an online calculator for estimating the total solar irradiance (Meteoexploration, 2021) to surfaces of defined dip and strike. As this model cannot account for shadowing (i.e. only calculates irradiance for an exposed plane), we set the crack plane as dipping vertically and orientated according to the measured strike of the cracks, in order to isolate the effect of plane strike on the total irradiance. For a vertical plane at 280°strike (crack A), the total average yearly irradiance is ~3.03 ± 1.04 kWh/m^2, whilst for a vertical plane at 190°(crack B), this value stands at 4.26 ± 0.54 kWh/m^2 (see appendix E for irradiance calculated for each month). Thus, over an average year, crack A may receive less direct solar irradiance at times of low solar azimuth than crack B, due to the difference in crack orientation. This may explain why there is a greater bleaching in crack B then would be expected based on its later formation compared to crack A. However, it may well be possible that the actual role of direct insolation in the crack is much smaller compared to that of the diffused light, since much of the crack will be in shadow for most of the time irrespective of its orientation. If this latter scenario is indeed the case, one may conclude that crack B probably formed shortly after crack A and hence the bleaching depths are only marginally smaller than those of crack A.

A more thorough assessment of the insolation in cracks is an investigatory stage recommended for a more comprehensive understanding of the bleaching patterns observed in different sized cracks with different geometries. It is suggested that future investigations focus on the effects of these variables on the bleaching of luminescence in cracks, and that if one would like to fully compare the relative bleaching extents in a series of cracks, then sampling should focus on cracks of similar widths and orientations. Future work will also be focused on the application of models to the data which will estimate the total light flux and subsequent detrapping rate of IRSL and IRPL along the crack planes.

6.5 Conclusions

We present here a novel demonstration of spatially resolved IRSL and IRPL measurements for investigating the bleaching of luminescence within three different cracks that have propagated since deposition on a glacial outwash terrace. We find that from tracing and comparing the bleached regions along the cracks, we can complete a relative chronology of crack formation, which is consistent with field observations. However, a more quantitative analysis is needed for establishing exact relative (or absolute) crack chronologies, that accounts for the respective crack widths and geometries. This method of spatially resolving IRPL and IRSL around cracks could pave the road for developing a tool for establishing the formation chronologies of cracks and cracked landscapes as well as offer greater insights into how light propagates through rocks and cracks.

6.6 Acknowledgements

The authors wish to thank Mark Bailey, Arne Miller and Torben Esmann Mølholt for their assistance with sample irradiation at the Risø High Dose Rate Reference Laboratory.

6.7 Appendix

A. Preliminary IRPL measurements

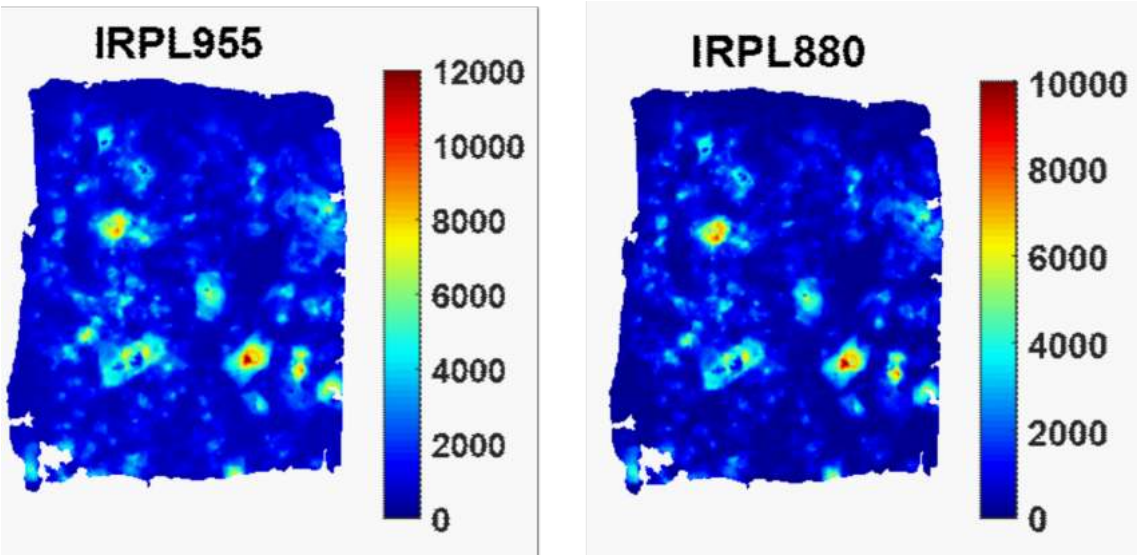

Figure 6.4: Natural (L_n) $IRPL_{880}$ and $IRPL_{955}$ images from initial tests on a slice from crack A.

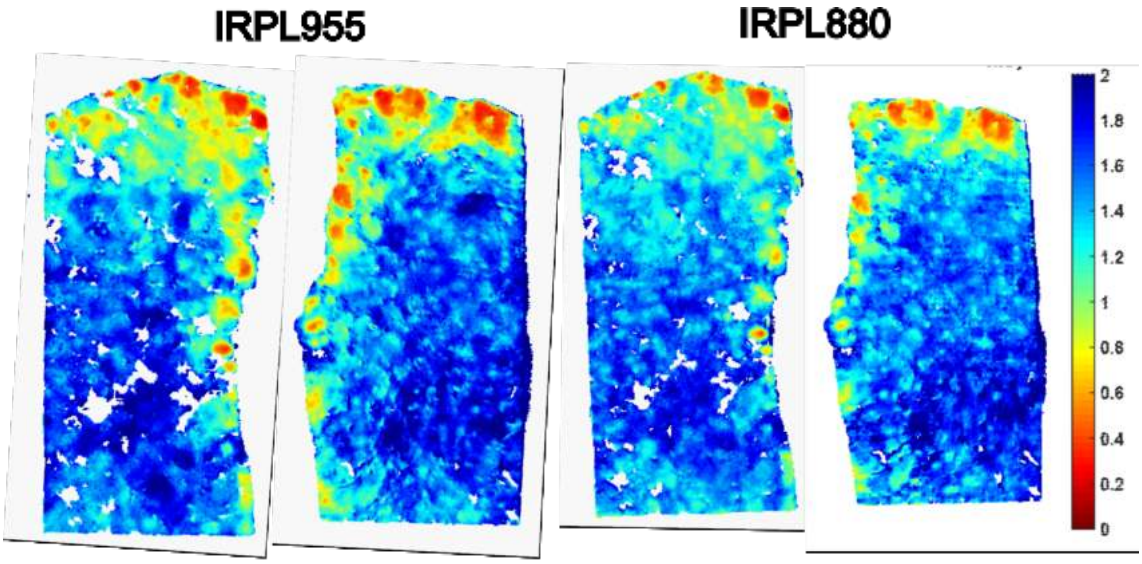

Figure 6.5: Preliminary measurements of IRPL from crack B. Here, the natural IRPL was normalised by IRPL after a 1kGy test dose.

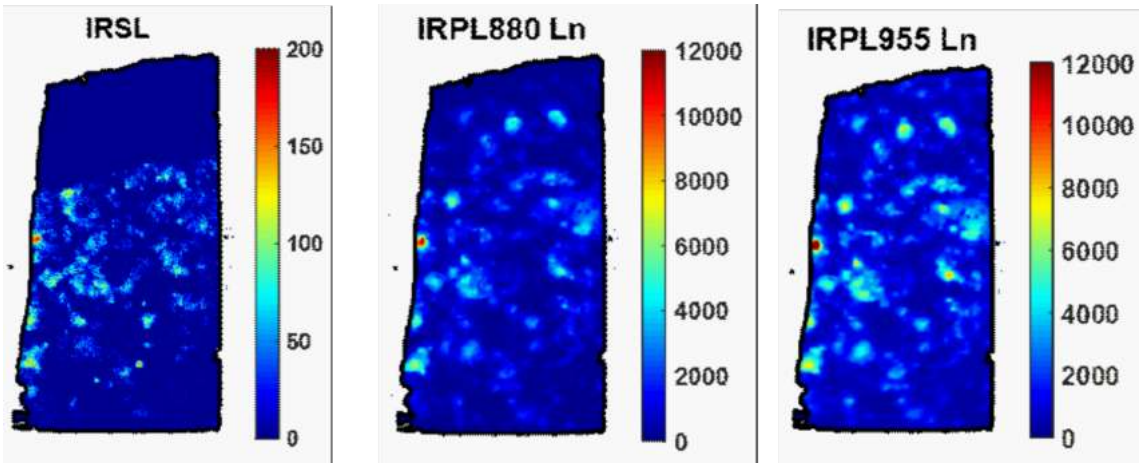

Figure 6.6: Preliminary measurements from a slice from crack C.

B. Stages of morphological image analysis for tracing bleaching boundaries, Crack A

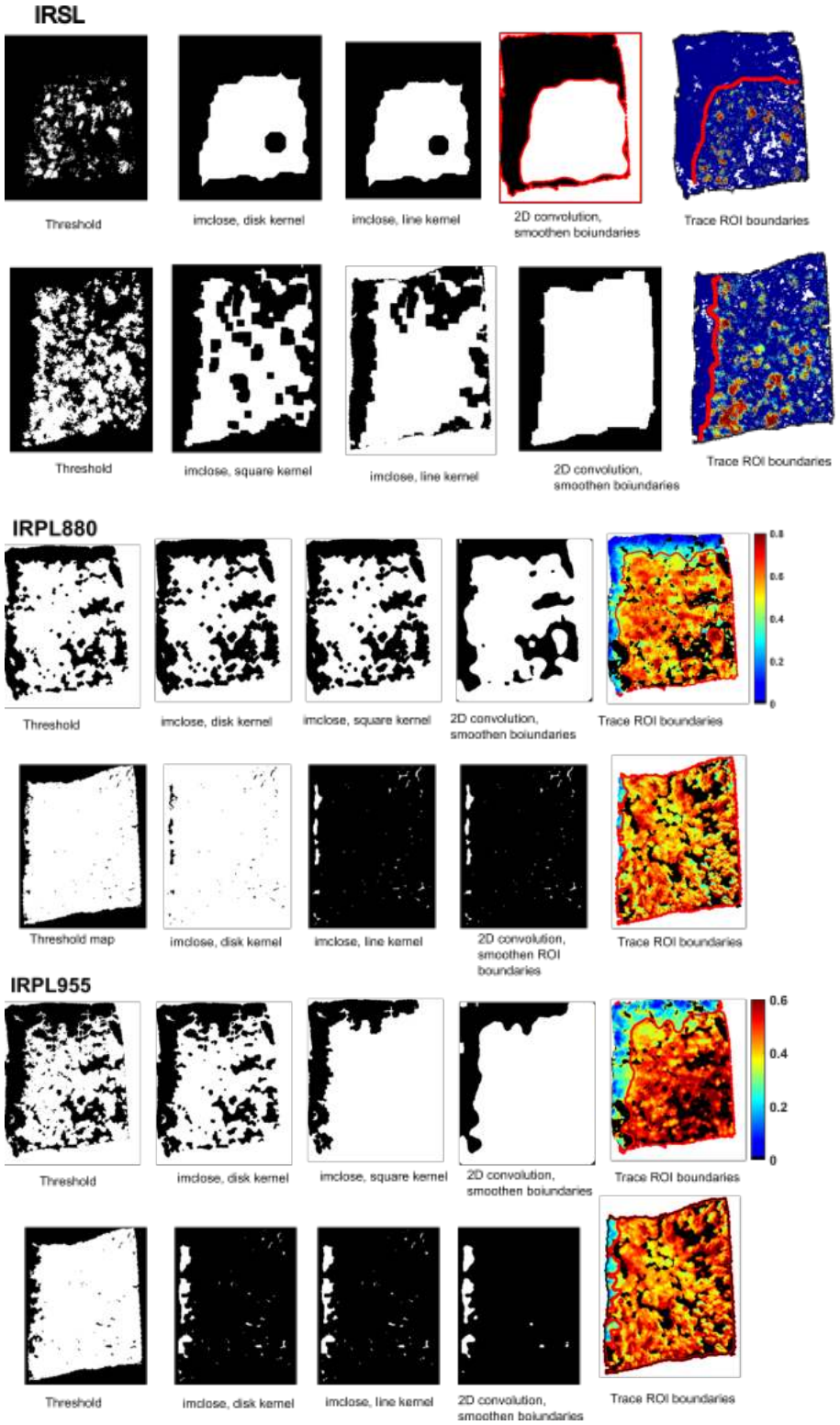

Figure 6.7: Appendix B: Sequence from left to right of the binary masks created via morphological analysis in order to trace the boundary of the bleached region around crack A. Top panel shows the IRSL masks, middle panel is for the $IRPL_{880}$ analysis, and the bottom panel shows the $IRPL_{955}$ analysis stages. The labels beneath each image state the stage of morphological analysis (i.e. function and kernel) which was conducted.

C: Crack B stages of morphological image analysis for tracing bleaching boundaries

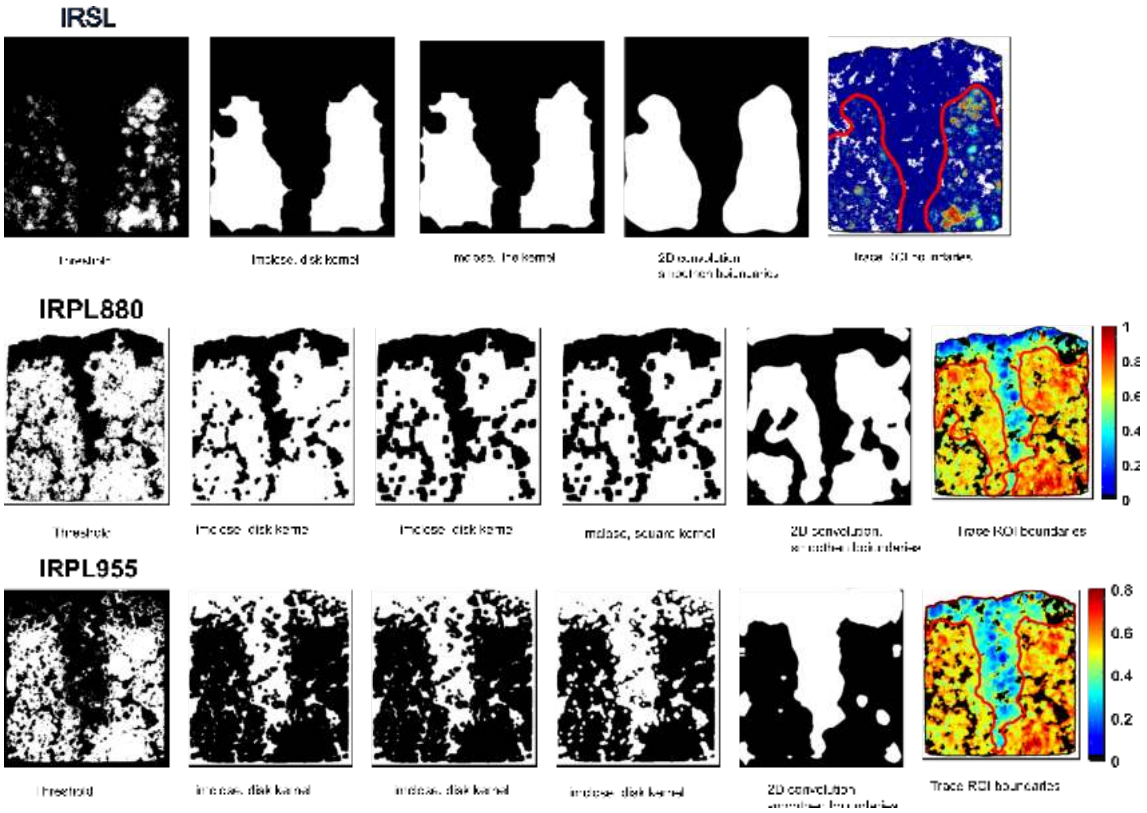

Figure 6.8: Appendix C: Sequence of the binary masks created via morphological analysis in order to trace the boundary of the bleached region around crack B. Top panel shows the IRSL masks, middle panel is for the $IRPL_{880}$ masks, and the bottom panel shows the $IRPL_{955}$ analysis stages.

D: Crack C stages of morphological image analysis for tracing bleaching boundaries

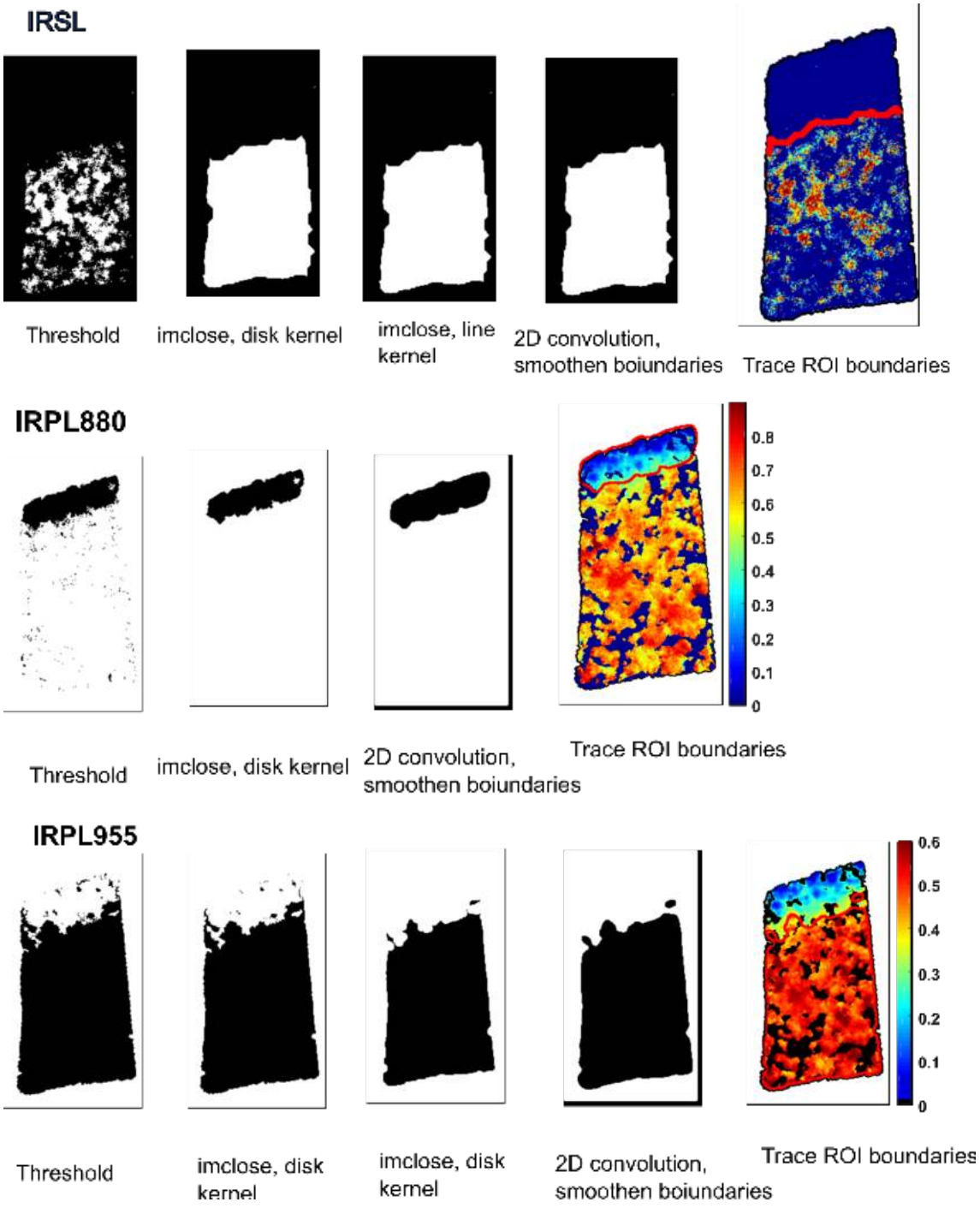

Figure 6.9: Appendix D: Sequence of the binary masks created via morphological analysis in order to trace the boundary of the bleached region around crack C. Top panel shows the IRSL masks, middle panel is for the $IRPL_{880}$ analysis, and the bottom panel shows the $IRPL_{955}$ analysis stages.

E: total irradiance per month for vertical planes of different orientations

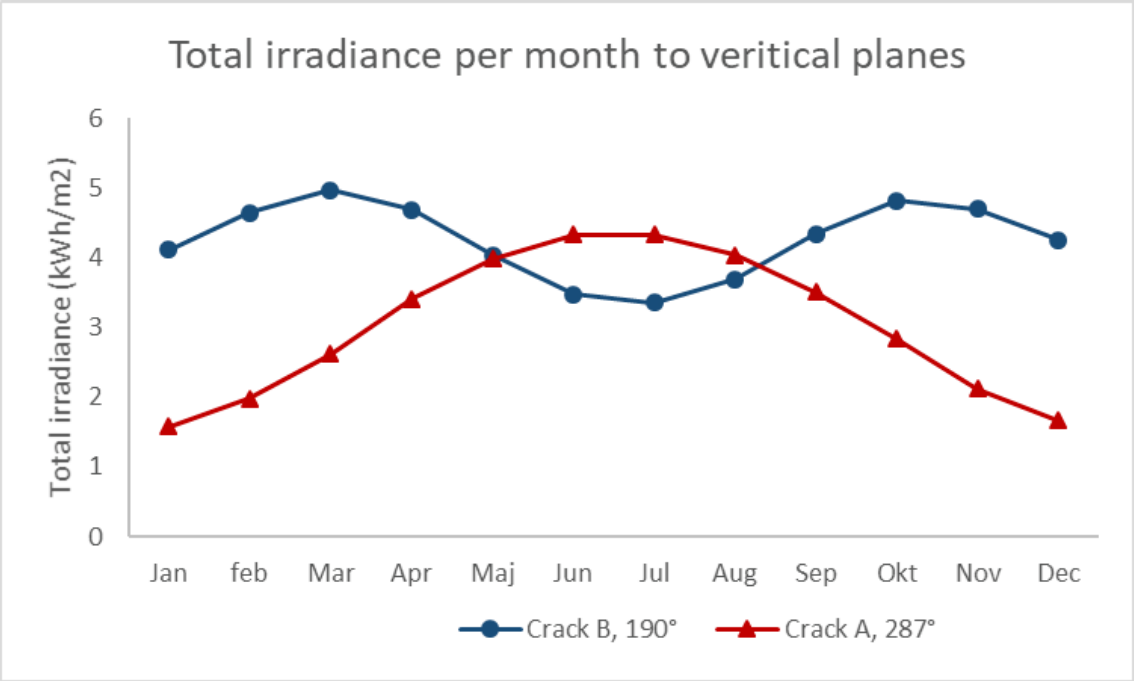

Figure 6.10: Appendix E: Total irradiance calculated for the first of each month using the model provided by Meteoexploration, (2021). Total irradiance was calculated by setting the strike of the plane to either 190°(crack B) or 287°(crack A), with the dip of the place set at 90°.

CHAPTER 7
Summary and Conclusions

This chapter concludes this PhD thesis with a summary of the main findings of the presented research. The main findings are discussed in regards to the initial objectives as defined in the introduction chapter, as well as to the overall scientific contribution to the field of rock surface dating using OSL imaging.

The aims of this PhD thesis surrounded the development and demonstration of instrumentation for the imaging of IRSL and two emission peaks of IRPL, with a focus on rock surface dating. These aims were built to address several limitations which are hindering the progression of OSL RSD methods. These limitations include extensive sampling and preparation requirements followed by lengthy measurement times only to achieve low-resolution data, as well as problems surrounding the stability and reproducibility of IRSL from feldspar. There are also limitations in the current age models used for rock surface exposure dating, where parameters are inadequately constrained and are thus a limitation on the reliability of the final ages. Spatially resolved luminescence measurements of whole rock surfaces was considered a logical progression for RSD applications, cutting both sample preparation and measurement times, and vastly increasing the resolution of the data. The characterisation of two IRPL emission peaks offered an alternative to IRSL measurements of feldspar, reducing the problems associated with fading and sensitivity faced by conventional IRSL measurements.

With these factors under consideration, I initially defined four research objectives for this research project, and have attempted to address each of them over the course of the last three years. Outlined below are summaries of how each of the objectives were met:

1. A conceptional design, development and testing of a high-resolution IRPL imaging system for rock surface dating.

A detailed description of the new instrumentation for spatially resolved IRPL and IRSL is now available as a publication, and is presented here in chapter 2. The instrumentation hosts multiple stimulation sources and filter combinations, suitable for measuring IRSL and IRPL at 880 nm and 955 nm. Not only is the IRPL able to be stimulated by the previously used 830 nm laser, but two other sources at 885 nm and 532 nm have been installed which enable investigation into the IRPL emissions, stability and sensitivity to these wavelengths. One of the most significant impacts of this instrumentation is that, contrary to the initial instrumentation as described by Sellwood et al. (2019), imaging of IRSL is now viable, after the stimulation power of the 850 nm LEDs was increased. Samples up to ~8 × 8 cm in size can be imaged. Good IRPL and IRSL measurement reproducibility were demonstrated. High system stability was also shown, with <2 % variation in IRPL intensity measured from replicated measurements, which is variation attributed to the internal temperature variation of the instrument. An appendix is supplied with chapter 2, where we establish experimentally that the effective depth of IR wavelengths through pure feldspar and granitic sample to be >1.4-2 mm. All other chapters in this thesis contain different applications of IRPL and IRSL imaging, where the high-resolution data is demonstrably beneficial for understanding (e.g.) IRPL and IRSL response to dose, bleaching behaviour and sensitivity changes.

2. Application of the instrument for rapid *in situ* assessment of bleaching-depth profiles.

Presented in chapter 3 is a study by which luminescence-depth profiles suitable for RSD can be reconstructed from images, without the need for a test dose for normalisation. Instead, it was recognised that taking the ratio between the two IRPL signals (IRPL 955/880 nm) would be sufficient, allowing reconstruction of a valley-shaped luminescence-depth profile, the width and breadth of which are indicative of the bleaching depth of the IRPL-depth profile. A luminescence-depth profile constructed by calculating the ΔIRPL (Jain et al., 2020) can act as a proxy for the IRSL profile, boasting usability where the IRSL cannot be detected (e.g. due to instrument limitations or when in the field). From measuring the whole IRSL decay curve, the natural IRSL can be normalised by a later part of the decay curve. These normalisation methods open up rock surface dating applications to laboratories where access to irradiation facilities is limited. They also offer means for obtaining luminescence-depth profiles in the field, as a profile can be constructed from as little as 2 images.

3. Application of different luminescence models on IRPL and IRSL bleaching profiles, and an understanding of the geochemical and compositional constraints on IRPL signal in feldspar

Chapter 5 presents an in-depth look at the development of luminescence-depth profiles as a function of both wavelength and time. It also discusses the suitability of applying the first or general order models to IRSL and IRPL luminescence-depth profiles for RSED. The high bleachability of IRSL leads to a faster progression of luminescence-depth profiles in granitic rocks, compared to $IRPL_{955}$ and $IRPL_{880}$ (least bleachable signal). Bleaching IRSL and IRPL with monochromatic light sources (405 nm, 532 nm or 885 nm) informs us that IRSL is bleached predominantly by IR-wavelengths, whereas bleaching of IRPL (both signals) is more efficient by shorter wavelengths (violet). This has implications as the shorter wavelengths are generally attenuated more through a material (see the appendix to chapter 2) and thus, the bleaching of IRPL with time will progress at a different rate than the IRSL. This chapter presents a novel data set displaying how IRPL profiles develop as a function of exposure time. From bleaching IRSL and IRPL with either halogen lamps or by natural sunlight for increasingly longer times, the luminescence-depth profiles progress to deeper depths from the surface. Estimates of μ (mm^{-1}) from fitting the FOM and the GOM decrease with increasing exposure times. This was expected, as we observe decreasing μ with increasing wavelength through rock slices, and thus the effective μ will decreases with increasing exposure time. From fitting the luminescence-depth profiles with the GOM, estimates of the kinetic order were all close to 1, suggesting that the bleaching of IRPL can be expressed by the FOM. We also found that estimates of the kinetic order from fitting the GOM to IRSL data were also close to 1, which contradicts the results as expressed by Freiesleben (2021), although it is currently not understood as to why we observe this difference.

An in-depth investigation into the geochemical constrains on IRPL was not able to be completed during this research project. It was initially planned that this work was to be completed as part of an external stay, but due to time constrains and the restrictions on travel implemented during the Corona pandemic, these plans were unfortunately not able to be fulfilled. A description of geochemical investigations which would be beneficial for understanding IRPL and IRSL is provided in the future perspective section below.

4. IRPL rock surface dating applications

Chapters 4 and 6 present novel applications of rock surface dating using spatially resolved measurements of IRSL and IRPL. Following the previous applications of RSED, an attempt at recovering known "burial" doses from the surface of two rock samples was made, as a demonstration for the suitability of the described instrumentation for RSBD applications (chapter 4).

Known IRSL "burial" doses were able to be recovered from the surface few mm (~5 mm) of both rock samples. The dose recovery using $IRPL_{955}$ and $IRPL_{880}$ was only successful for the sample with the higher burial dose (500 Gy), where the expected dose was recovered from the surface 0-2 mm. Chapter 6 presents a novel application of imaging the bleaching extent of IRSL and IRPL from cracks, with the aim of creating a chronology of crack formation. Through imaging the plane perpendicular to the crack face, it was possible to observe the extent of bleaching at both the top exposed rock surface, as well as down and into the crack. We were able to reconstruct a chronology of crack formations for three cracks of different sizes and orientations from a granitic boulder, which was consistent with field observations.

7.1 Scientific impact and future perspective

The results presented in this thesis are expected to have significant impact on future OSL RSD applications, and on the development of future instrumentation for spatially resolved measurements if luminescence. The described Risø Luminescence Imager is a relatively simple set-up which can be easily implemented in a luminescence lab, giving access to other research institutions to a means by which the bleaching of luminescence can be rapidly observed and luminescence-depth profiles can be rapidly reconstructed. The instrument also allows investigations of the whole spatial configurations involving entire mineral assemblages in a large sample - information which is difficult to obtain in in other EMCCD-based systems where only grains (e.g. Thomsen et al., 2015; MittelstraSS et al., 2021) or 1 cm diameter rock slices can be imaged (e.g. Duller et al., 2020b). Future work will be focused on developing a more commercial version of the instrument with specially developed software for instrument control and data analysis. There is also significant interest in the usability of IRPL for field instrumentation. The non-destructive nature of the measurement and high sensitivity is ideal for quick assessments of luminescence when sampling, and the measurements can later be reproduced in the laboratory.

The presented applications of rock surface dating using spatially resolved measurements of IRSL and IRPL demonstrate how beneficial such high-resolution data is for applying age models and understanding a rock samples' response to dose. Future applications using such measurements will benefit by being able to directly observe how a samples texture or composition influences the variation seen in luminescence-depth profiles from the same sample, and how absorbed doses are distributed through a buried rock sample (i.e. for RSBD). However, the applications here did not fully explore the full range of different measurement protocols for measuring IRPL and IRSL from large samples. Future work should focus on investigating the effects of different test doses and preheats on IRPL. I also encourage attempts to recover unknown burial doses from naturally buried rock surfaces using imaging, to fully determine the methods' suitability for rock surface burial dating applications.

The novel data sets from the bleaching experiments shown in chapter 5 will be of high interest to those who wish to continue advancing methods of rock surface dating. Through demonstrating how IRPL luminescence-depth profiles progress with increasing exposure times, it is possible to explore factors such as the minimum or maximum datable limits with IRPL RSD, or the relationship between the photoionisation cross-section of the principal trap and preferentially attenuated wavelengths with depth into a rock. Future applications will also benefit from our discussions of the model estimates obtained from fitting both the first order and general order models to the data sets, as future researchers will be better guided towards selecting the right model for their data set, and have a better understanding of the model estimates obtained from fitting.

For reconstructing the histories of different landscapes, a variety of different dating tools is demanded. We expect that the novel preliminary study presented in chapter 6, which uses the principles of OSL RSD to explore the formations of cracks, will have a high impact on the development of such tools. Future work is already planned for this data set presented here, where attempts will be made to apply age models to the data. We will also try to determine whether (for example) the obtained values of total flux from the models properly represents what is happening in nature, and whether we can truly quantify the crack formation rate and ages of the cracks. To fully develop this method into a fully-fledged dating tool for cracks, it is paramount that future work is also focused upon understanding the light flux through cracks of different geometries. I hope that this novel application catches the eye of scientists who wish to fully quantify and understand the forcing and responses of different rocky landscapes.

To summarise, the work presented in this PhD thesis will introduce researchers within the fields of radiation physics, geology and archaeology to instrumentation for investigating feldspar luminescence at high resolutions, help improve the reliability of rock surface dating, and offers novel ideas for potential applications which should be repeated and applied to more samples in the future.

Bibliography

Ageby, Lucas, Diego E Angelucci, Dominik Brill, Francesco Carrer, Helmut Brückner, and Nicole Klasen (2020). "Exploring the application of IRSL rock surface exposure dating of archaeological stone structures in Val di Sole, Italy." In: *EGU General Assembly Conference Abstracts*, p. 20236.

Aitken, Martin Jim (1998). *Introduction to optical dating: the dating of Quaternary sediments by the use of photon-stimulated luminescence*. Clarendon Press.

Aitken, MJ (1985). "Thermoluminescence dating: past progress and future trends." In: *Nuclear Tracks and Radiation Measurements (1982)* 10.1-2, pp. 3–6.

Aldred, Jennifer, Martha Cary Eppes, Kimberly Aquino, Rebecca Deal, Jacob Garbini, Suraj Swami, Alea Tuttle, and George Xanthos (2016). "The influence of solar-induced thermal stresses on the mechanical weathering of rocks in humid mid-latitudes." In: *Earth Surface Processes and Landforms* 41.5, pp. 603–614.

Auclair, Marie, Michel Lamothe, and Sebastien Huot (2003). "Measurement of anomalous fading for feldspar IRSL using SAR." In: *Radiation measurements* 37.4-5, pp. 487–492.

Bailiff, IK, D Bridgland, and Pedro P Cunha (2021). "Extending the range of optically stimulated luminescence dating using vein-quartz and quartzite sedimentary pebbles." In: *Quaternary geochronology* 65, p. 101180.

Bailiff, IK and VB Mikhailik (2003). "Spatially-resolved measurement of optically stimulated luminescence and time-resolved luminescence." In: *Radiation Measurements* 37.2, pp. 151–159.

Bailiff, IK and NRJ Poolton (1991). "Studies of charge transfer mechanisms in feldspars." In: *International Journal of Radiation Applications and Instrumentation. Part D. Nuclear Tracks and Radiation Measurements* 18.1-2, pp. 111–118.

Baril, Marc René (2004). "CCD imaging of the infra-red stimulated luminescence of feldspars." In: *Radiation measurements* 38.1, pp. 81–86.

Berberich, Samantha (2020). "A Chronosequence of Cracking in Mill Creek, California." PhD thesis. The University of North Carolina at Charlotte.

Bøtter-Jensen, L, GAT Duller, and NRJ Poolton (1994). "Excitation and emission spectrometry of stimulated luminescence from quartz and feldspars." In: *Radiation Measurements* 23.2-3, pp. 613–616.

Bøtter-Jensen, Lars, Kristina Jørkov Thomsen, and Mayank Jain (2010). "Review of optically stimulated luminescence (OSL) instrumental developments for retrospective dosimetry." In: *Radiation Measurements* 45.3-6, pp. 253–257.

Brill, Dominik, Simon Matthias May, Nadia Mhammdi, Georgina King, Christoph Burow, Dennis Wolf, Anja Zander, and Helmut Brückner (2020). "OSL rock surface exposure dating as a novel approach for reconstructing transport histories of coastal boulders over decadal to centennial timescales." In: *EGU General Assembly Conference Abstracts*, p. 18537.

Brill, Dominik, Simon Matthias May, Nadia Mhammdi, Georgina King, Benjamin Lehmann, Christoph Burow, Dennis Wolf, Anja Zander, and Helmut Brückner (2021). "Evaluating optically stimulated luminescence rock surface exposure dating as a novel approach for reconstructing coastal boulder movement on decadal to centennial timescales." In: *Earth Surface Dynamics* 9.2, pp. 205–234.

Brown, ND and S Moon (2019). "Revisiting erosion rate estimates from luminescence profiles in exposed bedrock surfaces using stochastic erosion simulations." In: *Earth and Planetary Science Letters* 528, p. 115842.

Buylaert, Jan-Pieter, Andrew S Murray, Kristina J Thomsen, and Mayank Jain (2009). "Testing the potential of an elevated temperature IRSL signal from K-feldspar." In: *Radiation Measurements* 44.5-6, pp. 560–565.

Chan, Marjorie A, W Adolph Yonkee, Dennis I Netoff, Winston M Seiler, and Richard L Ford (2008). "Polygonal cracks in bedrock on Earth and Mars: Implications for weathering." In: *Icarus* 194.1, pp. 65–71.

Chapot, Melissa S, Reza Sohbati, Andrew S Murray, Joel L Pederson, and Tammy M Rittenour (2012). "Constraining the age of rock art by dating a rockfall event using sediment and rock-surface luminescence dating techniques." In: *Quaternary Geochronology* 13, pp. 18–25.

Chauhan, N, P Adhyaru, H Vaghela, and AK Singhvi (2014). "EMCCD based luminescence imaging system for spatially resolved geo-chronometric and radiation dosimetric applications." In: *Journal of Instrumentation* 9.11, P11016.

Clark-Balzan, Laine and Jean-Luc Schwenninger (2012). "First steps toward spatially resolved OSL dating with electron multiplying charge-coupled devices (EMCCDs): System design and image analysis." In: *Radiation measurements* 47.9, pp. 797–802.

Colarossi, Debra, GAT Duller, and HM Roberts (2018). "Exploring the behaviour of luminescence signals from feldspars: implications for the single aliquot regenerative dose protocol." In: *Radiation Measurements* 109, pp. 35–44.

Daniels, Farrington, Charles A Boyd, and Donald F Saunders (1953). "Thermoluminescence as a research tool." In: *Science* 117.3040, pp. 343–349.

Deer, WA (2001). "Rock-forming minerals, 4A." In: *Framework Silicates: Feldspars* 971.

Duller, GAT (1991). "Equivalent dose determination using single aliquots." In: *International Journal of Radiation Applications and Instrumentation. Part D. Nuclear Tracks and Radiation Measurements* 18.4, pp. 371–378.

Duller, GAT, L Bøtter-Jensen, P Kohsiek, and AS Murray (1999). "A high-sensitivity optically stimulated luminescence scanning system for measurement of single sand-sized grains." In: *Radiation Protection Dosimetry* 84.1-4, pp. 325–330.

Duller, GAT, Lars Bøtter-Jensen, and BG Markey (1997). "A luminescence imaging system based on a CCD camera." In: *Radiation Measurements* 27.2, pp. 91–99.

Duller, GAT, Matt Gunn, and HM Roberts (2020a). "Single grain infrared photoluminescence (IRPL) measurements of feldspars for dating." In: *Radiation Measurements* 133, p. 106313.

Duller, GAT, Myungho Kook, Rosemary Jane Stirling, HM Roberts, and AS Murray (2015). "Spatially-resolved thermoluminescence from snail opercula using an EMCCD." In: *Radiation Measurements* 81, pp. 157–162.

Duller, GAT, HM Roberts, and RC Pinder (2020b). "A method for routinely monitoring the reproducibility of thermal pretreatment prior to optically stimulated luminescence measurements." In: *Radiation Measurements* 130, p. 106210.

Eppes, Martha Cary, Leslie D McFadden, Karl W Wegmann, and Louis A Scuderi (2010). "Cracks in desert pavement rocks: Further insights into mechanical weathering by directional insolation." In: *Geomorphology* 123.1-2, pp. 97–108.

Eppes, Martha-Cary, Andrew Willis, Jamie Molaro, Stephen Abernathy, and Beibei Zhou (2015). "Cracks in Martian boulders exhibit preferred orientations that point to solar-induced thermal stress." In: *Nature communications* 6.1, pp. 1–11.

Eppes, MC, B Magi, J Scheff, K Warren, S Ching, and T Feng (2020). "Warmer, Wetter Climates Accelerate Mechanical Weathering in Field Data, Independent of Stress-Loading." In: *Geophysical Research Letters* 47.24, 2020GL089062.

Freiesleben, Trine, Reza Sohbati, Andrew Murray, Mayank Jain, Sahar Al Khasawneh, Søren Hvidt, and Bo Jakobsen (2015). "Mathematical model quantifies multiple daylight exposure

and burial events for rock surfaces using luminescence dating." In: *Radiation Measurements* 81, pp. 16–22.

Freiesleben, Trine Holm (2021). "Developing and testing models for rock surface dating using optically stimulated luminescence." PhD thesis.

Fujita, Hiroki, Mayank Jain, and AS Murray (2011). "Retrospective dosimetry using Japanese brick quartz: a way forward despite an unstable fast decaying OSL signal." In: *Radiation measurements* 46.6-7, pp. 565–572.

Gallach, Xavi, Yves Perrette, Dominique Lafon, Émilie Chalmin, Philip Deline, Ludovic Ravanel, Julien Carcaillet, and Tanguy Wallet (2021). "A new method for dating the surface exposure age of granite rock walls in the Mont Blanc massif by reflectance spectroscopy." In: *Quaternary Geochronology* 64, p. 101156.

Galli, Anna, Alessia Artesani, Marco Martini, Emanuela Sibilia, Laura Panzeri, and Francesco Maspero (2017). "An empirical model of the sunlight bleaching efficiency of brick surfaces." In: *Radiation Measurements* 107.October, pp. 67–72. ISSN: 13504487. DOI: 10.1016/j.radmeas.2017.10.004. URL: http://linkinghub.elsevier.com/retrieve/pii/S1350448716303730%20https://doi.org/10.1016/j.radmeas.2017.10.004.

Gliganic, L. A., M.C. Meyer, R. Sohbati, M. Jain, and S. Barrett (2018). "OSL surface exposure dating of a lithic quarry in Tibet: Laboratory validation and application." In: *Quaternary Geochronology* February. ISSN: 18711014. DOI: 10.1016/j.quageo.2018.04.012. URL: https://doi.org/10.1016/j.quageo.2018.04.012.

Gliganic, Luke Andrew, Michael Christian Meyer, Jan Hendrik May, Mark Steven Aldenderfer, and Peter Tropper (2021). "Direct dating of lithic surface artifacts using luminescence." In: *Science Advances* 7.23, pp. 1–13. ISSN: 23752548. DOI: 10.1126/sciadv.abb3424.

Greilich, S, U. A. Glasmacher, and G.A. Wagner (2002). "Spatially resolved detection of luminescence: A unique tool for archaeochronometry." In: *Naturwissenschaften* 89.8, pp. 371–375. ISSN: 00281042. DOI: 10.1007/s00114-002-0341-z.

Guérin, G, N Mercier, and G Adamiec (2011). "Dose-rate conversion factors : Update." In: *Ancient TL* 29.1.

Guralnik, B and R Sohbati (2019). "Fundamentals of luminescence photo- and thermochronometry." In: *Advances in Physics and Applications of Optically and Thermally Stimulated Luminescence*, pp. 399–439. DOI: 10.1142/9781786345790{_}0011.

Guralnik, B et al. (2015a). "OSL-thermochronometry of feldspar from the KTB borehole, Germany." In: *Earth and Planetary Science Letters*. ISSN: 0012821X. DOI: 10.1016/j.epsl.2015.04.032.

Guralnik, B. et al. (2015b). "OSL-thermochronometry using bedrock quartz: A note of caution." In: *Quaternary Geochronology* 25, pp. 37–48. ISSN: 18711014. DOI: 10.1016/j.quageo.2014.09.001.

Habermann, Jan, Thomas Schilles, Regina Kalchgruber, and Günther A Wagner (2000). "Steps towards surface dating using luminescence." In: *Radiation Measurements* 32.5-6, pp. 847–851.

Hall, Brenda L, Carlo Baroni, and George H Denton (2008). "The most extensive Holocene advance in the Stauning Alper, East Greenland, occurred in the Little Ice age." In: *Polar Research* 27.2, pp. 128–134.

Hashimoto, T, S Notoya, T Ojima, and M Hoteida (1995). "Optically stimulated luminescence (OSL) and some other luminescence images from granite slices exposed with radiations." In: *Radiation measurements* 24.3, pp. 227–237.

Hashimoto, Tetsuo, Hayato Usuda, Naoki Mitamura, and Takashi Yawata (2003). "Imaging and measurement of red-infrared stimulated luminescence (R-IRSL) from feldspar samples." In: *Ancient TL* 21.1, pp. 1–6.

Herman, Frédéric, Edward J Rhodes, Jean Braun, and Lukas Heiniger (2010). "Uniform erosion rates and relief amplitude during glacial cycles in the Southern Alps of New Zealand, as revealed from OSL-thermochronology." In: *Earth and Planetary Science Letters* 297.1-2, pp. 183–189.

Hippe, Kristina, Susan Ivy-Ochs, Florian Kober, Jerzy Zasadni, R Wieler, Lukas Wacker, Peter W Kubk, and Christian Schlüchter (2014). "Chronology of Lateglacial ice flow reorganization and deglaciation in the Gotthard Pass area, Central Swiss Alps, based on cosmogenic 10Be and in situ 14C." In: *Quaternary Geochronology* 19, pp. 14–26.

Hooper, CE, RE Ansorge, and JG Rushbrooke (1994). "Low-light imaging technology in the life sciences." In: *Journal of bioluminescence and chemiluminescence* 9.3, pp. 113–122.

Huntley, David J, Dorothy I Godfrey-Smith, and Michael LW Thewalt (1985). "Optical dating of sediments." In: *Nature* 313.5998, pp. 105–107.

Huntley, David J and Michel Lamothe (2001). "Ubiquity of anomalous fading in K-feldspars and the measurement and correction for it in optical dating." In: *Canadian Journal of Earth Sciences* 38.7, pp. 1093–1106.

Hutt, G (1989). "Infrared stimulated photoluminescence dating of sediment." In: *Ancient TL* 7, p. 48.

Hütt, Galina, Ivar Jaek, and J Tchonka (1988). "Optical dating: K-feldspars optical response stimulation spectra." In: *Quaternary Science Reviews* 7.3-4, pp. 381–385.

Jain, Mayank and Christina Ankjærgaard (2011). "Towards a non-fading signal in feldspar: insight into charge transport and tunnelling from time-resolved optically stimulated luminescence." In: *Radiation Measurements* 46.3, pp. 292–309.

Jain, Mayank, Benny Guralnik, and Martin Thalbitzer Andersen (2012). "Stimulated luminescence emission from localized recombination in randomly distributed defects." In: *Journal of physics: Condensed matter* 24.38, p. 385402.

Jain, Mayank, Raju Kumar, and Myungho Kook (2020). "A novel coupled RPL/OSL system to understand the dynamics of the metastable states." In: *Scientific reports* 10.1, pp. 1–15.

Jain, Mayank, Reza Sohbati, Benny Guralnik, Andrew S Murray, M Kook, Torben Lapp, Amit Kumar Prasad, Kristina Jørkov Thomsen, and Jan-Pieter Buylaert (2015). "Kinetics of infrared stimulated luminescence from feldspars." In: *Radiation Measurements* 81, pp. 242–250.

Jenkins, GTH, GAT Duller, HM Roberts, Richard C Chiverrell, and NF Glasser (2018). "A new approach for luminescence dating glaciofluvial deposits-High precision optical dating of cobbles." In: *Quaternary Science Reviews* 192, pp. 263–273.

Kars, RH, FS Busschers, and J Wallinga (2012). "Validating post IR-IRSL dating on K-feldspars through comparison with quartz OSL ages." In: *Quaternary Geochronology* 12, pp. 74–86.

Kars, Romée H, Nigel RJ Poolton, Mayank Jain, Christina Ankjærgaard, Pieter Dorenbos, and Jakob Wallinga (2013). "On the trap depth of the IR-sensitive trap in Na-and K-feldspar." In: *Radiation Measurements* 59, pp. 103–113.

Khasawneh, Sahar al, Andrew Murray, and Fawzi Abudanah (2019). "A first radiometric chronology for the Khatt Shebib megalithic structure in Jordan using the luminescence dating of rock surfaces." In: *Quaternary Geochronology* 49, pp. 205–210.

King, Georgina E, Frédéric Herman, R Lambert, Pierre G Valla, and Benny Guralnik (2016). "Multi-OSL-thermochronometry of feldspar." In: *Quaternary Geochronology* 33, pp. 76–87.

Kook, M, R Kumar, AS Murray, KJ Thomsen, and M Jain (2018). "Instrumentation for the non-destructive optical measurement of trapped electrons in feldspar." In: *Radiation Measurements* 120, pp. 247–252.

Kook, M, Torben Lapp, AS Murray, Kristina Jørkov Thomsen, and Mayank Jain (2015). "A luminescence imaging system for the routine measurement of single-grain OSL dose distributions." In: *Radiation Measurements* 81, pp. 171–177.

Kook, MH, AS Murray, Torben Lapp, PH Denby, Christina Ankjærgaard, K Thomsen, Mayank Jain, JH Choi, and GH Kim (2011). "A portable luminescence dating instrument." In: *Nuclear Instruments and Methods in Physics Research Section B: Beam Interactions with Materials and Atoms* 269.12, pp. 1370–1378.

Krbetschek, MR, J Götze, A Dietrich, and T Trautmann (1997). "Spectral information from minerals relevant for luminescence dating." In: *Radiation Measurements* 27.5-6, pp. 695–748.

Kumar, Ankush and GU Kulkarni (2021a). "Time Evolution and Spatial Hierarchy of Crack Patterns." In: *Langmuir* 37.44, pp. 13141–13147.

Kumar, R, M Kook, and M Jain (2020a). "Understanding the metastable states in K-Na aluminosilicates using novel site-selective excitation-emission spectroscopy." In: *Journal of Physics D: Applied Physics* 53.46, p. 465301.

Kumar, R, M Kook, AS Murray, and M Jain (2018). "Towards direct measurement of electrons in metastable states in K-feldspar: do infrared-photoluminescence and radioluminescence probe the same trap?" In: *Radiation Measurements* 120, pp. 7–13.

Kumar, R, LIDJ Martin, Dirk Poelman, Dimitri Vandenberghe, Johan De Grave, M Kook, and M Jain (2020b). "Site-selective mapping of metastable states using electron-beam induced luminescence microscopy." In: *Scientific reports* 10.1, pp. 1–14.

Kumar, Raju, Myungho Kook, and Mayank Jain (2021b). "Sediment dating using infrared photoluminescence." In: *Quaternary Geochronology* 62, p. 101147.

Laskaris, Nikolaos and Ioannis Liritzis (2011). "A new mathematical approximation of sunlight attenuation in rocks for surface luminescence dating." In: *Journal of Luminescence* 131.9, pp. 1874–1884.

Lehmann, Benjamin, Frédéric Herman, Pierre G Valla, Georgina E King, and Rabiul H Biswas (2019). "Evaluating post-glacial bedrock erosion and surface exposure duration by coupling in situ optically stimulated luminescence and 10 Be dating." In: *Earth Surface Dynamics* 7.3, pp. 633–662.

Lehmann, Benjamin, Pierre G Valla, Georgina E King, and Frédéric Herman (2018). "Investigation of OSL surface exposure dating to reconstruct post-LIA glacier fluctuations in the French Alps (Mer de Glace, Mont Blanc massif)." In: *Quaternary geochronology* 44, pp. 63–74.

Li, Bo, Zenobia Jacobs, Richard G Roberts, and Sheng-Hua Li (2013). "Extending the age limit of luminescence dating using the dose-dependent sensitivity of MET-pIRIR signals from K-feldspar." In: *Quaternary Geochronology* 17, pp. 55–67.

Li, Bo and Sheng-Hua Li (2011). "Luminescence dating of K-feldspar from sediments: a protocol without anomalous fading correction." In: *Quaternary Geochronology* 6.5, pp. 468–479.

Lian, Olav B and Richard G Roberts (2006). "Dating the Quaternary: progress in luminescence dating of sediments." In: *Quaternary Science Reviews* 25.19-20, pp. 2449–2468.

Liritzis, I (1994). "A new dating method by thermoluminescence of carved megalithic stone building." In: *Comptes rendus de l'Académie des sciences. Série II, Mécanique, physique, chimie, sciences de l'univers, sciences de la terre* 319.5, pp. 603–610.

Liritzis, I and R Galloway (1999). "Dating implications from solar bleaching of thermoluminescence of ancient marble." In: *Journal of Radioanalytical and Nuclear Chemistry* 241.2, pp. 361–368.

Liritzis, I, P Guibert, F Foti, and M Schvoerer (1997). "The Temple of Apollo (Delphi) strengthens novel thermoluminescence dating method." In: *Geoarchaeology: An International Journal* 12.5, pp. 479–496.

Liritzis, I, GS Polymeris, and N Zacharias (2010). "Surface luminescence dating of Dragon Houses and Armena gate at Styra." In: *Mediterranean Archaeology and Archaeometry*.

Liritzis, Ioannis, George S Polymeris, Asimina Vafiadou, Athanasios Sideris, and Thomas E Levy (2019). "Luminescence dating of stone wall, tomb and ceramics of Kastrouli (Phokis, Greece) Late Helladic settlement: Case study." In: *Journal of Cultural Heritage* 35, pp. 76–85.

Liu, JF, Andrew Murray, Reza Sohbati, and Mayank Jain (2016). "The effect of test dose and first IR stimulation temperature on post-IR IRSL measurements of rock slices." In: *Geochronometria* 43.1, pp. 179–187.

Liu, Jinfeng et al. (2019). "Resetting of the luminescence signal in modern riverbed cobbles along the course of the Shiyang River, China." In: *Quaternary Geochronology* 49, pp. 184–190.

Luo, Ming et al. (2018). "A test of rock surface luminescence dating using glaciofluvial boulders from the Chinese Pamir." In: *Radiation Measurements* 120, pp. 290–297.

Lüthgens, Christopher, Eike F Rades, Lukas Bickel, and Markus Fiebig (2017). "Establishing age constraints for Middle Pleistocene glaciofluvial sediments in the European Alpine foreland-new insights from luminescence dating." In: *EGU General Assembly Conference Abstracts*, p. 15943.

Malins, AER, NRJ Poolton, FM Quinn, Ole Johnsen, and Phil M Denby (2004). "Luminescence excitation characteristics of Ca, Na and K-aluminosilicates (feldspars) in the stimulation range 5–40 eV: determination of the band-gap energies." In: *Journal of Physics D: Applied Physics* 37.10, p. 1439.

Mathworks (2017). *Image Processing Toolbox: Users' Guide (R2017b)*. URL: `https://se.mathworks.com/help/pdf_doc/images/images_tb.pdf`.

McFadden, LD, MC Eppes, AR Gillespie, and B Hallet (2005). "Physical weathering in arid landscapes due to diurnal variation in the direction of solar heating." In: *Geological Society of America Bulletin* 117.1-2, pp. 161–173.

McFee, CJ (1998). "The measurement of single grain IRSL EDs using an imaging photon detector." In: *Quaternary science reviews* 17.11, pp. 1001–1008.

Meteoexploration (2021). *meteoexploration.com*. URL: `https://www.meteoexploration.com/products/SolarCalculator.html`.

Meyer, MC, LA Gliganic, M Jain, Reza Sohbati, and D Schmidmair (2018). "Lithological controls on light penetration into rock surfaces–Implications for OSL and IRSL surface exposure dating." In: *Radiation Measurements* 120, pp. 298–304.

MittelstraSS, Dirk and Sebastian Kreutzer (2021). "Spatially resolved infrared radiofluorescence: single-grain K-feldspar dating using CCD imaging." In: *Geochronology* 3.1, pp. 299–319.

Moores, John E, Jon D Pelletier, and Peter H Smith (2008). "Crack propagation by differential insolation on desert surface clasts." In: *Geomorphology* 102.3-4, pp. 472–481.

Morgenstein, ME, Shangde Luo, T-L Ku, and J Feathers (2003). "URANIUM-SERIES AND LUMINESCENCE DATING OF VOLCANIC LITHIC ARTEFACTS." In: *Archaeometry* 45.3, pp. 503–518.

Mundupuzhakal, J, P Adhyaru, N Chauhan, H Vaghela, M Shah, B Chakrabarty, and Y Acharya (2014). "FPGA based TL OSL system with EMCCD for luminescence studies." In: *Journal of Instrumentation* 9.04, P04001.

Murray, Andrew S and Ann G Wintle (2003). "The single aliquot regenerative dose protocol: potential for improvements in reliability." In: *Radiation measurements* 37.4-5, pp. 377–381.

Murray, AS and RG Roberts (1998). "Measurement of the equivalent dose in quartz using a regenerative-dose single-aliquot protocol." In: *Radiation measurements* 29.5, pp. 503–515.

Narama, C, R Kondo, S Tsukamoto, T Kajiura, C Ormukov, and K Abdrakhmatov (2007). "OSL dating of glacial deposits during the Last Glacial in the Terskey-Alatoo Range, Kyrgyz Republic." In: *Quaternary Geochronology* 2.1-4, pp. 249–254.

Nyemann, Jacob S, Rosana M Turtos, Brian Julsgaard, Ludvig P Muren, and Peter Balling (2020). "Optical characterization of LiF: Mg, Cu, P–Towards 3D optically stimulated luminescence dosimetry." In: *Radiation Measurements* 138, p. 106390.

Olko, Pawe, ukasz Czopyk, Mariusz Kosowski, and Micha PR Waligórski (2008). "Thermoluminescence dosimetry using TL-readers equipped with CCD cameras." In: *Radiation measurements* 43.2-6, pp. 864–869.

Ou, XJ, HM Roberts, GAT Duller, MD Gunn, and WT Perkins (2018). "Attenuation of light in different rock types and implications for rock surface luminescence dating." In: *Radiation Measurements* 120, pp. 305–311.

Polikreti, K, CT Michael, and Y Maniatis (2002). "Authenticating marble sculpture with thermoluminescence." In: *Ancient TL* 20.1, pp. 11–18.

— (2003). "Thermoluminescence characteristics of marble and dating of freshly excavated marble objects." In: *Radiation Measurements* 37.1, pp. 87–94.

Pool, PJ, DG Morris, DJ Burt, RT Bell, AD Holland, and DR Smith (2005). "Application of electron multiplying CCD technology in space instrumentation." In: *Focal Plane Arrays for Space Telescopes II*. Vol. 5902. International Society for Optics and Photonics, 59020A.

Poolton, NRJ, RH Kars, J Wallinga, and AJJ Bos (2009). "Direct evidence for the participation of band-tails and excited-state tunnelling in the luminescence of irradiated feldspars." In: *Journal of Physics: Condensed Matter* 21.48, p. 485505.

Poolton, NRJ, AER Malins, FM Quinn, E Pantos, CE Andersen, L Bøtter-Jensen, O Johnsen, and AS Murray (2003). "Luminescence excitation characteristics of Ca-, Na-and K-aluminosilicates (feldspars), in the stimulation range 20–500 eV: optical detection of XAS." In: *Journal of Physics D: Applied Physics* 36.9, p. 1107.

Poolton, NRJ, KB Ozanyan, J Wallinga, AS Murray, and L Bøtter-Jensen (2002). "Electrons in feldspar II: a consideration of the influence of conduction band-tail states on luminescence processes." In: *Physics and Chemistry of Minerals* 29.3, pp. 217–225.

Prasad, Amit Kumar, Nigel RJ Poolton, Myungho Kook, and Mayank Jain (2017). "Optical dating in a new light: A direct, non-destructive probe of trapped electrons." In: *Scientific reports* 7.1, pp. 1–15.

Preusser, Frank, Detlev Degering, Markus Fuchs, Alexandra Hilgers, Annette Kadereit, Nicole Klasen, Matthias Krbetschek, Daniel Richter, and Joel QG Spencer (2008). "Luminescence dating: basics, methods and applications." In: *E&G Quaternary Science Journal* 57.1/2, pp. 95–149.

Rades, EF, R Sohbati, C Lüthgens, M Jain, and AS Murray (2018). "First luminescence-depth profiles from boulders from moraine deposits: Insights into glaciation chronology and transport dynamics in Malta valley, Austria." In: *Radiation Measurements* 120, pp. 281–289.

Randall, John Turton and Maurice Hugh Frederick Wilkins (1945). "Phosphorescence and electron traps-I. The study of trap distributions." In: *Proceedings of the Royal Society of London. Series A. Mathematical and Physical Sciences* 184.999, pp. 365–389.

Rhodes, Edward J, JS Singarayer, J-P Raynal, Kira E Westaway, and Fatima-Zohra Sbihi-Alaoui (2006). "New age estimates for the Palaeolithic assemblages and Pleistocene succession of Casablanca, Morocco." In: *Quaternary Science Reviews* 25.19-20, pp. 2569–2585.

Riedel-Lyngskær, Nicholas, Martynas Ribaconka, Mário Pó, Sune Thorsteinsson, Anders Thorseth, Carsten Dam-Hansen, and Michael L Jakobsen (2021a). "Spectral Albedo in Bifacial Photovoltaic Modeling: What can be Learned from Onsite Measurements?" In: *2021 IEEE 48th Photovoltaic Specialists Conference (PVSC)*. IEEE, pp. 0942–0949.

— (2021b). "Spectral Albedo in Bifacial Photovoltaic Modeling: What can be learned from Onsite Measurements?" In: *2021 IEEE 48th Photovoltaic Specialists Conference (PVSC)*, pp. 942–949. DOI: 10.1109/PVSC43889.2021.9519085.

Riedesel, Svenja and Martin Autzen (2020). "Beta and gamma dose rate attenuation in rocks and sediment." In: *Radiation Measurements* 133, p. 106295.

Rieser, U, MR Krbetschek, and W Stolz (1994). "CCD-camera based high sensitivity TL/OSL-spectrometer." In: *Radiation Measurements* 23.2-3, pp. 523–528.

Rood, Dylan H, Douglas W Burbank, and Robert C Finkel (2011). "Chronology of glaciations in the Sierra Nevada, California, from 10Be surface exposure dating." In: *Quaternary Science Reviews* 30.5-6, pp. 646–661.

Sellwood, EL, B Guralnik, M Kook, AK Prasad, R Sohbati, Kristina Hippe, J Wallinga, and M Jain (2019). "Optical bleaching front in bedrock revealed by spatially-resolved infrared photoluminescence." In: *Scientific reports* 9.1, pp. 1–12.

Sellwood, EL, M Kook, and M Jain (2021). "A 2D imaging system for mapping luminescence-depth profiles for rock surface dating." In: *Radiation Measurements*, p. 106697.

— (2022). "Rapid in situ assessment of luminescence-bleaching depths for deriving burial and exposure chronologies of rock surfaces." In: *Quaternary Geochronology* 67, p. 101227.

Simkins, Lauren M, Regina DeWitt, Alexander R Simms, Sophie Briggs, and Russell S Shapiro (2016). "Investigation of optically stimulated luminescence behavior of quartz from crystalline rock surfaces: A look forward." In: *Quaternary Geochronology* 36, pp. 161–173.

Simmons, Gene and Herman W Cooper (1978). "Thermal cycling cracks in three igneous rocks." In: *International Journal of Rock Mechanics and Mining Sciences & Geomechanics Abstracts*. Vol. 15. 4. Elsevier, pp. 145–148.

Simms, Alexander R, Regina DeWitt, Peter Kouremenos, and Ann Marie Drewry (2011). "A new approach to reconstructing sea levels in Antarctica using optically stimulated luminescence of cobble surfaces." In: *Quaternary Geochronology* 6.1, pp. 50–60.

Smedley, Rachel K, David Small, Richard S Jones, Stephen Brough, Jennifer Bradley, and Geraint TH Jenkins (2021). "Erosion rates in a wet, temperate climate derived from rock luminescence techniques." In: *Geochronology* 3.2, pp. 525–543.

Smith, BW, GCWS Wheeler, EJ Rhodes, and NA Spooner (1991). "Luminescence dating of zircon using an imaging photon detector." In: *International Journal of Radiation Applications and Instrumentation. Part D. Nuclear Tracks and Radiation Measurements* 18.1-2, pp. 273–278.

Sohbati, Reza, Mayank Jain, and Andrew Murray (2012a). "Surface exposure dating of non-terrestrial bodies using optically stimulated luminescence: A new method." In: *Icarus* 221.1, pp. 160–166.

Sohbati, Reza, Jinfeng Liu, Mayank Jain, Andrew Murray, David Egholm, Richard Paris, and Benny Guralnik (2018). "Centennial-to millennial-scale hard rock erosion rates deduced from luminescence-depth profiles." In: *Earth and Planetary Science Letters* 493, pp. 218–230.

Sohbati, Reza, Andrew S Murray, Jan-Pieter Buylaert, Nelson AC Almeida, and Pedro P Cunha (2012b). "Optically stimulated luminescence (OSL) dating of quartzite cobbles from the T apada do M ontinho archaeological site (east-central P ortugal)." In: *Boreas* 41.3, pp. 452–462.

Sohbati, Reza, Andrew S Murray, Melissa S Chapot, Mayank Jain, and Joel Pederson (2012c). "Optically stimulated luminescence (OSL) as a chronometer for surface exposure dating." In: *Journal of Geophysical Research: Solid Earth* 117.B9.

Sohbati, Reza, Andrew S Murray, Mayank Jain, Jan-Pieter Buylaert, and Kristina J Thomsen (2011). "Investigating the resetting of OSL signals in rock surfaces." In: *Geochronometria* 38.3, pp. 249–258.

Sohbati, Reza, AS Murray, N Porat, Mayank Jain, and U Avner (2015). "Age of a prehistoric Rodedian cult site constrained by sediment and rock surface luminescence dating techniques." In: *Quaternary Geochronology* 30, pp. 90–99.

Souza, Priscila E, Reza Sohbati, Andrew S Murray, Lars B Clemmensen, Aart Kroon, and Lars Nielsen (2021). "Optical dating of cobble surfaces determines the chronology of Holocene beach ridges in Greenland." In: *Boreas* 50.2, pp. 606–618.

Souza, Priscila E, Reza Sohbati, Andrew S Murray, Aart Kroon, Lars B Clemmensen, Mikkel U Hede, and Lars Nielsen (2019). "Luminescence dating of buried cobble surfaces from sandy beach ridges: a case study from Denmark." In: *Boreas* 48.4, pp. 841–855.

Spooner, Nigel A (1994). "The anomalous fading of infrared-stimulated luminescence from feldspars." In: *Radiation Measurements* 23.2-3, pp. 625–632.

Stanley, Philip E (1983). "Instrumentation for luminescence methods of analysis." In: *TrAC Trends in Analytical Chemistry* 2.11, pp. 248–251.

Sunta, C. M., W. E.F. Ayta, J. F.D. Chubaci, and S. Watanabe (2005). "A critical look at the kinetic models of thermoluminescence - I. First order kinetics." In: *Journal of Physics D: Applied Physics* 38.1, pp. 95–102. ISSN: 00223727. DOI: 10.1088/0022-3727/38/1/016.

Theocaris, PS, I Liritzis, and RB Galloway (1997). "Dating of two Hellenic pyramids by a novel application of thermoluminescence." In: *Journal of Archaeological Science* 24.5, pp. 399–405.

Thomsen, Kristina J, Andrew S Murray, and Mayank Jain (2011). "Stability of IRSL signals from sedimentary K-feldspar samples." In: *Geochronometria* 38.1, pp. 1–13.

Thomsen, Kristina Jørkov, M Kook, AS Murray, Mayank Jain, and Torben Lapp (2015). "Single-grain results from an EMCCD-based imaging system." In: *Radiation Measurements* 81, pp. 185–191.

Thomsen, Kristina Jørkov, Andrew S Murray, Mayank Jain, and Lars Bøtter-Jensen (2008). "Laboratory fading rates of various luminescence signals from feldspar-rich sediment extracts." In: *Radiation measurements* 43.9-10, pp. 1474–1486.

Tsakalos, Evangelos, Aiming Lin, Maria Kazantzaki, Yannis Bassiakos, Takafumi Nishiwaki, and Eleni Filippaki (2020). "Absolute Dating of Past Seismic Events Using the OSL Technique on Fault Gouge MaterialA Case Study of the Nojima Fault Zone, SW Japan." In: *Journal of Geophysical Research: Solid Earth* 125.8, e2019JB019257.

Vafiadou, Asimina, Andrew S Murray, and Ioannis Liritzis (2007). "Optically stimulated luminescence (OSL) dating investigations of rock and underlying soil from three case studies." In: *Journal of Archaeological Science* 34.10, pp. 1659–1669.

Wallinga, J, A S. Murray, and L Bøtter-Jensen (2002). "Measurement of the dose in quartz in the presence of feldspar contamination." In: *Radiation Protection Dosimetry* 101.1-4, pp. 367–370.

Wallinga, Jakob and Alastair C Cunningham (2015). "Luminescence dating, uncertainties and age range." In: *Encyclopedia of Scientific Dating Methods*. Springer Netherlands, pp. 440–445.

Wintle, AG (1977). "Detailed study of a thermoluminescent mineral exhibiting anomalous fading." In: *Journal of Luminescence* 15.4, pp. 385–393.

Wintle, AG and DJ Huntley (1980). "Thermoluminescence dating of ocean sediments." In: *Canadian Journal of Earth Sciences* 17.3, pp. 348–360.

Yi, Shuangwen, Jan-Pieter Buylaert, Andrew S Murray, Huayu Lu, Christine Thiel, and Lin Zeng (2016). "A detailed post-IR IRSL dating study of the Niuyangzigou loess site in northeastern China." In: *Boreas* 45.4, pp. 644–657.